Investigation et caracterisation de différents homologues de transporteurs ADP/ATP

Aleksandra Woźnicka-Misăilă

Communauté
UNIVERSITÉ Grenoble Alpes

THÈSE

Pour obtenir le grade de

DOCTEUR DE LA COMMUNAUTE UNIVERSITE GRENOBLE ALPES

Spécialité : **BIOLOGIE STRUCTURALE ET NANOBIOLOGIE**

Arrêté ministériel : 7 août 2006

Présentée par

Aleksandra Woźnicka-Misăilă

Thèse dirigée par Dr. **Stéphanie Ravaud**

préparée au sein du **Laboratoire : Institut de Biologie Structurale (Grenoble)**
dans **l'École Doctorale : Chimie et Science du Vivant**

An investigation and characterization of different ADP/ATP Carrier homologs

Thèse soutenue publiquement le **19 Septembre 2016**
devant le jury composé de :

Dr. Bruno Miroux Directeur de Recherche, IBPC, Paris	Rapporteur
Dr. Gergely Katona Professeur associé, Université de Gothenburg, Göteborg	Rapporteur
Dr. Cécile Breyton Directeur de Recherche, IBS, Grenoble	Examinateur
Dr. Jean-Michel Jault Directeur de Recherche, IBCP, Lyon	Examinateur
Dr. Stéphanie Ravaud Maître de Conférences UGA, IBS, Grenoble	Directrice de thèse

Dedication

To my son, Jacob

Acknowledgments

I would like to express my special thanks of gratitude to my supervisor Stéphanie Ravaud for great support, patience, encouragement, all precious advices and for guiding me during my all PhD. I would like to thank her additionally for great understanding and being a good friend in all performed work.

I would like to thank Eva Pebay-Peroula for giving me this golden opportunity to develop my skills in this field, for help and giving each time good ideas how to improve (always can be better!).

I would like to also express my best regards to all the members of NanoMem network thanks to whom I could have developed my skills and knowledge.

I would like to express my big thanks to Delphine Baud for great help in functional activity experiments, work would not go so well without her.

I would like to thank Manfred Burghammer, and Anastasya Shilova from ESRF for great collaboration in one of the projects. I would like to acknowledge Hugues Nury, for helping me to understand many new things in crystallography and data analysis.

I would like to thank Isabel de Moraes, Jacques-Philippe Colletier and François Dehez for encouragement and help in understanding the main point.

I would like to thank people from my team for their valuable advices and willingness of help, collegues from Cell-Free platform, especially Céline Juillan-Binard and Lionel Imbert.

I would like to also acknowledge Christine Ebel, Aline le Roy and Caroline Mas for helping in SEC-MALLS, AUC and CD data analysis.

Finally I would like to express my great thanks to my Family, my husband Andrei, my son Jacob and of course my parents. Without all of them this thesis would not arise.

Additionally, I would like to emphasize that the time during my PhD was special and unforgettable and fulfilled me with a lot of new experiences and friendships.

Abbreviations

AA – Amino Acid mix
AAC – ADP/ATP Carrier
ABC – an Adenosine triphosphate-Binding Cassette transporters
AcrB – the Bacterial Multidrug Efflux Transporter
ADP – Adenosine DiPhosphate
adPEO – autosomal dominant Progressive Ophtalmoplegia
AGC – mitochondrial Aspartate/Glutamate Carrier
AMP – Adenosine MonoPhosphate
ANT – an Adenosine Nucleotide Transporter
APC – mitochondrial ATP-Mg^{2+}/P_i Carrier
ATP – Adenosine TriPhosphate
AUC – Analytical UltraCentrifugation
BA – Bongkrekic Acid
bAAC – bovine ADP/ATP Carrier
BCA - BiCinchoninic Acid assay
BtuCD – *E. coli* vitamin B12 transporter (ABC transporter, Type II)
BtuF – *E. coli* periplasmic binding protein
bR - bacterioRhodopsin
BSA – Bovine Serum Albumine
CAC – mitochondrial Carnitine/Acylcarnitine Carrier
(C)ATR – (Carboxy)ATRactyloside
CD – Circular Dichroism
CIC – mitochondrial Citrate/malate Carrier
CPA^1 – Cation Proton Antiporter
c-state – cytosolic conformational state
DARP – Designed Ankyrin-Repeat Protein
DC – Desalting Column
DIC – mitochondrial DIcarboxylate Carrier
E1 – high affinity state for Na^+
E2 – high affinity state for K^+
EB – Elution Buffer
ECF – Energy-Coupling Factor transporters
EcfT – Energy-coupling factor transporter Transmembrane domain
E1P/E2P – phosphorylated intermediate states
EQB – EQuilibration Buffer
ER – Endoplasmic Reticulum
FSEC – Fluorescence Size Exclusion Chromatography
GC – mitochondrial Glutamate Carrier
GLIC – pentameric Ligand-Gated Ion Channel
GLUT1 – GLUcose Transporter 1
GltPh – Na^+-coupled aspartate transporter
GPCRs – G-Protein Coupled Receptors
H – transmembrane Helix
h – amphipathic, cytosolic helix
hAAC – human ADP/ATP Carrier
Hsc70 – Heat-shock cognate 70
Hsp90 – Heat-shock protein 90
IM – InterMembrane space
LacY – Lactose transporter Y
LB – Lysogeny Broth
LeuT – Na^+-coupled amino acid transporter
MAM – Mitochondrial Associated ER Membrane
MBP – Maltose Binding Protein
MCF – Mitochondrial Carrier Family
MCs – Mitochondrial Carriers
MDR – MultiDrug Resistance
Mj*NCX – sodium/calcium (Na^+/Ca^{2+}) eXchanger from *Methanococcus jannaschii
MMP – Matrix MetalloProteinase
MOMP – Mitochondrial Outer Membrane Permabilization
MsbA – *E. coli* lipid transporter (ABC transporters, Type III)
mRNA – messenger RNA
m-state – matrix conformational state

mtDNA – mitochondrial DNA
mtERs – mitochondrial Estrogen Receptors
NBDs – Nucleotide Binding Domains
NhaA – *E. coli* Na^+/H^+ Antiporter
NiNTA – Nickiel Resin
NKCC – Na^+-K^+-Cl^- Co-transporter
ODC – mitochondrial OxoDicarboxylate Carrier
OGC – mitochondrial OxoGlutarate Carrier
ORC – mitochondrial ORnitine/citruline Carrier
Oxa1 – mitochondrial Oxidase assembly 1
PCR – Polymerase Chain Reaction
PiC – mitochondrial Phosphate/H^+ Carrier
PM_AAC – Plasma Membrane ADP/ATP Carrier
PM-ANT1 – Plasma Membrane Adenosine Nucleotide Transporter 1
PMP – Plasma Membrane Protein
PyC – mitochondrial Pyruvate/H^+ Carrier
RB – Resolubilization Buffer
Rf – Restriction free cloning
RT – Room Temperature
SAMC – cytosolic S-AdenosylMethionine Carrier
SANS – Small-Angle Neutron Scattering
SB – Solubilization Buffer
Sav1866 – ABC transporter (Type III) from *S. aureus*
SDS-PAGE – SDS-PolyAcrylamid Gel Electrophoresis
SEC – Size Exclusion Chromatography
SSS – Solute Sodium Symporters
TAE – Tris-Acetate-EDTA buffer
TB – Terrific Broth medium
TIM – Translocase of the Inner Membrane
TM – TransMembrane
TMD – TransMembrane Domain
TOM – Translocase of the Outer Membrane
TPC – Thiamine Pyrophosphate Carrier
UCP – UnCoupling Protein
VDAC – Voltage Dependent Ion Channel protein
WB – Wash Buffer
WR – Working Reagent
vSGLT – Sodium-GaLactose Transporter from *Vibrio parahaemolyticus*
X-Fel – X-ray Free electron laser
yAac2 or 3 – yeast Adp/atp carrier 2 or 3

List of Figures

List of Tables

Table of Contents

Résumé

L'objectif principal de ce projet de thèse était d'obtenir de nouvelles données structurales sur les transporteurs ADP/ATP mitochondriaux et de développer des outils pour les approches de micro- et nano-cristallographie appliquées à la biologie structurale des protéines membranaires.

Le rôle principal du transporteur ADP/ATP (AAC) est d'importer et d'exporter respectivement de l'ADP^{3-} et l'ATP^{4-} à travers la membrane mitochondriale interne, entre l'espace intermembranaire et la matrice. AAC est le transporteur mitochondrial le mieux caractérisé de toute cette famille de protéines. De nombreuses études ont été menées pour caractériser sa fonction et sa structure. Toutefois, les données structurales n'étant disponibles que pour une conformation de la protéine, de nombreuses questions fondamentales notamment sur les différents états conformationnels adoptés par la protéine au cours du processus de transport restent encore posées. Dans cette thèse, nous avons étudié les 4 isoformes humaines d'AAC. Elles sont impliquées dans diverses maladies génétiques, mais jouent également un rôle dans la cancérogenèse. Cette thèse décrit ainsi en détail la caractérisation structurale et fonctionnelle de ces protéines et leur comparaison. C'est est une étape essentielle pour définir leurs propriétés, et constitue un point de départ précieux dans le développement de nouvelles thérapies.

Le domaine de la biologie structurale ne cesse de connaître de nouveaux développements, comme c'est le cas par exemple avec l'avènement de la cristallographie sérielle. Il y a donc un besoin constant de nouvelles approches notamment pour la préparation des échantillons, leur montage sur les lignes de lumière et les collectes de données afin de continuer à améliorer la qualité des données collectées au synchrotron. Ainsi, notre objectif était d'utiliser différents échantillons de protéines membranaires pour développer de nouvelles techniques de cristallisation et de montage d'échantillons sur les lignes de lumière afin de préserver au mieux la qualité des échantillons tout en permettant des collectes de données plus rapides, plus efficaces et plus simples.

Summary

The main objective of this PhD project was to gain new structural data on the mitochondrial ADP/ATP carriers and develop tools for micro- and nano-crystallography approaches applied to membrane protein structural biology.

The main role of the ADP/ATP carrier (AAC) is to import and export ADP^{3-} and ATP^{4-} respectively between the intermembrane space and the matrix through the inner mitochondrial membrane. AAC is the best characterized among all mitochondrial carriers. Much has been done to investigate its function and structure. However, since structural data are only available for one conformation of the protein some fundamental questions about the different conformational states adopted during the transport process still need to be answered.

In this thesis we considered 4 human AAC homologs as a main target. They are involved in different genetic diseases but play also a role in cancerogenesis. This thesis describes and compares in detail the functional and structural characterization of the human AAC isoforms. It was an essential step to give insight into their native properties and is a precious starting point for the drug development field.

Since the structural biology field is rapidly developing especially in serial crystallography techniques, there are more and more new applications for samples preparation, mounting and measurements in order to improve the quality of the data collected at the synchrotrons. Hence, our second objective was to use different membrane protein samples to develop new crystal-friendly crystallization set up combined with different sample environment on the beamline toward faster, more efficient and simpler data collection.

CHAPTER I

1 Introduction

1.1 Membrane transport

The cell is the smallest unit that exhibits all the molecular activity that underlies the transport processes. At the same time the cell is the largest unit that is common to all of the tissues and organs that perform all of the transport processes necessary to life. Considering that fact in the hierarchy of scale, cells are the bridge between molecular biology and physiology[1] (see Fig. 1).

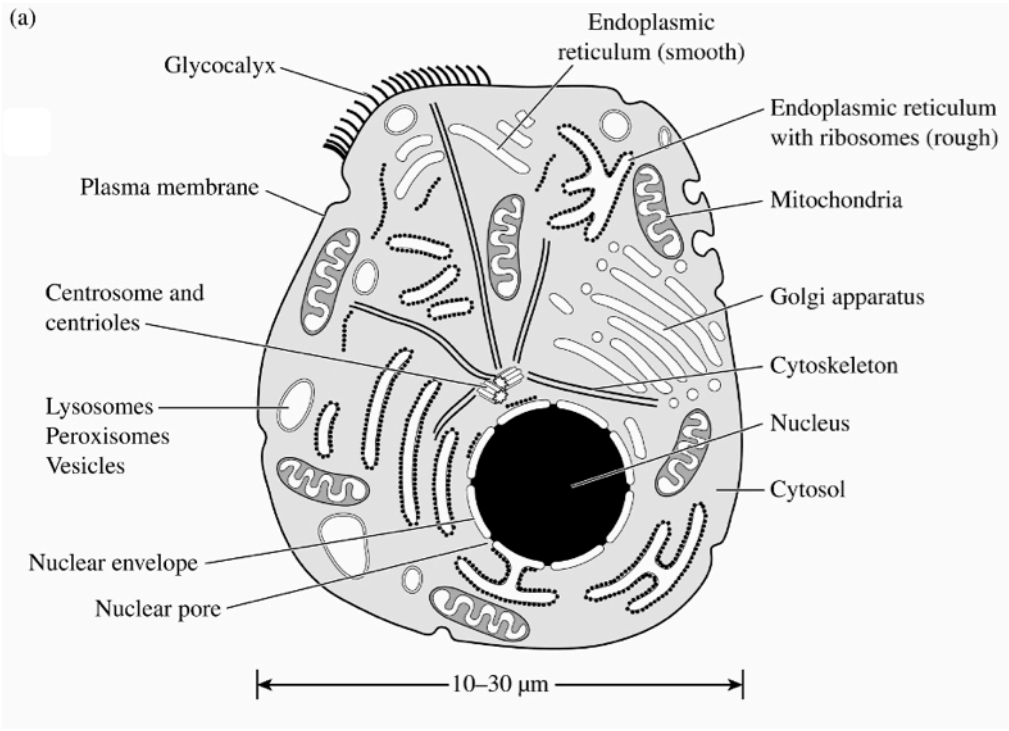

Figure 1 Model of the animal cell and some of its contents[1].

Cellular transport is a movement of compounds across the outlying cell membrane. It is an essential process since 1) it allows the cell to uptake and release many different molecules involved in its biological functions, for instance the uptake and release of the oxygen by red blood cells 2) it regulates the concentration of molecules and ions according to the metabolic needs *i.e.* by increasing the transport of glucose in the muscles during muscle contraction. Cell membranes are a perfect example of an organized interface with the outside world that establishes different mechanisms and behaviors to adapt to the

environmental circumstances. The differences in ionic composition across the membranes (see Table 1) influence the electrical behavior of the cells that underlies the function of nerves and muscles. Moreover, the whole family of the receptor proteins sense the chemical and physical environmental changes and initiate the cell response to it[1].

Component	Intracellular concentration (mM)	Extracellular concentration (mM)
Cations		
Na^+	12	145
K^+	140	4
Mg^{2+}	0.8	1.5
Ca^{2+}	0.0001	2
H^+	6.3×10^{8}	4×10^{8}
Anions		
Cl^-	5	110
HCO^{3-}, PO_4^{3-}, proteins, nucleic acids	148	42

Table 1 Intracelluar and extracellular concentrations of different ions in the human cell environment[1].

The structure of the cell membranes in the higher organisms share a common organization, to which specific components are added to meet the particular requirements of specific cell type and function of a tissue[1].

The main components of the cell membranes are proteins and lipids. The ratio between proteins/lipids varies considerably between different species but also within a single specie. Similarly the contribution of different lipids, for instance the cholesterol/phospholipid ratio can vary as well. The types of phospholipids (lipids with a phosphate group as a polar head and two long nonpolar hydrocarbon tails (see Fig. 2) that are usually the primary lipid component of each membrane can also be different from one cell to the other[1].

In terms of proteins, their amount far exceeds the number of lipids. Most of them are ion and water channels, carriers, receptors and gap junction proteins. Many of them are also associated to the cell membranes *via* amphipathic interactions (molecules have both polar (hydrophilic) and nonpolar (hydrophobic) elements) or lipid anchoring for example.

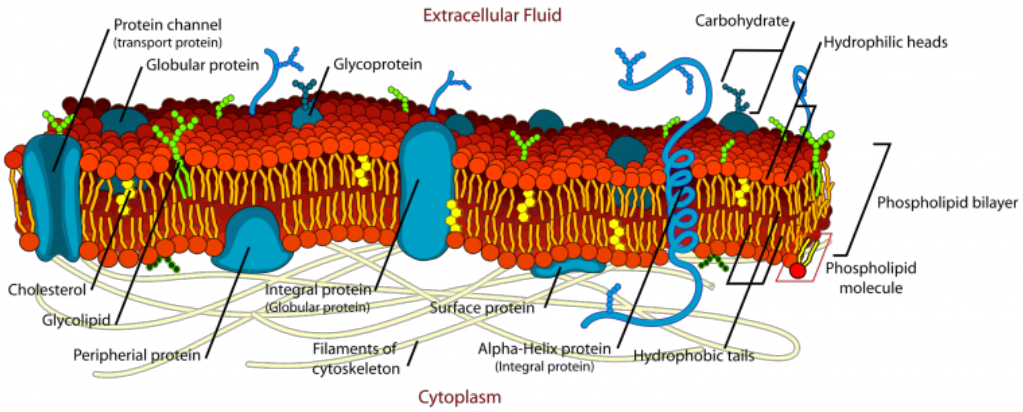

Figure 2 The mosaic model of the cell membrane. The proteins embedded in the bilayer can extend to a considerable distance into the aqueous phases adjacent to the membrane (picture adapted from: http://www.macroevolution.net/fluid-mosaic-model.html).

The cell membranes are crossed by various solutes whose polarities range significantly from strongly hydrophobic to strongly hydrophilic. These compounds differ also in terms of size. Therefore each cell membrane must provide a variety of transport pathways to accommodate the different kinds of substrates. The cell membranes (in prokaryotes and eukaryotes) are defining and controlling these transport pathways and thus the amount of the exchanged substrates[1]. In the eukaryotic cells the transport processes occur also between organelles and the cytoplasm. Substrate exchange between the organelles in the cell is essential in order to maintain cell well-being vitality. Hence, each organelle membrane possesses variety of membrane proteins and different composition of lipids to meet all of the cell-needs requirements.

1.1.1 Simple and Facilitated diffusion

In order to carry different components throughout the cells- and organelles-membranes different models of cell transport have been developed.

Simple diffusion refers to the transport of small and non-charged molecules or lipid soluble molecules that freely pass through the membrane and squeeze between the phospholipids to enter or to leave the cell. Compounds which are transported by simple diffusion (for instance oxygen or carbon dioxide) move from the areas of high concentration to the areas of low concentration (termed as a concentration gradient) (see Fig. 3)[2].

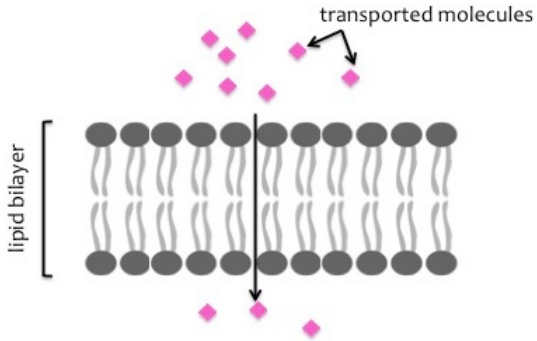

Figure 3 Illustration of the simple diffusion transport.

Osmosis names the simple diffusion of water molecules along their concentration gradient.

Facilitated diffusion refers to a passive–mediated transport of molecules or ions across a membrane via specific transmembrane integral proteins[2]. Passive transport does not require any energy such as ATP hydrolysis. Molecules and ions move along their concentration gradient. Facilitated diffusion varies from free diffusion process in three main principles: 1) the transport relies on molecular binding between the cargo and the membrane-embedded proteins, channels or carriers (see Fig. 4); 2) facilitated diffusion process can be saturated at a certain substrate concentration; 3) the temperature dependence in facilitated diffusion is significant since it is associated with activated binding event.

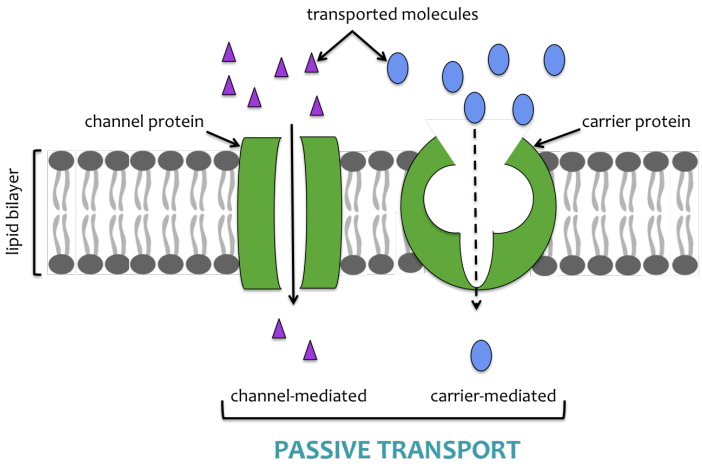

Figure 4 Illustration of passive transport pathways by channel or carrier proteins

Passive transport mechanism across the membrane is essentially

associated with the type and the size of the carried substrates. Channel proteins in most of the cases open and close and thus deregulate the flow of ions (Na^+, Ca^{2+}, K^+, and Cl^-) and small molecules (H_2O, D-glucides, polypeptides and nucleotides) across the membrane while carriers in order to transport the cargo, change their conformational state (see Fig 5).

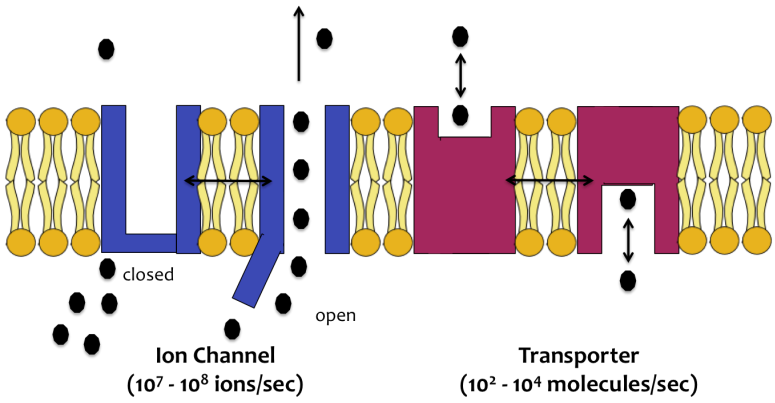

Figure 5 Representation of different passive transport mechanisms conducted by channels and carrier proteins.

The nature of the substrates transported by channels depends on two parameters: the diameter of the channel pore and the electrostatic forces within the channel. Different types of channel proteins can be distinguished: non-gated (transport of K^+ and Cl^- ions); gated (transport of Na^+ and Ca^{2+} ions); voltage-gated (opening and closing depend on the membrane potential, for instance voltage-gated Na^+, Ca^{2+}, K^+, and Cl^- ion channels which provide split second regulation in the nervous system and in muscles); ligand-gated (opening in response to the binding of an extracellular or intracellular regulatory molecule, for instance acetylcholine receptor); mechanically-gated (opening in response to the mechanical movement of an adjacent structure, for instance touch sensors in the skin); temperature-gated (opening in response either to an increase or a decrease in temperature, for instance in sensory neurons)[3].

Larger molecules such as glucose or amino-acids are transported by transmembrane carrier proteins such as permeases that change their conformational state depending if they carry a cargo or not. One of the most important examples in this class of proteins is the glucose transporter. Its membrane expression is controlled by the insulin concentration in some cells.

When the amount of insulin increases, the number of active glucose transporters is increasing as well and more glucose molecules enter the cells (see Fig. 6)[3].

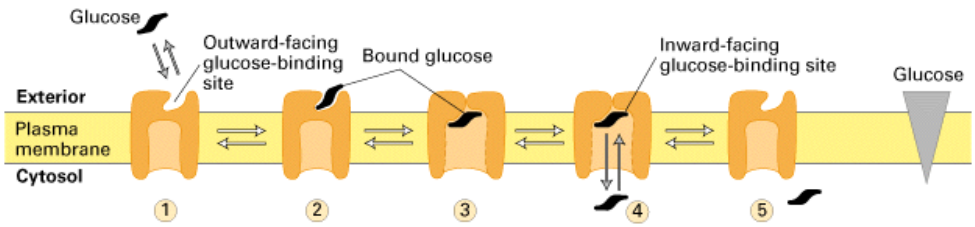

Figure 6 Transport of the glucose across the cell membrane by glucose transporter is an example of facilitated diffusion (picture adapted from: http://www.zoology.ubc.ca.htm).

GLUT1 is the glucose transporter, which enables the transport of glucose inside the erythrocytes and is the main supplier of this substrate to the brain and other organs. The crystal structure of the full-length human GLUT1 uniporter was solved at 3.2 Å resolution in an inward-open conformation[4].

1.1.2 The secondary active transport – symport and antiport

Three types of transporters are defined: uniporters (see glucose transporter), symporters and antiporters (see Fig. 7).

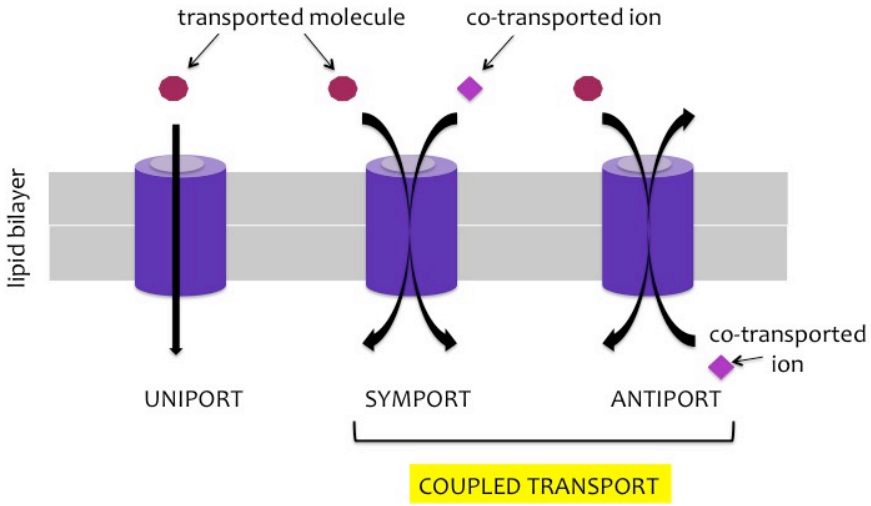

Figure 7 Representation of three different models of membrane transport: uniport, symport and antiport.

Symporters and antiporters are co-transporters which carry at least two different types of molecules across the cell membrane at the same time, in the same or in opposite directions respectively. Co-transporters belong to the secondary active transport membrane proteins group. Here, one of the molecules

is transported against its concentration gradient and the energy required for its transport across the cell membrane is brought by the co-transport of the other molecule along its concentration gradient (see Fig. 8).

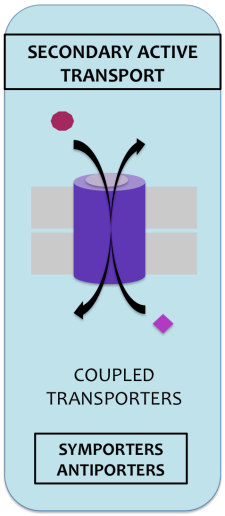

Figure 8 Symporters and antiporters are secondary active transporters.

1.1.2.1 Symporters

One example of symporter protein is the Na^+-K^+-Cl^- co-transporter (NKCC)[5,6]. The protein operates in conjunction with the Na^+ pump, a K^+ channel and a Cl^- channel to carry out the epithelial salt movement. They maintain electro-neutrality by moving two positively charged ions (Na^+ and K^+) alongside two molecules of a negatively charged solute, Cl^- in the following ratio: 1 Na^+ : 1 K^+ : 2 Cl^-.

Another known example of symporter is the sodium/galactose symporter that transport galactose while Na^+ electrochemical gradient is the main driven force for the symport. The structure of the *Vibrio parahaemolyticus* protein (vSGLT) was solved in an inward-open conformation first at 3 Å resolution[7] and later at 2.7 Å[8]. vSGLT possesses 14 transmembrane (TM) helices and a galactose molecule is bound in the center of the cavity (see Fig. 9A and B). Na^+/substrate stoichiometry is 1:1 for vSGLT protein but this ratio varies amongst solute sodium symporters (SSS). The precise binding position of Na^+ was not easy to establish since Na^+ and water molecule electron densities look similar. Nevertheless based on the comparison with the LeuT structure[9], the sequence conservation amongst SSS proteins and mutational analysis, the Na^+-binding

position was identified at the intersection of TM2 and TM9 approximately 10 Å away from the substrate–binding site (see Fig. 9C and D)[7].

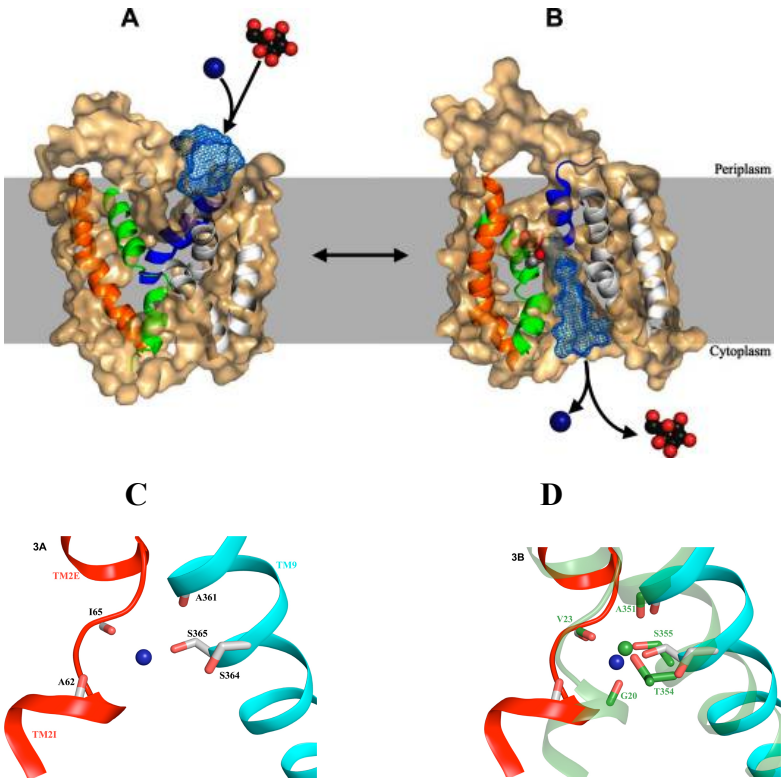

Figure 9 Symport of Na^+ and galactose via vSGLT transporter A) model of the vSGLT structure in the outward-facing position and viewed from the membrane plane showing the extracellular cavity (blue mesh), B) structure of vSGLT protein in the inward-facing position viewed from the membrane and showing intracellular cavity (blue mesh). Helices depicted in orange (TM3), green (TM7), and blue (TM11) present structural rearrangement, helices depicted in white are showing little movement. Surface is presented in beige. Galactose is shown as red and black spheres (O and C atoms respectively). Sodium ion is depicted in blue, C) Proposed Na^+-binding site. Residues involved in the Na^+ binding are depicted as sticks colored by atom type, red helix is representing TM2, cyan – TM9, D) Superposition of Na^+- binding site from LeuT structure[9] (green) and proposed Na^+- binding site of vSGLT protein[7].

1.1.2.2 Antiporters

One well–known and interesting example of an antiporter is the sodium/calcium (Na^+/Ca^{2+}) exchanger (NCX). The crystal structure of NCX from *Methanococcus jannaschii* (Mj) was solved at 1.9 Å resolution (crystals were grown in lipidic cubic phase – LCP) in an outward–facing conformation. The protein contains 10 transmembrane helices and the two halves of MjNCX share a similar structure with opposite orientation. Four ion–binding site clusters are placed in the center of the protein structure. One site is specific for one Ca^{2+} ion and the other three for three Na^+ ions. From the extracellular side two ways

allow Na^+ and Ca^{2+} to access the central ion–binding sites (see Fig. 10 A, B, C and D)[10].

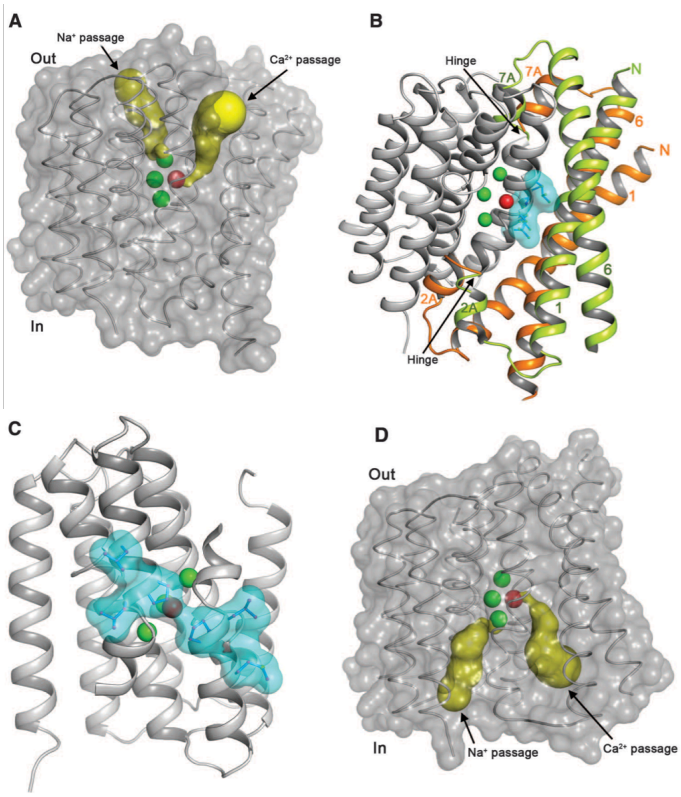

Figure 10 The outward–inward conformational change of MjNCX (A) The surface of MjNCX structure presents two independent external passages (yellow) for both ions to access the central ion–binding sites (green spheres – Na^+ and red – Ca^{2+}). (B) Side view of structural comparison of the outward–facing conformation (orange) and inward–acing protein conformation (green). Gray color represents the core part of the protein that remains the same in both conformations. The light blue color represents the residues that create the central hydrophobic patch. (C) The central hydrophobic patch (light blue) with transmembrane domains – 1, 2A, 6 and 7A removed for clarity. (D) The inward–facing protein conformation showing two independent ways (yellow) for intracellular ion access to the central ion–binding sites[10].

The structural mechanism of Na^+/Ca^{2+} exchange highly depends on NCX conformational state and on the alternating accessibility of the four central ion–binding sites (that have different specifity). Under physiological conditions the Ca^{2+} site is only specific to Ca^{2+} binding, whereas the other three are designed for Na^+ binding. While the Ca^{2+} site is alternatively accessible from each side of the protein, the three Na^+ sites are aligned in a winding single file with only one being accessible at the external site when outward-facing and at the internal site when inward-facing. The position of those two Na^+-specific sites on both extremities ensures the selective and bidirectional Na^+/Ca^{2+}-exchange function of NCX (see Fig. 11)[10].

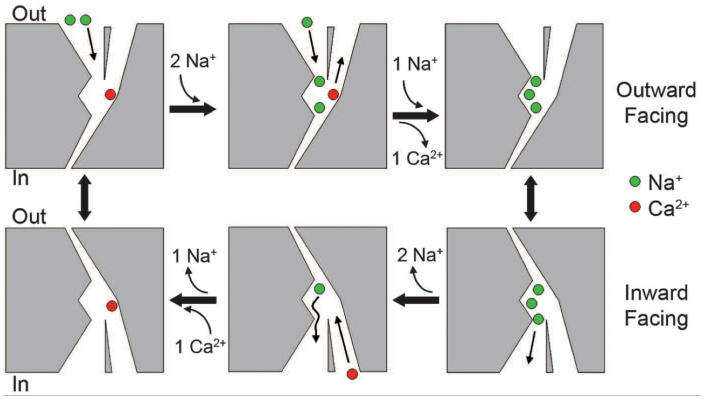

Figure 11 Cartoon representation of Na^+ and Ca^{2+} exchange of NCX in the classical 3 Na^+:1 Ca^{2+} mode[10].

Another good example of antiport is the Na^+/H^+ antiporter (NhaA transporter) for pH and Na^+ homeostasis at alkaline pH in *Escherichia coli* and many other enterobacteria. NhaA is a member of a very large family of secondary transporters, the monovalent cation-proton antiporter superfamily (CPA). NhaA exchanges 2 H^+ for 1 Na^+ (or 1 Li^+) ion. The crystal structure of NhaA was solved at 3.45 Å resolution and consists in 12 transmembrane helices with the amino- and carboxy-terminal sites facing the cytoplasm. NhaA protein shares a very strong dependence on pH with many other prokaryotic and eukaryotic antiporters (see Fig. 12)[11,12].

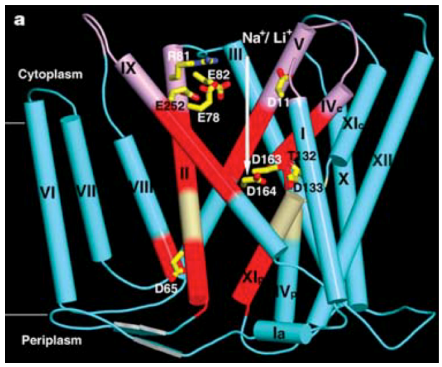

Figure 12 Model of the Na^+/H^+ (NhaA) transporter presented with the substrate passage and the periplasmic barrier. The transmembrane helices lining the cytoplasmic and the periplasmic cation passage are highlighted by colors in the cylinder representation. Fully hydrated Na^+/Li^+ can diffuse into the upper zone of the cytoplasmic funnel (light purple) but they can also enter from the lower part of it (red) or the periplasmic funnel (red). The barrier between the passages is colored in cream[11].

1.1.3 The primary active transport

The primary or direct active transport is a transport that requires external energy to allow a molecule to cross a membrane against its concentration gradient. The source of energy can be of different type: chemical

energy (such as from ATP hydrolysis), redox energy (for instance the reduction of NADH –used to allow the proton movement across the inner mitochondrial membrane against protons concentration gradient) or light energy (used by proteins involved in photosynthesis, the photons energy allows to create a proton gradient across the thylakoid membrane and also to generate NADPH)[13].

Most of the membrane proteins that perform primary active transport belong to ATPases, ABC transporters but also proton pumps and bacterial rhodopsins families (see Fig. 13).

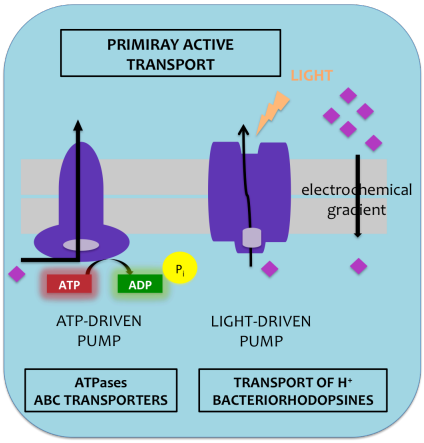

Figure 13 Models of primary active transport. ATPases, ABC Transporters, bacteriorhodopsins belong to the primary (direct) active transport proteins that are driven by ATP or light respectively.

1.1.3.1 P – type ATPases

In the 1950s a Danish scientist, Jens Christian Skou, discovered the sodium–potassium pump and was awarded with Nobel Prize in 1997. It marked an important step forward the understanding of how ions get into and out of the cells. It was particularly significant for nervous cells, which depend on this pump to respond to a variety of different impulses.

The sodium–potassium pump (Na^+/K^+ - ATPase) is one of the well–know example of primary active transport. The Na^+/K^+ -ATPase is present and widely expressed in all mammalian cells. It belongs to the P–type ion–translocating ATPases and its role is to maintain the electrochemical gradient of Na^+ and K^+ ions across the plasma membrane by exporting Na^+ ions outside the cell and importing K^+ ions inside of the cell both against their concentration gradient[14].

Na^+/K^+ ATPase is a protein complex composed of one large α subunit (110 kDa) and two smaller ones – β (80 kDa) and γ (8 kDa) (see Fig. 14A). During

the ATP–driven cycle three cytoplasmic Na^+ ions are exported in exchange with two extracellular K^+ ions through alternating E1/E1P and E2P/E2 states (see Fig. 14B) where E1 and E2 describe high affinity states for Na^+ and K^+ ions respectively and P designs a phosphorylated state. The binding of an ATP molecule and intracellular Na^+ ions stimulate the phosphorylation of one aspartic acid residue (Asp 369 – in the α1 isoform from pig) forming the sodium – occluded (Na_3)E1P – adenosine diphosphate (ADP) state. Afterwards an ADP is released and conformational changes lead to the opening of the extracellular pathway in the E2P state; Na^+ is then released and the binding of a K^+ ion stimulates the dephosphorylation forming the potassium–occluded (K_2)E2 state. Afterwards the subsequent ATP binding and the cytoplasmic release of K^+ ions lead to the sodium–bound E1 state and the cycle is repeated (see Fig. 14B)[14].

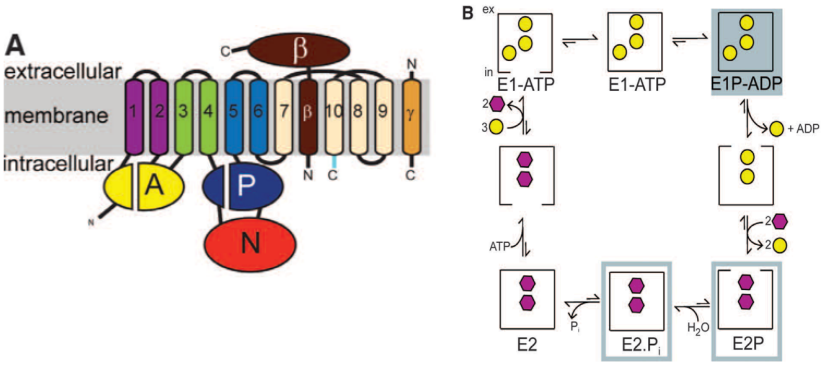

Figure 14 Na^+/K^+ ATPase (A) The α domain of the Na^+/K^+ ATPase is the major catalytic unit and it contains three cytoplasmic parts: the A (actuator, depicted in yellow), N (nucleotide binding – in red), and P (phosphorylation – in blue). The transmembrane domain consists in ten helices αM1 – α M10 and surrounds the ion–binding sites. The C–terminal helices are shown in wheat color and the α-Cterminal in cyan. The mobile parts of the transmembrane domain – αM1 – M2, αM3 – M4, αM5 – M6 are presented in purple, green, and blue respectively. The β domain is shown in brown and it consists in one transmembrane helix (βM) and one highly glycosylated extracellular domain that is associated with αM7 and αM10 helices. (B) Cartoon representation of the Na^+/K^+-ATPase cycle. Yellow circles and purple hexagons represent the Na^+ and K^+ ions respectively. E1P/E2P indicate phosphoenzyme intermediates. Closed, light–blue frames represents the occluded states. The "ex" and "in" refer respectively to the extracellular and intracellular sides of the membrane. The gray shaded box represents the state in which the crystal structure of the protein was solved[14].

The crystal structure of the Na^+-bound Na^+/K^+-ATPase was solved at 4.3 Å resolution. Comparing the Na^+-bound state with the K^+-bound state, large conformational changes are observed in the α domain while β and γ subunits structures seem to be conserved (see Fig. 15 A and B)[14].

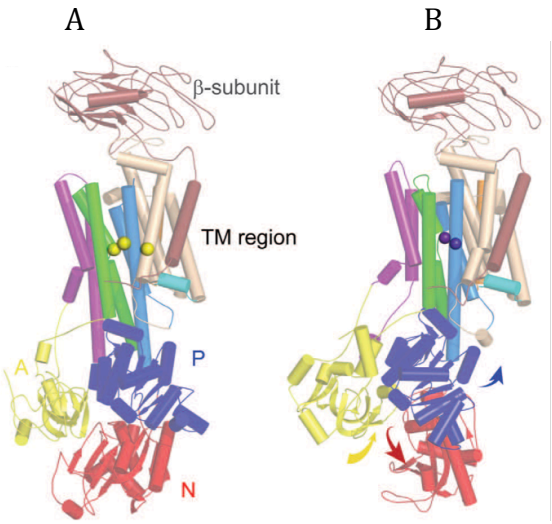

Figure 15 The crystal structure of the Na+ bound Na+/K+ ATPase (A) Cartoon representation of one αβγ complex of the $(Na_3)E1\text{-}AlF_4^-\text{-}ADP$ crystal structure with the protein colored as in Fig. 14A (see above) and with Na^+ ions depicted as yellow spheres. (B) Cartoon representation of the $(K_2)E2\text{-}MgF_x$ structure aligned with αM7 – M10 of the $(Na_3)E1P$ – ADP state colored as in Fig. 14A (see above) and with K^+ ions colored as purple spheres. The conformational changes of the cytoplasmic domains in the α subunit relative to the $(Na_3)E1P$ – ADP state are indicated as colored arrows[14].

Another crystal structure of the Na^+/K^+-ATPase from pig kidney was solved at 2.8 Å resolution with bound Na^+, ADP and aluminum fluoride, a stable phosphate analogue, with or without oligomycin that favors Na^+ occluded state. The crystal structure represents the conversion state prior to the phosphorylated intermediate state (E1P) where three Na^+ ions are occluded (see Fig 16 a and b)[15].

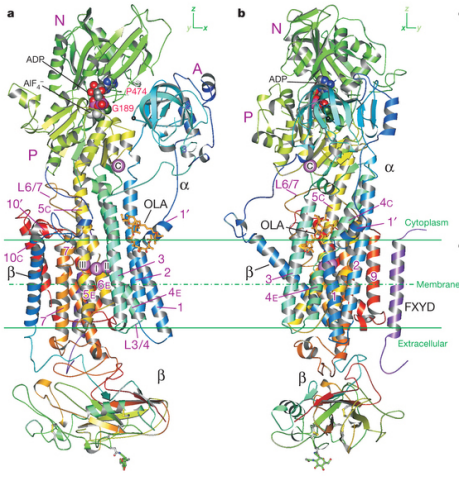

Figure 16 The crystal structure of Na^+/K^+-ATPase in $E1\sim P{\cdot}ADP{\cdot}3Na^+$ state. (a and b) Ribbon diagrams of the protein viewed in two orthogonal directions with colors marked gradually between N– and C– terminal sites, blue and red respectively for the α and β subunits. Sodium ions are depicted as a purple spheres (I – III) in the transmembrane region and one in the cytoplasmic part (C). The sugar molecules attached to the β subunit are presented as ball and stick. Oligomycin (OLA) is presented as brown sticks in αA subunit[15]

1.1.3.2 The ABC Transporters Family

The ATP–binding cassette (ABC) transporters couple the hydrolysis of ATP to the transport a large variety of substrates some being essential for cellular metabolic reactions. The ABC transporters may act as importers and exporters but so far there is no known example of ABC transporter that may export and import a molecule in both directions. In prokaryotes ABC

transporters exist as importers (they mediate amino acids, sugars, metals or ions transport) and exporters (they can efflux antibiotics and be involved in MultiDrug Resistance (MDR) phenotype). In eukaryotes ABC transporters are found only as exporters. In humans they traffic lipids, fatty acids or cholesterol[16]. They are also involved in MDR phenotype and can act as efflux pumps in cancer cells[17].

The ABC transporters share a common architecture that consists in a minimum of four domains: two transmembrane domains (TMDs) and two ABCs (nucleotide–binding domains NBDs) located in the cytoplasm. The sequences of ABC transporters exhibit characteristic conserved motifs. However the transmembrane domains are found to be very versatile depending on the transported substrate (see Fig. 17)[18]. Based on the known protein structures of ABC transporters the family has been divided in three main types: Type I and Type II importers and Type III exporters. For the importers the substrate is trafficked through a periplasmic protein[16]. Each class shows high diversity in terms of transmembrane helices. The Type I importers consist in roughly 2 x 5 core transmembrane helices while in some examples (for example the maltose transporter from *E. coli*[19]) extra two additional ones have been described. Type II importers are composed of 2 x 10 core transmembrane helices, as the *E. coli* vitamin B_{12} transporter BtuCD[20] described below (see Fig. 19) and more interestingly the helices from each subunit form distinct and independent domains. The third type of ABC transporters – Type III are composed of 2 x 6 core transmembrane helices as for example Sav1866[21] from *S. aureus* or the lipid transporter MsbA[22] from *E. coli*. The structures of the exporters show a large intermingling of helices between subunits and domains. They exhibit also an extension of transmembrane helices beyond the lipid bilayer named ICD (intracellular domain) keeping the NBDs further away from the membrane (see Fig. 19)[18].

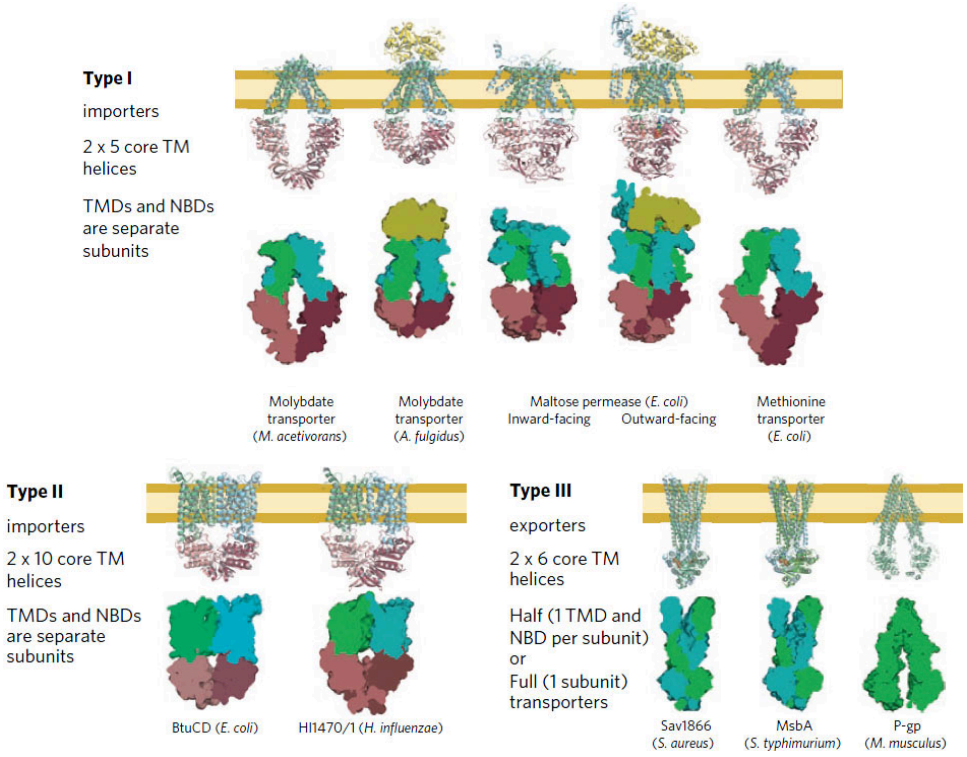

Figure 17 Classification of ABC transporters according to the TMD organization. The upper part in each diagram shows a ribbon representation of the protein structures, the lower part shows the protein structures represented as a surface. The subunits are depicted in different colors depending on the way they are encoded. Orange and yellow box presents the membrane, area below display cytoplasm of the cell. Nucleotides are depicted as spheres[18].

NBDs (nucleotide–binding domains) can be divided into two domains: a catalytic core that contains the highly conserved P–loop or Walker A motif (GXXGXGK(S/T)), a Walker B motif (ϕϕϕϕD, where ϕ is a hydrophobic residue), a Q–loop and a H–motif (termed also switch region) and a less conserved α–helical domain containing the ABC signature motif LSGGQ (see Fig. 18a-c)[16,23]. The nucleotide bound or unbound state determines the relative orientation of the helical and catalytic domains[24].

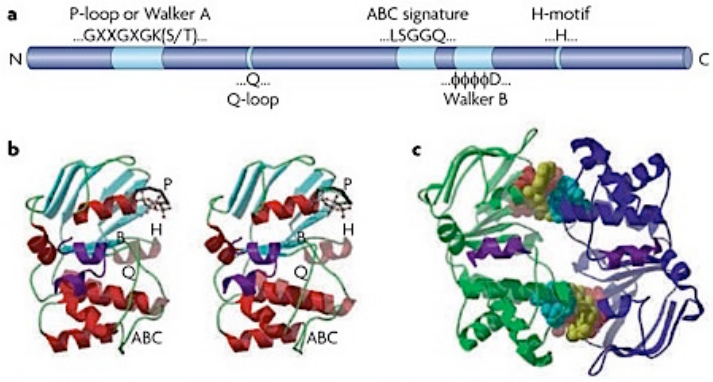

Figure 18 Nucleotide-binding domains (NBDs) of ABC transporters (a) The protein sequence of an ATP–binding cassette (ABC) subunit showing the relative positions of the highly conserved regions. (b) The ABC subunit of BtuD (Protein Data Bank (PDB) code – 1L7V) protein, the P–loop (P), Walker B motif (B), Q–loop (Q), H–motif (H) and ABC signature motif (ABC) are depicted along one surface of the subunit. A cyclotetravanadate is bounded to the P – loop and is shown as a ball and stick representation. (c) The ABC dimer of the *S. aureus* Sav1866 multidrug exporter. The two NBD are presented as green and dark blue ribbons with sandwiched AMPPNP (an analog of ATP) nucleotides depicted as a yellow space – filling models. The signature motifs and the P – loops are shown in cyan and red space–filling models respectively. The purple ribbons represent the TMDS helices that are in contact with the ABCs[16].

The structure of an ABC importer can be clearly illustrated with the structure of BtuCD (an adenosine triphosphate–binding cassette (ABC) importer) that mediates the import of vitamin B12 from the periplasmic binding protein BtuF into the cytoplasm of *E. coli*. The structure of this protein was solved at 2.6 Å resolution in complex with the binding protein BtuF and revealed that BtuF is bound to the periplasmic face of BtuCD (see Fig 21)[20].

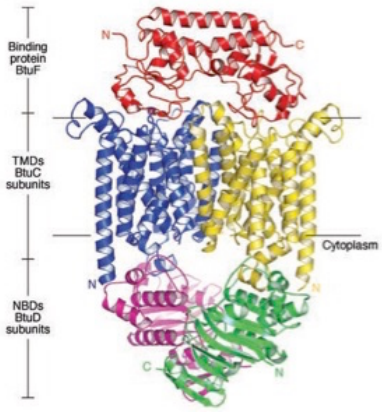

Figure 19 Representation of crystal structure of BtuCD–F complex from *E. coli*. The protein is viewed from the front and possesses five subunits. The horizontal lines represent the approximate borders of the lipid bilayer[20].

1.1.3.3 Different mechanisms of membrane transport

The transport mechanism of each membrane carrier is highly dependent

from the trafficked cargo. Different possible models of transport mechanisms are proposed and summarized on Figure 20. There, four distinct mechanisms are explained: rocker-switch, gated pore, elevator and toppling[25].

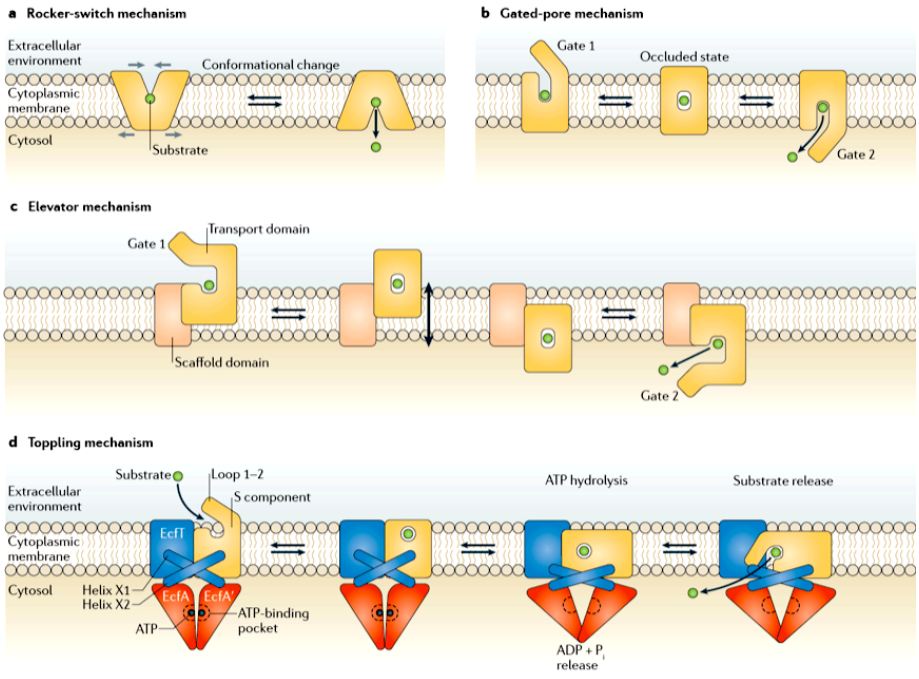

Figure 20 Different models of transport mechanisms of ABC transporters[25]. a) rocker-switch mechanism: the substrate is bound to a protein region close to the center of the membrane, further the protein undergoes conformational changes around the hinge region at the binding site (depicted as a grey arrows) that alternate the access between the extra- and intracellular sides of the membrane. Lactose transporter (LacY)[26] and some ABC exporters might use similar mechanism[21,27]; b) Gated-pore mechanism where the substrate-binding site is localized midway in the membrane and the alternating access is achieved by two gates. Upon closing both of the gates the occluded intermediate state takes place. LeuT (Na^+-coupled amino acid transporter)[28] and ABC importers – type II incorporate the elements of the gated-pore mechanism[29]; c) Elevator-mechanism: the substrate-binding site is controlled by two gates and the protein region that is bound to the substrate undergoes conformational change upon being in the occluded state. The Na^+-coupled aspartate transporter GltPh is one of the example that uses this type of mechanism[30]; d) Toppling mechanism which is a hypothetical model for ATP-driven transport by ECF transporters. Upon binding of an ATP molecule, two ATPases are considered to be in a close proximity that forces X-shaped helices of EcfT together. This mechanism is proposed to orient the S component with the substrate-binding site toward extracellular site. The ATP hydrolysis together with the release of an inorganic phosphate (P_i) and ADP leads to the toppling of the S component and thus the substrate-binding site is oriented toward the cytosol[31].

The transport of different metabolites via and within the cell membranes is essential to sustain the vitality and cell well–being state. The membrane proteins that take part in those processes are thus essential since they provide the required substrates. All of the above examples of different membrane carriers show their large diversity in terms of trafficked substrates, transport mechanisms and energy sources in order to maintain it. The structures and functions of membrane carriers highly depend on the transported substrate,

hence each organelle in the cell possesses its own highly specific transporters that contribute to overall cell-processes. One of these groups consists in mitochondrial membrane carriers.

1.2 Mitochondrial carriers

1.2.1 Mitochondrial transport

Mitochondria are double–membrane organelles that possess highly specified functions and morphology. Their size is approximately between 0.5 and 1 μm (see Fig. 21a - c). They possess their own genome with transcription and translation systems. They are the largest producers of energy in the cell in order to sustain various critical processes – metabolism, signaling and programmed cell-death. Upon fusion and fission events, mitochondria form very dynamic and tubular networks that continuously change their shape and do not have a fixed length. In numerous studies it was also revealed that in many cell types, mitochondria form elongated tubules that are often interconnected[32,33].

a) b) c)

Figure 21 Structure of mitochondria. (a) schematic cartoon representation, the outer and inner membranes (that creates "cristae") are composed of phospholipid bilayers and contain different proteins; the intermembrane space (IMS) is located in between[34]. (b) electron microscopy (EM) image, (c) electron tomography image[35] - peripheral inner membrane (IM), cristae (C), arrows indicate tubular regions connecting the cristae to the periphery, the diameter of the mitochondrion measured from the outer membrane is approximately 1.5 μm.

The outer mitochondrial membrane consists in approximately 40% of lipids and 60% of proteins (w/w), which is similar to the composition of the eukaryotic plasma membrane. The outer mitochondrial membrane is highly permeable thanks to the presence of a large number of integral membrane

proteins termed porins that allows ions and small molecules up to 5 kDa to cross the membrane. One of the main porin is the Voltage Dependent Ion Channel protein (VDAC1) that controls the metabolic cross–talk between the mitochondria and the rest of the cell[36] (see Fig. 22A - D).

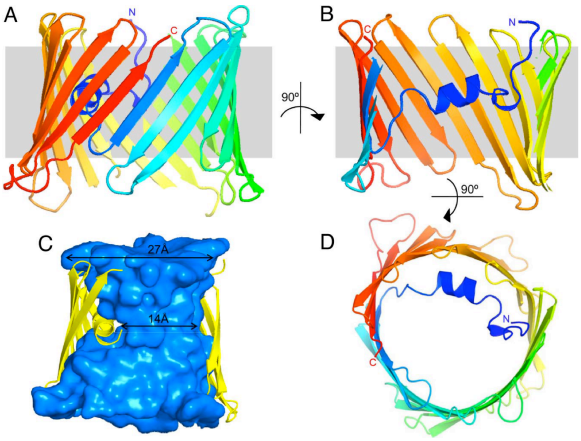

Figure 22 The β-stranded structure of the murine VDAC1 protein solved at 2.3 Å resolution. (A) protein structure in ribbon representation colored gradually (from blue – the N–terminus to red – the C–terminus) and viewed parallel to the plane of the membrane, (B) rotated protein structure in 90° clockwise, strands 3 to 7 were removed in order to visualize the N-terminal segment, (C) cross–section of the model viewed in A with 19 and 1 to 4 strands removed. The interior region of the protein channel is depicted in cyan and it illustrates the pore, (D) structure of VDAC1 in ribbon representation viewed from top with the same coloring like in A[37].

After disruption of the outer membrane, the proteins and other molecules that are present in the inner mitochondrial space leak to the cell cytosol, which causes the cell death. This phenomena is termed Mitochondrial Outer Membrane Permeabilization (MOMP) and it is considered as the "point of no return" since it promotes the apoptotic cascade and hence the cell death[38].

The endoplasmic reticulum (ER) may associate with the outer mitochondrial membrane and together they create a structure termed MAM (mitochondrial–associated ER-membrane). This membrane coupling plays a significant role in calcium signaling pathway but also in the lipid exchange between ER and mitochondria[39].

In contrast to the outer mitochondrial membrane, the inner lipid bilayer is highly impermeable to the molecules and almost all of the substrates require specific membrane transporters to cross the IM. The IM contains many proteins playing different roles in processes such as: oxidative phosphorylation, ATP synthesis, regulation of trafficked metabolites throughout the mitochondrial membranes, import machinery and mitochondrial fusion and fission proteins (see Fig. 23)[34]. The inner mitochondrial membrane is highly filled with membrane proteins and the protein–to–phospholipid mass ratio is more than

3:1 [34]. Additionally, the inner membrane is rich in cardiolipin (characteristic lipid of mitochondrial and bacterial plasma membranes) that plays a significant role in maintaining mitochondrial structure and functions and ultimately cell survival[40]. Most of these proteins are synthesized in the ER and further inserted in IM by TIM complex (translocase of the inner membrane) or by Oxa1[39].

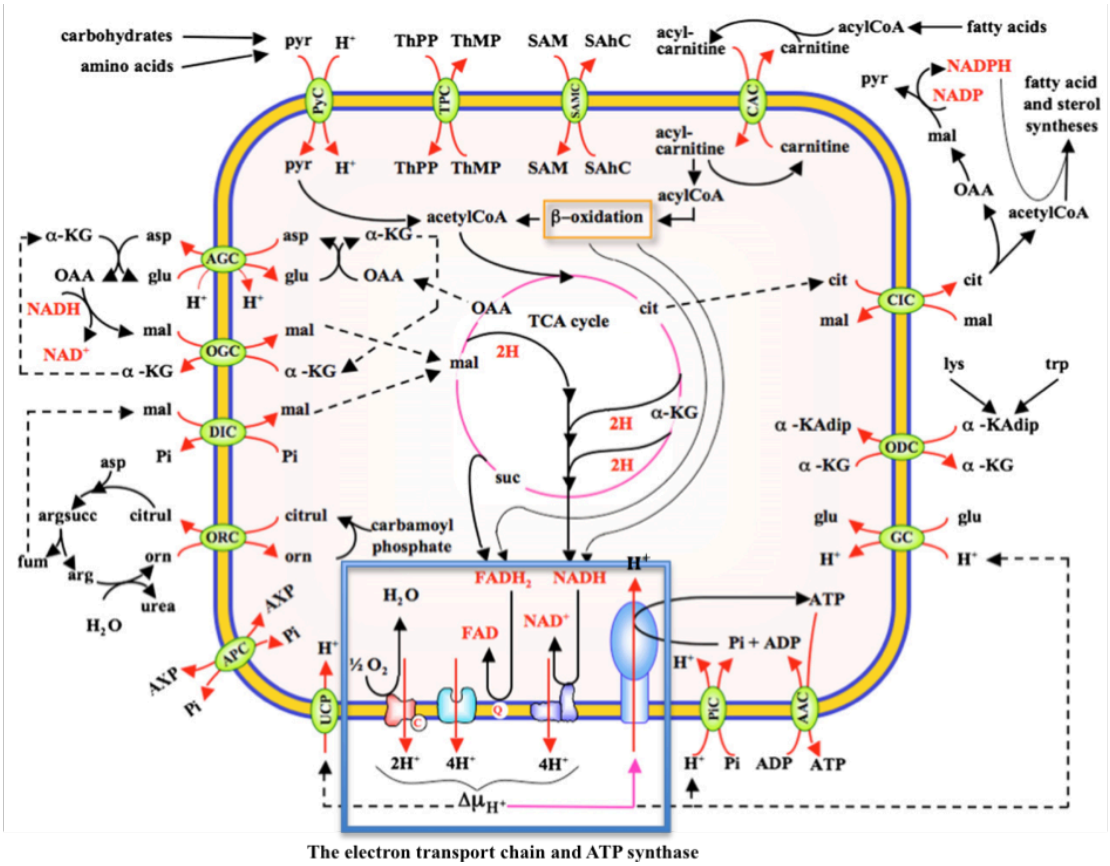

The electron transport chain and ATP synthase

Figure 23 The main processes in the mitochondria. The figure shows the different membrane transporters involved in mitochondrial and thus cell metabolism: oxidative phosphorylation (AAC, PiC, UCP), oxidative/reduction pathways (AGC, OGC, DIC, CIC, CAC, PyC); homeostasis (APC), methylation of mtDNA and mtRNA and some intra-mitochondrial proteins (SAMC); amino acid metabolism (AGC, ORC, GC, ODC; import of coenzyme thiamine pyrophosphate (ThPP) required for pyruvate and oxoglutarate – dehydrogenase complex activities (TPC)[41].

The inner mitochondrial membrane expands its surface area via characteristic structures termed "cristae" enhancing the ability to produce larger amount of ATP. In terms of surface size the inner mitochondrial membrane is approximately five times larger than the outer membrane. Muscle cells mitochondria contain more cristae than mitochondria in liver cells[34] because the required level of ATP is higher.

The mitochondrial matrix contains large amount of different enzymes involved in oxidation of pyruvate and fatty acids and in the citric acid cycle,

special mitochondrial ribosomes, mitochondrial DNA and tRNA. Mitochondria perform many different metabolic functions such as the regulation of the membrane potential[42], apoptosis-programmed cell death[43], calcium signaling[44], in cell metabolism[45], in signaling processes through mitochondrial reactive oxygen species[46] and further in steroid synthesis[47] and hormonal signaling (mitochondrial estrogen receptors - mtERs)[48]. However, the primary function of this organelle is to produce the cell energy currency – ATP. The energy source molecules and other compounds are imported and exported in or out of the mitochondria throughout mitochondrial carriers that play a significant role in cell metabolism (see Fig. 23).

1.2.2 Mitochondrial Carriers

The mitochondrial carriers (MCs), members of the Mitochondrial Carrier Family (MCF), are essential membrane proteins that are located in the inner mitochondrial membrane and control the exchange of a large variety of the substrates between the mitochondrial matrix and the intermembrane space. However, despite different substrate specificity all members of the family share similar features as described further. All the compounds that are carried out by the mitochondrial carriers (such as amino acids, inorganic ions, keto acids, nucleotides and vitamins (see Fig. 24) play significant roles in many important processes in the mitochondrial and thus in the cell metabolism[49,50]. Those processes include citric acid cycle, oxidative phosphorylation, fatty acid oxidation, gluconeogenesis, urea synthesis, amino acid synthesis and degradation, intramitochondrial DNA, RNA and protein synthesis, lipogenesis, transfer of reducing equivalents (see Fig. 23)[41].

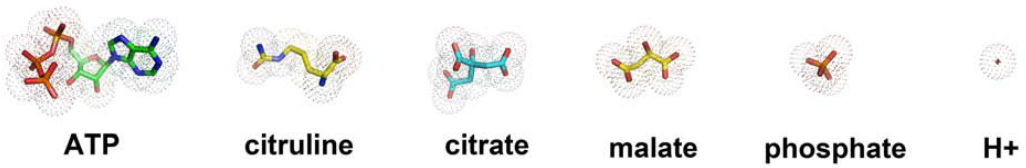

Figure 24 Examples of substrates carried by mitochondrial transporters.

Approximately 22 mitochondrial carrier subfamilies have been identified in terms of substrate specificity[51]. Substrate recognition is specific for each carrier but the sequence similarities suggest that mitochondrial carriers have similar structures and mechanisms for the substrate translocation[52].

1.2.2.1 Biogenesis of MCF proteins

The mitochondrial carriers are encoded in the cell nucleus and are translated by the cytosolic ribosomes. Following their transport through the cytosol, the protein signal sequence is recognized and inserted into specific receptor termed Translocase of the Outer Membrane (TOM) complex. The TOM complex consists in Tom70 import receptor which specifically interacts with ATP-dependent chaperone proteins Hsc70 (heat-shock cognate 70) and Hsp90 (heat-shock protein 90) that are maintaining, stabilizing and protecting the synthesized proteins[53,54]. Subsequently Tom70 interacts with general import pore Tom40. Afterwards the protein insertion into the inner mitochondrial membrane requires further interaction with the Tim9/Tim10 complex, that when associated to the carried preprotein, functions as a translocation chaperone from the outer mitochondrial membrane to the inner mitochondrial membrane. Further on the Tim9/Tim10 complex interacts directly with Tim22 complex which is embedded in the inner mitochondrial membrane that enables protein insertion into the membrane (see Fig. 25)[55,56].

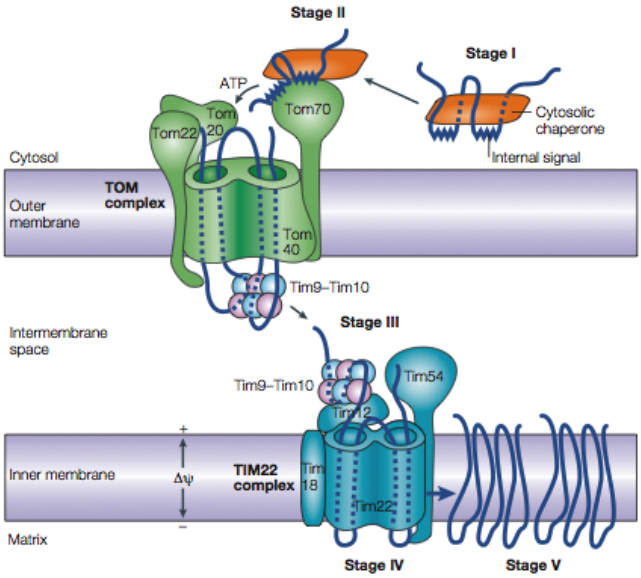

Figure 25 The mitochondrial carrier translocation into the inner mitochondrial membrane. In the Stage I the cytosolic chaperones Hsp90 and Hsp70 protect an unfolded protein precursor against aggregation. Afterwards in Stage II the protein precursor-chaperone complex interact with Tom70 import receptor through specific targeting signal. Subsequently in Stage III upon chaperones and ATP dissociation protein precursor is trafficked across the intermembrane space and further in Stage IV it interacts with Tim22 complex that anchors the mitochondrial carrier into the inner mitochondrial membrane (Stage V)[55].

1.2.2.2 Distribution

35, 58 and 50 different mitochondrial carriers are found respectively in the genomes of *Saccharomyces cerevisiae*, *Arabidopsis thaliana* and human[51]. Interestingly some MCFs were identified in other organelles such as thylakoids membranes[57], yeast peroxisome[58], and in the inner membrane of chloroplasts[59]. Additionally it was also reported that the genome of the giant virus *Mimiviridae mimivirus* encodes a member of the mitochondrial carrier family that transports dATP and dTTP[60]. A MCF ADP/ATP carrier was also recently identified in the plasma membrane of *Arabidopsis thaliana* (plant plasma membrane-ANT1, PM-ANT1)[61]. PM-ANT1 is expressed in mature pollen grains and consists in 330 amino acids. It contains the characteristic mitochondrial carrier motifs (MCF) that are specific for mitochondrial transporters.

1.2.2.3 Characteristic features of mitochondrial carriers

It was proposed that MCs in many different organisms share less then 20% of sequence similarity, however very high similarity in terms of MCF motif. It is also predicted that they consist in six transmembrane helices. The MCs possess three tandem repeats that consists in 100 amino acid each and that includes two transmembrane helices linked by a large loop[62]. The amino acid sequence of MCs has also a characteristic conserved signature MCF motif P-X-[DE]-X-X-[RK] (20-30 amino acid residues) [D/E]GXXXX[W/Y/F][K/R]G[63] (see Fig. 26 a and b). Moreover it is also observed that the MCs have similar substrate binding site[52,64]. The molecular mass of MCs varies between 30 – 34 kDa and they have a high isoelectric point.

1.2.2.4 The mitochondrial ADP/ATP Carrier (AAC) – protein topology and structures

Numerous studies have been devoted to ADP/ATP carriers in order to understand firstly their differential gene regulation and protein expression[65], secondly – their transport mechanism that includes substrate binding site, protein conformational changes and inhibition properties[66,67], thirdly their role in different diseases[68–70,70–73] including cancer[65].

The main role of ADP/ATP carrier (AAC) is to import and export ADP^{3-} and ATP^{4-} respectively between the intermembrane space and the matrix through the inner mitochondrial membrane. Due to the early identification of two specific inhibitors, the ADP/ATP carrier is the best characterized among all MCs and was further intensively studied in many different aspects[74,75].

The protein consists in 297 amino acid residues[76] and has six transmembrane helices (H1–H6) connected by two loops located in the intermembrane space (C1 and C2) and three loops on the matrix side containing three amphipathic helices (h1-2, h3-4, h5-6) (see Fig. 26 a and b)[77]. The N- and C-terminal sides are facing the intermembrane space. The odd-numbered helices (H1, H3 and H5) are tilted due to the presence of proline residues that belong to the conserved sequence PX(D/E)XX(K/R)[63,78] characteristic of MCF. The basic and acidic residues of the motif were shown to be involved in the formation of 3 salt bridges that play an

important role in the formation of the ADP-binding cavity[77]. They are also suggested to play an important role in the transport mechanism (see Fig. 27e)[79]. The six transmembrane helices of *b*AAC1 form a wide-open cavity toward intermembrane space that has maximal diameter of 20 Å and a depth of 30 Å (see Fig 27b).

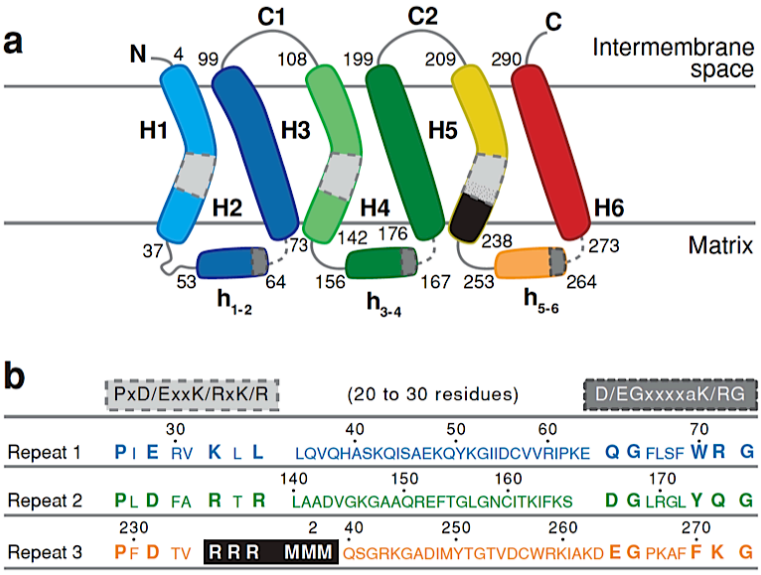

Figure 26 The topology of MCF and characteristic motifs of the bovine ADP/ATP carrier. a) The secondary structure of the protein; transmembrane, surface helices and intermembrane space loops are labeled H, h and C respectively. Helices comprise the following residues: 4–37 (H1), 53–64 (h1-2), 73–99 (H2), 108–142 (H3), 156–167 (h3-4), 176–199 (H4), 209–238 (H5), 253–264 (h5-6), 273–290 (H6). Kinks in odd-numbered helices (H1, H3 and H5) are induced by the presence of prolines. Regions that contain MCF motif residues are depicted in gray, the RRRMMM motif is shown in black. b) An alignment of the three MCF motifs. The sequence of MCF is marked as a gray box on the top. The RRRMMM signature motif in the third repeat is boxed in black[77,80].

The known structures of AACs were all solved in presence of an inhibitor that stabilizes the protein. Atractyloside (ATR) increased the yeast AAC3 protein stability and facilitated its 2D crystallization leading to 8 Å resolution projection map obtained by electron microscopy[81]. The 3D structure of bovine AAC1 was co-crystallized with CATR inhibitor and solved at 2.2 Å resolution (see Fig 27a-d)[77].

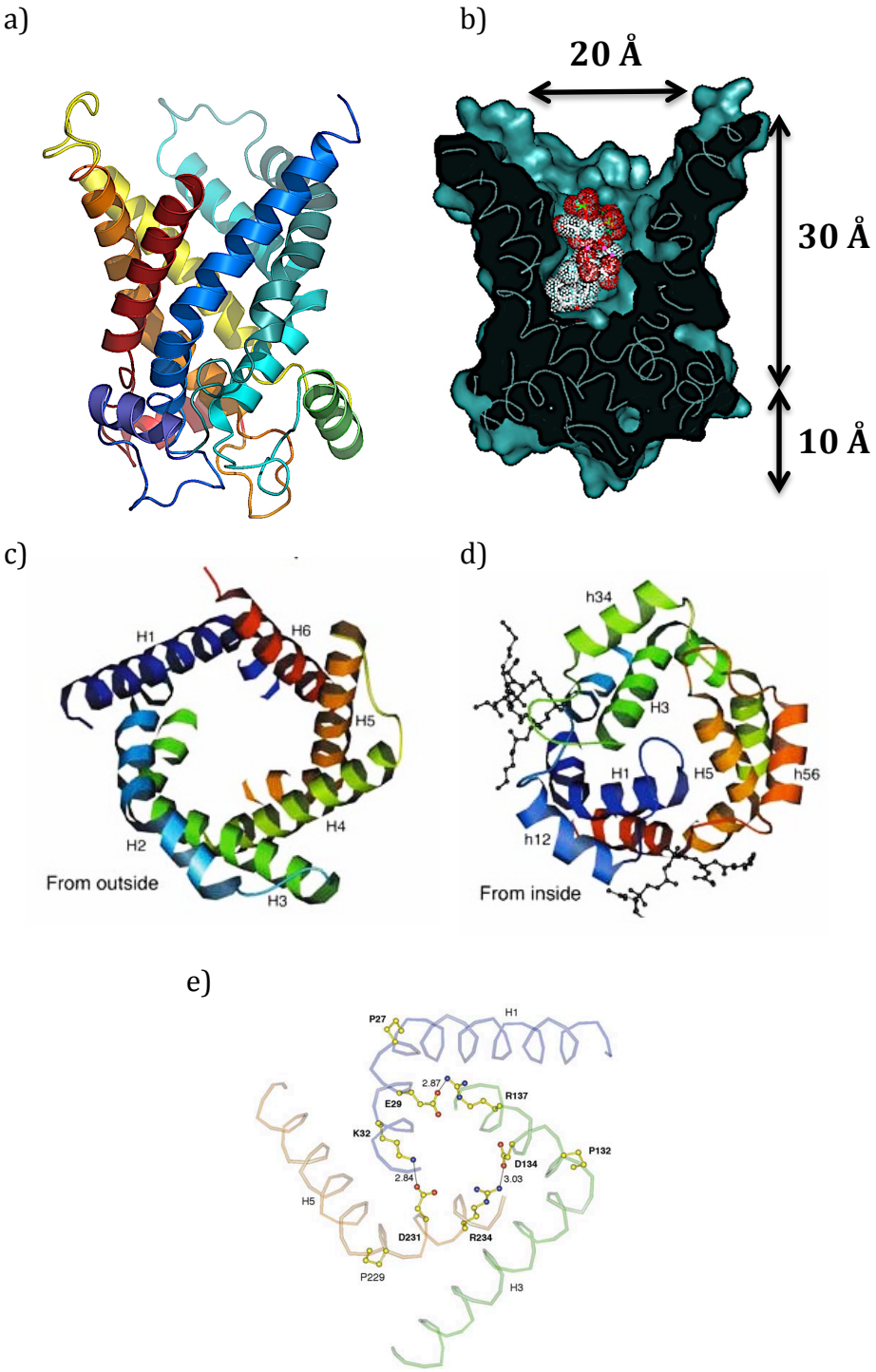

Figure 27 The structure of the bovine ADP/ATP carrier in ribbon diagram. The structure is colored according to the sequence from N-terminal side (blue) to C-terminal side (red). a) The carrier viewed from the side, b) Longitudinal cross-section of a carrier showing the binding cavity with CATR inhibitor depicted as red-white mesh. c) The structure viewed from outside and d) inside with two cardiolipins molecules represented as black balls and sticks, e) The closed conformation of the carrier viewed from the mitochondrial matrix. Only odd-numbered helices are shown with the residues involved in the PX(D/E)XX(K/R) sequence (labeled). Black lines connect atoms within hydrogen-bonding distances[77].

The CATR inhibitor in the bovine AAC1 structure is located at the bottom

of the protein cavity (see Fig. 27b) and it is arrested by many interactions with the protein including electrostatic interactions and hydrogen bonds. The structure of *b*AAC1 also revealed that three molecules of cardiolipins are located on the matrix side and are believed to stabilize the structure (see Fig. 27d)[82]. The third cardiolipin molecule was identified in a different crystal form[82].

In 2013 two crystal structures of yeast ADP/ATP carriers (Aac2p and Aac3p) were solved at 2.5 Å and 3.2 Å resolution respectively in complex with the CATR inhibitor (c-state) (see Fig. 28A-D)[83]. Both structures revealed a protein topology similar to that of the bovine AAC1 with small differences. In contrast to mammalian orthologues, the yeast carrier possesses a significantly extended N-terminal region. Additionally, one of the salt-bridge network interactions is braced by a glutamine residue that contributes to the energy barrier, preventing protein conversion toward matrix side unless substrate binding occurs. Moreover it was also reported that the serine kink in the third helix mimics the proline. As in the bovine AAC protein structure three cardiolipin molecules are bound to the yeast carriers (see Fig. 28A-D)[83].

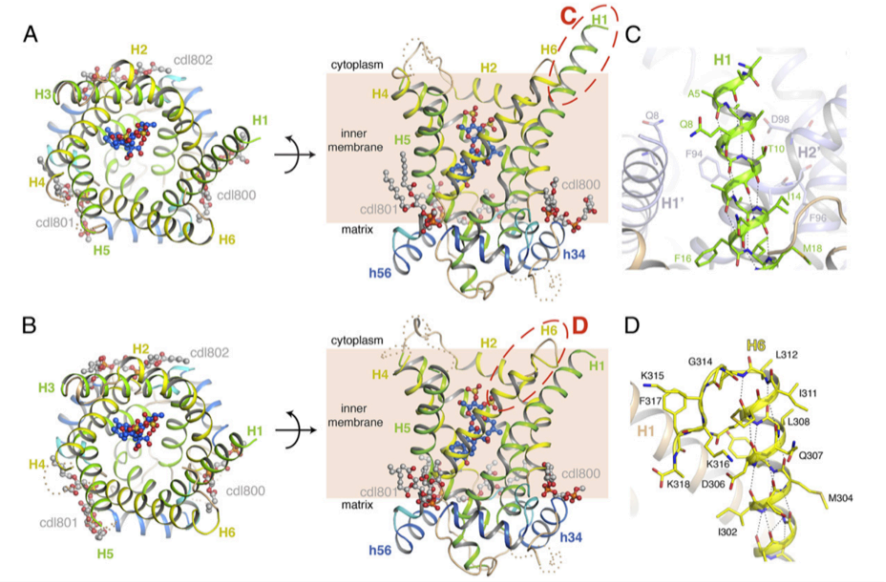

Figure 28 Structure of the yeast ADP/ATP carriers. (A) Aac3p viewed from the cytoplasm (left side) and from the membrane (right side). (B) Aac2p with equivalent views. Odd-numbered helices are coloured in green, even-numbered helices in yellow, matrix helices in blue, and linker helices in cyan. Cardiolipin (depicted as grey-colored carbons) and CATR (depicted as blue-colored carbons) molecules are shown as ball-and-stick representation. The cytoplasmic loop between H4 and H5 and part of the loop between H3 and matrix helix h34 are missing (depicted as wheat-colored dots), following the position of these elements in the bovine carrier. Red-dashed ovals represent the close-ups in C and D.(C) The N-terminal region of Aac3p - H1 (colored in green), rest of the structure in wheat. (D) The C-terminal region (colored in yellow) of Aac2p[83].

The mitochondrial uncoupling protein 2 (UCP2) structure has also been determined however characterized by NMR method. The local and secondary structures of the protein were determined by piecing together molecular fragments from the PDB that best fit experimental data from samples weakly aligned in a DNA nanotube liquid crystal. Here, it was reported that UCP2 closely resembles the bovine ADP/ATP carrier but the relative orientations of the helical segments are different, resulting in a wider opening on the matrix side of the inner membrane[84]. However, this structure is highly controversial[85].

1.2.2.4.1 Inhibitors and conformational states

The inhibitors of AAC played an essential role in protein studies. There are two main families: atractyloside (ATR) or carboxyatractyloside (CATR), and bongkrekic acids. The difference between ATR and CATR lies in additional carboxyl group in CATR molecule (see Fig 29a and b). The atractylosides belong to the lethal poisons found in *Atractylis gummifera* thistles of the Mediterranean region[86,87]. They were also identified in other plants[88,89]. Both of the compounds do not cross the inner mitochondrial membrane but bind to the AAC from intermembrane space side. The dissociation constant of ATR is around 100 nM while K_d of CATR is approximately 10 nM thus it not possible to displace the interaction by an excess of the substrate[90]. Bongkrekic acid (BA) (see Fig 29a and c) is an inhibitor that comes from bacteria - *Pseudomonas cocovenenans.* This compound is believed to inhibit AAC from the matrix side since its nature is lipophilic and thus capable to cross the inner mitochondrial membrane. The binding affinity of BA is similar to that of CATR (approximately 10 nM)[91]. More recently it was reported that some other molecules such as CD437 (synthetic retinoid that induces tumor growth arrest and apoptosis, see Annex 3, part 2), closantel (a proton ionophore that is believed to disrupt the proton gradient across the mitochondrial inner membrane, see Annex 3, part 2), leelamine (a natural product derived from the bark of pine trees and it has been reported to have several activities such as inhibition of pyruvate dehydrogenase kinase and disruption of cholesterol transport, see Annex 3, part 2), chebulinic acid (an ellagitannin that was discovered in the seeds of *Euphoria longana* or in the fruits of *Terminalia chebula,* see Annex 3, part 2) and suramin (the anti-cancer drug

but also used against sleeping sickness caused by trypanosomes, see Annex 3, part 2) might affect the transport activity of the ADP/ATP carrier[92], however there is no evidence yet that they act directly on AAC.

Upon importing ADP inside the mitochondria and exporting ATP outside to the mitochondrial intermembrane space, the carrier undergoes several conformational changes. Upon inhibition states (with CATR or BA) the AAC is usually characterized as being in "extreme" conformations. The c-state is described as open towards the intermembrane space and forming the cavity for ADP binding while the m-state is open towards the mitochondrial matrix side forming a groove for ATP binding[93].

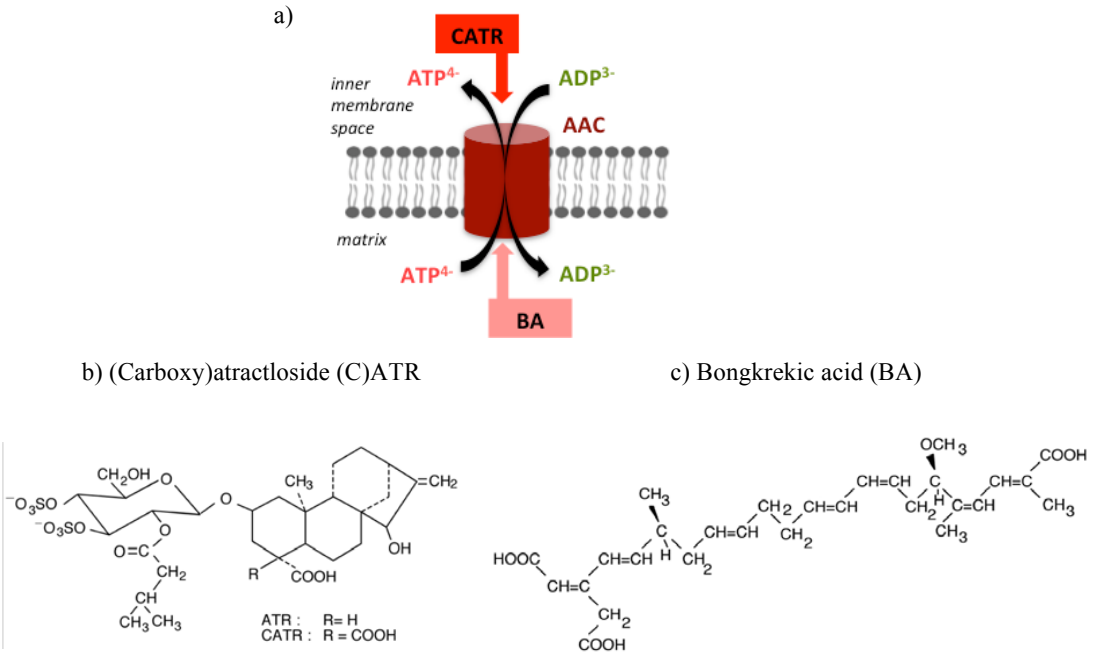

Figure 29 The AAC inhibitors – (Carboxy)atractyloside ((C)ATR) and bongkrekic acid (BA). a) CATR inhibits the protein from intermembrane space (c-state protein conformation), bongkrekic acid from mitochondrial matrix (m-state protein conformation), b) CATR and c) BA inhibitor structures.

1.2.2.4.2 Substrate specificity and transport hypothesis

AAC possesses high specificity to ADP and ATP[94]. Several compounds such as 8'Br-ATP, 2-azido ADP, 2-azido ATP, AMP were tested and none of them was transported[67]. The ATP transport against ADP is electrogenic and utilizes the chemiosmotic proton gradient. Approximately one third of it is consumed by the transport and another two third are necessary for ATP synthesis[95]. It was established by early studies that the transport stoichiometry in the mitochondria

is a 1:1 exchange[96–98]. While this was observed *in vivo*[99], in *in vitro* systems it may differ. Experiments performed in proteoliposomes showed that AAC can traffic a single nucleotide in one direction[100]. Upon many hypotheses the transport mechanism of mitochondrial ADP/ATP carrier is not yet clearly determined. Previous studies suggested for instance that the carrier binds alternately both its substrates which correspond to the so-called "ping-pong" mechanism[95]. Another possibility is a sequential mechanism in which the ADP and ATP must bind to the carrier before the exchange mechanism occurs. Following that idea the active complex would be a ternary complex (ADP-carrier-ATP) while in the "ping-pong" mechanism only binary – carrier-ATP and carrier-ADP would exist[101,102]. Later, the crystal structure of bovine AAC1 solved with CATR inhibitor[77] revealed that in the protein cavity some essential positively charged residues (K22, R79 and R279) and the tyrosine ladder might create a selectivity filter for the transported nucleotides (see Fig. 30a-c)[103].

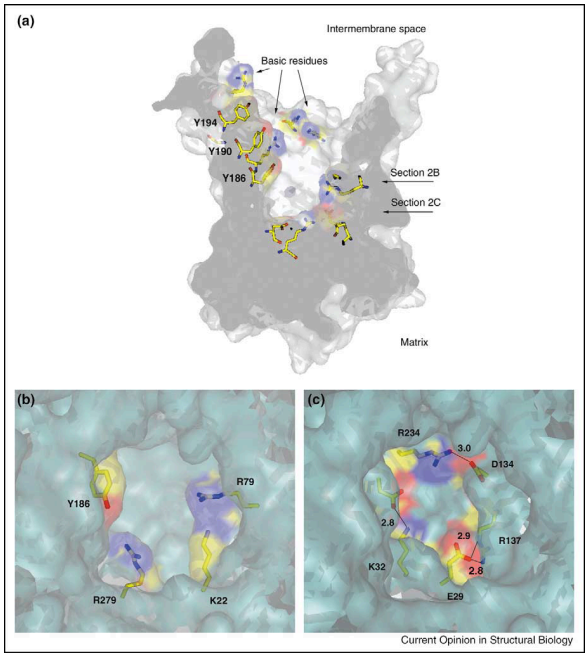

Figure 30 Surface representation of bovine mitochondrial AAC1 cavity. The residues are labeled and presented as balls-and-sticks; their surfaces are depicted in blue, red and yellow for nitrogen, oxygen and carbon respectively. a) Longitudinal cross-section through the protein cavity with labeled tyrosine and basic residues in the entrance; sections presented in b) and c) are marked by arrows; b) protein cavity viewed from the intermembrane space showing selectivity filter: the Y186 and basic residues K22, R79 and R279 are located about 6 Å from the bottom of the protein cavity; c) the view on the protein cavity like in b) showing bottom of the cavity with acidic and basic residues marked from the MCF motif[103].

Molecular dynamic simulation analysis on the apo-AAC (protein conformation without CATR inhibitor) revealed the presence of an electrostatic funnel that attracts the negatively charged nucleotides to the bottom of the cavity. Upon ADP binding protein changes its conformational state allowing the

nucleotide to pass. In this hypothesis the importance of proline residues responsible for the tilts in odd-numbered helices is emphasized (see Fig. 31)[104].

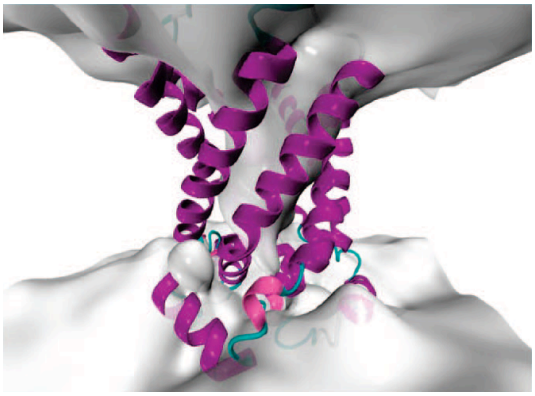

Figure 31 The 3D electrostatic isopotential map of apo-AAC showing a funnel that guides the ADP^{3-} towards the bottom of the protein cavity (closed conformation)[104].

The conserved symmetrical residues required for the transport mechanism were found to be accessible for the solvent. More importantly, they belong to the three PX[DE]XX[RK] motifs that are responsible for the salt bridge network the bottom of the protein cavity when the substrate-binding site is open towards the intermembrane space. It was observed that symmetrical residues in three [FY][DE]XX[RK] motifs are present on the cytoplasmic side of the cavity and thus could create the salt bridge network when the substrate-binding site is accessible from the mitochondrial matrix. Subsequently it has been suggested that the opening and closing mechanism of the carrier may be linked with the disruption and formation of those two salt bridge networks via a 3-fold rotary twist triggered by substrate-binding. Hence, the interaction energies of those networks allow AAC protein to be classified as strict exchangers (see Fig. 32) or uniporters [105,79].

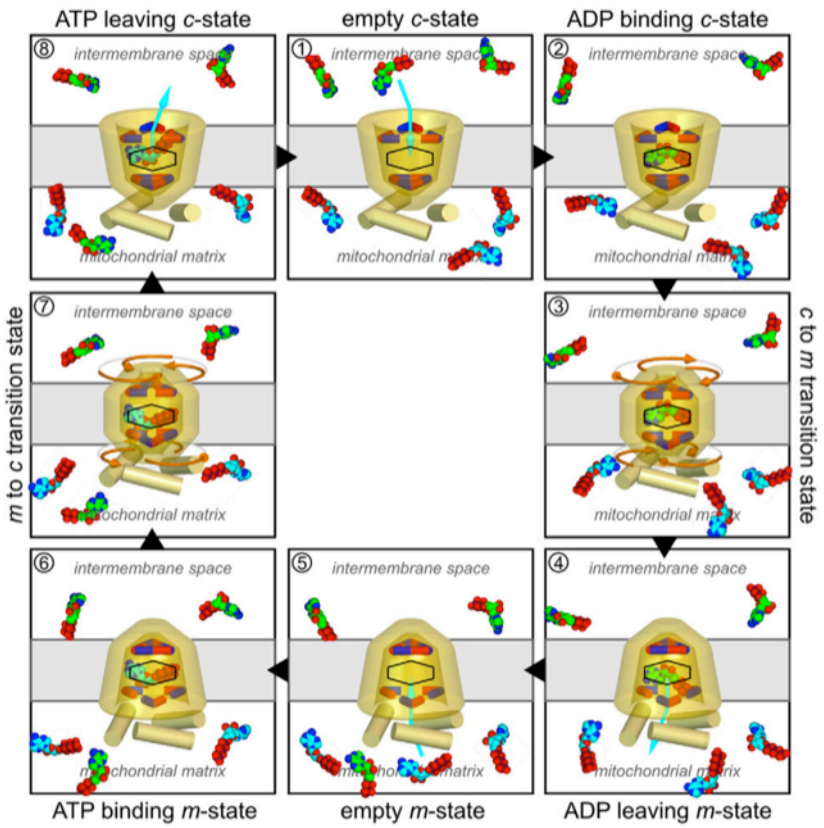

Figure 32 Proposed transport mechanism of AAC. The cartoon presents strict equimolar ADP-ATP exchange in which the AAC cycles between the cytoplasmic state (c-state) and matrix state (m-state). Positively and negatively charged residues of the salt bridge are depicted as blue and red respectively. ADP and ATP are shown as green and cyan respectively. The hexagon indicates the position of the asymmetric substrate-binding site. All transport steps are reversible, however the direction of transport (marked as black arrows) is determined by the membrane potential and by the chemical gradients of ADP and ATP. During substrate import, the matrix network on the odd-numbered α-helices is released while the cytoplasmic network on the even-numbered α-helices is formed, and the conversion of those conformational changes occurs also upon export. The structural changes might occur through the simultaneous rotation of the three domains (depicted as orange arrows)[66].

1.2.2.4.3 Protein oligomeric state

There are numerous studies about AAC oligomerization state. Initially AAC was believed to form a homodimer[67,106]. First hypothesis on the AAC oligomerization state were based on the idea that the protein rather should operate as a homodimer due to its small size in comparison with other membrane transporters that possesses approximately 12 core transmembrane helices. The studies that were performed on the bovine mitochondrial AAC1, such as analytical ultracentrifugation[107], substrate binding measurements[98] and small-angle neutron scattering (SANS)[108] were indicating that the carrier is a dimer. In the next years some analysis were performed on the bovine and yeast

carriers by inserting them into the inner mitochondrial membrane and performing cross-linking experiments. There, it was reported that in presence of different cross-linkers two carriers may link together between cysteines 56 creating a dimer[109,110]. Additionally the native electrophoresis[111,112] and functional studies on chimeric dimers[113–115] were also suggesting that the carrier functions as a dimer. Hence, all of those findings were suggesting that two separate translocation channels in each subunit were controlling the export and import of the ATP and ADP respectively in the independent or cooperative mode by inter-subunit contact[67]. There were also some studies based on stoichiometry of CATR inhibitor binding and fluorescence substrate probes, which suggested the tetrameric organization of the AAC with four nucleotide binding sites (two in the c-state and two in the m-state)[75,93,95,116]. The breakthrough appeared after the bovine AAC high-resolution 3D structure[77] was solved since it revealed that the carrier is structurally a monomer and this brought the idea that the protein might function in the same oligomerization state as well[81,103]. In the bovine AAC1 crystal structures two or three molecules of cardiolipins were identified[77,82]. The second crystal form of bovine AAC1 showed two cardiolipins that were sandwiched between two monomers that could mediate protein-protein interaction and thus suggesting the potential dimer[82]. Nevertheless the binding surface was too limited to be in favor of a biological dimer. Furthermore the analysis performed by analytical ultracentrifugation (AUC) showed that the bovine AAC1 solubilized in LAPAO detergent (3-laurylamido-N,N'-dimethylpropylaminoxide) is a monomer whereas in Triton X-100 and reduced Triton X-100, higher molecular mass species can also be identified[117]. Numerous studies were also performed on the yeast AAC. Based on differential tagging[118] and molecular mass determination of the protein in detergent environment[119] it was concluded that the yeast carrier is a functional monomer.

At first glance the number of publications supporting the hypothesis that the carrier might function as a dimer seem to be quite strong. However in many of those studies some critical factors were not fully appreciated. As it was mentioned before the structural analysis and sequence data are compatible only with the monomer. Moreover many functional studies confirmed that the mitochondrial carriers operate as an independent unit and thus all of those

factors indicate that the monomer is most likely the structural and functional form of the carrier[120].

1.2.2.4.4 Diseases associated with Mitochondrial Carrier Family

The proper function of human MCs is essential for maintaining the energy metabolism and cell well-being vitality, thus any disorders in the carrier are the case of pathologies[41,73,121]. The main ones are causing adult- and neonatal-onset type II citrullinemia, autosomal dominant progressive external opthalmoplegia (adPEO), Amish-type microcephaly, hyperornithinemia-hyperammonia-homocitrullinuria, carnitineacylcarnitine translocase deficiency, neonatal myoclonic epilepsy, type II diabetes and severe obesity[122]. With the exception of adPEO, the others are inherited in an autosomal recessive manner. The diseases linked with MCs can be divided into two main groups. The first one consists in defects in mitochondrial carriers (such as PiC and ADP/ATP carrier) that are related with oxidative phosphorylation and they result in insufficient energy production in many different tissues. The Sengers' syndrome and adPEO belong to this group and they are caused by ADP/ATP isoform 1 gene mutation, which lead to mtDNA instability. The second group of diseases (such as carnitine–acylcarnitine carrier (CAC) deficiency, HHH syndrome, aspartate/glutamate carrier isoform 2 (AGC2) deficiency and Amish microcephaly and neonatal myoclonic epilepsy) is linked with defects that influence mitochondrial functions in particular intermediary metabolism (see Table 2)[41].

Disorder	Gene	Carrier	Substrates
AAC1 deficiency	*SLC25A4*	AAC1	ADP/ATP
Sengers' syndrome	?	AAC1	ADP/ATP
PiC deficiency	*SLC25A3*	PiC	Phosphate
adPEO	*SLC25A4*	AAC1	ADP/ATP
CAC deficiency	*SLC25A20*	CAC	Carnitine/acylcarnitines
HHH syndrome	*SLC25A15*	ORC1	Ornithine/citrulline
NICCD/CTLN2	*SLC25A13*	AGC2	Aspartate/glutamate
Amish microcephaly	*SLC25A19*	TPC	Thiamine pyrophosphate
Neonatal myoclonic epilepsy	*SLC25A22*	GC1	Glutamate

Table 2 Disorders associated with different mutations in the genes encoding mitochondrial carriers[41].

There are three main disorders that are associated with the deficiency of AAC1 isoform that is highly abundant in heart and skeletal muscles: AAC1 deficiency[69,72], Sengers syndrome[71] and autosomal dominant progressive external ophthalmoplegia (adPEO)[68,70]. Five mutations in AAC1 (A90D, A114P, L98P, D104G, V289M) were found to be involved in several cases of autosomal dominant progressive ophthalmoplegia (adPEO) with typical symptoms as weakness of the external eye muscles, ptosis, mild descending myopathy. Interestingly none of those residues are key residues involved in the substrate or inhibitor binding as it can be concluded from the three-dimensional protein structure[77]. It was later proven in functional assays coupled to molecular dynamic simulations[122] that those mutations highly influence transport properties, and hence are responsible for severe genetic diseases. The mutations were classified in three main groups depending on the degree of the transport and ATP binding: 1) V289M and D104G; 2) L98P, A114P, and A90D; 3) A123D. The first group of mutants only partially reduced the transport rate but did not affect ATP binding. Those two residues are not highly conserved among AACs hence their mutation may not perturb nucleotide binding but only transport efficiency[122]. It was also described that the symptomatology of those two mutants is one of the mildest and associated with ptosis with a relatively late onset[68,123]. In the second group of mutants the protein activity of L98P, A114P and A90D is strongly reduced and those findings correlate with medical observations. The L98P mutation is associated with exercise intolerance, weakness and bipolar affective disorder[70]. A114P is mainly connected with adPEO[68]. The last residue from this group – A90D was identified in the patients with ptosis, schizoaffective disorder and exercise intolerance[124]. It was shown that the mutants of these first two groups modify the protein activity by reducing its conformational plasticity. A123 is highly conserved among AACs and is embedded deep in the protein cavity. Upon mutation into aspartate (A123D) it was observed that the transport is totally abolished[122] and that could be explained by a modification of the carrier electronic signature. This mutation A123D was found in patients suffering from AAC1 deficiency and is associated with exercise intolerance, lactic acidosis, hypertrophic cardiomyopathy and myopathy[41,75].

1.2.2.4.5 Human ADP/ATP Carriers

The functional and structural characterization of the human AAC isoforms combined with their comparison is an essential step that gives an insight into their native properties and hence they can become interesting targets in the drug development field.

In humans, four AAC isoforms are found – hAAC1, hAAC2, hAAC3 and hAAC4[51]. They are encoded by differentially regulated nuclear genes[125–127]. First three isoforms share approximately 98% sequence identity (see Fig. 33). All human AAC isoforms are located in the inner mitochondrial membrane however their expression is tissue specific and may depend on the proliferative capacity of the tissue and its energy requirements (such as oxidative phosphorylation or glycolysis)[51]. The initial classification was based on the analysis between AAC1 to AAC3 mRNA levels in rodents and human organs[128]. AAC1 isoform is highly expressed in heart (it represents 10% of all of the proteins embedded in inner mitochondrial membrane) and skeletal muscles and it is induced during myoblast differentiation[129]. AAC2 is either not or weakly expressed in all human tissues studied. However it is the most abundant isoform in proliferative tissues (such as lymphoid cells and the liver)[65]. It was observed additionally that in breast, cervix, colon and hepato-carcinoma cells, AAC2 mRNA is more abundant than AAC1 mRNA[128,130,131]. The overexpression of AAC2 is also significantly observed in primary tissues derived from patients with breast, ovary, lung, uterus, thyroid gland, bladder or testis cancer cells compared with its expression in healthy tissues[132]. AAC3 is expressed at a lower level independently of the tissue type[65]. The fourth isoform AAC4 was only found in healthy human brain, liver and testis unlike those of AAC1-3. Its sequence similarity is approximately 66-68% comparing with the other human AAC1-AAC3 isoforms[133].

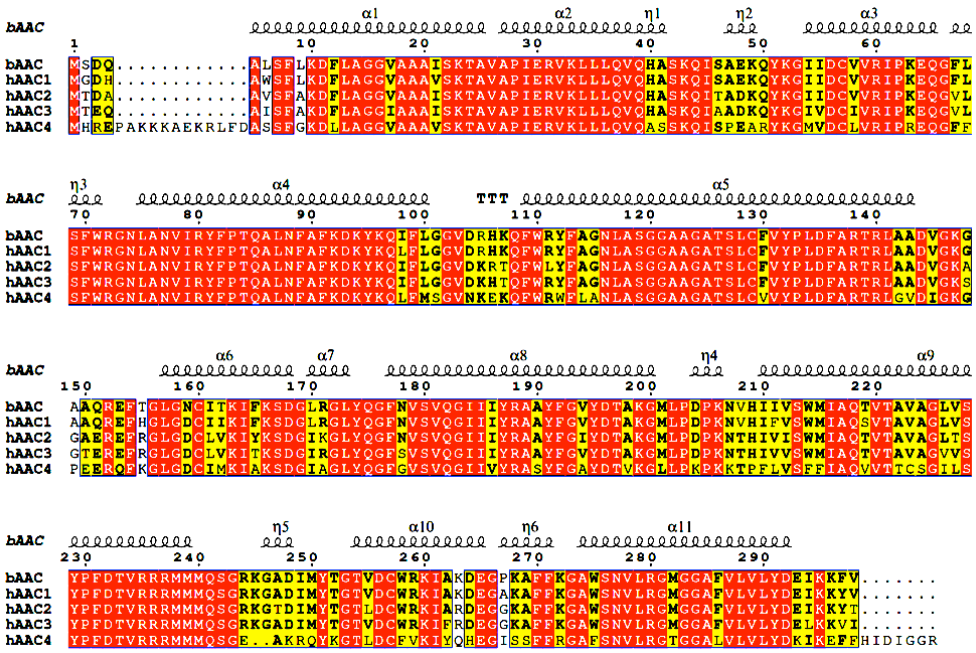

Figure 33 Sequence alignment of bovine and four human AAC isoforms. The secondary structure of the protein bAAC1 is indicated above the protein residues.

Up to now, some studies have been performed on human AAC isoforms expressed in yeast. The human AAC1 isoform was expressed in yeast, as the bovine isoform[134], by replacing the N-terminal region with corresponding region of yeast AAC2 (*y*AAC2) isoform. It was shown that the human carrier preserved its functional properties[135]. In another study it was demonstrated that three human AAC isoforms (*h*AAC1 to *h*AAC3) might be expressed in yeast under the control of the regulatory sequences and on the nonfermentable carbon source of yeast mutant strain lacking its three endogenous AAC[136]. Thus, for the first time the transport properties of those carriers were measured and analyzed in isolated mitochondria. It was also observed that *hAAC2* gene expression is determined by presence or absence of oxygen or heme[137].

The human AAC4 isoform was expressed in *E. coli*[133] (but in inclusion bodies) and yeast system[138]. AAC4 expressed in bacteria was reconstituted in liposomes and investigated in terms of functional properties and protein inhibition. It was shown that AAC4 maintains its function in the liposomes and exchanges nucleotides. Moreover, the carrier was also inhibited by CATR and BA[133]. Human AAC4 isoform was also expressed in AAC-deficient yeast strain. The results showed that the yeast growth and expression of the carrier was

possible only by introducing specific point protein mutation that might have been associated with phospholipids interaction. Additionally, data confirmed that the mutated human AAC4 and the wild-type exhibit similar nucleotide exchange rates[138].

1.2.2.4.6 Role of human ADP/ATP Carriers in apoptosis and cancer

Identification of new targets for the development of efficient apoptosis-modulation drugs is one of the most important tasks. Numerous studies revealed and demonstrated that the mitochondrial permeabilization is a central rate-limiting step for many different models of the cell-death. Moreover, the molecular and pharmacological studies proved that the ADP/ATP carrier could be a therapeutic target. First, since it is a bi-functional protein - it mediates the exchange of cytosolic ADP and mitochondrial ATP, and thus could contribute to apoptosis process via its capacity to become a lethal pore. Second, the carrier function is controlled by (anti)-oncogenes from the Bax/Bcl-2 family, and third, agents such as proteins, lipids, ions, pro-oxidants or chemotherapeutic agents can directly modulate the pore-forming activity of AAC[139].

Expression of the various AAC genes is different and tightly regulated[140]. According to the analysis of the 5`-flanking regions[141] of AAC genes it was demonstrated that their organizations vary between each other and thus it may influence protein function toward their pro- or anti-apoptotic program (see Fig. 34)[65].

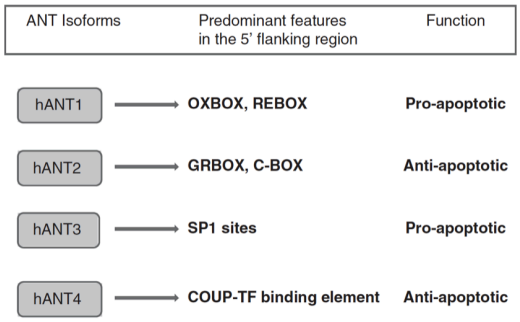

Figure 34 Representation of predominant features of the four AAC isoforms promoters with apoptosis linked-functions[65].

Human AAC1 isoform gene is located on chromosome 4 and possesses

characteristic transcriptional factors (OXBOX) that influence its high expression in heart and skeletal muscles (see Fig. 34 and 35)[126,142]. The systematic screening for dominant pro-apoptotic genes led to the conclusion that AAC1 is a pro-apoptotic factor[143]. Furthermore, the overexpression of AAC1 facilitates mitochondria-dependent apoptosis process[143–145,146]. It was also shown that the AAC1 transfection in breast adenocarcinoma cells induced apoptosis and finally stimulated tumor regression. Those findings validated the hypothesis that AAC1 might be a potential therapeutic target for cancer treatment[147].

Human AAC2 isoform gene is located on the chromosome X. The 5`-flanking region consists, among others, in a conserved AB box that is reported as AAC2 transcription activator and a C box that inhibits gene transcription (see Fig. 34 and 35)[65]. AAC2 gene is up-regulated in growth-activated cells and down-regulated upon growth inhibition. Expression of human AAC2 gene in highly proliferating cells is controlled by glycolysis-regulated box[131]. The suppressor regions in the AAC2 promoter[148,149] contribute to the gene regulation in a tissue-specific manner[129,140] and in response to different signals[128]. It was described that in some cancer cells the expression of the AAC2 is increased[130,132] hence it was proposed that AAC2 might have cytoprotective effect (proliferative and/or anti-apoptotic). Therefore, it was speculated that AAC2 1) may function in the reverse manner (import ATP into the mitochondrial matrix) to compensate for the decreased ATP production in the cancer cells[150] and 2) could interact with Bcl-2 in order to stabilize mitochondrial membranes through the inhibition of matrix metalloproteinase (MMP)[139]. It seems that AAC2 cytoprotective effects are opposite to AAC1 lethal effects. Preliminary data showed also that AAC2 is overexpressed frequently in hormone-dependent cancers (ovary, thyroid, testis, cervix, breasts) and thus being an anti-apoptotic protein in cancer[65].

Human AAC3 gene is also localized on chromosome X and is ubiquitously expressed. Among others elements, AAC3 gene is highly abundant in Sp1-binding sites that may favor apoptosis process since Sp1 induces inhibition of cell-cycle progression[151] (see Fig 34 and 36)[65]. In the apoptosis process, overexpression of AAC3[144,145] has a similar effect as AAC1 in HeLa cells and additionally it influences the lethal effects. Hence, hAAC3 remains in contrast with AAC2 that shows lack of apoptotic activity[143,144]. Preliminary results suggest that the AAC3

mRNA is up-regulated in many human tumors however those investigations need to be confirmed in terms of their pro-apoptotic activities[65].

The AAC4 gene is localized on the chromosome 4 and its expression is highly dependent on the organism and tissue[133]. The gene transcription region is highly methylated (see Fig. 34 and 36)[65] and thus it influences the gene expression. The gene promoter hypomethylation was observed in testis while hypermethylation was observed in somatic cells[152,153]. However, it was also reported that methylation process might be not a critical factor in the tissue-specific expression[141,152]. The overexpression of AAC4 in human cancer cells (such as HeLa) inhibits apoptotic signaling especially mitochondria-mediated cell death[154]. Hence, the loss of mitochondrial transmembrane potential, the activation of caspase-9 and nuclear alternations is prevented by AAC4 isoform. It was suggested that the anti-apoptotic activity of AAC4 could be mediated by ROS steady-state level modulation[154]. However referring to the recent discoveries regarding AAC4 the main function of this isoform in the cancer still remains unknown.

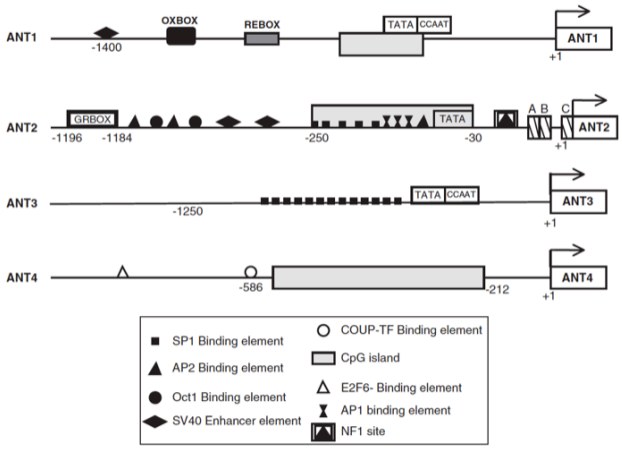

Figure 35 Human AAC gene isoforms organization scheme with indicated regulatory elements, transcription factor-binding sites for various promoter regions of the four AAC isoforms. The start site of transcription is marked as 1[65].

Taken together, the AAC1 isoform is pro-apoptotic and its expression is frequently repressed in cancer. AAC2 functions as a MMP inhibitor and can be up-regulated in hormone-dependent cancer. The AAC3 isoform is pro-apoptotic *in cellulo*, but can be up-regulated in cancer while AAC4 shows anti-apoptotic activity in human cancer cells[65].

1.3 Structural Biology of Membrane Proteins

Crystallization requires the production of large amounts of membrane proteins that are stable and well-folded. There are some membrane proteins that are highly abundant in their native membranes (for instance porins, bacterial photosynthetic reaction centers, ATPases) and consequently they became the first ones to have their structures solved. However, for many others, the recombinant expression is a necessity. This is the first bottleneck that must be tackled to receive enough amount of proteins for successful structural biology projects. Once sufficient expression is achieved, the next barrier is the purification of the protein in a functional and stable form. The native membrane environment imparts significantly to membrane protein stability through its lipid composition and physiochemical properties. Detergent environment is supposed to mimic native membranes, however vast majority of membrane proteins cannot be purified in such manner since they rapidly denature and often aggregate. Both issues, heterologous overexpression and stable purification, particularly concern membrane proteins from higher eukaryotes and most of the membrane proteins structures were solved from bacteria or archea. Once having suitable expression system and purification protocol that delivers pure, homogenous, stable and well-folded protein, crystallization part begins. Starting from high-throughput screenings, through conditions optimization and ending on well-diffracting crystals that are good enough to solve the protein structure, is the next bottleneck. Most membrane protein structures were solved using X-ray diffraction in combination with detergent crystallization protocols. In recent years an automation and miniaturization of crystallization trials improved substantially. The rate of progress is still increasing, the recent breakthroughs include structures of G protein-coupled receptors (GPCRs)[155,156], secondary active transporters[7,157], ATPases[158], ABC transporters[159] and ion channels[160]. Moreover, the number of structures from recombinant proteins increases constantly (see Fig. 36)[161].

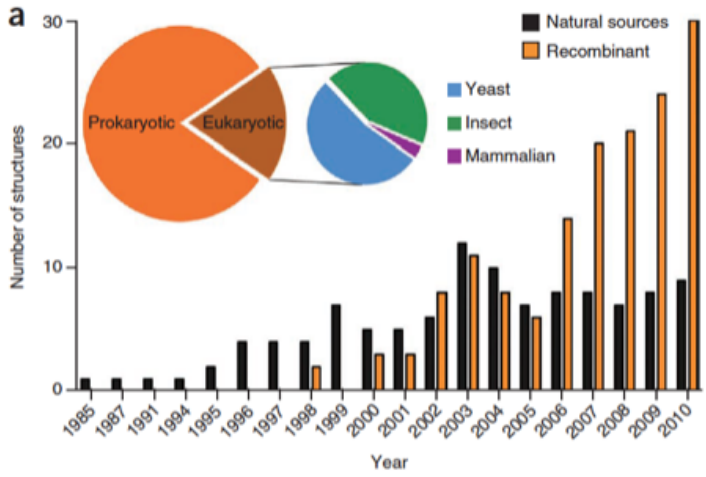

Figure 36 Summary of available prokaryotic and eukaryotic membrane protein structures. Different trends in production of recombinant membrane proteins used in structural studies[161].

Membrane proteins are difficult to crystallize and moreover, the full success relies on growing crystals of sufficient size which is even more demanding.

Therefore micro- and nano crystallography development are particularly useful to tackle such projects. Smaller crystals may be also better ordered, since they contain less long range disorder[162]. Upon performing classical measurements, increased dose of the X-ray beam to record the data from small-sized crystals leads to extensive damage before the diffraction signal can be recorded. Hence, much has been done to improve data collection from small and weekly diffracting crystals. Micro-diffraction aims to reduce the time-consuming process of crystal growth and enables the study of small crystals. The target protein crystals can be smaller than 20 μm and the beam sizes in the range of 1 to 20 μm[163]. The small size of the beam enhances signal-to-noise ratio in diffraction images obtained from micro-crystals by reducing background scattering from sample solvent and support [164,165]. One of the initiative was a development of a micro-focus beamline at the ESRF from which first diffraction data from microcrystals of bacteriorhodopsin (bR) were collected[166]. Still, the quality of recorded data from micro- and nano-crystals is limited by the X-ray induced radiation damage, that has a strong dependence on the type of protein and the packing of the protein in the crystals[167].

Following very rapid development of micro-and nano-crystallography new powerful methods for structure determination appeared. The latest and

revolutionary system is based on data collection of a single-crystal X-ray diffraction "snap-shot" from fully hydrated stream of nanocrystals using femtosecond pulses from a hard X-ray free electron laser (X-ray FEL) (see Fig. 37)[168,169].

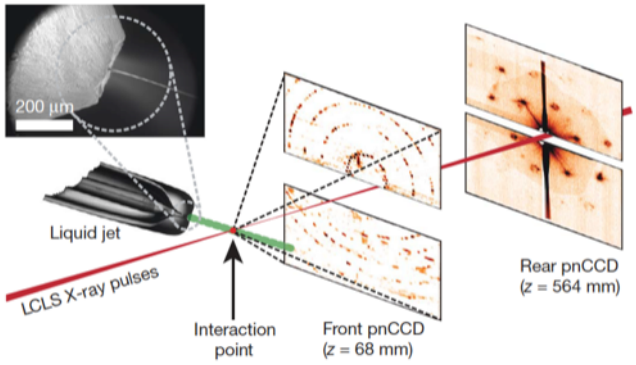

Figure 37 Femtosecond nanocrystallography. Stream of nanocrystals flow in their buffer solution in a gas-focused, 4 mm diameter jets at the velocity of 10 ms and perpendicular to the pulsed X-ray FEL beam that is focused on the jet. The arrival of the crystals in the beam is random in terms of time and orientation. Probability of hitting one crystal is proportional to the crystal concentration[168].

Currently, they are two available hard X-ray FELs: the Linac Coherent Light Source (LCLS) at SLAC/Stanford, USA[170] and the Spring-8 Ångström Compact Free-electron Laser (SACLA)[171] at Riken/Harima, Japan that allow studies in many different areas of science including structural analysis of biological molecules.

The brilliance of X-FEL sources that generate the femtosecond X-ray pulses created a great excitement across many scientific disciplines. This new approach is especially useful for membrane proteins that cannot crystallize up to sufficient sizes for studies using conventional synchrotron radiation beamlines or that are particularly sensitive to radiation damage. Hence, collection of the damage-free structural data from micron or submicron scale crystals of membrane proteins becomes a powerful tool and can significantly accelerate progress towards new insights into understanding of their structures and dynamics[168,172]. Therefore, nowadays serial crystallography is being more and more introduced on synchrotrons facilities.

2 Project objectives

As a member of Nanomem consortium that is dedicated to development of serial crystallography the main objective of my PhD project was to gain new structural data on the ADP/ATP carriers and develop tools for micro- and nano-crystallography, which is applied to membrane protein structural biology. However, since obtaining membrane protein crystals of AACs was a difficult target, therefore in parallel in my project we used different model of membrane proteins in order to study new serial crystallography approaches.

Much has been done to investigate the mitochondrial ADP/ATP carriers in order to understand mainly their transport mechanism, which includes characterization of the substrate binding site of the protein, its conformational changes and inhibition properties.

So far and despite constant efforts only the bovine and yeast ADP/ATP carriers three-dimensional structures were solved and all in the same conformation, in complex with CATR inhibitor (c-state)[77,83]. Therefore, since no structural data is available on the m-state some fundamental questions about the different conformational states adopted by the protein during the transport process still need to be answered.

During my PhD we decided to target AAC homologs other than the bovine and yeast ones. We first selected the 4 human AAC isoforms. They are involved in different genetic diseases but play also a role in cancerogenesis. Any new data on their structure and function can become a powerful tool in the drug development field. We investigated in detail and compared their functional properties, studied mutants in order to discover important residues (different then already described) that might be involved in protein conformational change and hence in the transport mechanism. Additionally, we developed expression and purification protocols in order to obtain new structural data on the proteins.

The functional studies of the human AACs are presented in the first part of the results. We investigated protein functional properties such as transport rate, ATP binding affinity, protein activity in presence of different inhibitors and additionally AAC mutants activity.

Production in cell-free system, purification using different detergents, characterization using variety of biophysical tools and finally crystallization studies of hAACs were also investigated and are described in the second part of the results.

We considered as well an AAC homologue recently identified in plant plasma membrane (PM_AAC) as an interesting target to investigate. Hence, in the third part of the results we described preliminary results regarding protein functional properties, protein production, characterization and crystallization assays.

Regarding the development for new crystallographic tools we initially planned to use AAC crystals to develop new methodologies. However as described in the first chapter of this manuscript we did not obtain reproducible crystallization conditions for any of our AAC target. Still we did not give up this objective but rather use other membrane proteins for which crystallization conditions and crystals were available. Since the structural biology field is rapidly developing especially in serial crystallography techniques, there are more and more new applications for samples preparation, mounting and measurements in order to improve the quality of the collected data from the synchrotrons. Hence, our objective was to developed new crystal-friendly crystallization set up combined with different sample installation toward faster, more efficient and simpler data collection. We used different proteins including membrane ones to explore the properties of particular crystallization and data collection set ups at the synchrotron that could also help in the future for serial crystallography measurements. The description of so far tested set ups and analyzed protein samples can be found in the fourth part of the result section.

CHAPTER II

3 Materials and methods

3.1 Molecular biology - recombinant DNA techniques

3.1.1 Transformation of DNA plasmid in competent cells

A 40 µL aliquot of chemically competent cells (TOP10, C43(DE3) (for human ADP/ATP Carriers constructs, see Table 3 and 4 in Annex 1bis), C41(DE3), Rosetta 2(DE3), BL21(DE3) (for plant Plasma Membrane Protein constructs, see Table 3 and 4 in Annex 1bis)) was gently thawed on ice. DNA plasmid (50-100 µg) was mixed with competent cells and incubated on ice during 30 min. Heat shock for the transformation reaction was performed during 45 – 50 s at 42°C in water-bath and afterwards the sample was rapidly transferred on ice and incubated additionally 2 min. Next, 200 µL of LB (Lysogeny Broth) Medium (*Sigma-Aldrich*) was added to the transformed cells and sample was incubated at 37°C for 60 min at 200 rpm. After incubation transformed cells were plated on LB Agar (*Sigma-Aldrich*) plates containing Ampicillin (*Euromedex*) or Kanamycin (*Euromedex*) antibiotic, depending on the construct (see Table 3 and 4 in Annex 1bis), and incubated at 37°C over-night.

3.1.2 Small scale plasmid DNA preparation (MiniPrep)

For small scale plasmid DNA preparation, 5 mL LB (*Sigma-Aldrich*) culture containing one single colony from the transformation plate and appropriate antibiotic (Ampicillin or Kanamycin) was grown at 37°C, 200 rpm over-night. Afterwards the culture was centrifuged at 4000 rpm for 20 min at 4°C. Further plasmid DNA purification protocol was performed according to the manufacturer`s protocol (*QIAprep Spin Miniprep Kit, Qiagen*). In the last step the purified DNA was eluted with 30 µL of filtered H_2O from the small-spin column and stored at -20°C.

3.1.3 Large scale plasmid DNA preparation (MidiPrep)

For large scale plasmid DNA preparation, 100 mL culture (containing appropriate antibiotic – Ampicillin or Kanamycin) was grown at 37°C, 200 rpm over-night. Afterwards the culture was centrifuged at 4000 rpm for 20 min at 4°C. Further plasmid DNA purification protocol was performed according to the manufacturer`s protocol (*Plasmid DNA Purification Kit, Macherey-Nagel*). In the last step the purified DNA was dissolved in 100 µL of filtered H_2O and stored at 20°C.

3.1.4 Agarose gel electrophoresis

Separation and analysis of DNA fragments were done using horizontal electrophoresis with 1% agarose (*Roche*) gel. The agarose was dissolved in 1 x TAE (Tris – Acetate – EDTA) buffer pH 8.3 and supplemented with ethidium bromide to a final concentration of approximately 0.2-0.5 µg/mL. Solution was later poured into a gel chamber. A DNA ladder (*Thermo Scientific*) and all samples (supplemented with 10 µL of 6 x DNA loading buffer (*Fermentas*)) were loaded to appropriate wells and the electrophoresis was performed on Mini Horizontal Gel Electrophoresis System (*Major Science*) at 100 V for 40 min.

3.1.5 Spectrophotometric analysis of DNA concentrations

DNA concentrations were measured using NanoDrop 2000c Spectrophotometer (*Thermo Scientific*) at a wavelength of 260 nm. The purity of DNA samples was analyzed according to the absorption spectrum between the wavelengths 220 nm and 320 nm. For pure DNA, the A260 nm/A280 nm ratio lies between 1.8 and 2.0.

3.1.6 Cloning methods

All the constructs were created using restriction/ligation cloning method (see Annex 1, point 1) and/or Restriction-free (Rf) cloning (see Annex 1, point 2) and/or Quick-Change Mutagenesis (see Annex 1, point 3).

3.1.7 Constructs

The protein sequences, the primers, the plasmids and the constructs used for the different cloning are presented in Tables 1, 2, 3 and 4 of Annex 1bis.

3.2 Biochemical methods for protein investigation

3.2.1 SDS-polyacrylamide gel electrophoresis (SDS-PAGE)

For the analysis of the protein samples, 12% acrylamide (*Euromedex*) SDS-PAGE (*Bio-Rad*) was used. Each protein sample was prior supplemented with 6X SDS Loading Dye (*Thermo Scientific*) and all of them were analyzed according to the Page Ruler Prestained or Unstained Protein Ladder (*Thermo Scientific*). Electrophoresis was performed at constant voltage of 200 V for 55 min and stained in Coomassie solution.

3.2.2 Western blotting

Proteins separated by SDS-PAGE as described in paragraph 3.3.1 were transferred to Nitrocellulose 0.45 µm (*Bio-Rad*) or Polyvinylidene fluoride (PVDF) membranes (*GE Healthcare*). The protein transfer proceeded for 40 min at 100 W and 350 mA. Afterwards the membrane was placed in 25 mL blocking solution (1X PBS – 0.03% Tween and 5% dry milk and rocked at room temperature (RT) for 30 min. The membrane was then incubated for 1h 30 min with addition of 12.5 µL of anti–MBP antibody (*New England Bio Labs*) or anti-His antibody (Monoclonal Anti-polyHistidine Peroxydase Conjugate, *Sigma*) at RT. After rinsing the membrane 3 times 10 min with 1X PBS – 0.03% Tween, the detection was performed using the DAB (3,3'-Diaminobenzidine tetrahydrochloride) two-component substrate system (*Sigma-Aldrich*).

3.2.3 Protein quantification using BCA Assay (*Thermo Fisher Scientific*)

The BCA Protein Assay is based on bicinchoninic acid (BCA) for the colorimetric detection and quantitation of protein sample. This method combines the well-known reduction of Cu^{2+} to Cu^{+} by protein in an alkaline medium (the biuret reaction) with the highly sensitive and selective colorimetric detection of the Cu^{+} ion using a unique reagent containing bicinchoninic acid. Chelation of two molecules of BCA substrate with one Cu ion results in the purple-colored reaction product. Absorbance is measured at 562 nm.

Protein concentrations were determined with reference to standard bovine serum albumin (BSA). A series of BSA dilutions of known concentrations were prepared and assayed alongside with Plasma Membrane Protein (PMP) in order to determine its concentration based on the standard curve.

For PM protein quantification series of *E. coli* membrane dilutions were prepared in 2 mL Eppendorf Tubes: 100X, 50X, 20X and 10X in total volume of 100 µL. 2 mL of Working Reagent (WR, previously prepared according to manufacturer`s protocol) were added and tubes were incubated at 37°C during 30 min. After incubation samples were transferred to plastic cuvettes and absorbance was measured on spectrophotometer (*Varian Cary 50 – Bio, UV Visible Spectrophotometer*) at 562 nm.

3.3 Production of human mitochondrial ADP/ATP Carriers

3.3.1 Protein expression using Cell-Free System

In general cell-based expression of membrane proteins is always a bottleneck in protein production since it results very often in low yield and stability but also in cell toxicity, protein aggregation and misfolding. Cell-free expression system allows membrane proteins synthesis directly into hydrophobic and artificial environments. This highly dynamic and versatile technique is an alternative method for the overexpression of membrane proteins since all of the transcription and translation processes are happening *in vitro* avoiding the influence of some inhibitors and toxins (which are normally present

in the cells) is avoided. Moreover this method is an open system enabling to improve the protein expression by adding different additives, for instance detergents, liposomes, cofactors. It is also time-saving since the expression (or co-expression) of the proteins is performed only during a couple of hours and the yield of the expressed protein is high.

Nowadays cell-free expression system is all the time being improved both in performance and for extended applications like labeling, proteomic analysis and throughput expression and most recently on the level of ribosome display, cell-free protein arrays for *in vitro* protein selection, functional screening and evolution[173,174,175,176,177,178].

Human AAC isoforms were cloned into pIVEX 2.3d vector with C-terminal His-tag (see Table 3 and 4 in Annex 1[bis]) or pIVEX2.4d vector with N-terminal His-tag (see Table 3 and 4 in Annex 1[bis]) vectors respectively using Restriction–Free Cloning (see paragraph 3.1.6.2). The expression system consists of a Reaction Mix (see Table 11 and Tables 1, 2 and 3 in Annex 2) and a Feeding Mix (see Table 12 below and Table 2, 3 and 4 in Annex 2) in the proportion 1:10 respectively.

Reaction Mix - 2 ml	
Component	**Volume (µL)**
Traduction Mix*	400
2 M Potasium Glutamate (*Sigma - Aldrich*)	200
4 mM Amino Acid Mix**	150
100 mM Magnesium Acetate (*Sigma - Aldrich*)	178
50 mM Acethyl Phosphate (*Sigma - Aldrich*)	50
S30 *E.coli* extract cell***	728
T7 DNA polymerase****	40
20 % Brij 35 (*Sigma - Aldrich*)	50
human AAC DNA	20 µg
ddH_2O	to fill up to 2 ml

Table 3 Components of the Reaction Mix used for Cell–Free expression of human ADP/ATP Carriers.

*** - see list of the components in Table 1 in Annex 2**
**** - see list of the components in Table 2 and 3 in Annex 2**
***** - S30 *E.coli* homemade extract was prepared by the Cell–Free Platform at IBS (Lionel Imbert and Céline Jullian-Binard)**
****** - T7 polymerase is homemade by Lionel Imbert at Cell–Free Platform, IBS**

Feeding Mix - 20 ml	
Component	**Volume (mL)**
Feeding Mix Solution*****	10
2 M Potasium Glutamate (*Sigma - Aldrich*)	2
100 mM Magnesium Acetate (*Sigma - Aldrich*)	2.8
20 % Brij 35 (*Sigma - Aldrich*)	0.5
ddH_2O	to fill up to 20 mL

***** - see list of the components in Table 4 in Annex 2

Table 4 Components of the Feeding Mix used for Cell–Free expression of human ADP/ATP Carriers.

After thawing gently on ice each component of the Reaction Mix (total volume of 2 mL) (see Table 11), the solution was loaded to a dialysis tube – GeBAflex Tube MWCO 12 – 14 kDa (*Gene Bio - Application L.T.D*). For each 2 mL of Reaction Mix, 10 mL of Feeding Mix was prepared. All the components of the Feeding Mix were gently thawed on ice and mixed in 50 mL Amicon Tube. Afterwards the dialysis tube with Reaction Mix was carefully placed inside the Amicon Tube containing the Feeding Mix and firmly closed. Before final incubation small stir bar was placed on each dialysis cap. Once prepared the set up was further turned upside-down and placed in glass beaker, Amicon Tubes were shielded with paper towel and beaker was later on placed on magnetic stirrer at 20°C over-night.

Some small-scale human AACs expression trials were also initially performed to identify the optimum construct (C–terminal or N–terminal His-tag; see Tables 3 and 4 in Annex 1) and the optimum detergents (0.5%/1% DDM (*Anatrace*), 1.2%/2.4% Cymal 5(*Anatrace*), 0.0053%/0.012% FC16 (*Anatrace*), 0.5%/1% Brij35 (*Sigma – Aldrich*) – 10X and 20X CMC respectively (for detergents details see Annex 3, part 1). For construct screening, eppendorf tubes were filled with 50 µL of Reaction Mix (with difference of only protein DNA construct) without any Feeding Mix. For detergent screening experiments, expression tubes contained also 50 µL of Reaction Mix (with different detergents combined with different concentrations) also without Feeding Mix. Incubations were carried out at RT during 4 – 5 h. Afterwards, 15 µL of the synthesis reaction was loaded on SDS-PAGE (see paragraph 3.2.1) and further analyzed on Western

Blot using anti – His antibody (Monoclonal Anti-polyHistidine Peroxydase Conjugate) (see paragraph 3.2.2) (see Fig. 38A and B)

A B

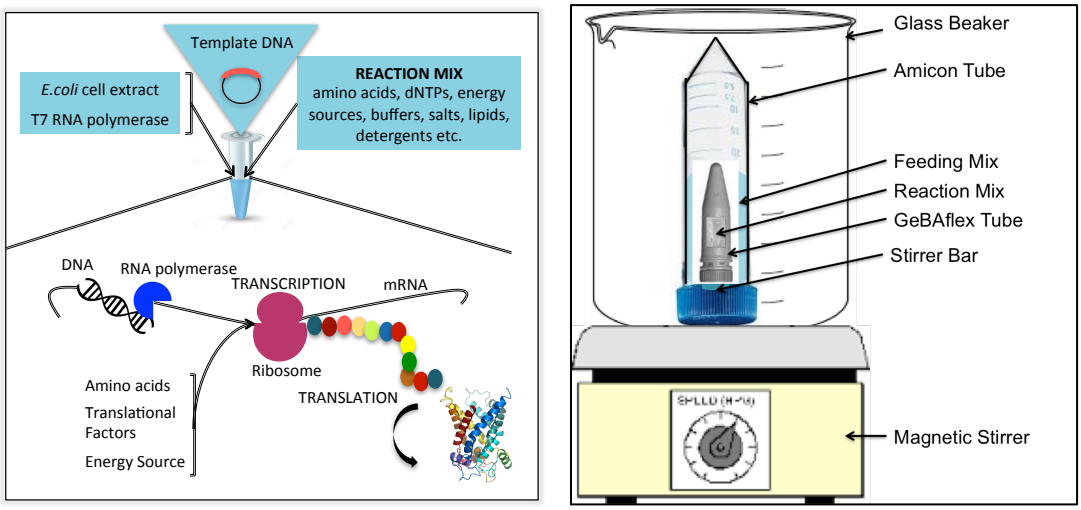

Figure 38 Cell – Free expression System. (A) The components of the Reaction Mix, (B) The cell–free expression system set up for a larger volume of protein expression in GeBAflex Tubes.

Some of the Cell-Free synthesis experiments were also performed in presence of 20 µM CATR (Carboxyatractyloside) inhibitor that was supplementing in Reaction and Feeding mix.

All the synthesis reactions preparation was performed in the RNAse-free lab of the Cell-Free Platform (IBS).

3.3.2 Protein purification using NiNTA Chromatography

Purification of the human ADP/ATP Carriers produced in cell–free system was performed and optimized on Nickel Resin (NiNTA) (*Clontech*) that binds His-tag. After over-night synthesis incubation 2 mL of Reaction Mix (where protein overexpression is expected) was transferred to 2 ml Eppendorf tube and centrifuged at 4°C during 10 min, at 13 000 rpm. 2.5 ml of NiNTA Resin was equilibrated with Equilibration Buffer (EQB) (see Table 13) and then 2 ml of centrifuged synthesis reaction was added to the NiNTA Resin which was additionally supplemented with 20 mL of: 50 mM HEPES pH 7.5 (*Sigma – Aldrich*), 200 mM NaCl (*Euromedex*), 10 mM Imidazole (*Euromedex*). Incubation with the NiNTA resin was performed during 2 h at 4°C with constant turning (wheel). After incubation, the resin was washed with Wash Buffers 1 to 4 (WB 1

– 4) containing an imidazole concentration that was gradually increased (see Table 13). Protein was eluted from the resin with Elution Buffer (EB) (see Table 13). Each fraction of each purification step was later analysed by SDS-PAGE (see paragraph 3.2.1).

Component	EQB	WB1	WB2	WB3	WB4	EB
50 mM HEPES pH 7.5	+	+	+	+	+	+
200 mM NaCl	+	+	+	+	+	+
Imidazole	-	10 mM	10 mM	20 mM	40 mM	200/300 mM
Detergent (*Anatrace*)	-	same as used in Cell-Free synthesis (2-4X CMC)	same or other as used in Cell-Free synthesis (2-10X CMC)	same or other as used in Cell-Free synthesis (2-10X CMC)	same or other as used in Cell-Free synthesis (2-10X CMC)	same or other as used in Cell-Free synthesis (2-10X CMC)

Table 5 Components of the Buffers used in purification of human ADP/ATP Carriers.

After NiNTA chromatography protein elution fractions were concentrated in 50 kDa Amicon - Ultra (*Merck Millipore*) Concentrator Tubes up to approximately 1 mL and loaded on desalting column – DC-10 (GE–Healthcare) in order to remove imidazole from the protein samples. Afterwards protein was eluted with 3.5 mL of buffer containing 50 mM HEPES pH 7.5, 200 mM NaCl and detergent (depending on the purification protocol). After the desalting column, the protein fraction without imidazole was concentrated in a 50 kDa Amicon – Ultra (*Merck Millipore*) Concentrator Tubes up to approximately 200 – 250 µL (depending on the purification protocol). Protein concentration was measured using NanoDrop (see paragraph 3.5.1). Protein was stored at 4°C.

3.3.3 Protein Purification using Size Exclusion Chromatography (SEC)

After NiNTA chromatography (see paragraph above) proteins were purified using Size Exclusion Chromatography System on a Superdex 200 10/300 GL (*GE Healthcare*) gel filtration column. Proteins (100 – 500 µL) were loaded on the column in Gel Filtration Buffer containing – 50 mM HEPES pH 7.5, 200 mM NaCl and detergent (depending on the one used during purification -

0.04% DDM, 0.01%/0.005% MNG3, 0.1% LAPAO etc. (for detergents details see Annex 3, part 1)) Purification was done using *Bio Rad* purification system and results were analysed using ChromLab system. The run was set up with a flow of 0.5 mL/min with 0.5 mL fractions collection. Each eluted fraction from SEC containing the protein of interest was later analysed by SDS-PAGE (see paragraph 3.2.1). Protein fractions after purification were concentrated using 50 kDa Amicon Ultra Concentration Tubes up to approximately 200 µL and stored at 4°C. Protein concentration was measured using NanoDrop (see paragraph 3.5.1).

3.4 Production of non–mitochondrial ADP/ATP Carrier – Plasma Membrane Protein (PMP) - from plants

3.4.1 Protein expression trials in *E.coli* system

PM Protein cDNA (see Table 1 and 2 in Annex 1^{bis}) was cloned into pET11/LIC or pET11/LIC fused with SUMO-tag vectors (see Table 3 and 4 in Annex 1^{bis}). Transformation of plasmid cDNA into competent cells was performed like described in paragraph 3.1.1. Four different *E.coli* competent cell strains were tested: BL21(DE3), Rosetta 2(DE3), C41(DE3) and C43(DE3). The next day 5 mL LB precultures were set up containing: 5 µL of 50 mg/mL Kanamycin and one single colony from the transformation plate. Incubation was performed at 37°C, over night at 200 rpm. The precultures were used to inoculate larger volume cultures containing: 25 mL of LB medium, 25 µL of 50 mg/mL Kanamycin and 2.5 mL of preculture. Cultures were further incubated at 37°C at 200 rpm until OD_{600nm} reached approximately 0.7 (measured on spectrophotometer – Ultraspec 10, *Amersham Biosciences*). The expression was then induced by adding 0.1 mM or 1 mM IPTG and later incubating at 20°C, over night at 200 rpm. Next day the cultures were centrifuged at 4°C, 15 min at 13000 rpm and the supernatant was discarded. 100 µL of 1X and 8 µL of 6X SDS Loading Dye was added to each aliquot of pellet (from each cell strain – non-induced, induced with 0.1 mM IPTG and induced with 1 mM IPTG). The samples were next mixed, centrifuged at 4°C, 20 min at 13 000 rpm and finally sonicated

before loading on SDS-PAGE (see paragraph 3.2.1) and further analysed with Western Blot using anti–His antibody (Monoclonal Anti-polyHistidine Peroxydase Conjugate) (see paragraph 3.2.2).

3.4.2 Large scale protein expression in *E.coli*

Transformation of plasmids containing PM protein gene into Rosetta 2(DE3) competent cells was performed like in paragraph 3.1.1.

The next day small volume of *E.coli* precultures were prepared with: 50 – 100 mL of TB Broth (*Sigma – Aldrich*) enriched with 8 mL of glycerol (*Carlo Erba*), 50–100 µL of 50 mg/mL Kanamycin and one single colony from the LB agar plate. Incubation was performed at 37°C, over night and at 200 rpm.

After over night incubation large volume cultures were prepared with: 1 L of TB Broth Medium enriched with 8 mL of glycerol and 1 mL of 50 mg/mL Kanamycin and inoculated with 10–20 mL of preculture. Cultures were incubated at 37°C, 200 rpm until OD_{600nm} reached approximately 0.7. The expression was induced adding 0.1 mM IPTG and later on the incubation was done at 20°C, over–night and at 200 rpm. The next day cells were harvested and spun down at 4°C, 20 min at 4000 rpm, pellets were frozen and stored at -20°C.

3.4.3 Membrane extraction

Cells pellets were gently thawed on ice and resolubilized in Lysis Buffer in the following proportion: 1 g of pellet in 10–15 mL of Lysis Buffer (see Table 14), homogenized using glass potter and broken by three passages in a microfluidizer (*Microfluidics M110 – P*) at 14000 psi. The broken cells were ultracentrifuged (*Beckman Coulter Optima LE – 80K Ultracentrifuge*) at 4°C, 20 min at 37 566 x g, the pellets were discarded and the supernatants centrifuged at 4°C, 1h at 158 728 x g. The membranes fraction was placed on ice and gently resuspended in Resolubilization Buffer (RB) (see Table 14) in the following proportion: 1 L of culture in 1 mL of the RB. Supernatant fractions obtained after the first and the second ultracentrifugations and a fraction taken from the resolubilized membranes were later analysed by SDS-PAGE (see paragraph 3.2.1). The protein concentration in the membranes was measured using BCA Assay (*Thermo Fisher*

Scientific) (see paragraph 3.2.3). Resolubilized membranes were finally aliquoted in 2 mL Eppendorf tubes, frozen in liquid nitrogen and stored at -80°C.

3.4.4 Solubilization trials

Membranes containing overexpressed PM Protein were thawed on ice and diluted to approximately 3 mg/mL with ten different Solubilization Buffers (SB) (see Table 14) enriched in ten different detergents: 1% DDM, 1% Cymal 5, 2% OG, 1% LDAO, 1% CHAPS, 1% $C_{12}E_9$, 1% FC12, 1% LAPAO, 1% FC16 and 1% Brij35 (see detergents details in Annex 3, part 1) in a final volume of 1 mL. Solubilization was performed at 4°C during 1.5 h on the turning wheel. Membranes were then transferred to microcentrifuge tubes (*Beckman*) and ultracentrifuged (*Beckman Optima TL Ultracentrifuge*) at 4°C, 1h at 134 877 x g. 10 µL aliquot from each sample supernatant and an aliquot of each pellet (tip of the pipet) were analyzed with Western Blot (see paragraph 3.2.2).

3.4.5 Protein purification using NiNTA chromatography

Membranes containing overexpressed PM Protein were thawed on ice, solubilized in Solubilization Buffer (SB) (see Table 14) and incubated at 4°C, 1h on the turning wheel. Afterwards solubilized protein was ultracentrifuged (*Beckman Coulter Optima LE – 80K Ultracentrifuge*) at 4°C, 1h, at 164 243 x g. After centrifugation the pellets were discarded. Remaining supernatant was mixed gently with 2 mL of previously equilibrated NiNTA Resin (*Clontech*) with Equilibration Buffer (EQB) (see Table 14). Incubation with NiNTA Resin was performed at 4°C during 1.5h with constant turning (wheel). After incubation, resin was washed with Wash Buffers 1 and 2 (WB 1 – 2) containing imidazole concentration which was gradually increased (see Table 14). Protein was eluted from the resin with Elution Buffer (EB) (see Table 14). Each fraction of each purification step was later analysed by SDS-PAGE (see paragraph 3.2.1).

Component	LB	RB	SB	EQB	WB1	WB2	EB
50 mM HEPES pH 7.5	+	+	+	+	+	+	+
300 mM NaCl	+	+	+	+	+	+	+
20% Glycerol (*Carlo Erba*)	+	-	-	-	-	-	-
1X CLAPA	+	-	+	-	-	-	-
β-mercaptoethanol (*Carl Roth*)	-	-	4 mM	-	2 mM	2mM	2 mM
1 mM Benzamidine - HCl (*Calbiochem*)	+	-	+	-	-	-	-
Detergent (*Anatrace*)	-	-	1%	-	2-4X CMC	2-4X CMC	2-4X CMC
Imidazole (*Euromedex*)	-	-	-	-	50 mM	100 mM	300 mM
50 mM Sucrose (*Sigma - Aldrich*)	-	+	-	-	-	-	-
1 mM EDTA (*Euromedex*)	-	+	-	-	-	-	-

Table 6 Components of all of the buffers used for membrane extraction and Plasma Membrane Protein purification.

After the NiNTA chromatography protein elution fractions were concentrated in 30 kDa or 50 kDa Amicon - Ultra Concentrator Tubes up to approximately 1 mL and loaded on desalting column – DC-10 (*GE–Healthcare*) in order to remove the imidazole from the protein samples. Afterwards the protein was eluted with 3.5 mL of buffer containing 50 mM HEPES pH 7.5, 200 mM NaCl and detergent (depending on the purification protocol). After desalting column, the protein fraction without imidazole was concentrated anew in 30 kDa or 50 kDa Amicon – Ultra Concentrator Tubes up to approximately 200 – 250 µL (depending on the purification protocol). Protein concentration was measured using NanoDrop (see paragraph 3.5.1). Protein was stored at 4°C.

3.4.6 Protein Purification using Size Exclusion Chromatography (SEC)

After NiNTA chromatography (see paragraph above) proteins were purified using Size Exclusion Chromatography System on a Superdex 200

10/300 GL (*GE Healthcare*) gel filtration column. Proteins (100 – 500 µL) were loaded on the column in Gel Filtration Buffer containing – 50 mM HEPES pH 7.5, 300 mM NaCl and detergent (same as for the purification) Purification was done using *Bio Rad* purification system and results were analysed using ChromLab system. The runs were set up with a flow of 0.5 mL/min with 0.5 mL fraction collection. Each elution fraction from SEC containing the protein of interest was later analysed by SDS-PAGE (see paragraph 3.2.1). Protein fractions after purification were concentrated using 30 kDa or 50 kDa Amicon Ultra Concentration Tubes up to approximately 200 µL and stored at 4°C. Protein concentration was measured using NanoDrop (see paragraph 3.5.1).

3.5 Biophysical Methods

3.5.1 Spectrophotometric analysis of protein concentration

Protein concentrations were measured from the absorbance at 280 nm using the NanoDrop 2000c spectrophotometer and considering the theoretical ε value deduced from the aminoacid sequence.

3.5.2 Circular dichroism (CD) measurements

Circular dichroism (CD) was used to analyze protein folding and measure thermal stability. CD is the difference in light absorbance between left- (L-CPL) and right-circularly polarized light (R-CPL). This spectroscopic technique allows investigating different kinds of chiral materials in solution for instance: polymers, small molecules (drugs) and also biopolymers (nucleic acid, proteins, lipids).

A primary use of CD is to determine the secondary structure of the macromolecules. Protein conformation depends on many different factors and is highly sensitive to its environment, temperature or pH. CD allows observing how the protein secondary structure can change according to environmental conditions or upon interaction with other molecules. Moreover it is possible to derive kinetic and thermodynamic information[179].

CD experiments combined with beamline analysis (CD - beamline experiment) were performed at B23 Diamond Light Source, UK. Two human mitochondrial ADP/ATP Carriers were investigated – isoform 1 and 3. Both of them were expressed, purified and subsequently resuspended in the following buffer: 50 mM HEPES pH 7.5, 200 mM NaCl and 0.005% MNG3 as described above in paragraphs 3.3.2 and 3.3.3. Protein folding determination was performed using 5 µL of human AAC1 and AAC3 protein at 1.7 mg/mL and 2.2 mg/mL respectively. The protein solutions were gently loaded into 0.01 cm glass cylindrical windows and placed in Beamline Module A with customized UHV Olis DSM20 monochromator for further analysis. Temperature melting measurements were performed using 30 µL of the protein samples at the same concentrations as given above, however in these experiments the protein samples were gently loaded into 0.2 cm glass cylindrical window. CD-beamline measurements were performed in far-UV (190 – 260 nm). The beam size was 0.5 mm^2 to 2 mm x 4mm with flux at sample point of: 0.9×10^{12}. The experiments were analyzed with OLIS Work-Book software available at B23 beamline.

CD experiments were also performed on the ISBG Biophysical platform using a JASCO J-1100 CD machine. Two human mitochondrial ADP/ATP carriers were investigated – isoforms 1 and 3. Both of them were expressed, purified and subsequently resuspended in the following buffer: 50 mM HEPES pH 7.5, 200 mM NaCl and 0.005% MNG3 or in 0.04% DDM as described above in paragraphs 3.3.2 and 3.3.3. Protein samples were measured at a concentration of 40 µM each in 300 µL buffer. The protein solutions were gently loaded into 0.1 cm glass cuvette and placed in the monochromator. Temperature melting measurements were performed with samples that were heated on a thermal block or PCR machine prior to the experiment at the following temperatures: 45, 55, 65, 75 and 90° during 15 min. Some experiments were performed in the presence of 0.1 mM CATR (the protein was incubated with the inhibitor 30 min on ice prior to the experiments and to the heating). Data analysis was done using Graph-Pad Prism software (http://www.graphpad.com/scientific-software/prism/).

3.5.3 Thermal stability assays

3.5.3.1 Thermal stability assay using CPM dye

The temperature increase causes protein unfolding that allows thiol – specific fluorochrome – CPM (7 - Diethylamino – 3 - (4' - Maleimidylphenyl) – 4 - Methylcoumarin) (*Invitrogen*) to bind to available cysteines. The fluorescence of CPM dye signal is measured on fluorescence spectrophotometer[180].

Prior to use, CPM dye (4 mg/mL) was diluted in 1:40 in DMSO and stock aliquots were stored at -80°C. The thermal denaturation assay was performed in a total volume of 130 µL. The amount of protein used for the experiment was 20 µg. Some of the samples were supplemented with CATR inhibitor (final concentration was ranging between 60-80 µM) or with different additives, depending on the experiment. To each sample 10 µL of 1/20 diluted CPM dye (dilution in protein buffer) was added and the solution was incubated for 30 min on ice covered with aluminum foil (to reduce photo-bleaching effect). All the samples were transferred to the quartz cuvettes and heated with a Peltier system with a temperature rate of 2°C per minute in a Varian Cary Eclipse Fluorescence Spectrophotometer. The excitation wavelength was set at 387 nm, while the emission wavelength was 463 nm. Assays were performed over a temperature range starting from 4°C and ending at 90°C[180]. Results were later analyzed with Varian Cary Eclipse Program.

3.5.3.2 Determination of protein stability using tryptophan fluorescence – FSEC

Most of the fluorescence emissions of a folded protein are due to excitation of tryptophan residues, with some emissions due to tyrosine and phenylalanine. Typically, tryptophan has a wavelength of maximum absorption of 280 nm and an emission peak that is ranging from 300 to 350 nm depending on the polarity of the local environment. In addition, tryptophan is a relatively rare amino acid; many proteins contain only one or a few tryptophan residues.

Therefore, tryptophan fluorescence can be a very sensitive measurement of the conformational state of individual tryptophan residues.

Fluorescence Size Exclusion Chromatography (FSEC) is a method that allows to evaluate the thermostability of nanogram-to-microgram amounts of the target protein under a variety of conditions also without purification of the protein but directly in the cell suspension[181,182]. All the experiments were performed after protein purification and concentration of the sample (see paragraph 3.3.2 and 3.3.3) using tryptophan fluorescence of the protein itself. Before the experiment the samples were heated up to 25, 35, 45, 50, 55, 60, 65, 75, 80°C respectively on a thermal block or on a PCR machine. Each sample contained 50-100 µg of the protein diluted in the buffer 50 mM HEPES pH 7.5, 200 mM NaCl and 0.04% of DDM or 0.005% of MNG3 depending on purification. Some experiments were performed in the same manner but supplemented with CATR inhibitor. Afterwards protein samples were ultracentrifuged (*Beckman Optima TL Ultracentrifuge*) at 4°C during 30 min at 278 088 x g, then transferred to 2 mL glass vials (*VWR, We Enable Science*) and analysed on the NGC Chromatography System (*Bio–Rad*) combined with its Autosampler (see Fig. 39). The results were further analysed using ChromLab system.

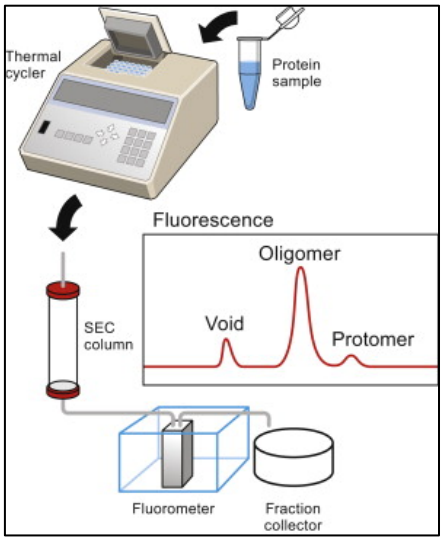

Figure 39 Scheme of the Fluorescence Size Exclusion Chromatography (FSEC) technique. After the heat treatment and ultracentrifugation, protein sample is loaded onto SEC column which is combined with fluorescence detector to monitor tryptophan fluorescence.[182]

3.5.4 Determination of protein oligomerization state

All the SEC–MALLS and AUC experiments were performed using ISBG (Integrated Structural Biology Grenoble) platforms, in particular PAOL platform (IBS). Protein samples were run and analyzed by PAOL platform researcher.

3.5.4.1 Size Exclusion Chromatography combined with Multi Angle Laser Light Scattering: SEC - MALLS

Determination of the oligomerization state of a membrane protein by applying only Size Exclusion Chromatography (SEC) is a very challenging task since the amount of the detergent that is associated with the protein is very often unknown. Thus by simply using only SEC we are not able to clearly establish molecular mass of our protein. However Size Exclusion Chromatography combined with SLS – static light scattering, UV – ultraviolet absorbance and RI – refractive index provides a way for the determination of the molecular masses of protein–protein and also protein–detergent complexes. The Intensity at zero angle is directly proportional to the sample molecular mass and additionally indifferent to the protein shape. Moreover any other contributions like bound detergent molecules can be quantitatively accounted by implementing UV detector and refractive index information[183]. Therefore SEC-MALLS (Size Exclusion Chromatography – Multi Angle Laser Light Scattering) is one of the method to analyze monomeric and oligomeric forms of polypeptides including membrane proteins.[184]

Human AAC1 and AAC3 isoforms were analyzed using SEC–MALLS technique. The two isoforms were expressed, purified and subsequently resuspended in the following buffer: 50 mM HEPES pH 7.5, 200 mM NaCl and in 0.005% MNG3 or in 0.022% Brij35 as described above in paragraphs 3.3.2 and 3.3.3. Afterwards the protein sample (concentration ranging from 2–12 mg/mL, depending on the purification) was ultracentrifuged at 4°C during 10 min at 32000 rpm. Subsequently protein sample was injected on SEC-MALLS system which consists in a HPLC (*Schimadzu*) equipped with a degasser DGU-20AD, a LC-20AD pump, an autosampler SIL20-AC_{HT}, a column oven XL-Therm (*WynSep*),

a communication interface CBM-20A, a UV-Vis detector SPD-M20A, a static light scattering detector miniDawn Treos (*Wyatt*), a dynamic light scattering detector DynaPro NANOSTAR (*Wyatt*), and a refractive index detector Optilab rEX (*Wyatt*). All the experiments were performed in the sample buffer additionally filtered and degassed through 0.1 µm filter (*Merck Millipore*). The data treatment and analysis were conducted using Astra 5.3.4 System.

3.5.4.2 Analytical Ultracentrifugation – AUC

Analytical ultracentrifugation (AUC) system consists in preparative ultracentrifuge combined with optical detection system that permits measuring sample concentration inside the centrifuge cell during or after sedimentation. This technique can be used for a large number of applications like determination of sample homogeneity, characterization of assembly and disassembly mechanisms of biomolecular complexes, determination of subunit stoichiometry but also for the detection and characterization of macromolecular conformational changes[185].

Human AAC1 and AAC3 isoforms were analyzed using AUC technique. The proteins were prepared in the following buffer 50 mM HEPES pH 7.5, 200 mM NaCl and 0.005% MNG3 as described in paragraphs 3.3.2 and 3.3.3. Sedimentation velocity experiments were performed on an analytical ultracentrifuge XLI (*Beckman Coulter, Proteome Lab XL - I*) at 4°C with a rotor (Anti-60) speed of 42000 rpm and double-sector cells of optical path length 3 mm with Sapphire windows. Acquisitions were made using absorbance at 280 nm and interference optics. The reference was the sample buffer. The data treatment and analysis were performed with the SEDFIT software, version 147g, Gussi 1.0.9g and Redate 0.2.1.

3.5.5 N-terminal sequencing analysis

N-terminal sequencing analysis consists in many different chemical reactions, which remove one amino acid at the time from the N-terminus of purified proteins. The amount of the analyzed material is very low, it varies from

10 to 20 pmol of the purified protein with an unmodified N-terminal side. N-terminal sequencing method still remains a method of choice for different analysis: identifying proteins isolated from species where most of the genome has not yet been sequenced, verifying the N-terminal boundary of recombinant proteins, mapping modified or cross-linked sites in proteins or to determining the N-terminal sites of protease-resistant domains.[186]

Human AAC1 was analyzed using N–terminal sequencing in order to detect and analyze the contaminant which was present on the SDS-PAGE. Protein sample was loaded on SDS-PAGE (see paragraph 3.2.1), which was transferred on the PVDF membrane (*GE - Healthcare*). Amino acid sequence determination is based on Edman degradation and was performed using an Applied Biosystems gas-phase sequencer model 492. Phenylthiohydantoin amino acid derivatives generated at each sequence cycle are identified on-line with an Applied Biosystems Model 140C HPLC system using the data analysis system for protein sequencing from Applied Biosystems Model 610A (Software version 2.1).

All the experiments were performed on the N-TER sequencing platform (IBS).

3.6 Functional assays

3.6.1 Radioactivity assays

The ATP uptake assays were done directly on *E. coli* cells expressing the carriers using ^{32}P radiolabelled ATP. The experiments were performed as described in Ravaud et al., ACS *Chem. Biol.*, 2012[122].

All tested proteins (human AACs and PMP) were expressed in 50 mL LB *E. coli* cultures as described in 3.4.2 paragraph. The cells were harvested and centrifuged at 4°C, 20 min at 4000 rpm. Cell pellets were afterwards washed with 30 mL of 50 mM KPi Buffer pH 7.0 (mixture of 1 M K_2HPO_4 (*Sigma – Aldrich*) and 1 M KH_2PO_4 (*Sigma – Aldrich*) buffers), centrifuged at 4°C, 20 min at 4000 rpm. Subsequently the cells were resuspended in the KPi Buffer at a ratio of 0.1 g of cells in 1 mL of KPi Buffer.

Radiolabeled ATP (*Sigma – Aldrich*) stock solution was prepared mixing 25 mM ATP with ^{32}P radioactive source to reach 10 μCi concentration in KPi Buffer.

30 μL of cells were incubated with 1 μL of ^{32}P radiolabeled ATP at room temperature (RT) during 30 min. Each measurement was done in triplicate. For kinetic studies the cells overexpressing each protein were incubated with 1.75, 3, 6.125, 12.5, 25, 50, 100, 200 μM ATP during 30 min. After incubation 1 mL of ice–cold KPi Buffer was added to each sample to stop the transport of ATP through the membranes. Subsequently cell suspension was filtered through a 0.22 μm filter (*Merck Millipore*) that was next washed three times with 1 mL of ice-cold KPi buffer. A control without any cells was obtained by adding 1 μL of ^{32}P-ATP to 1 mL of ice-cold KPi Buffer. Filters were gently transferred to plastic scintillation vials with 3.5 ml of distilled water. Stock reference of total radioactivity was measured by adding 1 μL of ^{32}P into scintillation vials containing 3.5 mL of distilled water. Radioactivity was counted for 1 min using Liquid Scintillation Counting System.

The results were analysed with the Graph–Pad Prism software. The values were calculated and fitted with the Michaelis-Menten equation:

$$V_0 = V_{max}\left(\frac{[Substrate]}{[Substrate] + K_m}\right)$$

$\mathbf{V_0}$ - velocity of the reaction; $\boldsymbol{V_{max}}$ - the maximal rate of the reaction; **[Substrate]** - the concentration of the substrate; $\boldsymbol{K_m}$ - the Michaelis-Menten constant that indicates the apparent concentration of the substrate when the reaction velocity is equal to 1/2 of the maximal velocity of the reaction. In performed experiments V_{max} value was calculated accordingly: the uptake of radiolabelled α-^{32}P-ATP was collected first in radioactivity count units (CPMA), which were further converted into μmol of ATP and divided by the incubation time (incubation time: 30 min) and by the amount of expressed protein (in mg).

The protein expression was analysed by Western Blot (see paragraph 3.2.2) using anti–MBP antibodies (see Fig. 40).

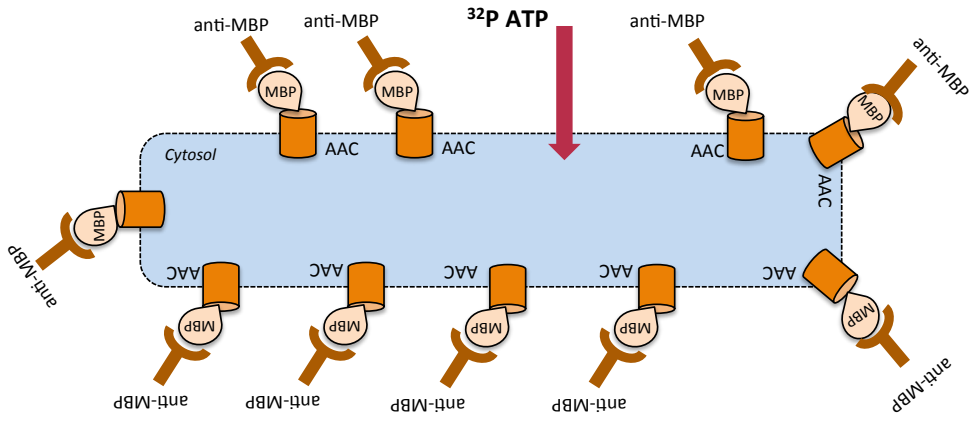

Figure 40 General scheme of the ^{32}P radiolabeled ATP uptake by *E. coli* cells expressing the human ADP/ATP Carriers. The ADP/ATP carriers were cloned in pET20b vector with an MBP fusion at the N-terminus. The anti-MBP antibodies detect the MBP protein located in the preamble *E. coli* membrane.

3.6.2 Experiments performed in liposomes

Liposomes are small and spherical-shaped vesicles that could contain different kind of lipids like phospholipids, phosphatidylethanolamine and also pure surfactant components like DOPE (dioleoylphosphatidylethanolamine). Due to their structural properties they are extremely versatile thus have a large number of applications including pharmaceutical, cosmetics and food industrial fields[187,188] .

In this project we prepared liposomes to investigate the activity of human AAC1 protein.

Mixture of lipids was prepared in the following proportion: 3.2:1:0.8:0.8 - POPC, POPE, POPE and cardiolipins (all *Avanti Polar Lipids, INT.*) and dried under N_2 air in vacuum. Afterwards it was resuspended in the buffer: 50 mM HEPES pH 7.5 and 200 mM NaCl. Resuspended lipids were subsequently loaded into glass syringes and extruded (*Avanti Extruder*) through 0.8 mm and 0.4 mm filters (starting from 0.8 mm). The diameter of the liposomes was investigated using Dynamic Light Scattering – DLS – (*Wyatt*) on PAOL platform (IBS). Liposomes were stored at 4°C.

3.7 Crystallization trials

Crystallization in vapour diffusion was conducted in HTX Lab (EMBL, Grenoble, ISBG platform) while LCP crystallization trials were performed on Membrane Crystallization Protein Platform (ISBG).

3.7.1 Lipidic Cubic Phase (LCP) crystallization

Lipidic cubic phase (LCP) became one of the most intriguing trends for the crystallization of membrane proteins. It is a special membrane system that consists in lipid, water and protein in appropriate proportion. Once combined together, all of them form a transparent and highly structured complex of three-dimensional lipidic array that is pervaded by an intercommunicating aqueous channel system. By lateral diffusion of protein molecules in the bilayer, crystals can nucleate and grow. By using LCP method some protein structures were obtained, for instance bacteriorhodpsin or G protein coupled receptors (GPCRs)[189,190] (see Fig. 41).

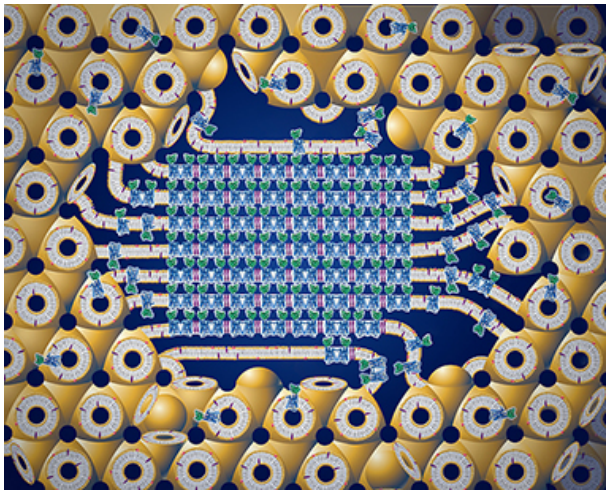

Figure 41 Cartoon representation of the crystallization process in the lipidic cubic phase (LCP). Integral membrane protein molecules (depicted in blue and green) are initially embedded in the lipid bilayer of the LCP (in yellow), which provides a connection for the 3D diffusion. The presence of precipitant induces a crystal nucleation. The crystal (in the center) is attached to the bulk LCP through a multilamellar lipid portal, which feeds the growing crystal with the protein molecules (Cherezov V. et al).

LCP crystallization trials were performed for three of the four human AAC isoforms (human AAC1, 2 and 3) and for Plasma Membrane Protein. The proteins

were prepared as described in paragraphs 3.3.2 and 3.3.3 and concentrated up to 10 – 15 mg/mL. For standard sample preparation 30 µL of the protein was gently mixed with approximately 20 – 25 µL of MonoOlein – MO (*Anatrace*) using two 100 µm glass syringes connected together with a coupler. Protein sample was carefully loaded in one glass syringe while the heated (up to 42°C) monoolein was loaded into the second syringe. After connecting them tightly together with metal syringe coupler, solution was pushed back-and-forth until it became homogenous and transparent. Subsequently, all the phase was transferred to one glass syringe and mounted in a robot, nanovolume dispenser (NT8 from *Formulatrix*) that allows screening 96 precipitant conditions with small amount of sample (5 - 10 µL per plate) in less than 10 min. For the crystallization trials we used following 96 – wells commercial kits: MemGold/MemPlus, SCSG+, MemStart + MemSys (*Molecular Dimensions*), Crystal I & Crystal II, QCPI, QCPII (*Hampton Research*) and for all of them the protein + lipids to buffer/precipitant ratio was 80 - 100 nL + 800 nl respectively. Plates were stored at 20°C in an automated imaging system, RockImager 1500 (*Formulatrix*) that enables to visualize crystallization drops under visible, polarized and UV lights.

3.7.2 LCP-FRAP: LCP–Fluorescence Recovery After Photo-bleaching

FRAP (Fluorescence Recovery After Photo-bleaching) is a method that allows to measure lateral diffusion of proteins inserted in a lipidic bilayer. Proteins are labeled with a fluorescent marker. Proteins a small part of LCP drop are then bleached using a special laser. Afterwards, this spot is imaged in order to measure the time that is necessary for the fluorescence to recover. This technique is very useful prior to LCP crystallization set up. It is a good prerequisite for the crystal nucleation and growth to occur.

The experiments were performed using Formulartix System that enables to work in high-throughput mode (96-well LCP plates) constantly screening the diffusion rate and mobile fraction of the membrane protein.

Cy3 (*Thermo Fisher Scientific*) dye was added to the purified protein sample (hAAC3), previously dissolved in DMSO at a final concentration of 5 mg/mL. 10 µL of the dye was added to 1 mL of the protein sample at a concentration of around 1 mg/mL and afterwards the sample was incubated in

the dark at 4°C for 4h on the turning wheel. Excess of the Cy3 dye was removed by using PD10 columns (*GE – Healthcare*). 500 µL of the protein sample was loaded on the column and eluted with 1 mL of the sample buffer (described above), afterwards protein was concentrated, loaded newly on the column, eluted and concentrated. This procedure was repeated three times and each time PD10 column was fresh. After removal of unspecific bound dye protein was concentrated up to final volume of 100 – 150 µL and centrifuged at 4°C during 10 min at high speed - 13 000 rpm to remove possible aggregates. After, protein sample was mixed with monoolein - MO (*Anatrace*) like described in the paragraph 3.7.1 and distributed on the 96–well plate using nanovolume dispenser (NT8 from *Formulatrix*) in the following ratio: 40 nL sample (protein + MO) + 800 nL of precipitant. Plates were stored over-night in the dark. Next day FRAP experiment (using *Formulatrix*) was performed and recovery time (T), mobile fraction (M) and diffusion (D) coefficients were analysed[191].

3.7.3 Vapour diffusion crystallization

Vapour diffusion technique is one of the most common one used for protein crystallization. It involves an aqueous drop with protein solution and crystallization agents (precipitant), which are mixed in the drop. The drop is equilibrated against the reservoir containing a higher precipitant concentration. Gradually the protein and the crystallization agents in the drop concentrate until equilibrium (see Fig. 42A and B). In the hanging-drop method, the drop that contains protein and crystallization agents (max. volume 10 µL), hangs from glass cover slip above reservoir. The sandwich drop and the sitting drop can accommodate larger drop volumes resting on the surface close to the reservoir. Vapour diffusion technique (similarly to microbatch) does not also require large quantities of the materials comparing for instance with classical batch crystallization method[192] (see Fig. 42A and B).

A B

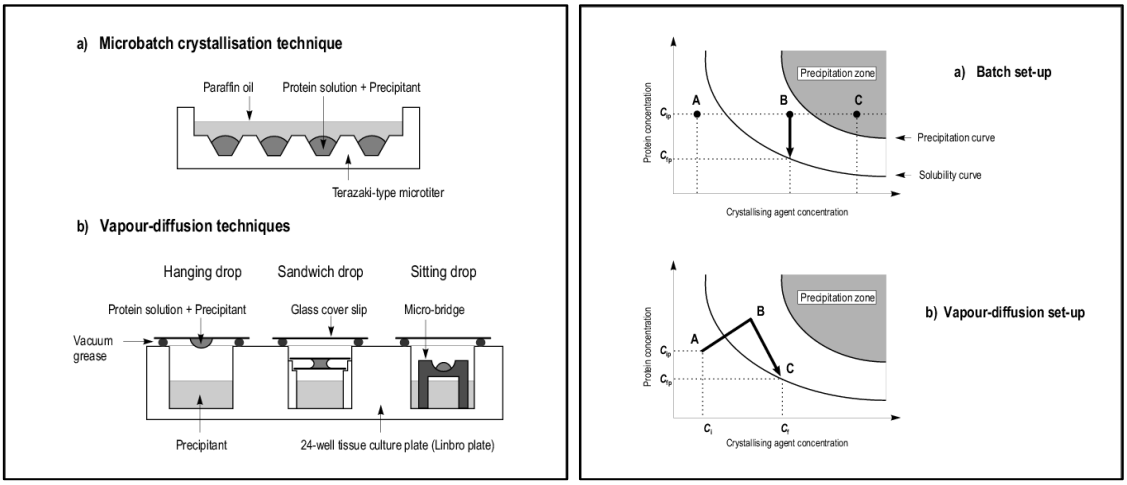

Figure 42 Protein crystallization techniques. (A) Schematic representation of a) microbatch, b) vapour-diffusion crystallization techniques widely used in growing of protein crystals, (B) Various crystallization set-ups presented in terms of phase diagrams. Schematic representation of solubility phase diagram and correlation between protein and crystallizing agent concentrations in a) batch, b) vapour-diffusion crystallization experiments. C_{ip} and C_i are the initial concentrations of protein and crystallizing agent respectively, C_{fp} and C_f and are their final concentrations; point A defines protein unsaturated state at concentration C_{ip}, B–supersaturated state and C-solubility curve at concentration C_{fp}[192].

Crystallization set up using vapour diffusion technique was applied to all of the membrane proteins investigated in this project. Protein concentration was ranging from 6 – 18 mg/mL.

The crystallization experiments were conducted using a Cartesian PixSys 4200 crystallization robot (*Genomic Solutions*). Drops were usually set up with 100 nL of the protein sample mixed with 100 nL of crystallizing agent. Several commercial kits were used: Classic Suite, PEGs - I (*Quiagen/Nextal*), JCSG+, Pact Premier, Morpheus_MD (*Molecular Dimensions*), Salt Grid, Salt RX, Index (*Hampton Research*), Wizard I & II (*Rigaku Reagents*). Each plate inspection was performed using an automatic imaging device linked to the CRIMS System (CRistalization Information Managing System) developed by EMBL, Grenoble.

3.8 Different crystallization set ups for serial nano- and micro development techniques

3.8.1 Protein samples

3.8.1.1 Lysozyme

Lysozyme was purchased from *Sigma-Aldrich* and diluted in distilled water at the following concentrations: 20, 40, 60 and 80 mg/mL.

Crystallization of the lysozyme was performed using:

a) Standard vapour diffusion (see paragraph 3.7.3) set up (24-well plate) with following precipitant conditions: 0.6 – 1.1 M NaCl (*Sigma Aldrich*), 0.1 M NaAcetate pH 4.2-4.8 (*Sigma-Aldrich*).
b) Crystal Direct (CD) plates (see paragraph 3.8.2.1.1) with following precipitant conditions: 3.1-3.4 NaCl, 0.1 M NaAcetate pH 4.6, 10-15.5% PEG 6000 (*Sigma-Aldrich*)
c) Silicone nitride membranes (see paragraph 3.8.2.1.2) with the same crystallization condition as in a).
d) Lipidic Cubic Phase (LCP) (see paragraph 3.7.1) with the same crystallization conditions as in a).

All crystallization plates and LCP-syringes were stored at 20°C. The size of the crystals obtained in different crystallization conditions was varying approximately between 20 and 150 μm.

3.8.1.2 Thaumatine

Thaumatine was purchased from *Sigma-Aldrich* and diluted in distilled water at the following concentrations: 20, 40, 60 and 80 mg/mL.

Crystallization of the thaumatine was performed using CD plates (see paragraph 3.8.2.1.1) with the following conditions: 1 M Na/K tartrate (*Sigma-Aldrich*) and 0.1 M HEPES pH 7.5 (*Sigma-Aldrich*). Crystallization plates were stored at 20°C. The size of the crystals obtained in above crystallization condition was varying approximately between 20 and 100 μm.

3.8.1.3 Bacterial multidrug efflux transporter – AcrB

Bacterial AcrB protein was expressed and purified in the team according to the protocol described elsewhere[193]. The protein was concentrated up to 12 mg/mL, frozen and stored at -80°C.

Crystallization of AcrB was performed using standard vapour diffusion set up (see paragraph 3.7.3) (24-well plate), CD plates (see paragraph 3.8.2.1.1) and silicone nitride membranes (see paragraph 3.8.2.1.2). Crystals were grown at 20°C in two different conditions:

1) 8% PEG 3350 (*Sigma-Aldrich*), 0.1M $MgCl_2$ (*Sigma-Aldrich*), 0.1M HEPES pH 8.0 (*Sigma-Aldrich*)
2) 20% PEG 200 (*Hampton Research*), 0.2 M KSCN (*Sigma-Aldrich*), 0.1M HEPES pH 7.5 (*Sigma-Aldrich*)

The size of the crystals obtained with the first condition was varying approximately between 20 and 90 µm, while microcrystals of 5 to 20 µm were obtained in the second condition.

3.8.1.4 Pentameric Ligand-Gated Ion Channel GLIC

The protein was kindly provided by Marc Delarue (Institut Pasteur)[194]. The protein was concentrated to 10 mg/mL and stored at -80°C.

Crystallization was performed using standard vapour diffusion (see paragraph 3.7.3) set up (24-well plate), CD plates (see paragraph 3.8.2.1.1) and silicone nitride membranes (see paragraph 3.8.2.1.2). Crystallization conditions were: 10-16% PEG 4000 (*Sigma-Aldrich*), 0.1 NaAcetate pH 4.0, 0.4 M NaSCN (*Sigma-Aldrich*). Crystallization plates were stored at 20°C. The size of the crystals obtained in above crystallization condition was varying approximately between 50 and 100 µm.

3.8.1.5 Mouse serotonin 5-HT3 receptor

5-HT3 serotonin receptor was expressed and purified by L. Peclinovska (PhD student in the team) following a protocol previously published[195,196] with minor modifications.

The protein sample was concentrated up to 7-8 mg/mL and mixed with the VHH15 nanobody and Cymal 6 (*Anatrace*) detergent for crystallization trials. Crystallization of 5-HT3 protein was performed using standard vapour diffusion (see paragraph 3.7.3) set up (24-well plate), CD plates (see paragraph 3.8.2.1.1) and silicone nitride membranes (see paragraph 3.8.2.1.2). The starting crystallization conditions were the following: 21% PEG 10 000 (*Sigma-Aldrich*), 0.1M Na_2SO_4 (*Sigma-Aldrich*), 0.1M Tris pH 8.0 (*Sigma-Aldrich*) and the plates were stored at 12°C. In order to obtain microcrystals the conditions were optimized as presented below on the Figure 43. The size of the crystals obtained in different crystallization conditions is described in detail in Chapter III, Result part IV.

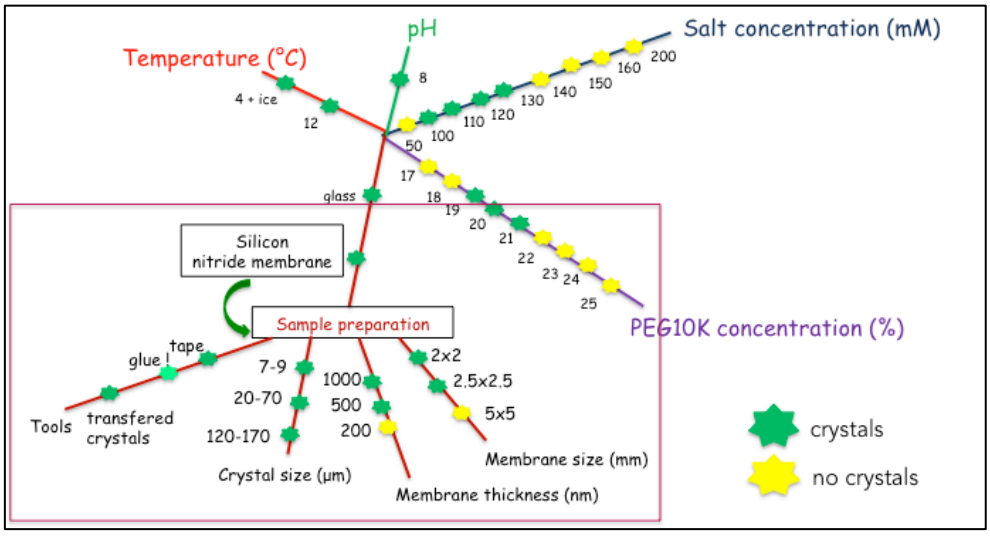

Figure 43 Screening of new crystallization conditions for the 5-HT3 serotonin receptor. The starting conditions were the following: 21% PEG 10K, 0.1M Na_2SO_4, 0.1M Tris pH 8.0, 12°C. The red frame indicates the changes for the sample preparation using the Silicone Nitride Membranes set up regarding the membrane size and thickness, the crystal size and the mounting tools.

3.8.2 Crystallogenesis

3.8.2.1 Vapour diffusion

Vapour diffusion crystallization (see details in paragraph 3.7.3) was applied to all samples studied in this project and using 3 different set-ups: standard sitting drops 24 wells or 96 well plates, CD plates and silicone nitride membranes.

3.8.2.1.1 Crystal Direct (CD) Plates

Recently Crystal Direct (CD) system has been developed to enable full automation of the crystal harvesting-process[197]. Crystal Direct Plates allows growing crystals on ultrathin films on a specially designed vapour-diffusion crystallization plate (see Fig. 44A). Crystals are recovered by excision of the film through laser-induced photoablation[197]. The film, which contains crystalline material, is then directly transferred to the X-ray beam. This new system, barring the fact that it eliminates the `crystal-fishing` step and reduces mechanical stress, offers the possibility for *in situ* crystal screening with minimal X-ray background (see Fig. 44B). Crystallization experiments were carried out at the High Throughput Crystallization Laboratory (EMBL, Grenoble) using the sitting-drop vapour-diffusion method and Crystal-Direct plates (*MiTeGen, Ithaca*). Crystallization experiments were set up with 100 nL of the protein sample and 100 nL of the crystallization solution on the inner surface of the film using a Cartesian PixSys robot (*Cartesian Technologies*). The reservoirs contained 45 µL of the crystallization solution prepared with the Formulator-16 robot (*Fomulatrix Inc.*) (see Fig. 44A). The plates were sealed on their upper side with Crystal-Clear film (*Hampton Research*), stored at 20°C and imaged under either visible or UV light[198].

A B

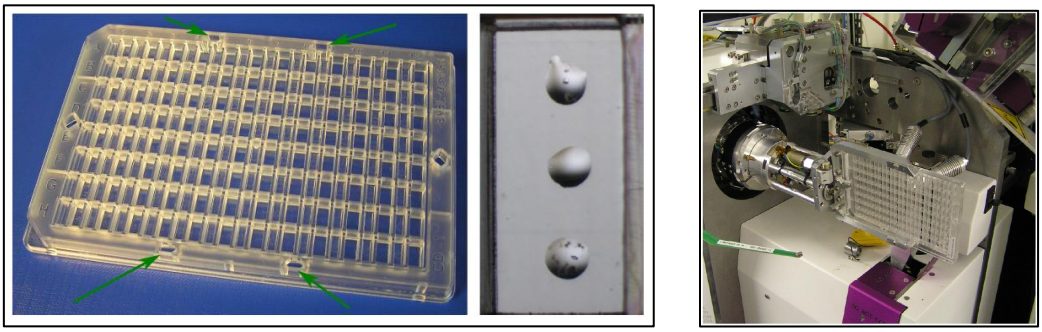

Figure 44 Crystal Direct (CD) plate technique A) Example of a Crystal Direct plate, three drops can be set up in each well with for instance different protein concentrations. B) Crystal Direct plate set up on the dedicated goniometer head for in-situ experiments (BM14, ESRF) (pictures adapted from HTX CRIMS platform: https://embl.fr/htxlab/).

3.8.2.1.2 Silicone nitride membranes

Silicone nitride membranes (Si_3N_4 membrane sandwich)[199] were tested for X-ray diffraction analysis (Fig. 45a and b). Protein crystals were either directly grown on the membranes or transferred on them just prior the diffraction experiment. Interestingly, this method does not require large quantity of material, which is a significant advantage for membrane proteins. Moreover, the mounting procedure in the X-ray beam does not require crystal manipulation and can therefore be used for fragile micro-crystals. It is also minimizing background scattering during X-ray diffraction experiments. Data collection can be performed at RT avoiding the use of cryoprotectants that often modify the diffraction quality. These membranes are supposed to be mounted into humidity controlled cells as windows but we decided for the first attempts not to use any.

Silicone Nitride Membranes were purchased from *Silson Ltd*. The standard silicon nitride membrane window consists in a square silicon nitride membrane placed in a square silicon supporting frame. The membranes used in the experiments were 1.5, 2.0, 2.5, and 5.0 mm large and 200, 500 and 1000 nm thick. In the crystallization set up, steel washer was glued directly on the cover-glass lamella (see Fig 45a) (in some of the cases the membranes were directly glued on the glass-lamella using only classical tape). The membranes were glued on top of the washer with up-directed flat membrane surface. Subsequently 1 µL of the protein mixed with 1 µL of the precipitant were gently dispersed on the membrane surface. The glass lamella together with the washer and the membrane were finally turned upside-down and mounted above 1 mL reservoir on 24-well plate. Plates were stored at 12 or 20°C.

Before measurements on the beamline, the membrane containing the crystallization drop was covered with another membrane (flat to flat surface) to create a "sandwich". Afterwards, the edges of the two membranes were glued together to avoid evaporation. The "sandwich" was finally glued to the glass and brass pin and mounted on the beam (see Fig. 45b).

a)

b)

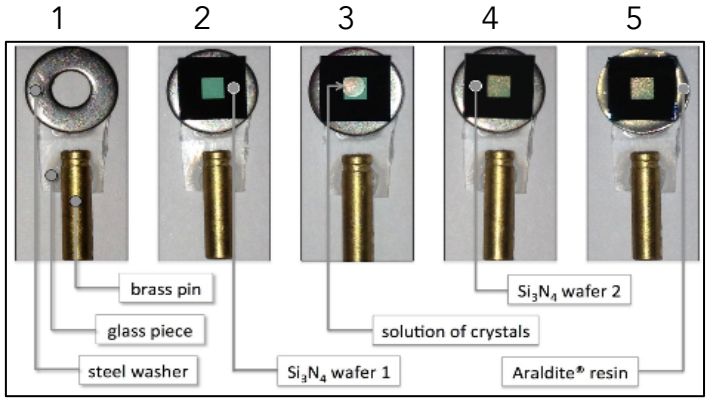

Figure 45 Crystal set up on silicone nitride membranes. a) medium or small sized membranes are glued to the steel washer which is glued to glass lamella, subsequently, drop of the protein and precipitant is gently placed on membrane surface and next, glass coverslip is turned upside-down facing precipitant well on the crystallization plate; b) Samples dispersed on silicon-nitride membranes with solid state support – 1 – the steel washer is glued to the glass and brass pin; 2 – the curved part of the first silicone nitride membrane is glued to the washer; 3 - the crystals solution is gently transferred onto the membrane window; 4 – the flat side of the second silicone nitride membrane faces the first Si_3N_4 wafer and closes the "sandwich"; 5 – the sandwich is sealed with glue in order to avoid evaporation.

3.8.2.2 Lipidic Cubic Phase (LCP)

LCP crystallization principle is detailed in paragraph 3.7.1.

LCP – syringe set up for SFX (serial femtosecond crystallography)

LCP-SPX data collection requires the use of a LCP injector[200] and a special protocol for unusual sample preparation. The main goal of this particular sample preparation is to obtain approximately 50 µL of the LCP that is homogenously filled with microcrystals (<10 µm in size) at high density. The first stage of the preparation involves high-throughput crystallization screening using special LCP plates and robots in order to detect the best conditions that lead to a high rate of nucleation and to the formation of a large number of microcrystals. Once the first step is successful, the next one involves scaling up the crystallization volume

which is not a trivial task considering LCP peculiar texture and diffusion process of soluble components.

The main purpose of this experiment was to grow crystals in LCP injected in syringes and afterwards to deposit the LCP crystalline material on the silicone nitride membranes described above to analyze them in the X-ray beam. The protocol was established for the lysozyme following this protocol (see Fig. 46)[201].

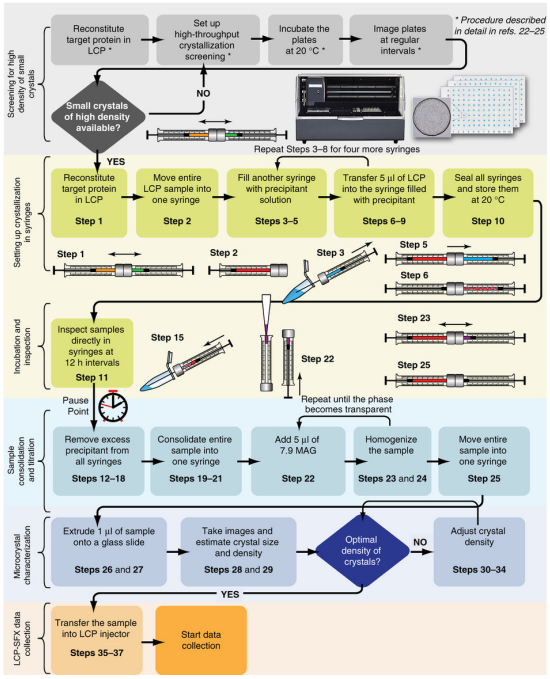

Figure 46 LCP-syringe sets up for SXF presented in several steps. Each substance is labeled with different colors (in orange-LCP host lipid; in green-protein solution; in red-LCP; in blue-precipitant solution; in purple-7.9 MAG)[201].

1) Lysozyme reconstitution in LCP: a first syringe (n°1) was filled with 15 µL of monoolein, while a second syringe (n°2) was filled with 20 µL of the protein solution; both syringes were connected together using a syringe coupler. The sample was homogenized by pushing it back-and-forth the in the two syringes through the coupler until a transparent LCP was formed.
2) Crystallization in the syringes: the entire LCP sample was placed in the syringe n°1 while the syringe n°2 was disconnected (the syringe coupler was left attached to syringe n°1); a third syringe of 100 µL (n°3) was filled with 60 µL of a precipitant solution and connected to the syringe n°1 thanks to the coupler; 5 µL of the LCP sample was injected to the syringe

n°3. This syringe was finally disconnected and sealed tightly with a parafilm. The procedure was repeated in three other syringes.

3) Incubation and inspections: all four syringes were placed in sealed plastic bags with a moist fiber-free tissue to maintain a high level of humidity and stored at 20°C. The samples were directly inspected in the syringes every 12h using a microscope equipped with cross-polarized light. Microcrystals appeared after 3 days of incubation as densely packed bright dots as observed under cross-polarizers.
4) Sample consolidation: after the incubation, the parafilm was removed from all the syringes. The needle stopper of the syringe n°3 was replaced with a needle and the precipitant was removed from the syringe by gentle pushing. Afterwards the needle was replaced with a needle stopper. This procedure was repeated with three other syringes and finally all LCP-samples were transferred to the syringe n°3. The syringe n°1 was attached to the syringe n°3 with a coupler and the LCP-sample was homogenized back-and-forth until it was fully homogenous and transparent. The entire LCP-sample was afterwards transferred to the syringe n°3, the syringe n°1 being disconnected.
5) Transfer of the LCP sample to silicone nitride membranes: 5 µL of the LCP sample was transferred to the curved part of a first medium sized Si_3N_4 membrane (1000 nm thick) and later covered with the second part of the Si_3N_4 membrane in flat face-to-face manner. Both membranes were sealed with SuperGlue and attached to glass and brass pin ready for X-ray beam analysis.

CHAPTER III

4 Results

4.1 **Part I** – Human Mitochondrial ADP/ATP Carrier

4.1.1 Functional characterization of the four human AAC isoforms

The transport mechanism of ADP/ATP carriers is not yet fully established. Besides working to get new structural data, functional studies can already shed lights on transport molecular determinants as illustrated in previous publications[122,94,202]. The human genome contains 4 isoforms of the mitochondrial ADT/ATP carrier. The sequence homology between first three of them is approximately 98% while the sequence similarity between hAAC4 and hAAC1 is only 68% (see Fig 47A). The 4 human AAC isoforms were functionally characterized using activity assays and mutagenesis experiments coupled to molecular dynamics (MD) simulations analysis.

4.1.1.1 3D models of the four human ADP/ATP carriers

Lacking structural data on the 4 human isoforms we generated 3D models (using Expasy Swiss-Modeling Tool: http://swissmodel.expasy.org/workspace/) based on the known bovine ADP/ATP carrier (*b*AAC) structure[77]. These models were used in MD simulations experiments in collaboration with F. Dehez (Nancy University) and served as a structural basis to analyse and discuss the transport activity that we performed on the WT proteins and on specific mutants (see paragraphs 4.1.1.2 and 4.1.1.3).

Models were also generated with the predicted position of the CATR inhibitor bound inside the protein cavity (see Supplementary Data, Fig. 1A-D, page 110). By comparing the bovine AAC structure and the models of the four human AAC, we observed no significant differences in particular no obvious structural rearrangements. MD simulations gave us an insight on protein flexible regions among all of those five homologs (see Fig. 47B).

A

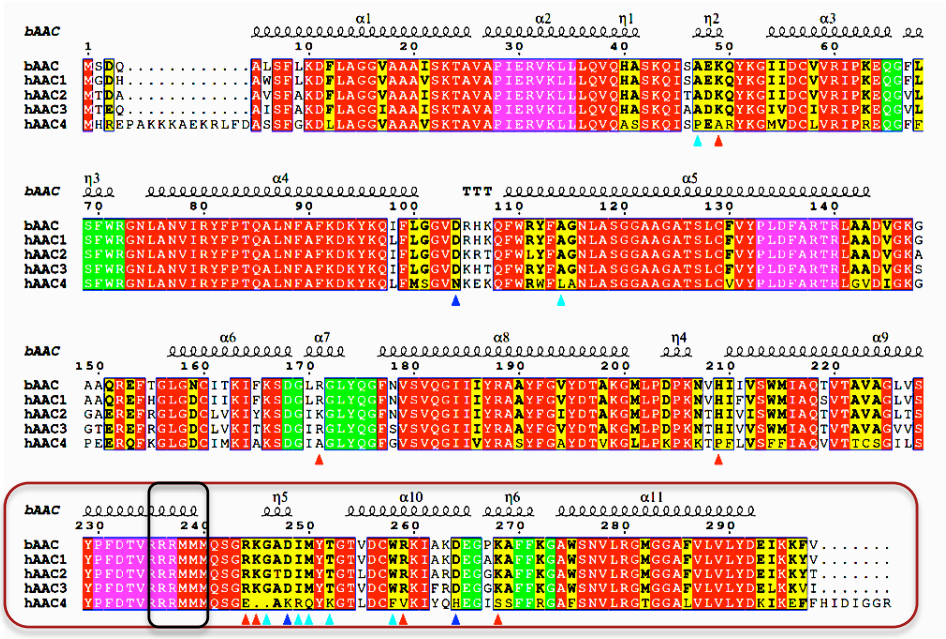

B

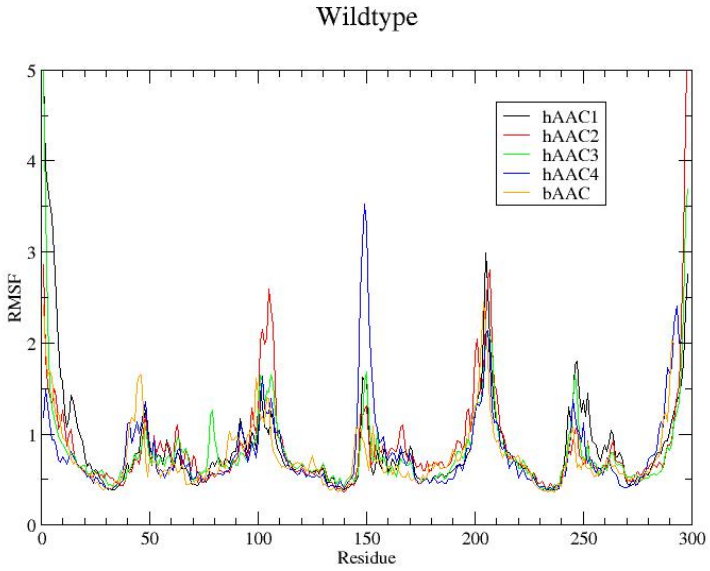

Figure 47 Sequence analysis of bovine and four human AAC isoforms (A) Sequence alignment of bovine AAC1 (bAAC1), and all 4 human isoforms with the secondary structure from bAAC1 on the top. Regions containing MCF motifs are colored in purple and green respectively. The ADP/ATP carrier signature is present in the third repeat and it is boxed in black. The mutated residues are indicated as triangles and are colored accordingly: positively (red) and negatively (dark blue) charged residues and the remaining ones in light-blue. Dark-red frame indicate residues embedded in 5th and 6th protein helices. (B) The RMSF (root mean square fluctuation) of simulation of the four human isoforms of AAC per residue. The RMSF is a measure of the average mobility of the residues. Data used for analysis: last 30 ns of a 70 ns trajectory. The simulations were performed once for each human isoform.

The regions with increased protein flexibility are the same in all the isoforms and correspond to the protein sections between the helices (see Fig. 47B). There, an increased wide range of flexibility is visible between the odd-numbered and the even-numbered helices, h12, h34 and h56 (residues 40-70, 140-170 and 240-270) and a smaller range between the even-numbered and odd-numbered helices (between H2 and H3 around residue 100 and between H4 and H5 around residue 205). All of these sections are pointing out of the membrane into the solvent: the latter (H2/H3 and H4/H5) face the outside of the cell and the first (H1/h12/H2, H3/h34/H4 and H5/h56/H6) face the inside, respectively. Thus an increased flexibility in these regions is not surprising. The region of the protein between 100 and 109 residue exhibits overall high flexibility and points towards the solvent. Here, hAAC2 shows larger deviation and hence higher flexibility while compared with other three isoforms (see Fig. 47B). The section between residues 148 and 151 shows also an increased protein flexibility (see Fig. 47B), however hAAC4 exhibits the highest. One of the interesting changes in this sequence part is the residue 105 (which is a proline for hAAC4 and alanine or glycine for hAAC1, hAAC2 and hAAC3) and residue 106 (for hAAC4 negatively charged glutamic acid and neutral alanine or threonine in the other isoforms).

According to the visual analysis of the trajectory data the PX(D/E)XX(K/R) and RRRMMM motives exhibit high stability. There, overall D/E residues form salt bridges to one or two basic residues. However, the salt bridges at the bottom of the cavity (R235-D135, R138-E30 and K33-D232) are not formed entirely. The acidic residues are bridged temporary or simultaneously to different basic residues and those interactions vary over the time of trajectory. This may be the reason for the different flexibilities in some regions of the different isoforms and therefore mutations in this area may influence these interactions.

4.1.1.2 Transport properties of the wild-type proteins

The *E. coli* expression of hAAC1 proved to be a unique and powerful tool for studying its transport properties[122]. The functional expression of hAAC1 in *E.*

coli membranes was achieved by fusing at the N-terminus of the protein the Maltose binding Protein (MBP). We followed the same approach for the other three AAC isoforms and cloned the three genes fused to a periplasmic MBP at the N-terminus (for clarity the resulting MBP-hAAC (1, 2, 3 or 4) are further simply named hAAC1, hAAC2, hAAC3 or hAAC4) (see paragraph 3.6.1). The 4 isoforms were successfully expressed in *E. coli* as seen on Fig. 48. The hAAC4 expression level is lower compared with the other proteins. The transport properties of the 4 wild type proteins were then investigated directly in *E.coli* cells, which do not import ATP, as described in Material and Methods. Cells expressing hAAC1, hAAC2, hAAC3 or hAAC4 showed an uptake of [α-^{32}P]-ATP above the background level (see Fig. 49 a, c, e and g). Addition of the AAC highly specific inhibitors – CATR (carboxyatractyloside)[86,87] or BA (bongkrekic acid)[91] or both inhibitors together resulted in almost complete inhibition of the transport (see Fig. 49 a, c, e and g).

Other recently reported potential AACs inhibitors were also tested – CD437, Closantel, Suramin, Chebulinic Acid and Leelamine[92,203]. Addition of CD437 and Closantel, which are dissolved in DMSO, showed lowered transport activity for all isoforms, however the influence of DMSO on protein transport properties was also observed (see Fig. 49 b, d, f and h). Suramin lowered transport activity of 3-10% of the wild-type AACs activity. Addition of 3.5 μM Chebulinic acid inhibited transport up to 50% for first three human isoforms and up to 25% for hAAC4 (see Fig. 49 b, d, f and h). In presence of Leelamine that is dissolved in ethanol, no transport inhibition was observed and moreover the results were difficult to interpret (similarly like with CD437 and Closantel inhibitors) since ethanol affected protein transport properties (see Fig. 49 b, d, f and h).

For the first time the kinetic properties of the 4 isoforms were as well investigated in the same system and therefore could be compared. K_m and V_{max} values were computed from dose-response curves (see Fig. 50 and Table 7). hAAC1, hAAC2 and hAAC3 that share very high protein sequence similarity have similar affinity for ATP with K_m of approximately 21.3 ± 2.9, 23.8 ± 3.1 and 22.3 ± 3.7 μM respectively. In terms of transport rate, V_{max} values remain also in the same range: 3.3 ± 0.1, 3.7 ± 0.2 and 2.5 ± 0.1 μmol min^{-1} mg^{-1} of protein for

hAAC1, hAAC2 and hAAC3 respectively. hAAC4 exhibits a lower affinity for ATP (K_m of 53.3 ± 15.1 μM) and the V_{max} value of 5.7 ± 0.6 μmol min^{-1} mg^{-1} of protein is slightly higher than for the other three isoforms. This may suggest that the nucleotide binding properties of this particular isoform can differ from the others.

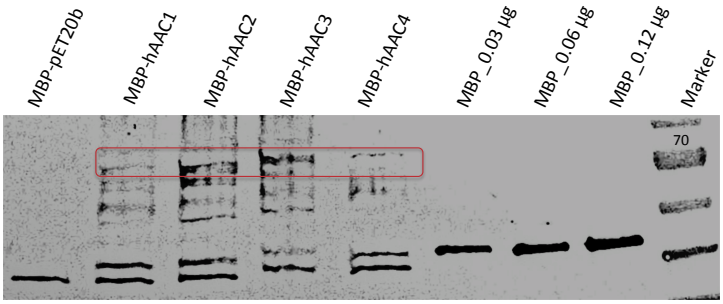

Figure 48 Expression levels of human AAC isoforms in *E. coli*. Western Blot analysis of the expression of the 4 MBP-hAACs in *E. coli* using an anti-MBP antibody. The MBP-hAACs molecular weight constructs vary between 74-76 kDa. The level of expressed protein was calculated according to the level of the MBP protein (approximately 42 kDa), which was diluted 100X and loaded on the gel in following amount: 0.5 μL (0.03 μg), 1 μL (0.06 μg) and 2 μL (0.12 μg). An approximate amount of the expressed protein was estimated using GelDOC Quantification Tool (*BioRad*) based on pixel intensity values. The lower bands on the Western Blot represents *E. coli* MBP and MBP protein cleaved from the constructs.

a)

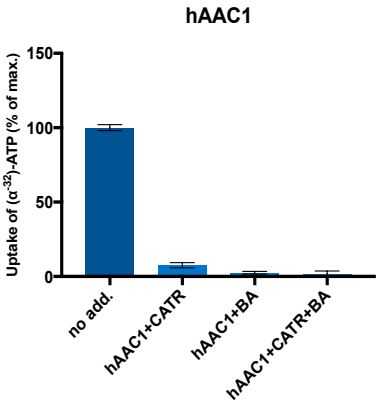
hAAC1
Uptake of (α-32)-ATP (% of max.)
150
100
50
0
no add.
hAAC1+CATR
hAAC1+BA
hAAC1+CATR+BA

b)

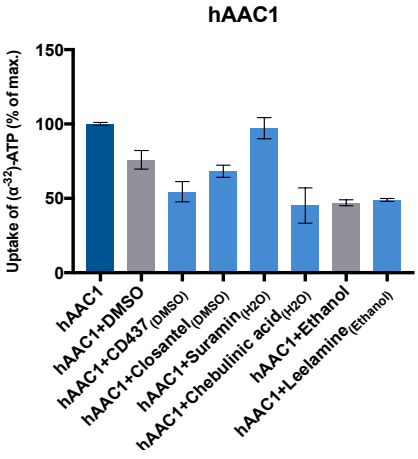
hAAC1
Uptake of (α-32)-ATP (% of max.)
150
100
50
0
hAAC1
hAAC1+DMSO
hAAC1+CD437 (DMSO)
hAAC1+Closantel (DMSO)
hAAC1+Suramin (H2O)
hAAC1+Chebulinic acid (H2O)
hAAC1+Ethanol
hAAC1+Leelamine (Ethanol)

c)

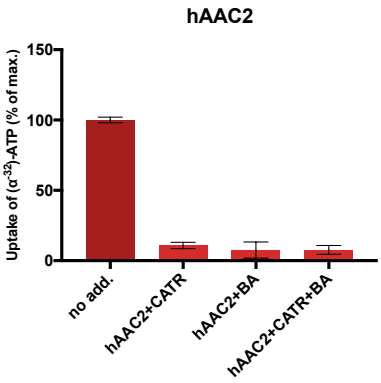
hAAC2
Uptake of (α-32)-ATP (% of max.)
150
100
50
0
no add.
hAAC2+CATR
hAAC2+BA
hAAC2+CATR+BA

d)

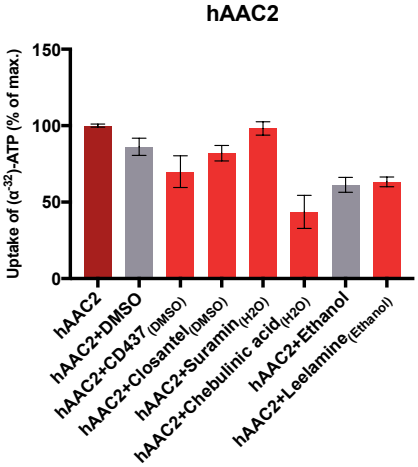
hAAC2
Uptake of (α-32)-ATP (% of max.)
150
100
50
0
hAAC2
hAAC2+DMSO
hAAC2+CD437 (DMSO)
hAAC2+Closantel (DMSO)
hAAC2+Suramin (H2O)
hAAC2+Chebulinic acid (H2O)
hAAC2+Ethanol
hAAC2+Leelamine (Ethanol)

e)

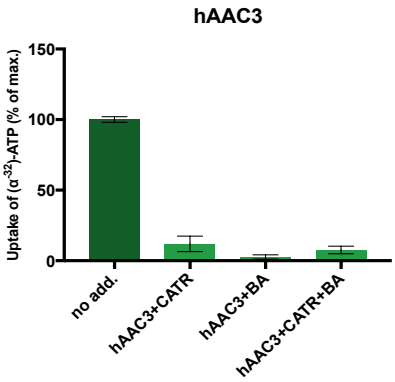
hAAC3
Uptake of (α-32)-ATP (% of max.)
150
100
50
0
no add.
hAAC3+CATR
hAAC3+BA
hAAC3+CATR+BA

f)

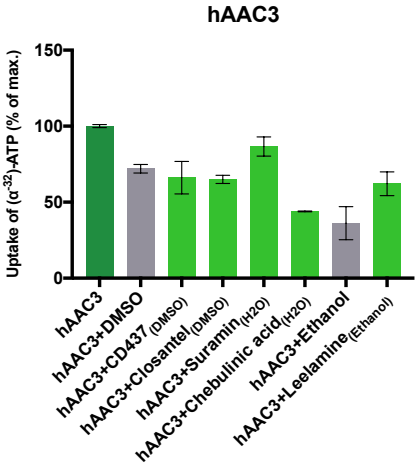
hAAC3
Uptake of (α-32)-ATP (% of max.)
150
100
50
0
hAAC3
hAAC3+DMSO
hAAC3+CD437 (DMSO)
hAAC3+Closantel (DMSO)
hAAC3+Suramin (H2O)
hAAC3+Chebulinic acid (H2O)
hAAC3+Ethanol
hAAC3+Leelamine (Ethanol)

g)

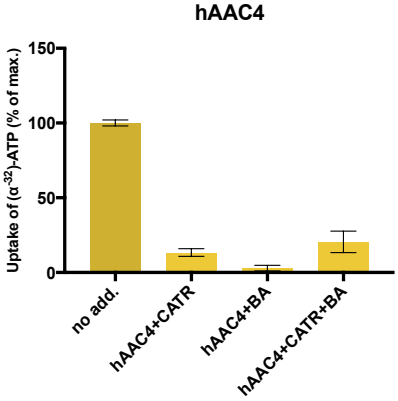
hAAC4
Uptake of (α-32)-ATP (% of max.)
150
100
50
0
no add.
hAAC4+CATR
hAAC4+BA
hAAC4+CATR+BA

h)

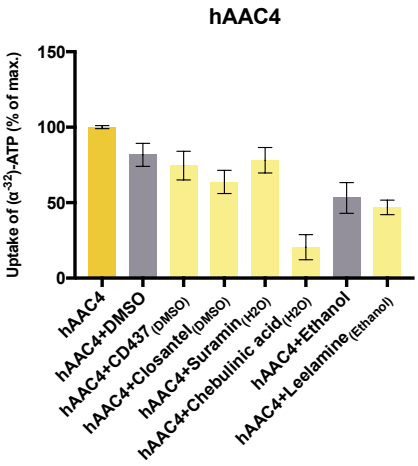
hAAC4
Uptake of (α-32)-ATP (% of max.)
150
100
50
0
hAAC4
hAAC4+DMSO
hAAC4+CD437 (DMSO)
hAAC4+Closantel (DMSO)
hAAC4+Suramin (H2O)
hAAC4+Chebulinic acid (H2O)
hAAC4+Ethanol
hAAC4+Leelamine (Ethanol)

Figure 49 All human AACs are functionally expressed in *E. coli* membranes. [α-^{32}P]-ATP uptake of *E. coli* cells expressing a-b) MBP-hAAC1, c-d) MBP-hAAC2, e-f) MBP-hAAC3, g-h) MBP-hAAC4 was measured in presence of 10 µM labeled ATP and when indicated 100 µM inhibitors - CATR and/or BA (a, c, e, g), 100 µM CD437, Closantel and Leelamine; 10 µM of Suramin and 3.5 µM of Chebulinic acid (b, d, f, h). The measurements were performed in triplicates. The rate of the transport in the absence of additives was set to 100%. The values for the control nucleotide uptake (empty vector) were subtracted.

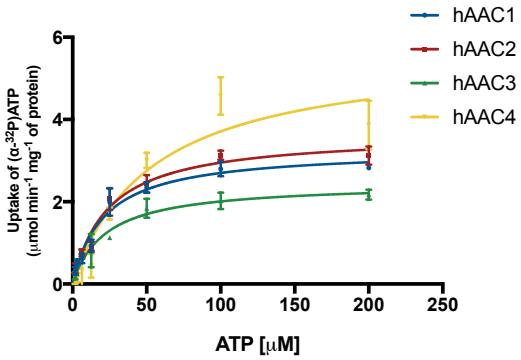

Figure 50 Substrate saturation curves of [α-^{32}P]-ATP uptake by cells expressing hAAC1, hAAC2, hAAC3 or hAAC4. The control nucleotide uptake (empty vector) was subtracted. The K_m and V_{max} values were extrapolated from the experimental data fitted with the Michaelis-Menten equation using Prism (GraphPad software). V_{max} values were based and are highly dependent on the protein quantification. Data points and error bars are the mean ± SD of three independent experiments.

Protein	$K_{m(ATP)}$ (µM)	V_{max} (µmol min^{-1} mg^{-1} of the protein)
hAAC1	21.3 ± 2.9	3.3 ± 0.1
hAAC2	23.8 ± 3.1	3.7 ± 0.2
hAAC3	22.3 ± 3.7	2.5 ± 0.1
hAAC4	53.3 ± 15.0	5.7 ± 0.6

Table 7 Kinetic properties of the wild-types human AAC isoforms. The K_m and V_{max} values for ATP of the proteins expressed in *E. coli* cells were calculated from the substrate saturation curves shown on Fig. 3 and fitted with the Michaelis-Menten equation using GraphPad Prism.

4.1.1.3 Transport properties of hAACs mutants

Taking here advantages of our unique functional tool and having the 4 hAAC isoforms functionally expressed in the same system we considered the following coupling mutagenesis experiments and transport measurements. Design of the mutants was based on the sequence comparison between the different isoforms and in particular between hAAC1 and hAAC4 (see Fig. 47A). Most of the differences are found in helices 5 and 6 and at the N- and C-terminus

that are around 10 residues longer in hAAC4. We swapped highly conserved residues present in the sequences of hAAC1, hAAC2 and hAAC3 with residues found in hAAC4 (often charged oppositely) and vice versa. Each mutant was expressed in *E. coli* and its transport properties assessed as for the wild type protein (see Table 8).

Residue/Position[a]		Location[b]	Mutation[c]	
hAAC1	hAAC4		hAAC1	hAAC4
A47	**P59**	M1	P	A
K49	**A51**	M1	A	**K**
D104	**N116**	C1	N	**D**
A114	**L126**	H3	L & P	A & P
R171	**A183**	M2	A	**R**
H209	**P221**	C2	P	H
No N-term$_{12aa}$	**N-term$_{12aa}$**	N_{term}	-	N-term$_{12aa}$truncation
No C-term$_{8aa}$	**C-term$_{8aa}$**	C_{term}	-	C-term$_{8aa}$truncation
No N/C-term$_{12/8aa}$	**N/C-term$_{12/8aa}$**	N/C_{terms}	-	N/C-term$_{12/8aa}$trunc
^{244}RKG^{246}	**^{256}EA-^{257}**	M3	-	**RK**G
^{248}DIM^{250}	**^{258}KRQ^{260}**	M3	-	**D**IM
T252	**K262**	M3	-	T
W258	**F268**	h_{56}	-	W
R259	**V269**	h_{56}	-	**R**
D264	**H274**	h_{56}	-	**D**
K268	**S278**	M3	-	**K**

Table 8 Summary of the hAAC1 and hAAC4 mutants generated. [a] Residues targeted for the mutations Amino acids are presented as a one-letter code (positively charged residues are highlighted in red, negatively charged in blue) and followed with their numbering in the hAAC1 and hAAC4 sequences. [b]location of the amino acids according to the 3D structure of bAAC1.; [c]mutations that were performed in this study. Abbreviations: H1-H6 (TM helixes from 1 to 6); M1-M3 (matrix loops from 1 to 3); C1-C2 (cytosolic loops 1 and 2); h_{56} (small helice in M3 loop); N-term (N-terminal region); C-term (C-terminal region).

In the following chapters the transport properties of hAAC1 and hAAC4 mutants will be discussed. Up to now the majority of the residues targeted for the mutations on those two isoforms were not yet described as involved in the transport mechanism, ATP binding or interaction with CATR inhibitor. However, majority of them significantly influence protein transport properties.

4.1.1.3.1 Functional properties of human AAC1 mutants

7 hAAC1 mutants were generated and expressed in *E. coli* in approximately similar level (see Fig. 51A). They can be clustered in three

different groups according to their transport activity (see Fig 51 C): 1) same activity as the wild-type hAAC1 (K49A), 2) higher activity than the WT (A47P, A114L) and 3) lower activity than the WT (D104N, A114P, R171A and H209P) (see Fig. 51 C). Kinetic studies were performed on A47P, A114L, D104N and H209P mutants to determine their K_m and V_{max} values (see Fig. 51 D and Table 9). A114P (in helix 3) and R171 A (in matrix loop 2) showed almost complete transport inhibition and therefore were not included in the kinetics experiments.

A47 is located in the matrix loop 1 (M1) (see Fig. 51 B) and highly conserved in hAAC1, 2 and 3 isoforms, but not in hAAC4. The ATP binding affinity and V_{max} values of A47P mutant remain in the similar range as for the wild type hAAC4 (see Fig. 51 D and Table 9).

A114 residue is located in helix 3 (H3) (see Fig. 51 B). A114L mutant showed a significant increase of transport activity compared to the wild-type protein (activity of 200% compared to the WT) (see Fig. 51 C). The apparent K_m value remains in the same range, while transport rate significantly increases comparing with WT protein (see Fig. 51 D and Table 9). Interestingly the same residue mutated in proline (A114P) has shown almost complete transport inhibition (see Fig. 51C).

D104 and H209 residues are located in the cytosolic loops 1 (C1) and 2 (C2) respectively (see Fig. 51B). For D104N mutant the ATP affinity and the V_{max} are slightly higher than the wild-type hAAC1 values (see Fig. 51 D and Table 9). In contrast to the D104N mutant, H209P differs significantly in terms of ATP binding as seen from K_m (38.6 ± 6.5 μM), however the V_{max} value (4.5 ± 0.3 μmol min^{-1} mg^{-1} of protein) is slightly higher then for wild-type hAAC4 (see Fig. 51D and Table 9).

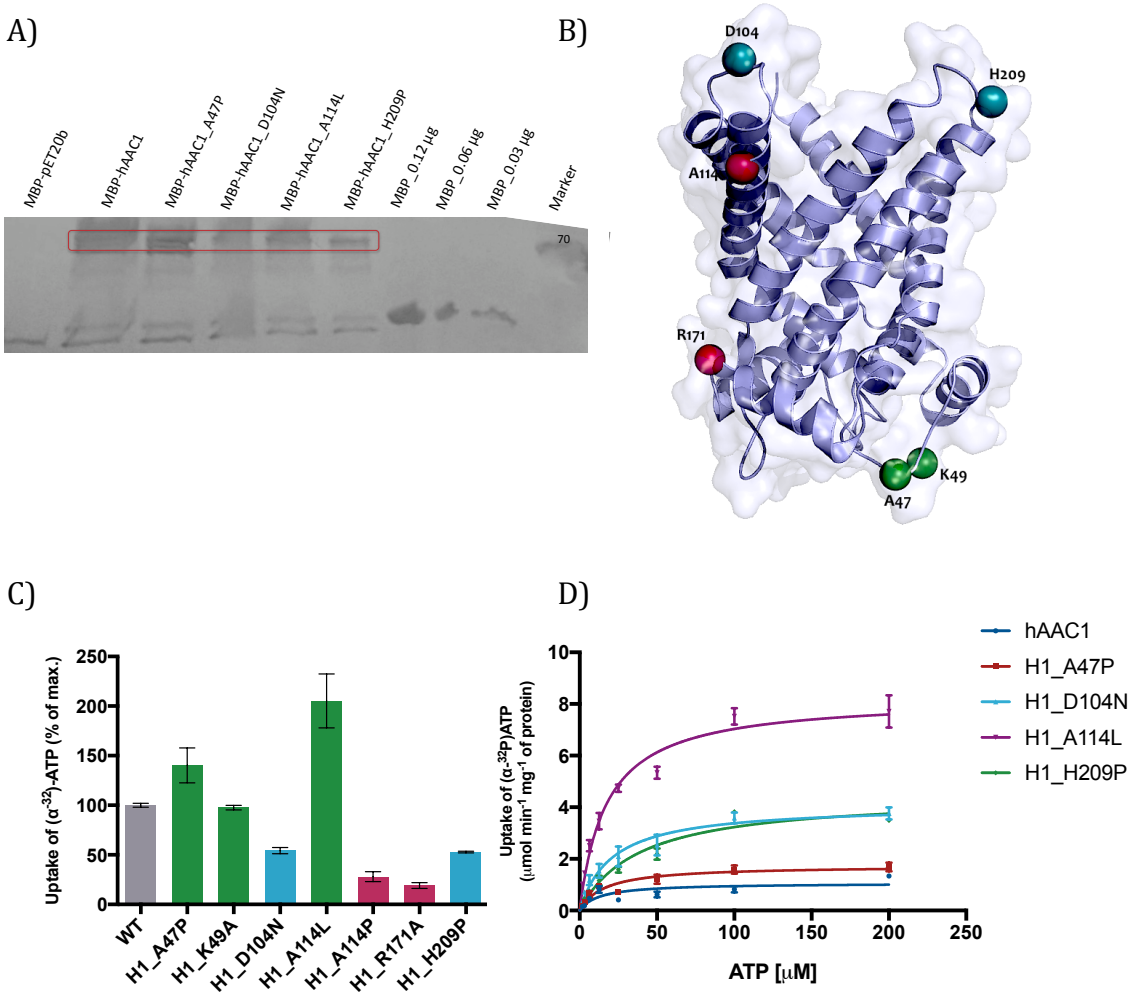

Figure 51 Functional properties of human AAC1 mutants (A) Western Blot analysis of the expression levels of the 7 human AAC1 mutants in *E. col* using an anti-MBP antibody. The MBP-hAACs constructs vary between 74-76 kDa. The level of expressed protein was calculated according to the level of the MBP protein (approximately 42 kDa), which was diluted 100X and loaded on the gel in following amount: 0.5 µL (0.03 µg), 1 µL (0.06 µg) and 2 µL (0.12 µg). The lower bands on the Western Blot represent *E. coli* MBP and MBP protein cleaved from the constructs (B) hAAC1 3D model based on the bAAC1 3D structure (PDB access code: 1OKC). A47, K49 and R171 are located in M1 and M2 matrix loops respectively; D104 and H209 are located on top of the protein structure in C1 and C2 cytosolic loop respectively; A114 is borne by H3 helix. The residues in (B) and columns in (C) are colored according to the impact of the mutations on the transport activity: in green - higher or similar activity of the WT AAC1; light blue - approximately 50% of the WT and in dark pink – low activity compared with WT. (C) [α-^{32}P]-ATP uptake of *E. coli* cells expressing MBP-hAAC1_wild type (hAAC1) and following hAAC1 mutants: A47P, K49A, D104N, A114L, AII4P, R171A and H209P was measured in presence of 10 µM labeled ATP. (D) Substrate saturation curves of [α-^{32}P]-ATP uptake of cells expressing hAAC1 wild type and four hAAC1 mutants. The control nucleotide uptake (empty vector) was subtracted. The K_m and V_{max} values were extrapolated from the experimental data fitted with the Michaelis-Menten equation using Prism. Data points and error bars are the mean ± SD of three measurements.

Protein	$K_{m(ATP)}$ (µM)	V_{max} (µmol min^{-1} mg^{-1} of the protein)
hAAC1_WT	17.8 ± 1.1	1.1 ± 0.1
H1_A47P	16.0 ± 3.3	1.7 ± 0.1
H1_D104N	20.9 ± 3.0	4.0 ± 0.2
H1_A114L	17.4 ± 1.9	8.3 ± 0.3
H1_H209P	38.6 ± 6.5	4.5 ± 0.3

Table 9 Kinetic properties of the wild-type (hAAC1) and of hAAC1 mutants. The K_m and V_{max} values for ATP of the wild-type human AAC1 and of the four mutants expressed in *E. coli* cells. The values were calculated based on substrate saturation curves of [α-^{32}P]-ATP uptake (see Fig. 51 D) and fitted with the Michaelis-Menten equation using GraphPad Prism. V_{max} values were based and are highly dependent on the protein quantification.

4.1.1.3.2 Functional properties of hAAC4 mutants

17 mutants of hAAC4 were designed including the truncations of the N-, C- or both termini (see Table 8). They were expressed in *E. coli* as for the wild type protein and their transport activity measured and compared to hAAC4 WT. 2 main types of behaviors were observed: 1) the N-terminal truncation, the C-terminal truncation, the N/C-termini truncation, P59A, A61K, A183R and P221H exhibit increased or slightly lower transport activity than hAAC4 WT 2) N116D, L126A, L126P, ^{256}EA-^{257}/RKG, ^{258}KRQ^{260}/DIM, K262T, F268W, V269R, H274D and S278K show a strong decrease of the transport activity (see Fig. 52 B and C).

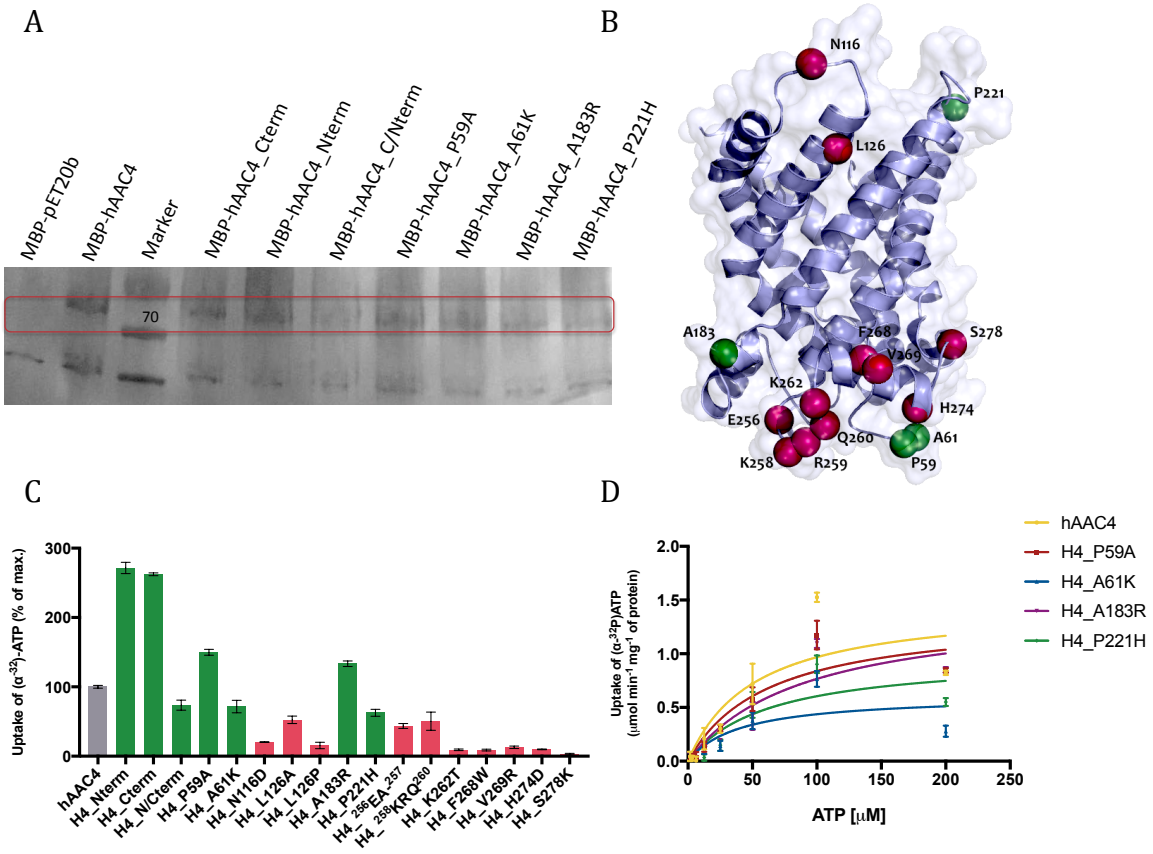

Figure 52 Functional properties of human AAC4 mutants (A) Western Blot analysis of the expression levels of the 17 human AAC4 mutants in *E. col* using an anti-MBP antibody. The MBP-hAACs constructs vary between 74-76 kDa. The level of expressed protein was calculated according to the level of the MBP protein (approximately 42 kDa), which was diluted 100X and loaded on the gel in following amount: 0.5 µL (0.03 µg), 1 µL (0.06 µg) and 2 µL (0.12 µg) (see Fig. 51A). The lower bands on the Western Blot represent *E. coli* MBP and MBP protein cleaved from the constructs (B) 3D model of hAAC4 based on the bAAC1 3D structure (PDB access code: 1OKC). P59, A61 are located in M1 matrix loop; N116 is in cytosolic loop 1 (C1), L126 in helix 3 (H3), A183 in matrix 2 loop (M2), H221 is in cytosolic loop 2 (C2), E256, ^{258}KRQ^{260}, K262 and S278 are situated in matrix 3 loop (M3), F268, V269 and H274 are located in small helix 56 (h_{56}). The residues in (B) and the columns in (C) are colored according to the impact of the mutations on the transport activity. (C) [α-^{32}P]-ATP uptake of *E. coli* cells expressing MBP-hAAC4_wild type (WT) and the following mutants of MBP-hAAC4: Nterm-, Cterm- and N/Cterm truncations; P59A, A61K, N116D, L126A, L126P, A183R, P221H, ^{256}EA-^{257}, ^{258}KRQ^{260}, K262T, F268W, V259R, H274D, S278K was measured in the presence of 10 µM labeled ATP. The measurements were performed in triplicates. The rate of the transport in the absence of additives was set to 100%. The values for the control nucleotide uptake (empty vector) were subtracted (D) Substrate saturation curves of [α-^{32}P]-ATP uptake of cells expressing hAAC4 wild type and four hAAC4 mutants. The control nucleotide uptake (empty vector) was subtracted. The K_m and V_{max} values were extrapolated from the experimental data fitted with the Michaelis-Menten equation using Prism. Data points and error bars are the mean ± SD of three measurements.

Protein	$K_{m(ATP)}$ (µM)	V_{max} (µmol min^{-1} mg^{-1} of the protein)
hAAC4_WT	51.9 ± 26.4	1.5 ± 0.3
H4_P59A	62.7 ± 23.1	1.4 ± 0.2
H4_A61K	40.5 ± 27.6	0.6 ± 0.2
H4_A183R	89.6 ± 37.1	1.4 ± 0.3
H4_P221H	61.9 ± 31.8	1.0 ± 0.2

Table 10 Kinetic properties of the wild-type (hAAC4) and of hAAC4 mutants. The K_m and V_{max} values for ATP of the wild-type human AAC4 and of the four mutants expressed in *E. coli* cells. The values were calculated based on substrate saturation curves of [α-^{32}P]-ATP uptake (see Fig. 52 D) and fitted with the Michaelis-Menten equation using GraphPad Prism. V_{max} values were based and are highly dependent on the protein quantification.

The N- and C-termini truncations show more then double transport activity comparing with WT, while N/C-termini truncations mutant retained almost the same transport activity then hAAC4 (see Fig. 52 C). Mutations of residues 59 and 61 (hAAC4 numbering, corresponding to 47 and 49 in hAAC1) in Ala and Lys respectively show approximately 150% and 80% of the wild type hAAC4 activity (see Fig. 52 B and C). The residue A183 while mutated into positively charged arginine exhibits higher transport activity of approximately 130% of the wild type hAAC4 (see Fig. 52 B and C). The last residue from this group, P221 retained approximately 55% of the hAAC4 activity (see Fig. 52 B and C).

The second group of hAAC4 mutants show lower transport activity or complete transport inhibition. Mutation of N116 (corresponding to D104 residue in hAAC1) decreased transport activity to 20% (see Fig. 52 B and C). The residue L126 was mutated into Ala and Pro. In both cases the transport is reduced by 60-90% compared to the WT (see Fig. 52 B and C). The mutations ^{256}EA-^{257}/RKG and ^{258}KRQ^{260}/DIM decreased the transport activity to 40-45% while K262T, F268W, V269R, H274D and S278K mutants abolished the transport activity to approximately 3-10% of the wild type hAAC4.

Kinetic studies were performed on P59A, A61K, A183R and P221H mutants to determine their K_m and V_{max} values (see Fig. 52 D and Table 10). Residue P59 and A61 are located in the matrix loop 1 (M1) (see Fig. 52 B). The ATP binding affinity value of P59A mutant is slightly higher then for the wild

type, while the V_{max} value remains in the same range as the wild-type hAAC4 (see Fig. 52 D and Table 10). The apparent K_m value of A61K mutant is lower then hAAC4, while transport rate increases approximately twice comparing with WT protein (see Fig. 52 D and Table 10).

A183 is located in the matrix loop 2 (M2) (see Fig. 52 B). The ATP binding affinity of this mutant is significantly lower then the wild-type, however the transport rate remains at the same range as for the wild-type hAAC4 (see Fig. 52 D and Table 10).

The last investigated residue P221 is located in cytosolic loop 2 (C2) and it is highly conserved in bovine and all human AACs except human AAC4. The apparent K_m value for P221H mutant is slightly higher comparing with the wild-type while transport rate is slightly higher then for the hAAC4 (see Fig. 52 D and Table 10).

4.1.2 Discussion and conclusions

Following the same strategy as described for hAAC1[122], the three other human AACs were successfully and functionally expressed in *E. coli* membranes. The sequence of hAAC4 is only 68% similar to hAAC1. Our data have shown that the expression level and the transport properties of this isoform differ from the other three. hAAC4 is less expressed than the others. The transport rates and ATP binding affinity are similar for the first three isoforms while they are significantly lower for the human AAC4 (K_m is of 53.25 ± 15.1 μM, V_{max} is of 5.7 ± 0.6 μmol min^{-1} mg^{-1} of the protein). Additionally, our results have proven that two specific inhibitors – CATR and BA inhibit all the human AAC isoforms. Moreover, the transport properties of the wild-type isoforms are also abolished after addition of chebulinic acid – not specific AAC inhibitor as it was described by Todisco S. et al. 2015 Biochemical Pharmacology[203]. Presence of other previously described inhibitors – CD437, Closantel, Leelamine[92] or Suramin[203] does not affect significantly protein activity (see Fig. 49 a-h).

Kinetic values for hAACs vary considerably in literature[67]. The previously reported K_m values of hAAC4 (72 μM for ADP and 120 μM for ATP) are higher than ours. They were obtained in a liposome reconstitution system using

purified hAAC4 produced in *E. coli* inclusion bodies[133]. Our results, compared with the ones already published for the hAAC1 isoform[122], present higher V_{max} values, however they still remain in the same range as some of them[138]. Additionally, it is worth emphasizing that it was technically challenging to determine the ADP/ATP transport rate values of wild-type hAACs and mutants since the determination of the final overexpressed protein quantity might be overestimated because of two reasons; 1) the bands corresponding to the MBP-hAAC on the Western Blots were sometimes blurry and therefore difficult to quantify and 2) it looks that some of the protein was already cleaved (missing MBP-tag). It remains unclear weather the cleaved protein is well inserted into the membrane and participates in the ATP import. Moreover, it was not quantified on the Western Blot with the anti-MBP antibody.

Comparing the transport properties of hAAC1 and hAAC4 mutants, different protein behaviors were observed. In hAAC1, A47 and K49 correspond to P59 and A61 in hAAC4 (see Fig. 47 A and Table 8) respectively. Both of those residues are embedded in the matrix loop 1 (M1) (see Fig. 51 B and 52 B). MD simulation data analysis showed that they are facing the matrix side and that they belong to the most flexible region of the protein (see Fig. 47 B). Those residues are highly conserved in hAAC1, 2 and 3 isoforms, however they are not strictly conserved among all AACs. Hence, their mutation might not perturb significantly the nucleotides transport. A47P mutation in hAAC1 and corresponding mutation in hAAC4 (P59A) increases transport efficiency (see Fig. 53). The ATP binding affinity is quite high for A47P mutant in hAAC1 while for P59A mutant in hAAC4 is very low. However both of the mutation retained similar transport rate (see Table 9 and 10). Interestingly, A61K mutant in hAAC4 exhibited higher ATP binding affinity and transport rate then wild-type hAAC4 (see Fig. 52 D and Table 10). K49 residue in hAAC1 and corresponding A61 in hAAC4 when mutated into Ala and Lys respectively have shown similar transport properties (see Fig. 53).

A114 residue in hAAC1 corresponds to L126 in hAAC4 isoform (see Fig. 47 A and Table 8). Those two residues situated in helix 3 (H3) should face the protein funnel as seen in the 3D models of the proteins (see Fig. 51 B and 52 B). Furthermore, according to the MD simulation results, A114 or L126 residues are

located in a more rigid protein region (see Fig. 47 B). Mutation of these residues could therefore have a great impact on the protein flexibility and hence, leads to transport inhibition. Sequence alignment shows that A114 residue is conserved among almost all AACs (with small exceptions in plants, where glycine is found in this location), but not in hAAC4. Surprisingly, when mutated into Leu (in hAAC1) or Ala (in hAAC4), two distinct behaviors might be observed in terms of protein activity (see Fig. 53). A114L in hAAC1 has shown almost twice higher protein activity than the wild-type while corresponding L126A in hAAC4 retained only 50% activity of the wild-type hAAC4 (see Fig. 53). However, when mutated into Pro (A114P in hAAC1 and L126P in hAAC4) both proteins showed a transport inhibition (see Fig. 53). Prolines are known to cause a characteristic helix kink that changes the helix properties and thus may lead to protein inactivation. Additionally, A114P mutant in hAAC1 was reported to be associated with opthalmoplegia (adPEO)[68] and its transport properties and substrate affinity were previously described showing that this mutation significantly influences protein flexibility[122].

By analyzing the human AACs MD models, it was observed that residues R171 in hAAC1 and corresponding A183 in hAAC4 are located in the matrix loop 2 (M2) of the protein (conserved MCF motif) (see Fig. 47 A, 51 B and 52 B), which still belongs to a flexible part of the protein (see Fig. 47 B). The residue is not highly conserved in all AACs, however, alanine, arginine and lysine are the most common residues found at this position. In human AACs, AAC1 and AAC3 possess arginine in this position, hAAC2 and hAAC4 – lysine and alanine respectively. So far it was not reported that R171 and A183 residues are directly implicated in the transport mechanism. However, the mutation of this charged residue into alanine caused transport inhibition in hAAC1 in contrast to A183R mutant that increased protein activity (see Fig. 53). Additionally, it was observed that the apparent ATP binding affinity of A183R mutant in hAAC4 is lower, however the transport rate remains is in the similar range as for the wild-type hAAC4 (see Table 10). Nonetheless, it is possible that upon protein conformational change acquired during substrate trafficking, this particular arginine might be involved in the further steps of the nucleotide translocation. Hence, it seems that between hAAC1 and hAAC4 isoforms swapping the residues

in this position from arginine to alanine and from alanine to arginine respectively influences distinctly transport properties.

D104 and H209 residues in hAAC1 isoform and corresponding N116 and P221 in hAAC4 isoform are located on the top of the protein structure (see Fig. 51 B and 52 B). According to MD simulation analysis, they belong to a flexible region of the protein (see Fig. 47 B). Both residues are conserved among majority of AACs (except plants, where lysine is found in this position), except in hAAC4. Data have shown that upon the mutation of those residues in both of the isoforms, protein transport activity is reduced, however hAAC1 mutants exhibits higher (D104N) and lower (H209P) activity of those mutated in hAAC4 (see Fig. 53). Comparing the two human AAC models, D104 and H209 in hAAC1 are located in the vicinity of charged residues on the top of the protein structure: K92, K96, R105 and K199, K206 respectively. In hAAC4 isoform corresponding residues are also located in a close distance to those charged residues: K104, K108, K117, K119, R123 and K211, K216, K218, K219 respectively. Positively charged residues favor the attraction of negatively charged nucleotides towards the protein cavity. Nevertheless, D104 and H209 and corresponding N116 and P221 residues seem to be not directly linked with the nucleotide pathway in protein cavity and hence, mutation of those residues might only reduce protein transport rate (see Fig. 51 C). Additionally, the ATP binding affinity of P221H mutant is slightly lower then of the wild-type and the transport rate remains at the similar range as for the hAAC4 (see Fig. 52 D and Table 10). While substrate affinity and transport rate for D104N mutant remains in similar range as the wild-type hAAC1, the mutation of H209 residue into proline significantly changes protein transport properties, the substrate binding affinity and the transport rate (see Fig. 51 D and Table 9). Moreover, it was reported for hAAC1 isoform that D104 residue when mutated in glycine exhibits approximately 30% of the wild-type activity[122] and it is associated with mild symptomatology of adPEO disease[68,204].

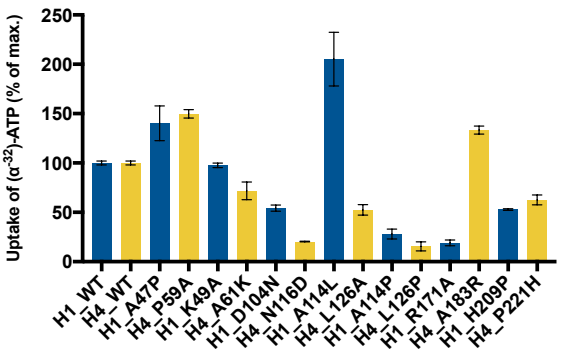

Figure 53 Comparison of [α-^{32}P]-ATP uptake of *E. coli* cells expressing MBP-hAAC1_wild-type (WT) and MBP-hAAC4_wild-type (WT) and the following mutants of MBP-hAAC1: A47P, K49A, D104N, A114L, AII4P, R171A and H209P with corresponding MBP-hAAC4 mutants: P59A, A61K, N116D, L126A, L126P, A183R and P221H respectively was measured in the presence of 10 µM labeled ATP. The measurements were performed in triplicates. The rate of the transport in the absence of additives was set to 100%. The values for the control nucleotide uptake (empty vector) were subtracted.

The swapped mutations that were created between hAAC1 and hAAC4 isoforms showed both similar and different transport properties depending on the mutated residue. By mutating following residues D104, A114 (in leucine) and R171 in hAAC1 and corresponding N116, L126 in alanine) and A183 in hAAC4 divergent protein behaviors were observed. Mutation of A47, K49, A114 (in proline) and H209 in hAAC1 and corresponding ones P59, A61, L126 (in proline) and P221 in hAAC4 exhibited similar protein behavior (see Fig. 53). Additionally, based on the MD simulation models, all those mutated residues in both isoforms seem not to be involved directly in nucleotide transport nor in CATR binding site. Human AAC4 protein sequence is similar only in 66 to 68% to hAAC1 isoform (see Fig 47 A), and consequently an involvement of particular residues in the conformational change of the protein during substrate trafficking might differ between those two isoforms that may explain those distinct behaviors.

Subsequently, comparing sequence alignment of hAAC1 and hAAC4 proteins, following hAAC4 mutants were generated: N-terminal truncation, C-terminal truncation and N/C-terminal truncations, ^{256}EA-^{257}/RKG, ^{258}KRQ^{260}/DIM, K262T, F268W, V269R, H274D and S278K. Interestingly, the N-terminal, C-terminal and N/C-terminal truncated mutants exhibited significantly higher (N- and C-terminal truncation mutants) or equal (N/C-terminal truncation mutant) protein activity (see Fig. 52 C). Moreover, their expression level is quite high (see Fig. 52 A). Among all human AAC isoforms only hAAC4 possesses longer N- and C-termini (see Fig. 47 A) and apparently those regions might play an important roles in the protein folding. N-terminal seems to be involved in protein translocation into inner mitochondrial membrane. Based on

the three-dimensional structure of yeast AAC2, it was reported that the protein N-terminal region is extended[83] and it plays a significant role in protein expression. Additionally, it was also described that human AAC1 is expressed in yeast system by replacing the N-terminal region with corresponding region of yeast AAC2 (yAAC2) isoform[135]. Data have shown that the C-terminus is also an important region, adding a fusion protein on the C-terminal site is for example known to hinder protein expression.

The following mutants of hAAC4: ^{256}EA-^{257}/RKG, ^{258}KRQ^{260}/DIM, K262T, F268W, V269R, H274D and S278K exhibited decreased or completely abolished transport activity. All of them are located in the matrix loop 3 (M3) and in the small matrix helix h_{56} (see Table 8) The sequence alignment of all human AACs shows that the region of hAAC4 consisting in helix 5 (H5), matrix loop 3 (M3), small matrix loop h_{56} and helix 6 (H6) is significantly different from the other isoforms (see Fig. 47A). Considering predicted model of the hAAC4 structure, which is based on bAAC1 structure, is seems that none of those residues might be directly implicated in CATR and substrate binding nor in salt bridge network interactions (see Fig. 52 B). The molecular dynamic simulation showed that the region between 240 to 270 residues is characterized by higher protein flexibility for all of the human isoforms. Therefore, it is possible that upon protein conformational change those particular residues might be involved in the further steps of the nucleotide translocation.

Supplementary Data

A) B)

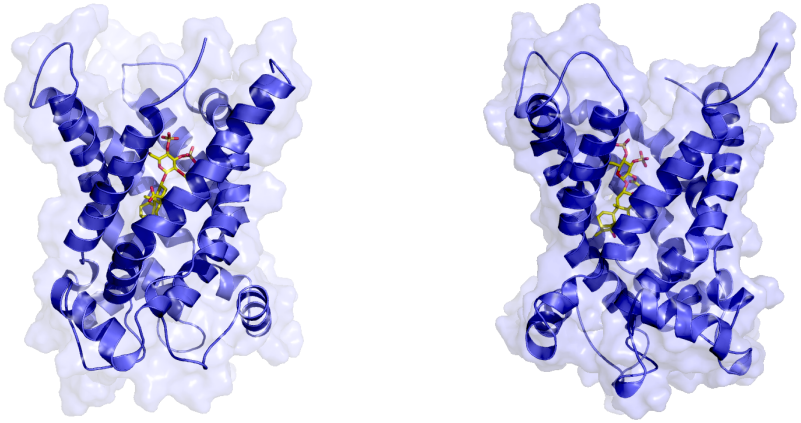

C) D)

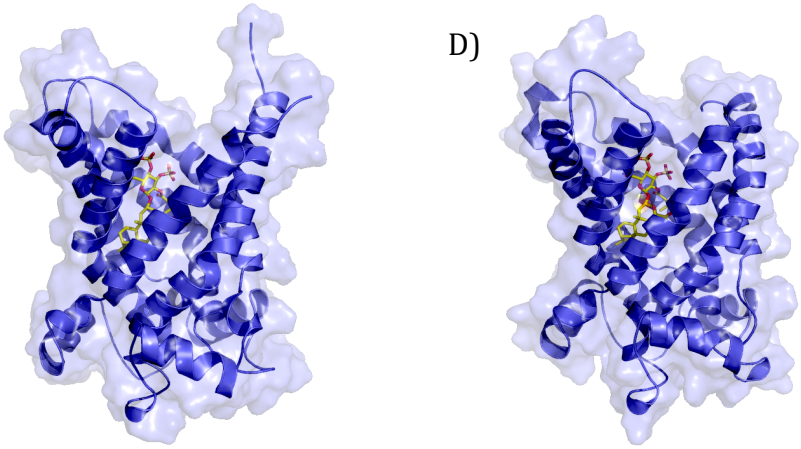

Figure 1 3D models of human AAC1, 2, 3 and 4 with CATR inhibitor embedded inside the protein cavity (depicted as yellow and red sticks) were generated using Expasy, MD simulations and rendered with COOT combined with PyMOL softwares. The models of all human AACs were based on the bAAC1 3D structure (PDB access code: 1OKC).

4.2 **Part II** - Human ADP/ATP carriers production, characterization and crystallization

4.2.1 Human AACs are efficiently produced using *E. coli* extract (ECE) in cell-free expression system

The genes that encode all human ADP/ATP carrier (hAACs) isoforms were inserted into pIVEX 2.3d and pIVEX 2.4d vectors with a His-tag fused at their C-termini and N-termini respectively. However only the N-termini His-tag fusion (pIVEX 2.4d) led to a successful expression of all full-length human AACs in cell-free system (see Fig. 54 left and right panels). This particular expression system relies on the *in vitro* production of a protein in a reaction mixture containing the expression plasmid and *E. coli* extract combined with energy sources, amino acids necessary for the protein synthesis and recycling enzymes (see Materials and Methods, paragraph 3.3.1)[173,174,175,177]. Expression of soluble hAACs required the presence of detergent in the reaction mixture. Several detergents were tested to find the one giving the highest level of soluble protein: Brij35, DDM, Cymal5 and FC16. The immunoblot displayed in Figure 54 (right panel) showed that hAAC3 is expressed successfully in presence of almost all detergents, with a significantly lower yield in Cymal5. hAAC1, hAAC2 and hAAC4 exhibited a similar expression protein level and solubility as hAAC3 with a lower expression level in Cymal5. For large protein production batches, the expression of the proteins were conducted in the presence of 0.5% Brij35 in which fully solubilized hAACs were obtained.

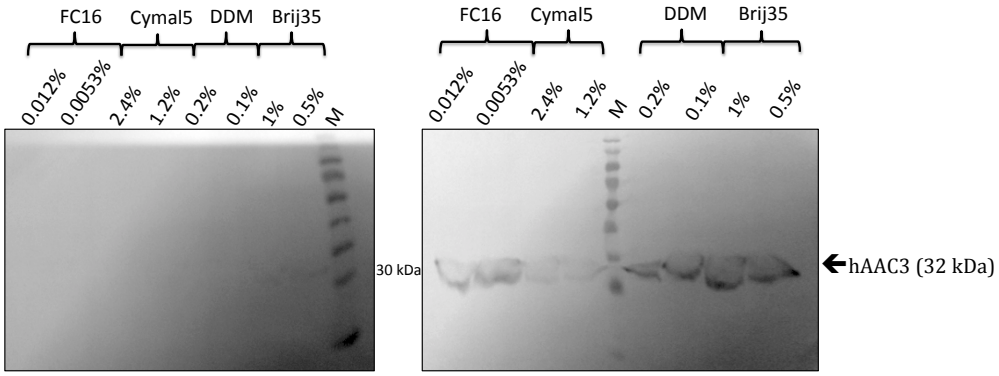

Figure 54 Cell-free expression of hAAC3 cloned in the pIVEX 2.3d vector (with His-tag fused at C-termini (left panel) or pIVEX 2.4d vector (with His-tag fused at N-termini) (right panel) in presence of four different detergents used at 10x or 20x their cmc: 0.012% and 0.0053% FC16, 2.4% and 1.2% Cymal5, 0.2% and 0.1% DDM and 1% and 0.5% Brij35. The tests were performed in 50 µL of cell-free reaction and incubated during 4h in 20°C. Subsequently, 10 µL of each cell-free reaction (followed with centrifugation step in order to remove non-soluble parts), was analyzed on SDS-PAGE followed with Western Blot analysis. The expression of full-length hAAC3 (bands are indicated with the black arrow) was detected using anti-His antibody.

Purification trials were performed for the four human AAC isoforms expressed in cell free system. The protein yields obtained for hAAC1 and hAAC3 were significantly higher than for hAAC2 and hAAC4, we therefore focused on hAAC1 and hAAC3 and investigated their folding, oligomerization state and thermal stability. To gain also some insight into their structures, many crystallization trials were performed in vapour diffusion and in lipidic cubic phase (LCP), which supposed to favor crystallization process of membrane proteins.

4.2.2 hAAC1 and hAAC3 were obtained in a pure and homogenous form in DDM and MNG-3 detergents

One of the major challenges in the expression and purification of membrane proteins is to isolate the protein of interest in a pure form without formation of aggregates. The N-terminal His-tag allowed us to obtain pure hAAC1 and hAAC3 proteins using a single affinity-purification step starting from the cell-free reaction mix that contained the solubilized protein in 0.5% Brij35. During the purification procedure, while performing washing steps, 0.5% Brij35 was subsequently exchanged in different detergents such as: 0.1% LAPAO, 0.2% Cymal5, 0.1% FC12, 0.1% OG, 0.04% DDM and 0.005% MNG-3. The protein

purity was the best in DDM and MNG-3 (see Fig. 55A, C, E, G). The concentration of MNG-3 and DDM during the affinity chromatography was slightly increased to 0.06% and 0.008% respectively in order to reduce the unspecific binding. Subsequently, final elution fractions of hAAC1 and hAAC3 in 0.005% MNG-3 and 0.04% DDM showed that both of the human isoforms are more pure in MNG-3 detergent than in DDM (see Fig. 55A, C, E, G).

To further characterize purified hAAC1 and hAAC3 size exclusion chromatography was performed. hAAC1 and hAAC3 eluted in both detergents as a major and single peak (see Fig. 55B, D, F, H). In all performed purifications, the minor peaks eluting before the main ones, contain protein aggregates (void volume around 8 mL) and contaminants (between 9-11 mL elution volume) (see Fig. 55B, D, F, H). hAAC1-detergent complex eluted with an apparent molecular mass of about 102 kDa and 91 kDa in 0.005% MNG3 and 0.04% DDM, respectively, while hAAC3-detergent complex eluted with an apparent molecular mass of 112 kDa and 88 kDa, respectively (see Fig. 56). It was reported for membrane proteins[205], that the molecular mass of the protein-detergent complex should be around the sum of molecular masses of the protein and a pure detergent micelle (for MNG-3 approximately in a range of 60 to 65 kDa for DDM approximately in a range of 60 to 75 kDa size). The MW of hAAC1 and hAAC3 is approximately 32 kDa, therefore the data would be consistent with a monomer of protein.

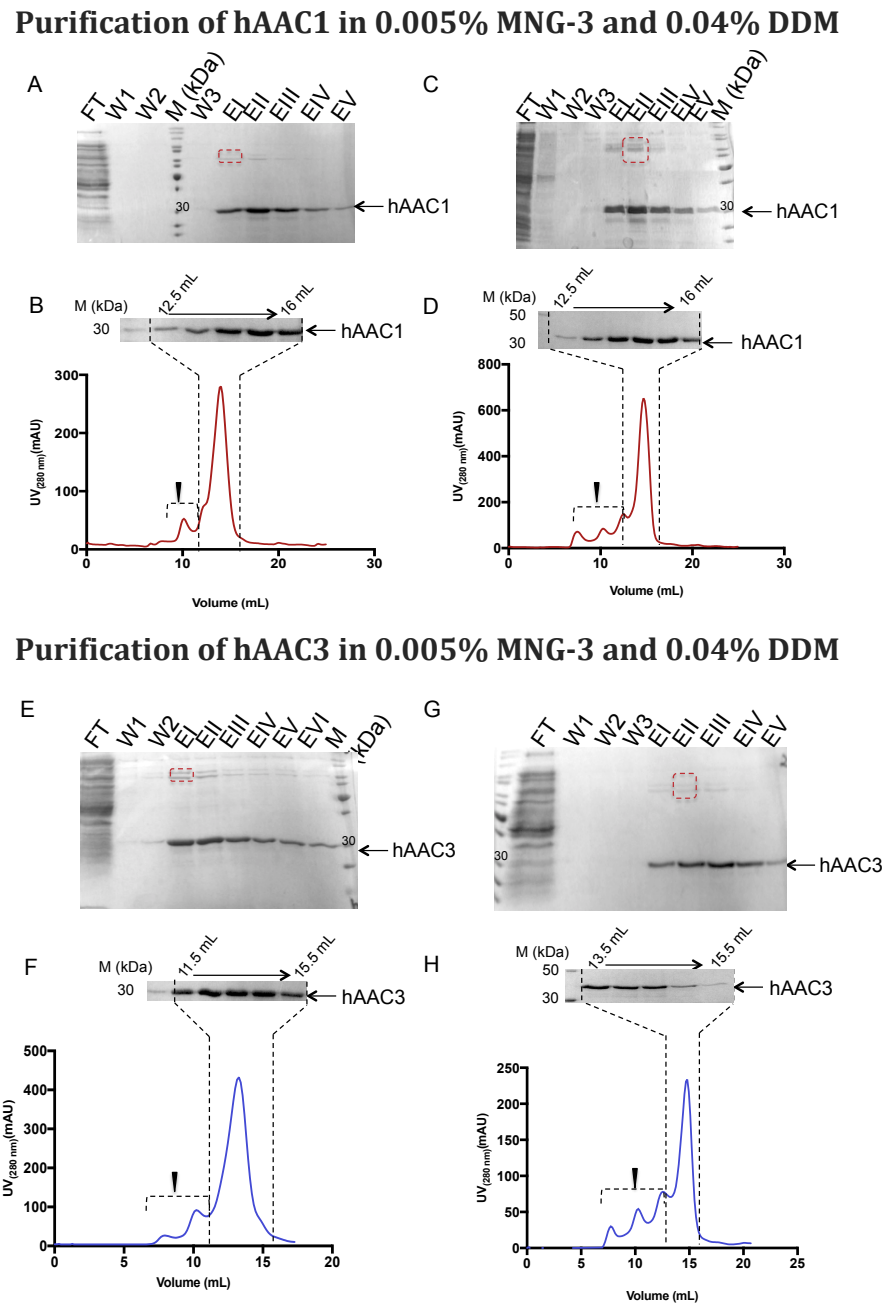

Figure 55 Purification of fullength human AAC1 and AAC3 in 0.005% MNG-3 and 0.04% DDM by affinity chromatography and size exclusion chromatography. (A, C, E, G) Full-length hAAC1 and hAAC3 (N-term His-tag) were expressed in cell-free system in presence of 0.5% Brij35 and Brij35 was exchanged during the affinity purification for 0.008% MNG-3 or 0.06% DDM. The final detergent concentrations in the elution fractions were 0.005% MNG-3 (A and E) or 0.04% DDM (C and G). Protein samples were analyzed on SDS-PAGE stained by Coomassie blue. FT, flow through; W1, wash 1 containing 0.022% Brij35 and 10 mM imidazole; W2, wash 2 with 0.008% MNG-3 or 0.06% DDM and 40 mM imidazole; W3, additional washing with 0.008% MNG-3 and 45 mM imidazole (in order to remove more impurities); EI to EVI, elution fractions with 0.005% MNG-3 or 0.04% DDM and 200 mM imidazole; M, marker (kDa). The black arrows indicate the band corresponding to hAAC1 or hAAC3. The red-dotted box corresponds to a contaminant identified by N-terminal sequencing as transformylase – an *E.coli* enzyme that exists in methionine and purine biosynthesis. (B, D, F, H) Size exclusion chromatography on a Superdex 200 10/300 column of hAAC1 and hAAC3 in 0.005% MNG-3 and 0.04% DDM with EI to EV or EVI elution fractions. The elution profile of hAAC1 or hAAC3 is drawn as a solid line in red and blue respectively. Coomassie stained SDS-PAGE of the collected fractions is shown above each protein chromatographic profile. Elution volume of hAAC1 in 0.006% MNG3 and 0.04% DDM is 14 mL and 14.8 mL while for hAAC3, 13.4 mL and 14.8 mL respectively. The region with small peaks eluting before the main peak of proteins of interest is marked with a horizontal dotted line with black arrow above which indicates protein aggregates.

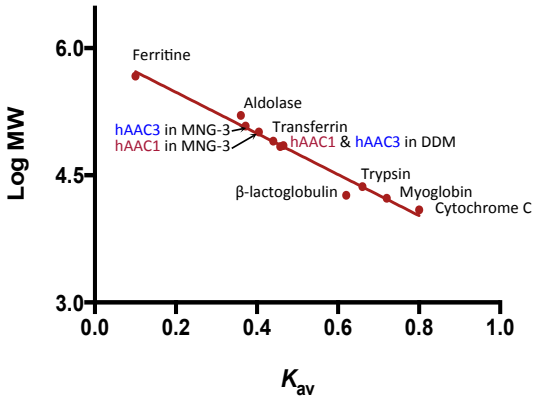

Figure 56 Molecular weight calibration curve of the size exclusion chromatography column established using protein standards indicated on the plot. The K_{av} values for each protein in MNG3 or DDM are indicated.

Final yield of purified hAAC1 and hAAC3 in 0.04% DDM was about 4 mg (from 10 mL of cell-free reaction) and 2.1 mg (from 6 mL) respectively while the yield obtained from purification in 0.005% MNG-3 was 3.45 mg (from 8 mL of cell-free reaction) and 5.6 mg (from 8 mL) respectively. We tested the addition of CATR and cardiolipins into expression and purification steps since these compounds are known to stabilize AAC. However neither the protein stability nor the yield were improved.

4.2.3 hAAC1 and hAAC3 folding determination

The far UV circular dichroism (CD) spectrum of hAAC1 and hAAC3 eluted from size exclusion chromatography in 0.005% MNG-3 and 0.04% DDM showed typical spectra of α-helical folding with two minima at 208 and 222 nm and a maximum at 192 nm (Fig. 57A and B).

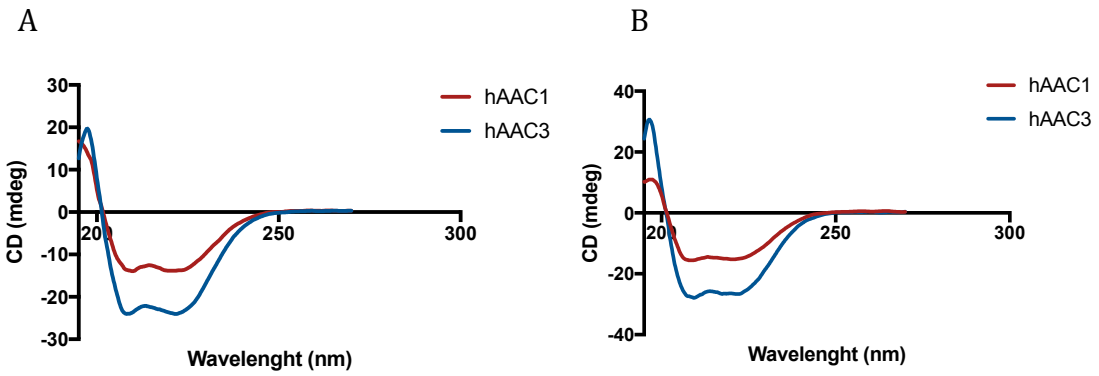

Figure 57 Far UV circular dichroism (CD) spectrum of hAAC1 (red line) and hAAC3 (blue line) after purification by size exclusion chromatography in 0.005% MNG-3 (A) and 0.04% DDM (B) detergents. Measurements were carried out in a 0.1 cm path length quartz cuvette with hAAC1 and hAAC3 at a concentration of 40 µM. Each measurement was performed in triplicates.

The data analysis suggest that hAAC3 exhibit a better protein folding than hAAC1 in 0.005% MNG-3 and in 0.04% DDM. The spectral deconvolution yields to an α-helix content of 50–56% and 34-36%, turn content of 19–22% and 20-23% and β-sheet content (that is not present in the protein structure of bovine ADP/ATP Carrier) of 8–9% and 15-17% for hAAC3 and hAAC1 respectively.

4.2.4 Thermal stability properties of hAAC1 and hAAC3

Thermo-denaturation experiments were performed in order to verify the protein stability for future crystallization assays. T_m values for both human isoforms were determined using three independent methods: Circular Dichroism (CD), Fluorescence Size Exclusion Chromatography (FSEC) and CPM dye fluorescence.

4.2.4.1 Thermal stability measurements performed by CD

Analysis of CD spectra performed as a function of temperature allowed determining the thermodynamics of protein folding[206]. The CD spectra of hAAC1 and hAAC3 in 0.04% DDM (see Fig. 58 A and C) possess the largest ellipticities at 222 nm while for hAAC1 and hAAC3 in 0.005% MNG-3 (see Fig. 58 B and D) at 222 and 208 nm respectively. We used these wavelengths to follow proteins unfolding (see Fig. 58 A-D). Our results showed that hAAC1 in 0.04% DDM has an apparent T_m value of approximately 39.3 ± 2.9°C, but in presence of CATR inhibitor the T_m increases up to 55 ± 1.8°C (see Fig. 58 A and Table 11). In MNG-3 hAAC1 alone possesses higher T_m of approximately 57.6 ± 0.3°C than in DDM, however thermal stability of this isoform could not have been determined in this detergent after adding CATR inhibitor (see Fig. 58 B and Table 11). T_m value of hAAC3 in 0.04% DDM is approximately 47.6 ± 10.3°C, however after incubation with CATR inhibitor Tm increases up to 55.5 ± 7.6°C (see Fig. 58 C and Table 11). The Tm value of the same protein in 0.005% MNG-3 without CATR inhibitor is considerably high of 61.7 ± 0.6°C, while in presence of CATR it slightly increases to 66 ± 7.0°C (see Fig 58 D and Table 11). Therefore, CATR seem to stabilize both human isoforms – AAC1 in DDM and AAC3 in both detergents.

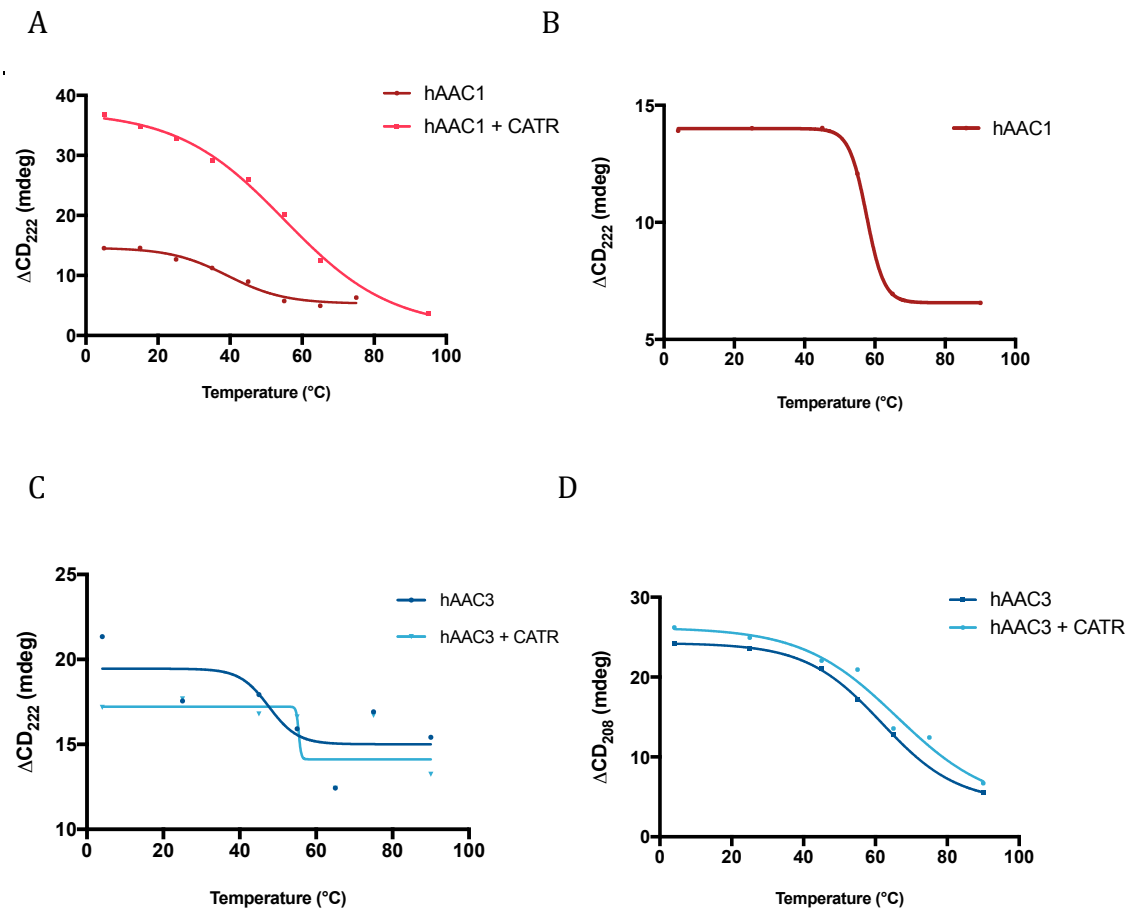

Figure 58 Thermo-denaturation assays using far UV circular dichroism (CD) spectrum of: hAAC1 in 0.04% DDM (A) or 0.005% MNG-3 (B) with (pink line) and without 0.1 mM CATR inhibitor (dark red line) recorded at the largest elipticiticity at 222 nm; hAAC3 in 0.04% DDM (C) and in 0.005% MNG-3 (D) with (light blue line) and without 0.1 mM CATR (dark blue line) recorded at the elipticiticity of 222 and 208 nm respectively. Measurements were carried out in a 0.1 cm path length quartz cuvette with hAAC1 and hAAC3 at a concentration of 40 µM. The measurements were performed in triplicates and the average values were used to draw the plots. Thermal stability curves were generated using Boltzmann equation.

4.2.4.2 Thermal stability measurements performed by FSEC

Most of the fluorescence emissions of folded proteins are due to tryptophan residues, which have a maximum of excitation at 280 nm, and an emission peak that is ranging from 300 to 350 nm depending on the polarity of the local environment. In addition, many proteins contain only one or a few tryptophan residues. Therefore, tryptophan fluorescence can be a very sensitive measurement of the environment of individual tryptophan residues and thus of the folding of the protein close to the tryptophan. In order to determine thermal stability of hAAC1 and hAAC3 (they contain 6 tryptophan residues) in MNG-3

and DDM detergents, hAAC1 and hAAC3 were analyzed by size exclusion chromatography coupled with a fluorescence detector. The apparent T_m of hAAC1 in 0.04% DDM is approximately 47 ± 8.2°C, while in presence of CATR inhibitor, it reaches 57 ± 2.2°C (see Fig 59 A and Table 11). More interestingly, hAAC1 seems to be more stable in MNG-3 detergent than in DDM and its T_m value is around 59 ± 2.3°C (see Fig. 59 B and Table 11), however surprisingly in presence of CATR inhibitor it decreases to 54.9 ± 4.8°C (see Fig. 59 B and Table 11). For hAAC3 in 0.04% DDM, the apparent T_m value is significantly low, of around 21.3 ± 15.7°C, however after adding the inhibitor it increases to 39 ± 6.5°C (see Fig. 59 C see Table 11). hAAC3 appeared to be more stable in 0.005% MNG-3 (see Fig. 59 C and D and Table 11). T_m value without inhibitor is approximately 31.6 ± 1.3°C, and around 57.8 ± 1.3°C in presence of CATR (see Fig. 59 D and Table 11).

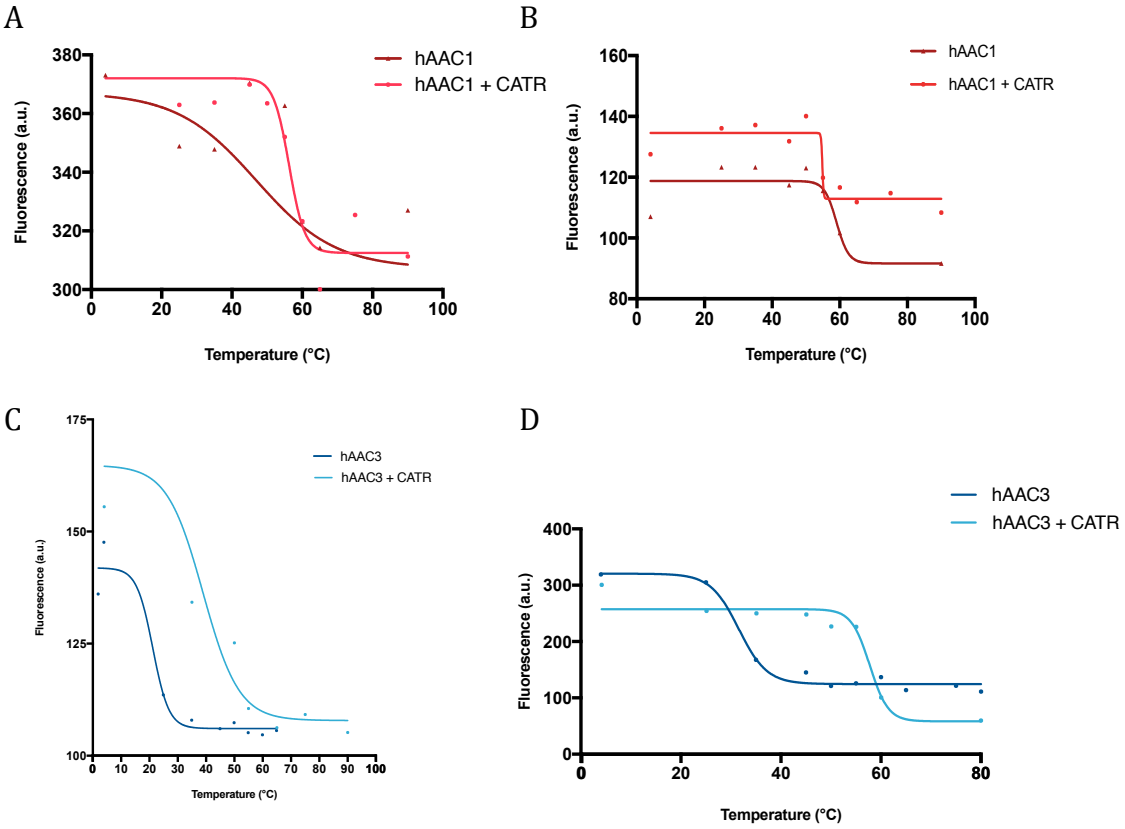

Figure 59 Thermo-denaturation assays performed using Fluorescence Size Exclusion Chromatography (FSEC) method (A) hAAC1 in 0.04% DDM with (pink line) and without 0.1 mM CATR inhibitor (dark red line); (B) hAAC1 in 0.005% MNG-3 without 0.1 mM CATR inhibitor (C) hAAC3 in 0.04% DDM with (light blue line) and without 0.1 mM CATR (dark blue line); (D) hAAC3 in 0.005% MNG-3 with (light blue line) and without 0.1 mM CATR (dark blue line) Measurements were carried out using BioRad Size Exclusion Chromatography system combined with fluorimeter using from 50 to 100 µg of hAAC1 or hAAC3. Fluorescence maxima from each SEC-run between 4°C to 90°C were applied on the plots. Thermal stability curves were generated and fitted using Boltzmann equation.

4.2.4.3 Thermal stability measurements performed using CPM dye

The stability properties of hAAC1 and hAAC3 were also investigated with the addition of specific fluorochrome, CPM dye (see Material and Methods, paragraph 3.5.3.1) that is supposed to bind upon protein unfolding to the available cysteins and provide the fluorescence signal. We performed the experiments on both isoforms in both detergents – DDM and MNG-3. T_m value of hAAC1 in MNG-3 detergent is approximately 48.7 ± 0.4°C while after incubation with inhibitor it surprisingly decreases to 33.8 ± 0.6°C (see Fig. 60 A and Table 11). T_m of hAAC3 in 0.04% DDM is around 36 ± 1.0°C and increases up to around 49 ± 1.2°C in presence of CATR (see Fig. 60 B and Table 11). Such behavior was also observed using FSEC (see Fig. 59 C and Table 11), nonetheless the T_m values are a bit different (see Fig. 59 C, 60 B and Table 11). When purified in 0.005% MNG-3 hAAC3 has a T_m value of 48 ± 0.6°C and seems to be slightly stabilized by CATR with a T_m that increases to 51 ± 0.5°C (see Fig. 60 C and Table 11).

A

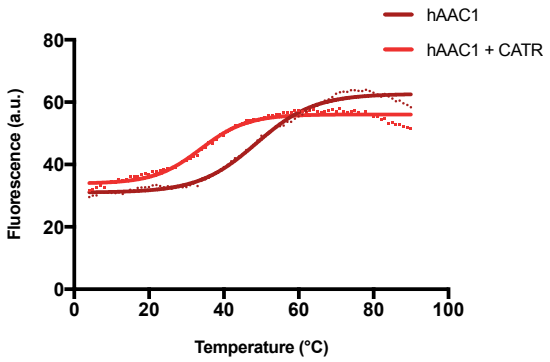

B

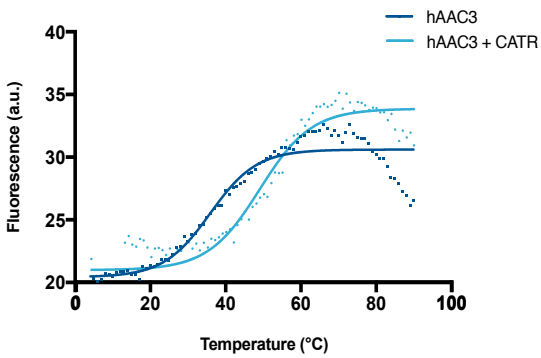

C

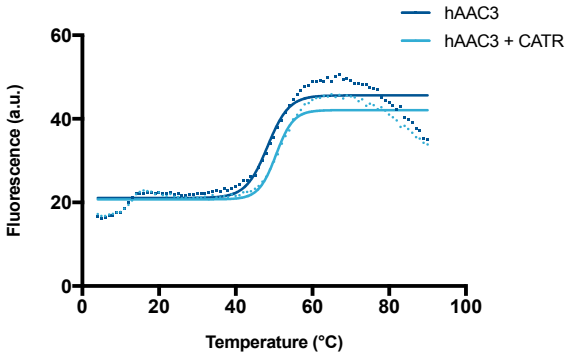

Figure 60 Thermo-denaturation assays performed using CPM dye. (A) hAAC3 in 0.04% DDM with (light blue line) and without 0.1 mM CATR (dark blue line); (B) hAAC3 in 0.01% MNG-3 with (light blue line) and without 0.1 mM CATR (dark blue line) Measurements were carried out in quartz cuvettes using Varian Cary Eclipse Fluorescence Spectrophotometer Protein amount used for the assays was ranging from 20 to 40 µg of hAAC3. Experiments were performed in temperature range between 4°C to 90°C Thermal stability curves were generated using Boltzmann equation.

Protein	Circular Dichroism (CD)				Fluorescence Size Exclusion Chromatography (FSEC)				TSA with CPM dye			
	MNG-3		DDM		MNG-3		DDM		MNG-3		DDM	
	- CATR	+ CATR	- CATR	+ CATR	- CATR	+ CATR	- CATR	+ CATR	- CATR	+ CATR	- CATR	+ CATR
T_m of hAAC1	57.6 ± 0.3°C	N/D	39.3 ± 2.9°C	55 ± 1.8°C	59 ± 2.4°C	54.9 ± 4.8°C	47 ± 8.2°C	57 ± 2.2°C	48.7 ± 0.4°C	33.8 ± 0.6°C	N/D	N/D
T_m of hAAC3	61.7 ± 0.6°C	66 ± 7.0°C	47.6 ± 10.3°C	55.5 ± 7.6°C	31.6 ± 1.3°C	57.8 ± 1.3°C	21.3 ± 15.7°C	39 ± 6.5°C	48 ± 0.6°C	51 ± 0.5°C	36 ± 1.0°C	49 ± 1.2°C

Table 11 Summary table of thermal stability data of hAAC1 and hAAC3 in 0.005% MNG-3 and 0.04% DDM with or without CATR inhibitor measured using three independent techniques: CD, FSEC and TSA using CPM dye.

4.2.5 hAAC1 and hAAC3 oligomerization state

Multi Angle Laser Light Scattering (MALLS) and analytical ultracentrifugation (AUC) experiments were performed in order to determine human AAC1 and hAAC3 oligomerization state in DDM and MNG-3 detergents.

4.2.5.1 SEC-MALLS analysis

The analysis of SEC-MALLS data for hAAC1 and hAAC3 in DDM and MNG-3 detergent showed very similar results that were actually difficult to interpret. In DDM detergent, one major peak is detected at A_{280} with an elution volume at 10,7 mL (Peak "LS" on Figure 61) and one major peak is detected by measuring the refractive index and light scattering and is eluted at 11.1 mL (Peak "UV" on Figure 61). In addition, a small shoulder was detected at 9.9 mL (Peak "Shoulder" on Fig. 61). For unclear reasons, there is a shift depending on the detection system. Performing further analysis we suppose that protein and detergent micelles are not well separated (see Fig. 61) and therefore the molecular weight of the protein and the quantity of bound detergent cannot be calculated. In order to improve the level of separation, a different column Superdex 75 10/300GL was tested, however the obtained results were very similar to the previous ones (data not shown).

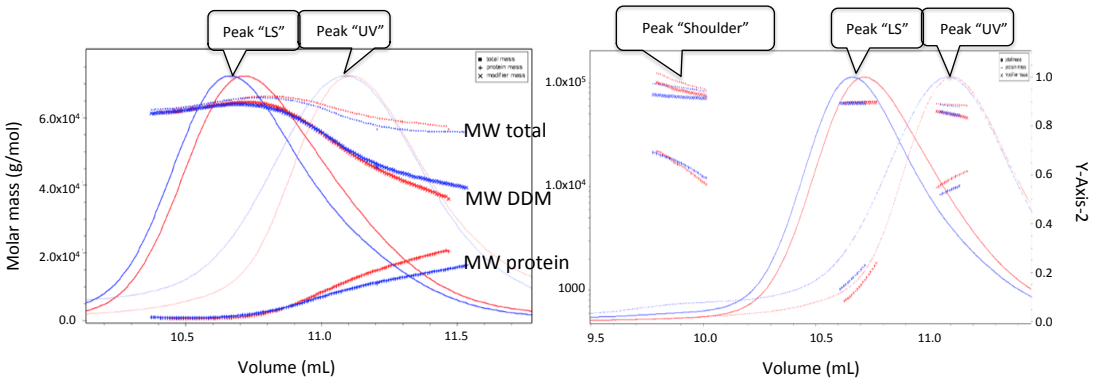

Figure 61 SEC-MALLS data analysis of molecular mass estimation for hAAC1 and hAAC3 in 0.04% DDM at 16 and 14.8 mg/mL respectively. Left panel represent the close up of the right panel. Red lines corresponds to data analysis of hAAC1, blue line corresponds to hAAC3. Style line descriptions are provided below the graph. Name of each peak is highlighted in the black frame. The molecular masses of protein-detergent complex (Mw total), the modifier (Mw DDM) and the protein (Mw prot) are given in the middle of the two graphs and correspond to the lines. Data analysis were performed on PAOL platform, IBS.

In MNG-3 detergent the results are very similar and show one main peak that is shifted depending on the detector (see Fig. 62). The maximum at A_{280} is at 15.1 mL and 15.3 mL for hAAC1 and hAAC3 respectively while for the refractive index and light scattering detection the maximum is at approximately 14.8 mL for both isoforms. The elution volumes are shifted to larger values compared to DDM (see Fig 62). The smaller shoulder is hardly detected for both proteins. Similarly like the results obtained in DDM detergent, data analysis of both of the isoforms in MNG-3 showed that protein and detergent micelles are not well separated (see Fig. 62) and thus calculation of MW of the protein in complex with detergent cannot be determined.

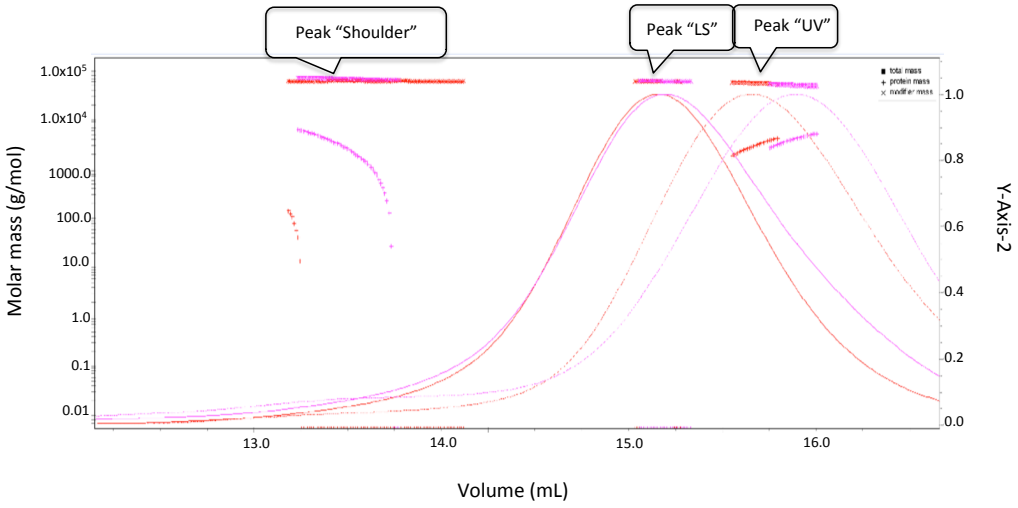

_ LS; -- UV; ▪▪▪ Mw total; +++ Mw protein; xxx Mw DDM; hAAC1; hAAC3

Figure 62 SEC-MALLS data analysis of molecular masses estimation for hAAC1 and hAAC3 in 0.005% MNG-3 at 6.7 and 7 mg/mL respectively. Red lines corresponds to data analysis of hAAC1, pink line corresponds to hAAC3. Style line descriptions are provided below the graph. Name of each peak is highlighted in the black frame. Abbreviations: protein-detergent complex (Mw total), the modifier (Mw DDM) and the protein (Mw protein). Data analysis were performed on PAOL platform, IBS.

4.2.5.2 AUC analysis

Since SEC-MALLS data analysis provided unclear data difficult to interpret in terms of protein oligomerization state, AUC analysis of both human isoforms in DDM detergent was performed. Our results showed that all samples exhibit one main peak at 1.96 +/- 0.11 S (s20w= 3.43 +/- 0.2S, with the partial specific volume of DDM) that corresponds to about 90% of the total signal in interference and 75% at 280 nm, interpreted as DDM micelles (published s20w= 3.12 S). The

values of extinction coefficient and concentration of detergent micelles were high reaching between 0.086 and 0.152 $(mg/mL)^{-1}cm^{-1}$, and between 14.2 and 22.7 mg/mL respectively. The minor peak at 3.03S +- 0.12 S (s_{20w}= 5.11 +/- 0.21S) would correspond to the hAAC-DDM complex (see Fig. 63). Considering a globular compact shape (f/fmin=1.25), this s-value correspond to 2.9 -/+ 0.3 or 0.5 -/+ 0.2 g/g of bound detergent, considering a monomer or a dimer, respectively.

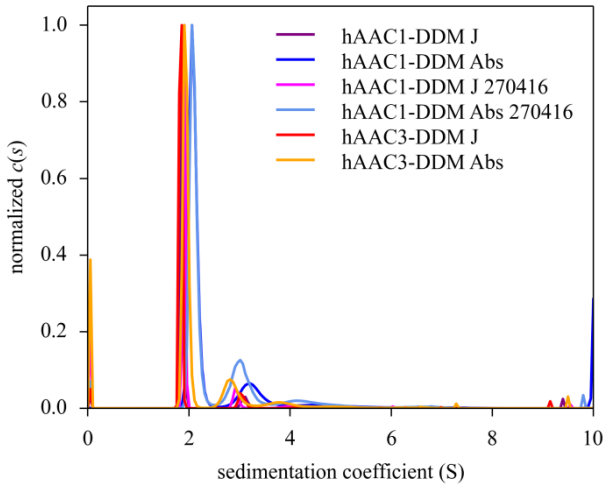

Figure 63 Sedimentation velocity (AUC) data analysis of hAAC1 and hAAC3 in 0.04% DDM at 10 or 19.2 and 25 mg/mL. Each curve is highlighted appropriately to the analyzed sample. Data analysis was performed on PAOL platform, IBS

4.2.6 Crystallisation trials on human AACs

Lipidic Cubic Phase (LCP) and vapour diffusion crystallization were the methods used for the crystallization trials. LCP method uses a membrane-mimetic matrix suitable for stabilization and crystallization of membrane proteins in lipid environment[207]. Vapour diffusion method is a common technique for protein crystallization widely used for soluble proteins.

Prior to the LCP trials, FRAP (Fluorescence Recovery After Photobleaching) experiments have been realized. Labelling of the protein with a dye gives an opportunity to observe if the protein is diffusing well into the lipidic phase (since only couple experiments were done using this technique, results are not presented in this study).

4.2.6.1 LCP crystallization

hAAC1 and hAAC3 have been subjected to crystallization trials in concentration ranging from 10 to 15 mg/mL in DDM and MNG-3. Only commercial screens (96 well-plates) have been used for crystallization. We obtained one interesting result from hAAC3 in DDM detergent at a concentration of 9.6 mg/mL from the MemFac/JBScreen plate. The crystal appeared between 20-28 day after setting crystallization plate and had a size of approximately 50 µm (see Fig. 64A), while after 35 days had already around 200 µm (see Fig. 64B). Morover, the crystal was also visible under UV light (see Fig. 64B). The precipitant conditions were the following: 0.1M Ammonium sulphate, 0.1M HEPES pH 7.5 and 30% PEG400 (see Fig.64A-C).

A B

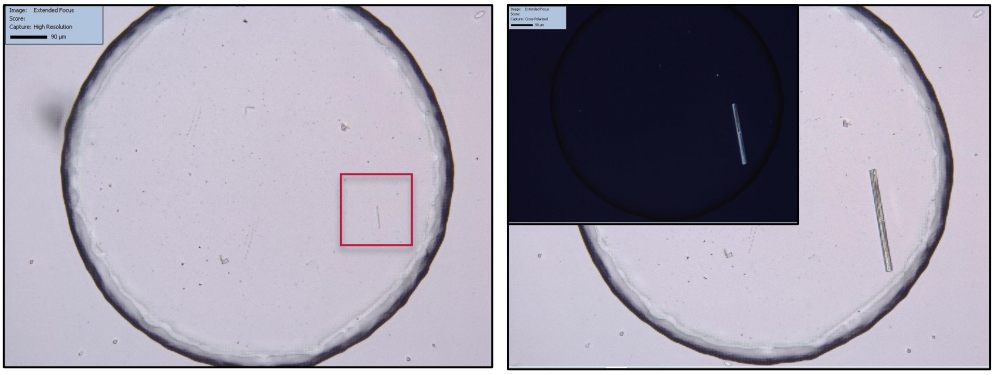

C

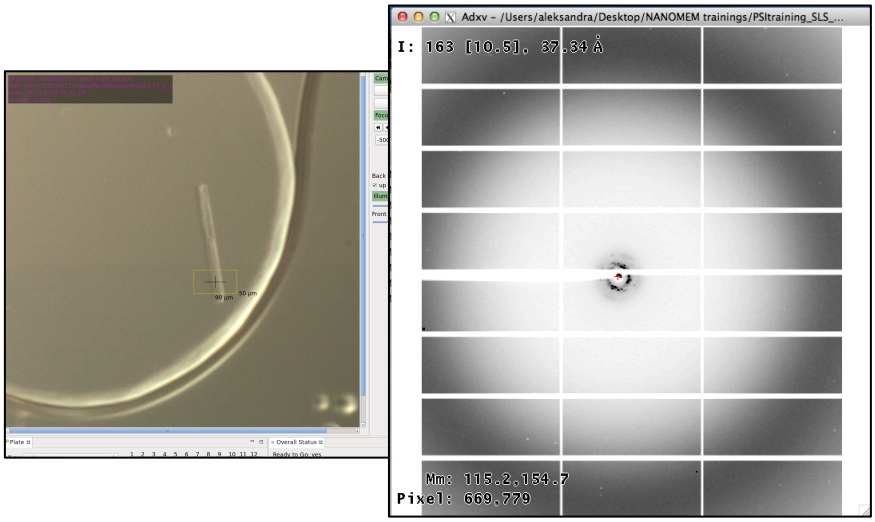

Figure 64 LCP crystallization of hAAC3 in DDM detergent in the MemFac/JBScreen (C1 drop) – A) under visible light - crystal after 28 days (red frame), B) under visible light - crystal after 35 days and in the left up corner crystal under UV light, C) left panel - crystal in visible light before testing it at the synchrotron – SLS, PXIII beamline (Villingen, Switzerland) and right panel – diffraction pattern of the crystal – zoom on the image center, best spot approx. at 37 Å resolution. The plate was set up on the High Throughput membrane crystallization platform (IBS).

The crystal was tested in Villingen (Switzerland) on SLS, PXIII beamline directly in the LCP plate. Diffraction spots were observed at 37Å resolution, however the noise at the center of the diffraction pattern made the data interpretation difficult. In order to obtain better X-ray diffraction resolution, further optimization trials were conducted, nonetheless no crystal was obtained.

4.2.6.2 Vapour diffusion (sitting drop) crystallization

Many crystallization plates were set up for both human isoforms: hAAC1 in DDM (at a concentration of 10 mg/mL) and hAAC3 in DDM and MNG3 (at a concentration from 6 to 18 mg/mL). One interesting result was obtained for hAAC3 in MNG3 detergent at 6 mg/mL (see Fig. 65) from PACT_qiagen plate. Two crystals were obtained of approximately 50 µm and 30 µm size (see Fig. 65) and they were also visible under the UV light. The crystals was harvested and tested on the ESRF but it did not show any diffraction.

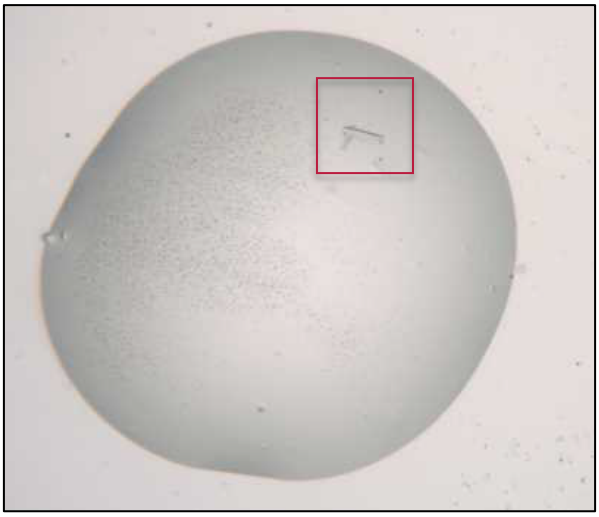

Figure 65 Crystal of hAAC3 at 6 mg/mL in 0.01% MNG3 detergent obtained from crystallization plate PACT_qiagen – H8 drop. The plate was set up on the HTX platform (EMBL).

The analysis of crystallization plates (LCP and vapour diffusion) brought the limited sets of outcomes that can be clearly identified by eye from images. Many identified crystallization drops included clear drops, phase separation, precipitate, skin formation, possible crystals, and junk. In LCP and vapour diffusion plates most of the drops were clear or contained precipitate, sporadically phase-separation was observed. Clear drops provided information

about undersaturated conditions that could have been distinguished from metastable ones where for instance phase separation or crystal was obtained. Precipitation was observed in the drops in two forms: bad (typically amorphous) and good (microcrystalline). Crystalline precipitation was patterned and had sandy appearance, which indicates that the protein was in the chemical environment that permits the native conformation to remain intact and therefore those conditions could possibly lead to crystals formation.

4.2.7 Discussion and conclusions

Human ADP/ATP carriers play an essential role in the cell metabolism by providing the energy source for many critical processes. Obtaining three-dimensional structures of bovine[77] and yeast[83] AACs significantly improved the understanding of protein properties and function. However, more detailed studies that could answer some questions regarding the different conformational states adopted during the transport mechanism and the biochemical and biophysical protein properties would be extremely valuable. In order to answer some of them we investigated in greater detail two out of four human ADP/ATP isoforms – hAAC1 and hAAC3. It was previously reported that human AACs (hAAC1, 2 and 3) can be expressed and remain functional in yeast system[208,136]. Moreover, hAAC1 fused to the MBP at the N-terminus was expressed in *E. coli* system and also proved to be functional[122]. Here, for the first time we present that full-length human AAC1 and 3 isoforms are successfully expressed in sufficient quantities in the cell-free system (see Fig. 54) and that both of them exist in a well-folded form (see Fig. 57A and B). N-termini His-tagged hAAC1 and hAAC3 were expressed in presence of 0.5% Brij35 (see Fig. 54) and purified in 0.04% DDM and 0.005% MNG-3 detergents. Data analysis from His-tagged affinity chromatography showed that for both human AAC isoforms the proteins are slightly purer in MNG-3 detergent than in DDM (see Fig. 55A and C, E and G). Performing classical size exclusion chromatography enabled us to estimate the oligomerization state of both proteins (see Fig. 55B, D, F, H). While purifying hAAC1 and hAAC3 in 0.04% DDM detergent the estimated molecular masses of the protein-detergent complexes are approximately 88 and 91 kDa respectively

while in 0.005% MNG-3, 102 and 112 kDa respectively, suggesting that both isoforms exist as a monomer (see Fig 56). Since SEC is not a fully precise technique to determine protein oligomerization state, SEC-MALLS and sedimentation velocity (AUC) experiments were performed. SEC-MALLS data analysis showed that for both proteins and in both detergents the elution volume of the main peak depends on the detection system (see Fig. 61 and 62). Hence, data interpretation of those results occurred to be not really clear and therefore the molecular mass estimation for hAAC1 and hAAC3 was not possible. We assumed, that hAAC1 and hAAC3 (MW of around 32 kDa) presumably co-eluted with free detergent micelles. We carried out sedimentation velocity (AUC) experiments in DDM detergent to confirm our initial findings. It was shown that the protein sample mainly consists in monomers (see Fig. 63). It is worth mentioning that bovine AAC high-resolution 3D structure[77] revealed that the carrier is structurally a monomer and this brought the idea that the protein might function in the same oligomerization state (c-state) as well[81,103]. Furthermore the analysis performed by AUC showed that the bovine AAC1 solubilized in LAPAO detergent (3-laurylamido-N,N'-dimethylpropylaminoxide) is a monomer whereas in Triton X-100 and reduced Triton X-100 (hydrogenated Triton X-100), higher molecular mass species can also be identified[117]. Additionally, numerous studies were also performed on the yeast AAC and based on differential tagging[118] and molecular mass determination of the protein in detergent environment[119] it was concluded that the yeast carrier is functionally a monomer.

Regarding the protein folding, CD assays proved that both hAAC1 and hAAC3 exhibit typical α-helical folding in MNG-3 and DDM detergent (see Fig. 57A and B). hAAC3 seems better folded than hAAC1 in both tested detergents (see Fig. 57A and B).

Since thermal stability of the protein is a very important criterium for crystallization, many thermo-denaturation trials were performed using three independent methods: CD, FSEC and TSA using CPM dye fluorescence. Data analysis provided a positive sign suggesting that the protein is still able to bind CATR and be stabilized by it as shown for bAAC1 (see Fig. 58 A, C, D; Fig. 59 A-D; Fig. 60 A-C and Table 11).

Protein	Circular Dichroism (CD)				Fluorescence Size Exclusion Chromatography (FSEC)				TSA with CPM dye			
	MNG-3		DDM		MNG-3		DDM		MNG-3		DDM	
	- CATR	+ CATR	- CATR	+ CATR	- CATR	+ CATR	- CATR	+ CATR	- CATR	+ CATR	- CATR	+ CATR
T_m of hAAC1	57.6 ± 0.3°C	N/D	39.3 ± 2.9°C	55 ± 1.8°C	59 ± 2.4°C	54.9 ± 4.8°C	47 ± 8.2°C	57 ± 2.2°C	48.7 ± 0.4°C	33.8 ± 0.6°C	N/D	N/D
T_m of hAAC3	61.7 ± 0.6°C	66 ± 7.0°C	47.6 ± 10.3°C	55.5 ± 7.6°C	31.6 ± 1.3°C	57.8 ± 1.3°C	21.3 ± 15.7°C	39 ± 6.5°C	48 ± 0.6°C	51 ± 0.5°C	36 ± 1.0°C	49 ± 1.2°C

Table 11 Summary table of thermal stability data of hAAC1 and hAAC3 in 0.005% MNG-3 and 0.04% DDM with or without CATR inhibitor measured using three independent techniques: CD, FSEC and TSA using CPM dye.

For hAAC1, the T_m values measured by CD or FSEC are quite similar. The protein seems to be more stable in MNG-3 detergent than in DDM (see Table 11) and interestingly this was already seen for other membrane proteins[209,210] However, surprisingly in MNG-3 detergent CATR inhibitor does not stabilize the protein, since the T_m value decreases (see Table 11). For hAAC3 the T_m values are more variable depending on the method used for the measurement, but in each case an increase is observed when adding CATR (see Table 11). Surprisingly, using FSEC method, in MNG3 the T_m is almost 30°C higher in presence of CATR. However, when measured using CD or CPM assay, T_m of hAAC3 exhibits only 4.3°C and 3°C temperature difference respectively in presence or without inhibitor (see Table 11). Considering hAAC3 in 0.04% DDM, T_m values measured using FSEC and CPM fluorescence are differing but the temperature difference with and without inhibitor is around 17°C and 13°C respectively. Moreover, T_m value of hAAC3 in DDM measured by FSEC is surprisingly low, only 21.3 ± 15.7°C, nonetheless it increases after adding the inhibitor (see Table 11). The differences in T_m values measured by different methods might come from different sample quality and additionally from differences between each instrument. The influence of bongkrekic acid (BA) on thermal stability of the proteins was not yet investigated.

Crystallization trials were regularly set up along the project but did not provide any significant result. It is worth highlighting that the MNG-3 and DDM concentration used for protein purification was 5x and 4x CMC respectively and hence final concentration of the detergent in the crystallization drops is considerably high. Therefore, lowering detergent concentration in the size

exclusion chromatography step would be reasonable since too high concentration of detergent in crystallization assays do not favor protein crystal growth. Biophysical data analysis (AUC) showed additionally that the protein most probably is in the monomeric state, however since the results indicated also the presence of the dimers in the sample, thus presumably protein is not homogenous enough to crystallize. Moreover, more crystallization trials should be performed in presence of CATR inhibitor considering the stabilizing effect measured by thermal stability assays.

The availability of full-length hAAC1 and hAAC3 in a purified, detergent-solubilized form opens the perspective for biochemical *in vitro* functional and structural studies of those essential proteins.

4.3 **Part III** - Non-mitochondrial ADP/ATP transporters: plant plasma membrane ADP/ATP Carrier (PM_AAC)

In an effort to search for a good candidate for structural studies of AACs, we considered also non-mitochondrial membrane transporters. Indeed, some of the ADP/ATP carriers from the MCF family are found elsewhere than in the inner mitochondrial membrane. One carrier is for example found in the plant plasma membrane. The protein, named PM_AAC is assumed to export ATP outside the plant plasma membrane but its function is not still fully established. The *Arabidopsis thaliana* PM_AAC shares around 48% sequence similarity with the *A. thaliana* mitochondrial AAC1 isoform found in the inner mitochondrial membrane[61]. Here, we present preliminary results of PM_AAC expression, purification and characterization.

4.3.1 PM_AAC is successfully expressed in bacterial system

Plant plasma membrane protein was subcloned into pET11_LIC_SUMOtag vector with an N-terminal His-tag and SUMO-tag and successfully expressed in *E. coli* cells. Four different strains were tested in order to find the best level of expression (see Fig 66). PM_AAC molecular weight is approximately 33 kDa but the protein possesses N-terminal fusion SUMO-tag that is around 12 kDa, thus the complete molecular weight is approximately 45 kDa.

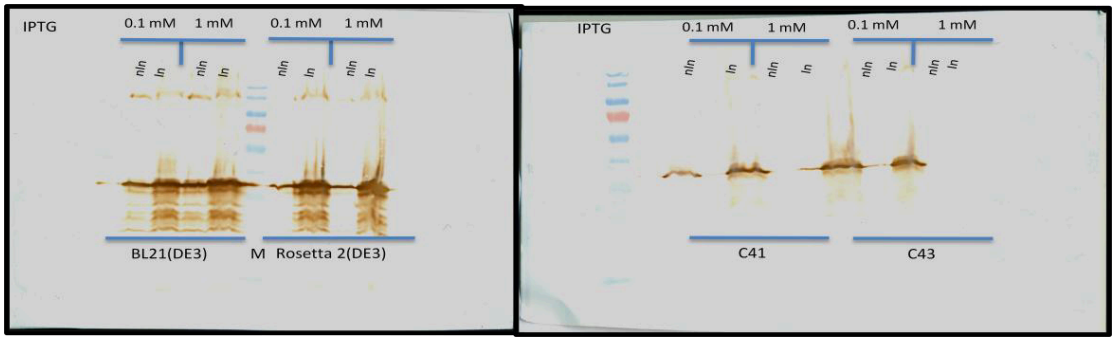

Figure 66 Investigation of PM_AAC expression levels in different *E.coli* cells - BL21(DE3), Rosetta 2(DE3), C41(DE3) and C43(DE3). Cells were grown at 37°C until OD reached approximately 0.7 and later were induced using two IPTG concentrations: 0.1mM or 1 mM at 20°C and over-night. Not-induced cells (NIN) and induced cells (IN) were loaded on SDS PAGE and analyzed on Western Blot using α-antiHis antibodies.

Based on Western Blot analysis, the best result was obtained using Rosetta 2(DE3) cells with an induction at 0.1 mM IPTG (see Fig 66 left panel) and hence, further protein expression was performed using this particular cell line.

4.3.2 PM_AAC solubilisation and purification in detergent

After expression trials, detergent solubilization tests were performed (see Material and Methods, paragraph 3.4.4) (see Fig. 67).

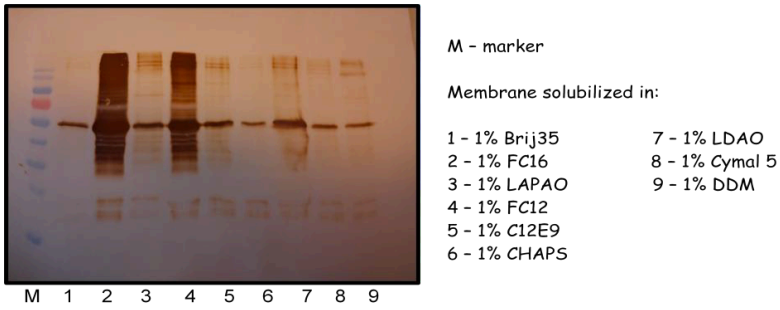

Figure 67 Solubilization tests. Cell membranes enriched with the protein of interest (PM_AAC) were solubilized in nine different detergents (indicated on the right) in order to determine the best candidate for the protein solubilization. Membrane solubilization was conducted during 1h and at 4°C. After ultracentrifugation at 50 000 rpm during 1 h and at 4°C), 10 µL of supernatant was loaded on SDS-PAGE and further using Western Blot the signal was detected with α-antiHis antibodies.

It seems that the solubilization of PM_AAC is the most efficient in foscholine detergent, LAPAO, C12E9 and LDAO. The N-terminal His- and SUMO-tag allowed us to obtain pure PM_AAC using a single affinity-purification step starting from *E. coli* membrane solubilization in LAPAO. During the purification procedure, while performing washing steps, 1% LAPAO was subsequently exchanged in different detergents such as: LAPAO, DDM, C12E9, FC12, C12E9, LDAO, Cymal 5. However, the proteins purity was the best in LAPAO (see Fig. 68).

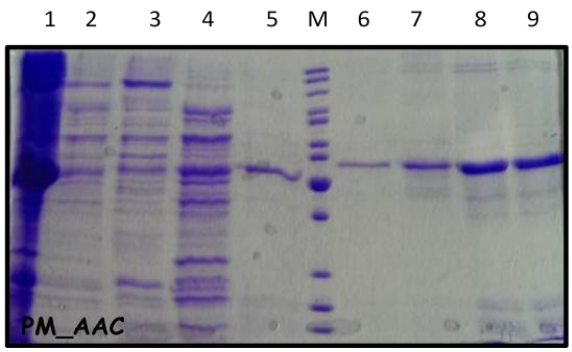

Figure 68 SDS PAGE analysis (Coomassie staining) of the NiNTA affinity chromatography of PM_AAC in 0.1% LAPAO; 1–membrane fraction, 2-supernatant after solubilization, 3-flow through, 4-wash 1 with 50 mM imidazole, 5-wash 2 with 100 mM imidazole, 6-9: elutions from 1 to 4 with 300 mM imidazole, M – MW markers. The MW of PM_AAC is around 45 kDa (with SUMO-tag).

Following NiNTA chromatography, the protein was subjected to Size Exclusion Chromatography (Fig. 69). Using LAPAO detergent two main peaks can be observed: the first elutes in the column void volume and corresponds to aggregates and the second (with a small shoulder) contains the protein of interest. PM_AAC eluted with an apparent molecular mass of about 178 kDa in 0.1% LAPAO (see Results, Part II - Human ADP/ATP carriers production, characterization and crystallization, paragraph 4.2.2, Fig 56). LAPAO detergent micelle is approximately in a range of 38 to 45 kDa), hence, if the MW of PM_AAC is approximately 45 kDa (with an N-terminal SUMO-tag), one can infer that the size of LAPAO micelle containing PM_AAC monomer would be around 83-90 kDa. Therefore, since the apparent mass MW of PM_AAC-detergent complex in LAPAO assessed by gel-filtration is approximately 178 kDa, this would suggest an oligomeric arrangement of the protein, presumably a dimer. Small shoulder that is eluting just after the main peak (see Fig. 69) could contain however smaller oligomeric species. The elution fractions corresponding to the main peak on Figure 69 were pooled together and taken for crystallization trials.

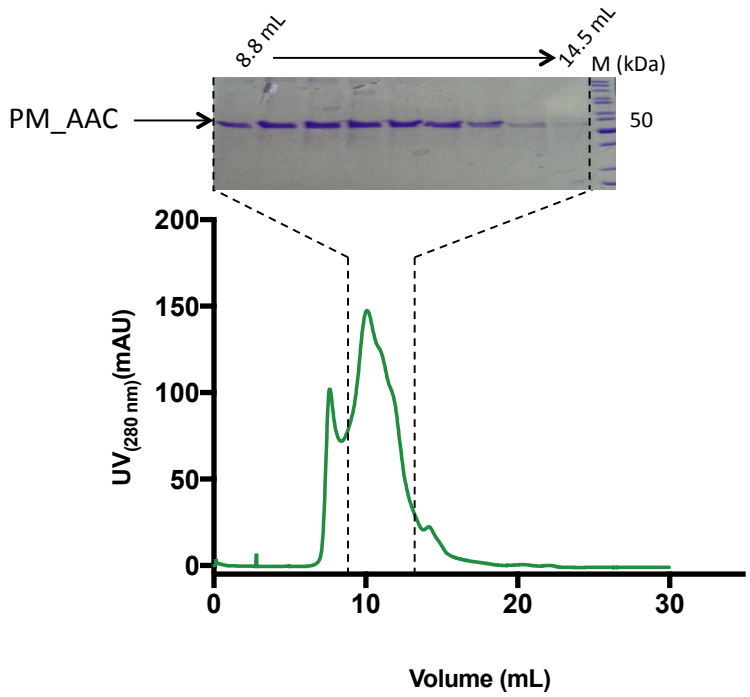

Figure 69 Size Exclusion Chromatography of PM_AAC was performed in 50mM Hepes pH 7.5, 200 mM NaCl and 0.1% LAPAO. SDS-PAGE analysis of the collected fractions is shown above the chromatographic profile. Elution volume of PM_AAC is 10.3 mL The region with a peak eluting before the main peak of proteins of interest corresponds to protein aggregates.

4.3.3 PM_AAC characterization

4.3.3.1 Functional studies

PM_AAC activity was measured directly in *E. coli* cells expressing the protein using [α-^{32}P]-ATP. Following the same procedure as for hAACs functional studies, PM_MBP_pET20b construct was tested as a first one, but plant Plasma Membrane AAC remained inactive. Afterwards, different constructs were investigated as well as different cell-growing conditions, however protein activity was still not detected (see Fig. 70).

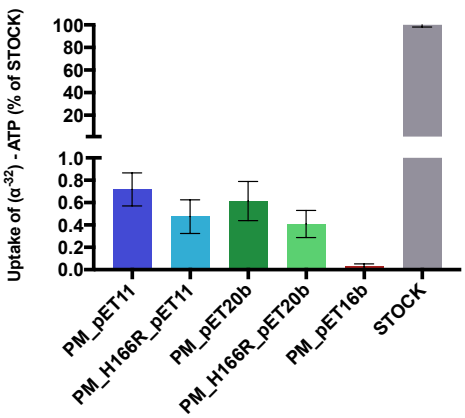

Figure 70 PM_AAC functional studies. [α-^{32}P]-ATP uptake of *E. coli* cells expressing PM_AAC in different vectors: pET11, pET20b and pET16 and mutated PM_AAC in pET11 and in pET20b at position 116 were measured in presence of 10 µM labeled ATP and. The measurements were performed in triplicates. The rate of the transport was set to 100% for STOCK. The values for the control nucleotide uptake (empty vector) were subtracted. Data analysis were performed in Prism GraphPad software.

While all human AAC isoforms seems to be functionally expressed, plasma membrane protein does not show significant activity while it is possible to obtain very good yield of purified protein. This lack of activity could be due to various issues; one explanation could be the difference in the sequence of this protein compared which human isoforms in strategic points. For instance salt bridges which are present and highly conserved in human proteins in the characteristic motif - PX(D/E)XX(K/R) are not strictly preserved in plant homolog: in the second motif an histidine replaces an arginine PX(D/E)XX(K/R/H). This can suggest that the protein might be sensitive to pH. However, further functional experiments performed at different pHs (5.5 - 6.5, pKa of His - 6.5) and mutation of some strategic residues in salt bridges region (H166K and H166R) did not show any protein activity (see Fig. 70).

4.3.3.2 Thermal stability assays

Thermal stability of PM_AAC protein was investigated using CPM fluorescence. The apparent T_m of PM_AAC was approximately 50.2 ± 0.4°C and this result was reproducible in many different experiments (see Fig. 71). The impact of CATR inhibitor on PM_AAC is still unknown and hence T_m of PM_AAC in presence of CATR was not investigated.

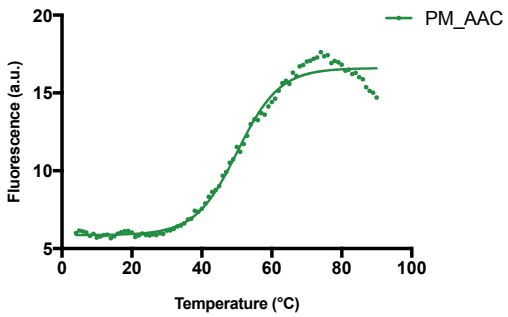

Figure 71 Thermo-denaturation assays performed using CPM dye of PM_AAC purified in 0.1% LAPAO. Measurements were carried out in quartz cuvettes using Varian Cary Eclipse Fluorescence Spectrophotometer. Protein amount used for the assays was 40 µg of hAAC3. Experiments were performed in temperature range between 4°C to 90°C Thermal stability curves were generated using Boltzmann equation.

4.3.3.3 Crystallization trials

Some crystallization tests of PM_AAC in 0.1% LAPAO were performed using LCP and vapour diffusion approaches and commercial screens with protein

concentration ranging from 2.7 mg/mL to 15 mg/mL, however no significant results were obtained (see Fig. 72).

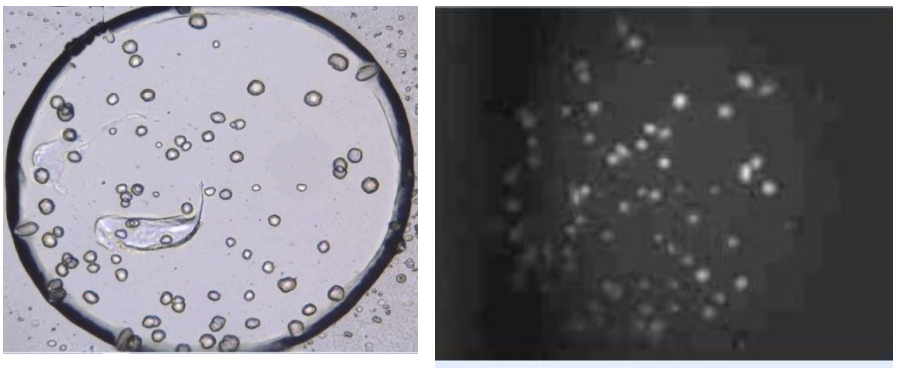

Figure 72 Example of LCP crystallization drop with 2.7 mg/ mL PM_AAC in 0.1% LAPAO (QCPI plate/C1 drop – 0.6 M Na/K phosphate pH5.8). Small round balls can be observed under visible light (left picture) and under UV light (right picture) and thus it might suggest that it could be protein (aggregation?).

There were a lot of divergent crystallization conditions in which the drops were rather with predominance of precipitant. Only in couple of them clear drops were obtained and in a few the formation of small round objects was detected that presumably could have been the protein (see Fig. 72).

4.3.4 Discussion and conclusions

Non-mitochondrial ADP/ATP transporter that was discovered in plant plasma membrane (PM_AAC) was successfully expressed in *E. coli* cells (see Fig. 66). In further purification steps it occurred to be solubilized in many different detergents (see Fig. 67), nonetheless, LAPAO detergent was the best in terms of protein purity and final protein yield (Fig. 68 and 69). Size exclusion chromatography profile exhibited a main peak that corresponds to the protein of interest. However the peak is not symmetric suggesting that the sample is not homogenous and may contain different species (see Fig. 69). Performing classical size exclusion chromatography enabled us to estimate the oligomerization state of the protein. While purifying PM_AAC in 0.1% LAPAO detergent the estimated molecular mass of the protein-detergent complex is approximately 178 kDa, suggesting that PM_AAC exists as a dimer (main peak) with smaller oligomeric species in the shoulder eluting just after (see Fig 69). It is however worth mentioning that oligomerization state determination by Size Exclusion Chromatography is not the most precise method, hence more accurate

techniques such as SEC-MALLS or AUC would be more reliable. Additional thermal stability tests proved that PM_AAC is relatively stable in 0.1% LAPAO and its T_m value is approximately 48°C (see Fig. 71). Preliminary crystallization trials did not provide so far any compelling results (see Fig. 72).

In terms of protein functionality, interestingly, our results seem to be opposite to the ones already published that demonstrate full-length PM_AAC protein activity[61]. Much has been done and many different protein constructs were tested, however we could not detect any protein activity (see Fig. 70). Additionally, introducing different protein mutations and changing pH of the environment did not give any improvement. Hence, it remains still unclear what could be the main reason of PM_AAC inactivity.

Finally, since PM_AAC was not showing any activity, we decided to focus only on human AAC isoforms.

4.4 **Part IV** - Different protein crystallization methods for developing serial nano- and micro-crystallography techniques

The project is conducted in collaboration with Manfred Burghammer and Anastasya Shilova from ESRF. My role in the project considered providing all the protein samples for the experiments, growing and optimizing protein crystals and subsequently testing different techniques of sample mounting. In each conducted beamline experiment I was helping in data collection and analysis.

Measurements of protein crystals at room temperature, directly in crystallization plates or on other specially designed supports, enable to investigate samples, which are hardly crystallizing to the required size (thus cannot be fished and measured in classical way) or are very fragile and sensitive. Moreover, performing diffraction measurements at room temperature may give additional insight into protein structure in terms of its flexibility. Our main goal in this project was to find the most suitable methods for crystallization of membrane proteins in which we could reduce the risk of crystal damage during sample preparation but also calibrate exposure and radiation damage during analysis on the beamline.

Different methods for crystals growth were tested. Based on the vapour diffusion technique, silicone nitride membranes and Crystal Direct (CD) plates were investigated for all proteins considered in this project. Crystallization trials for lysozyme, thaumatine, GLIC, 5-HT3 serotonin receptor and AcrB were set up according to the conditions described in Materials and Methods (see paragraph 3.8.1 and 3.8.2). All diffraction experiments were conducted at room temperature.

All measurements described here were performed on the microfocus branch of the ESRF ID13 beamline, which delivers $2*10^{11}$ photons/sec in a micro-beam of 1 μm diameter/cross section. Diffraction patterns were recorded with a 2-D detector (Eiger 4M). Data were processed using Crystfel[211] and NanoPeakCell[199] softwares.

4.4.1 Crystallization of lysozyme and thaumatine

Lysozyme and thaumatine are soluble proteins (14 and 22 kDa respectively) that are commonly used as test proteins for crystallization and crystallography experiments since they crystallize very easily and in a short time.

Both of those proteins were used as controls during our experiments and measurements. Crystallization of lysozyme was performed using CD plates and silicone nitride membranes, however surprisingly, crystals grew only on CD plates. Sample measurements were conducted directly in the plates after removal of the precipitant (using special tool that absorbs the liquid) or in presence of the precipitant in order to analyse if this parameter could impact the resolution. Datasets were recorded with diffraction up to 1.8 and 1.9Å resolution respectively (see Table 12), showing equivalent resolution for those two approaches. Thaumatine crystallization assays were so far only performed in CD plates from which we obtained a dataset of 1.9 Å maximal resolution (see Table 12).

4.4.2 Crystallization of 5-HT3 serotonin receptor

The serotonin-gated 5-HT3 receptor belongs to the family of pentameric neurotransmitter-gated ion channels that are termed Cys-loop receptors. This membrane protein is a target for drugs that relieve some post-chemotherapy and post-operative nausea or vomiting effects and also have an influence on curing various psychiatric disorders. 5-HT3 serotonin receptor is bullet-shaped and contains five subunits. Subunits are arranged symmetrically in the membrane around an axis that coincides with the ion pathway while a central ion pathway is perpendicular to the membrane plane. The structure of the mouse 5-HT3 receptor has been solved in presence of llama-derived single chain antibodies (nanobody, VHH15) at 3.5 Å resolution. Five VHH15 nanobodies bind radially to the interface between subunits at the level of serotonin binding sites (see Fig. 73a-c)[195].

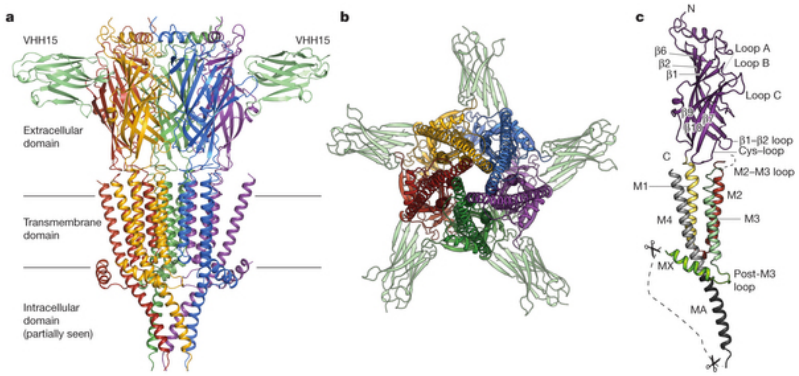

Figure 73 Crystal structure of mouse 5-HT3 serotonin receptor. (a) Cartoon representation of m5-HT3 receptor seen parallel to the plane of the membrane. Only two out of five VHH15 molecules are shown (pale green), (b) Top view on the complex, perpendicular to the membrane, (c) A single subunit of the 5-HT3 receptor is viewed parallel to the plane of the membrane. The large fragment (extracellular domain, first three transmembrane helices, post-M3 and MX) is in color, small fragments - helices MA and M4 - are in greyscale. The segment removed by proteolysis is indicated as a dashed line. Secondary structure elements and important loops are noted[195].

After some attempts, first crystals of 5-HT3 serotonin receptor were obtained on silicone nitride membranes exhibiting different sizes (see Fig. 74A and B). Subsequently, crystals were tested on the beamline (see Fig. 75A-C).

A B

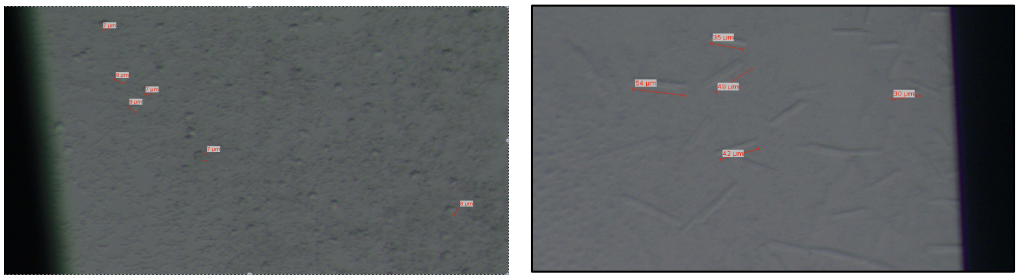

Figure 74 Examples of mouse 5-HT3 serotonin receptor crystals obtained on (A) small size membranes (conditions: 21% PEG 10K, 0.1 M Na_2SO_4, 0.1M Tris pH 8.5, 12°C; membrane size: 2x2 mm ; membrane thickness: 200 nm ; cubic microcrystals (7 - 9 µm) and (B) medium size membranes (conditions: 20% PEG 10K, 0.1 M Na_2SO_4, 0.1M Tris pH 8.5, 12°C ; membrane size : 2.5x2.5mm ; membrane thickness: 1000 nm, crystals (20 - 70 µm)) mounted with classical tape on glass coverslip.

A

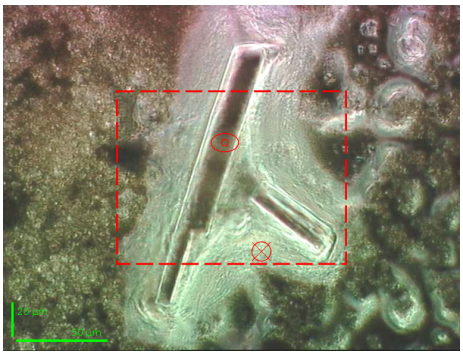

B C

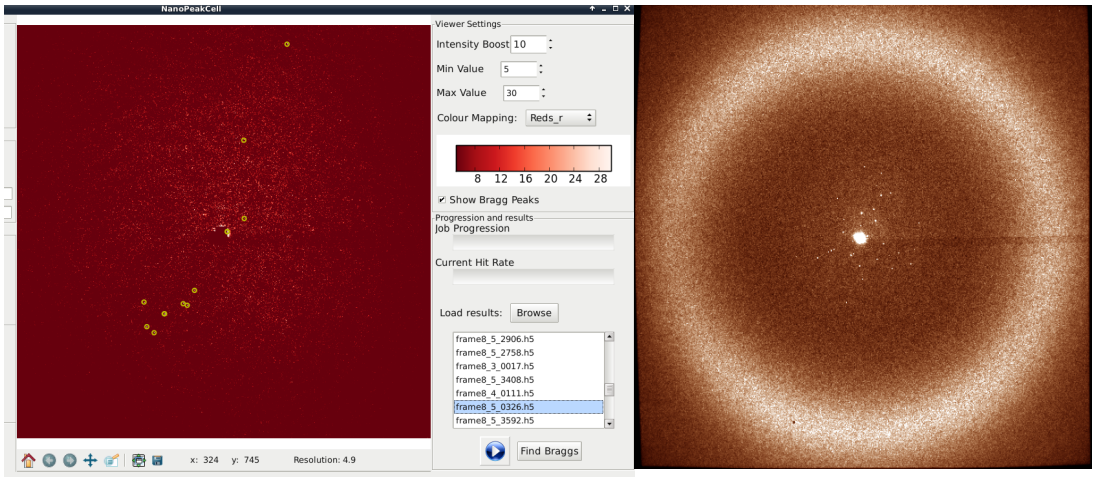

Figure 75 An example of the diffraction pattern of mouse 5-HT3 serotonin receptor crystal. (A) Crystal of mouse 5-HT3 receptor grown on silicone nitride membrane and seen under the beamline microscope. (B) Data analysis from the Nanopeakcell (left panel) and diffraction pattern of the protein (right panel).

We collected more than 100'000 images of which less than 1'000 were classified as hits using the Nanopeakcell program, giving an average hit rate of 0.8%. Microcrystals obtained on the nitride membranes did not give any diffraction pattern but for the larger crystals we were able to collect some data and eventually the best hit recovered was diffracting at 4.9 Å resolution (see Fig. 75C and Table 12). Nevertheless, results were not sufficient to solve the structure of the serotonin receptor. Further method optimization will be required to obtain crystals of better quality.

We tested also crystal growth in CD plates, however only small needle-shaped crystals were obtained, which in turn gave very weak diffraction.

4.4.3 Crystallization of the bacterial GLIC ion channel

We next turned our efforts to another protein of the family of the 5-HT3 receptor. This protein called GLIC[194] is also a pentameric ligand-gated ion channel, but a bacterial one. Its structure has been solved at 2.4 Å resolution (see Fig. 76A). We reasoned that this ability to form crystals of better quality than the 5-HT3 receptor for classical experiments might be transfered in the framework of our micro-crystallography trials.

Crystallization assays were performed using CD plates (see Fig. 76B). It occurred that crystals of GLIC protein are large enough, stable and of high quality, hence they fulfilled all the expectations in order to be a favourable testing material.

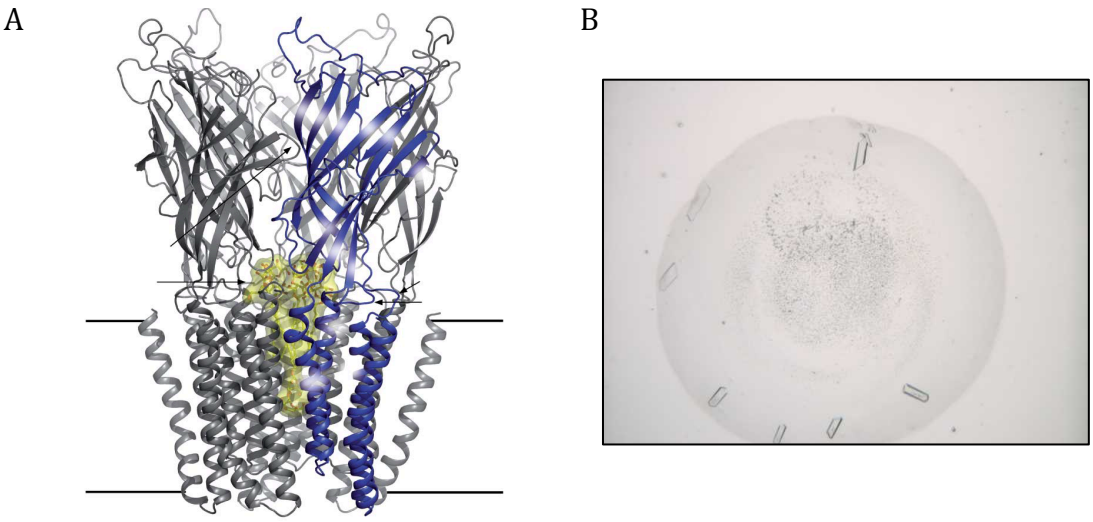

Figure 76 GLIC protein (A) Structure of GLIC protein at 2.4 Å resolution in ribbon representation viewed from the membrane plane. The molecules of DDM are bound inside protein channel (depicted as yellow sticks and van der Waals surface). Horizontal lines represent the membrane borders[194]. (B) An image of cuboid-shaped crystals of GLIC grown on Crystal Direct Plates.

Eventually, the best dataset (using softwares mentioned above) presented a 3.9 Å maximal resolution (see Table 12) and yielded an electron density map equivalent to the maps derived from the original datasets recorded in cryo conditions[194]. The maps show clearly the positions of the helices (unchanged compared to the structure at cryo temperature)(see Fig. 77A and B).

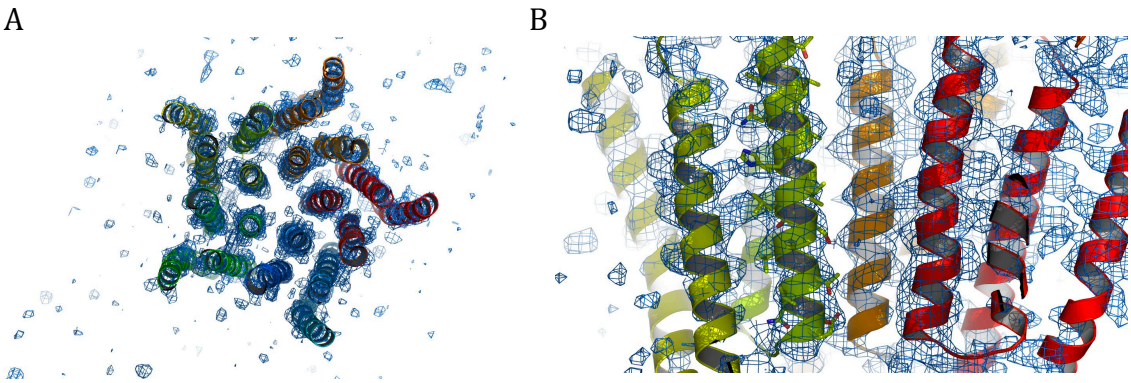

Figure 77. Electron density maps derived from serial microcrystallography diffraction of GLIC with top (A) and side view (B).

4.4.4 Crystallization of the bacterial Multidrug Efflux Transporter - AcrB

The Bacterial Multidrug Efflux Transporter AcrB is a drug efflux protein complex, which possesses broad substrate specificity and uses the proton motive force to export different compounds. There are many publications reporting AcrB protein structures like for instance AcrB structure without ligands[193] that was obtained at 3.5 Å resolution (see Fig. 78A); in complex with a designed ankyrin-repeat protein (DARPin) inhibitor at 2.5 Å resolution[212] and structure of AcrB in complex with deoxycholate at 3.85 Å resolution[213].

AcrB protein was tested in different crystallization conditions in order to determine the best one for obtaining small-sized crystals of maximum 15 µm as described in Materials and Methods (see paragraph 3.8.1 and 3.8.2). Crystallization of AcrB protein was performed using silicone nitride membranes and CD plates, however the best results were obtained using the plates (see Fig. 78B). So far the best dataset presented a maximal resolution of 3.9 Å (see Table 12).

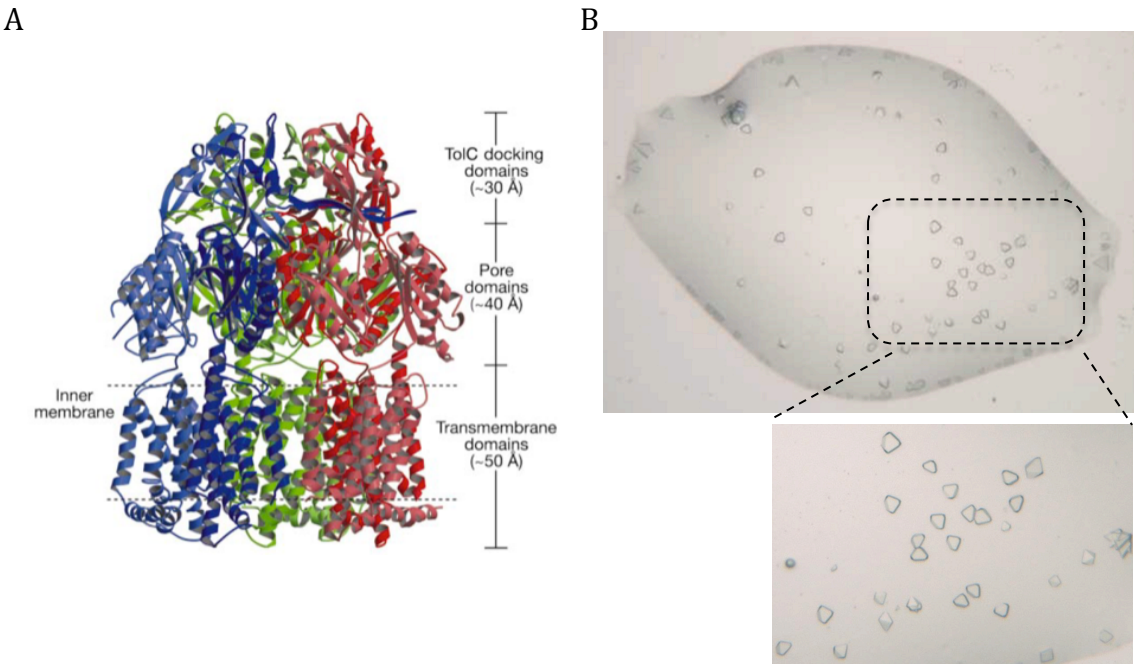

Figure 78 AcrB protein (A) Side view of AcrB structure in ribbon representation. Three subunits are individually colored in blue, green and red. Membrane border is marked with two horizontal lines. (B) Microcrystals of AcrB in the shape of small triangles that were obtained on Crystal Direct plates, close up of part of the drop is presented below the main image.

4.4.5 Discussion and conclusions

In classical approach, which is based on crystal fishing and cryo-frezzing, many issues have to be overcome in order to keep the sample in good conditions. In many cases however, proteins do not crystalize up to favourable and suitable size. Moreover, small and fragile crystals are much more difficult to manipulate with addition of their weak resistance on surrounding conditions. Therefore, introducing different *in situ* measurements could significantly improve samples mounting and measurements. Several new approaches have been proposed to overcome this problem like for instance flowing protein crystals across the path of an X-ray beam[214], using a liquid jet[215], using a lipidic cubic phase injector[200], ejecting crystals in droplets using acoustic waves[216] or using silicone nitride membranes[199] and Crystal Direct (CD) plates[197].

In this project we investigated the application of silicon nitride membranes and CD plates and we worked with proteins at both ends of the spectrum: very easy (lysozyme) and very hard (membrane proteins, including those which structure was solved less than 3 years ago). We managed to show

proof-of-concept results with small crystals with mentioned above adapted supports following beamline environment resulting in diffraction data.

So far, from all investigated proteins, all of them were crystallizing either on silicone nitride membranes or CD plates or both. The obtained resolution for all of tested samples was less than 5 Å, nonetheless majority of the best hits were gathered from CD plates (see Table 12). Beamline measurements of lysozyme that were performed with or without precipitant showed small improvement in the resolution without precipitant (see Table 12), however such a comparison was not yet tested on other protein samples. One bottleneck, which is difficult to overcome, is that upon liquid removal crystals may dry faster and subsequently the resolution will decrease.

Protein	Lysozyme with liquid	Lysozyme w/o liquid	Thaumatin	5-HT3 serotonin receptor	GLIC	AcrB
Crystallization method	CD Plates	CD plates	CD plates	Si_3N_4 Membrane	CD plates	CD plates
Wavelength	0.954	0.954	0.954	0.954	0.954	0.954
Beam size, µm²	2*2	2*2	2*2	2*2	2*2	2*2
Average crystal size, µm	15-18	15-18	10-30	7 – 9; 20 - 70	15-30	5 – 20 ; 30 - 100
Space group	P 4_32_12	P 4_32_12	N/D	N/D	C 121	N/D
Unit cell, Å	a=b=78.65, c=38.48; α=β=γ=90º	a=b=78.54, c=38.56; α=β=γ=90º	N/D	N/D	a=181.84, b=132.96, c=165.00; α=90º β=104.21º, γ=90º	N/D
Exposure time, ms	0.1	0.1	0.05	0.05-0.1	0.05	0.05
No. collected frames	257 040	257 040	?	?	1 360 000	?
Hit rate (NanoPeakCell), %	22.6	23.5	?	?	1	?
No. of indexed patterns (CrystFEL)	41 672	47 643	9123	607	10159	1500+...
Resolution range, Å	55.54-1.8	55.54-1.8	...-1.9	...-4.9	24.99-4.0	...-3.9
Completeness, %	100	100	100	N/D	45	?
Rsplit	8.66	7.92	23.15	N/D	27.81	?

Table 12 Summary of results obtained so far from lysozyme, thaumatine, 5-HT3 receptor, GLIC and AcrB crystals.

Silicone nitride membranes occurred to be an interesting method to grow and measure directly (*in situ*) crystalline material. Nonetheless, the protein crystals seem to have better quality when grown on CD plates and furthermore the resolution was much better. However, for instance for the 5-HT3 serotonin receptor, good quality crystals were obtained only on silicone nitride

membranes. Using CD plates the diffraction signal was very low or not detectible at all. One of the most promising data set was obtained from GLIC protein, the protein structure could have been almost solved and compared with already published data (see Fig. 77A and B). For AcrB complete data analysis of this protein sample is still in progress, however the best resolution was approximately 3.9 Å. Still, solving the structure of this protein is not an easy task since it is difficult to determine the crystal space group. Hence, more crystals need to be tested to make the final statements.

Performing measurements on silicone nitride membranes and CD plates provided a great possibility to meet all the requirements that are necessary to analyse the most fragile protein samples. Additionally, after many attempts, the set up and the measurements have became substantially improved in order to perform friendly-user experiments. After some software modification, the beamline microscope goes to each single drop on the CD plate automatically and the diffraction patterns are generated only from the previously indicated areas of each drop. Hence, finally the recent achievement was the speed of collected data that reduced to 1.5 ms/frame.

The most promising samples, which could be further investigated, are GLIC and AcrB. More tests will be conducted in order to improve X-ray diffraction by optimizing different variables starting from sample preparation tools through sample mounting and pointing and ending on data treatment and analysis.

5 General Conclusions

The main goal of this PhD thesis was to gain new structural data on the ADP/ATP carriers and develop tools for micro- and nano-crystallography approaches applied to membrane protein structural biology.

Membrane transport between and within the cells of variety of compounds is a crucial process to maintain cell well-being vitality. The membrane proteins that take part in those processes are thus essential since they provide the required substrates. The structures and functions of membrane carriers highly depend on the transported substrate and hence the knowledge about their precise transport mechanism remains of high value. Much has been done in order to discover and describe Mitochondrial Carriers Family (MCs) transport mechanism, however there are still some missing parts of the most probable scenario. Mitochondrial ADP/ATP carriers (AAC) are responsible for the export to the rest of the cells of the ATP, the cellular energy currency essential to many different processes. AACs are also involved in cell apoptosis process, genetic diseases and in cancerogenesis. Numerous literature has been published on the mitochondrial ADP/ATP carriers describing for instance protein functional and inhibition properties and providing structural data. So far and despite constant efforts only the bovine and yeast ADP/ATP carriers three-dimensional structures were solved and all in the same conformation, in complex with CATR inhibitor (known as c-state)[77,83]. Therefore, since no structural data is available on the m-state (the conformation supposed to be opened to the matrix side) some fundamental questions about the different conformational states adopted by the protein during the transport process still need to be answered.

In an effort to search for a good candidate for structural studies of AACs, we considered the human AACs isoforms and also non-mitochondrial AAC like the *Arabidpsis thaliana* plasma membrane ADP/ATP carrier (PM_AAC). We were able to express this protein in *E. coli* cells and purify it in LAPAO with a very good purity and yield. Preliminary characterization proved also that the protein was quite stable and we therefore performed a few crystallization assays. Nonetheless, the protein occurred to be not functional and we decided to focus

only on our other targets, the human AAC isoforms, hAAC1, hAAC2, hAAC3 and hAAC4.

In terms of protein functional properties we proved that all human AACs were successfully and functionally expressed in *E. coli* membranes, which was a very good starting point. It was unexpected for us that PM_AAC was not functional since we could have rather foreseen that it would have been an easier protein to work with.

In terms of human AACs, our results have shown additionally that the expression level and the transport properties of hAAC4, the most divergent human isoform in terms of sequence (the sequence of hAAC4 is only 66-68% similar to the first one) differ from the other three. Following those observation we compared in more details the transport properties of several hAAC1 and hAAC4 mutants. These mutants were generated by swapping residues between hAAC1 and hAAC4. The mutants exhibited both similar and different transport properties compared to the wild types proteins depending on the mutated residue. MD simulation analysis showed that the mutated residues in both isoforms seem not to be involved directly in nucleotide transport nor in CATR binding, still some of them influence the proteins function. Since hAAC1 and hAAC4 exhibited sequence differences, the residues involved in the conformational changes of the proteins during substrate trafficking might differ between them, which would explain some distinct functional behaviors revealed by our experiments. Still, it was sometimes not an easy task to interpret the results generated by all the mutations we have done. Since there is no structure of the protein in the m-state conformation and the involvement of particular residues in conformational changes remains hypothetical. Nonetheless, interestingly, some mutations of hAAC1 (D104N and H209P), which exhibited a decrease of activity, showed the same and significantly decreased transport properties respectively compared with wild-type hAAC1. Interestingly, A61K mutant in hAAC4 exhibited higher ATP binding affinity and the transport rate, while for instance P59A and P221H (corresponding H209P in hAAC1) showed slightly lower ATP binding affinity then the wild-type, however the transport rate was maintained at the same range as for the wild-type hAAC4. In the perspective of all above mutagenesis studies that were performed on human

AACs and already described and investigated mutations, it would be of interest to perform random mutagenesis screening in order to discover different significant residues that might play an important role in protein conformational change.

We developed in parallel expression and purification protocols in order to obtain new structural data on these proteins. Among the different systems available in the lab we chose the cell free system. Indeed initial promising results were obtained on hAAC1. We successfully expressed in this system two human isoforms, hAAC1 and hAAC3. We performed detergent screening for the solubilization and purification of the proteins and found that DDM and MNG-3 occurred to be the most appropriate, leading to the most homogenous and pure proteins. Based on Size Exclusion Chromatography analysis and Analytical Ultracentrifugation (AUC) data we assumed that the oligomeric state of hAAC1 and hAAC3 in both detergents, is likely to be a monomer. Performing additional Circular Dichroism (CD) experiments proved also that both proteins are properly folded. hAAC3 exhibited better spectra than hAAC1. Moreover, thermal stability experiments, which were conducted prior to crystallization experiments, showed that the two human AAC isoforms are more stable in presence of CATR inhibitor (however for hAAC1 it can be only observed when protein is purified in DDM detergent), which is a very good sign that the protein is in a proper state. Being able to produce the full-length hAAC1 and hAAC3 in a purified, detergent-solubilized and well-folded state was an essential achievement that opens the perspective for biochemical functional *in vitro* studies and new structural approaches of those essential proteins.

Crystallization trials in Lipidic Cubic Phase (LCP) and vapour diffusion were regularly set up along the project. We obtained some crystals in LCP and vapour diffusion that were also visible clearly under UV light. The results however were quite puzzling since it was not certain if they are detergent or protein crystals or both. Therefore, it would be good if we could perform definitely more crystallization trials in presence of CATR inhibitor considering its stabilizing effect but also playing with the detergent concentration, one of the major parameter when crystallizing membrane protein.

It is a difficult task to obtain membrane protein crystals, which would be

additionally easy to manipulate and have appropriate size for diffraction analysis. We initially planned to use AAC crystals to develop new crystallographic methodologies and perform tests with serial crystallography experiments. However as described in the third chapter of this manuscript we did not achieve obtaining reproducible crystallization conditions for any of our AAC target. In classical approach, which is based on crystal fishing and cryo-protecting, many issues have to be overcome in order to keep the sample in good conditions. Introducing different *in situ* measurements could significantly improve samples mounting and diffraction measurements. In this project we investigated the application of silicon nitride membranes and CD plates and we worked with proteins at both ends of the spectrum: from very easy and soluble (lysozyme and thaumatine) to very demanding such as membrane proteins: mouse 5-HT serotonin receptor, GLIC Ion Channel and Bacterial Multidrug Efflux Transporter, AcrB. We managed to show proof-of-concept results with small crystals with above mentioned adapted supports. We reached resolution for all of the tested samples of less than 5 Å. Performing measurements on silicone nitride membranes and CD plates provided a great possibility to meet all the requirements that are necessary to analyse the most fragile protein samples.

First tests using CD plates and silicone nitride membranes were very time-consuming and measurements were extended in time. Each time however, we were adjusting crystallization conditions for each particular sample, softwares, beamline set ups with different designed supports. Finally after many attempts, all assembly fulfilled with measurements and data collection have became substantially improved in order to perform friendly-user experiments in short period of time. Moreover, development of these methods seems to be applicable to many different protein samples, providing that they form microcrystals and are stable at room temperature. An additional advantage, which we always take an account, is that, after many improvements the method should not be expensive for regular users.

6 ANNEXES

ANNEX 1: Cloning techniques

1. Restriction and ligation

Some of the constructs were created using restriction/ligation cloning method (for constructs see Tables 3 and 4 in Annex 1[bis]). cDNA was amplified in PCR reaction. 50 µL *o*f the PCR reaction mix contained following components (see Table 1):

Components	Volume (µL)
50-100% dsDNA template	1
100% Forward Oligonucleotide Primer	2 (10 x diluted)
100% Reverse Oligonucleotide Primer	2 (10 x diluted)
10X Pfu Buffer (*Agilent Technologies*)	5
100 mM $MgSO_4$ (*New England BioLabs*)	2
10 mM dNTP mix (*Thermo Scientific*)	1
Polymerase DNA Pfu (*Agilent Technologies*)	1
ddH_2O	36

Table 1 Components of PCR reaction mix used in performing restriction/ligation cloning.

All PCR reactions were performed using Eppendorf`s Mastercycler Gradient with following temperature cycles (see Table 2):

	Time	Temperature (°C)	Cycles
Denaturation	2 min	95	1
Denaturation **Annealing** **Elongation**	30 sec 30 sec 3 min, 10 sec	95 68 68	18 - 25
Final Elongation	10 min	68	1

Table 2 Thermal cycling conditions for PCR reaction used for the restriction/ligation technique.

The amplified DNA in PCR reaction was then analyzed with 1% agarose gel electrophoresis (see paragraph 3.1.4) and genes of interest were later on extracted from the gel and DNA was purified using QIAquick Gel Extraction Kit (*Qiagen*) according to the manufacture`s protocol. Then the purified PCR products (insert) and vector (plasmid) were digested with appropriate restriction enzymes (*Thermo Scientific*) according to the supplier instruction.

Afterwards the digested fragments were loaded on 1% agarose gel (see paragraph 3.1.4) and in the same manner the bands of interest were extracted from the gel using QIAquick Gel Extraction Kit. In each sample DNA concentration was measured using NanoDrop (see paragraph 3.1.5). Then the purified fragments (plasmid and insert) were ligated using DNA Ligation Kit (*Thermo Scientific*) and approximately 10 µL of ligation mixture was transformed into *E. coli* TOP 10 competent cells. In the last step after transformation (see paragraph 3.1.1), small-scale DNA preparation (see paragraph 3.1.2) and DNA purification (manufacturer`s protocol, *Qiagen*) the obtained constructs were sent for sequencing.

2. Restriction Free (Rf) cloning

Some of the constructs were created using Restriction Free cloning method (for constructs see Tables 3 and 4 in Annex 1[bis]). Restriction-free cloning is a simple method by which a DNA sequence can be inserted to a circular plasmid, independently of restriction and ligation sites. In this approach a PCR fragment encoding the gene of interest is used as a pair of long primers (with approximately 48 – 50 bp per each primer). First, cDNA fragments are amplified in PCR reaction in order to create `sticky-ends`. 50 µL of the PCR reaction contained following components (see Table 3):

Components	Volume (µL)
50-100% dsDNA template	1
100% Forward Oligonucleotide Primer	2 (10 x diluted)
100% Reverse Oligonucleotide Primer	2 (10 x diluted)
Master Mix (*Thermo Scientific*)	25
ddH_2O	20

Table 3 Components of PCR reaction mix used in Restriction – free cloning.

All PCR reactions were performed using Eppendorf`s Mastercycler Gradient with following temperature cycles (see Table 4):

	Time	Temperature (°C)	Cycles
Denaturation	2 min	95 - 98	1
Denaturation **Annealing** **Elongation**	30 sec 30 sec 30 sec - 1 min	95 - 98 67 (primer Tm!) 72	25 - 35
Final Elongation **STOP**	5 min 10 min	72 4 - 10	1 1

Table 4 Thermal cycling conditions for PCR reaction using the Restriction – free (Rf) cloning technique (1st PCR reaction).

The amplified DNA in PCR reaction was then analyzed with 1% agarose gel electrophoresis (see paragraph 3.1.4) and genes of interest were later on extracted from the gel and DNA was purified using QIAquick Gel Extraction Kit according to the manufacture`s protocol. In each sample DNA concentration was measured using NanoDrop (see paragraph 3.1.5). This PCR product was then used in the second PCR reaction and inserted into the target plasmid (the composition of PCR mixture is the same as the one used for cloning by restriction/ligation but without $MgSO_4$ (see Table 1). Second PCR reaction was performed with the following temperature cycles (see Table 5):

	Time	Temperature (°C)	Cycles
Denaturation	1 min 20 sec - 2 min	95	1
Denaturation **Annealing** **Elongation**	20 - 30 sec 30 sec 1 min 20 sec	95 67 (primer Tm!) 70	25 - 35
Final Elongation **STOP**	5 min 10 min	70 4 - 10	1 1

Table 5 Thermal cycling conditions for PCR reaction using the Restriction – free (Rf) cloning technique (2nd PCR reaction).

Afterwards the PCR product was incubated with 2 µL of the Dpn I (*Thermo Scientific*) restriction enzyme for 1 h at 37 °C in order to digest parental cDNA. A few µL of the reaction mix were then transformed in *E. coli* TOP 10 competent cells and after small-scale DNA preparation (see paragraph 3.1.2) and DNA purification (manufacturer`s protocol, *Qiagen*) the obtained constructs were sent to sequencing.

3. Quick – Change Mutagenesis

Quick-Change method introduces single mutations or small insertions/deletions while Rf cloning method inserts complete genes without an introduction of unwanted extra residues.[217,218]

Some of the human AAC mutants (for mutants see Table 4 in Annex 1[bis]) were created using Quick Change Site-directed mutagenesis. cDNA fragments were amplified in PCR reaction. 50 µL or 25 µL of the PCR reaction were prepared. The mixture contained either the same compounds as in the Table 3 or the components of the Quick Change Lighting Site – Directed Mutagenesis kit (*Agilent technologies*) (see Table 6) or the components detailed in Table 7.

Components (Quick Change Lighting Site - directed Mutagenesis)	Volume (µL)
50-100% dsDNA template	1
100% Forward Oligonucleotide Primer	2 (10 x diluted)
100% Reverse Oligonucleotide Primer	2 (10 x diluted)
Quick Solution Reagent	1.5
dNTP mix	1
Quick Change Lighting Enzyme	1
ddH_2O	16.5

Table 6 Components of the PCR reaction mix used for the QuickChange Site – directed Mutagenesis (Quick Change Lightning Site-directed mutagenesis kit (*Agilent technologies*).

Components	Volume (µL)
50-100% dsDNA template	1
100% Forward Oligonucleotide Primer	2 (10 x diluted)
100% Reverse Oligonucleotide Primer	2 (10 x diluted)
10X Turbo Buffer (*Stratagene*)	5
10 mM dNTP mix (*Thermo Scientific*)	1
Polymerase DNA Turbo (*Agilent Technologies*)	1
ddH_2O	38

Table 7 Components of PCR reaction mix used for the QuickChange Site – directed Mutagenesis.

All PCR reactions were performed using Eppendorf's Mastercycler Gradient with following temperature cycles (see Table 8):

	Time	Temperature (°C)	Cycles
Denaturation	1 min	95	1
Denaturation **Annealing** **Elongation**	30 sec 1 min 18 min	95 57 72	18 - 25
Final Elongation **STOP**	10 min 5 min	72 4	1

Table 8 Thermal cycling conditions for PCR reaction performed using Quick Change Site – directed mutagenesis.

The PCR product was then incubated with 2 µL of the Dpn I restriction enzyme for 1 h at 37 °C in order to digest parental cDNA. A few µL of the reaction mix were then transformed in *E. coli* TOP 10 competent cells and after small-scale DNA preparation (see paragraph 3.1.2) and DNA purification (manufacturer`s protocol, *Qiagen*) the obtained constructs were sent to sequencing.

ANNEX 1bis: Sequences, primers, plasmids and constructs design

1. Protein sequences

All protein sequences were taken from UniProt Data Base (http://www.uniprot.org) (see Table 1):

Name of the Protein	Protein sequence
Human mitochondrial ADP/ATP Carrier 1 (AAC1)	MGDHAWSFLKDFLAGGVAAAVSKTAVAPIERVKLLLQVQHASKQ ISAEKQYKGIIDCVVRIPKEQGFLSFWRGNLANVIRYFPTQALNFAF KDKYKQLFLGGVDRHKQFWRYFAGNLASGGAAGATSLCFVYPLDF ARTRLAADVGKGAAQREFHGLGDCIIKIFKSDGLRGLYQGFNVSVQ GIIIYRAAYFGVYDTAKGMLPDPKNVHIFVSWMIAQSVTAVAGLVS YPFDTVRRRMMMQSGRKGADIMYTGTVDCWRKIAKDEGAKAFFK GAWSNVLRGMGGAFVLVLYDEIKKYV
Human mitochondrial ADP/ATP Carrier 2 (AAC2)	MTDAAVSFAKDFLAGGVAAAISKTAVAPIERVKLLLQVQHASKQIT ADKQYKGIIDCVVRIPKEQGVLSFWRGNLANVIRYFPTQALNFAFK DKYKQIFLGGVDKRTQFWRYFAGNLASGGAAGATSLCFVYPLDFA RTRLAADVGKAGAEREFRGLGDCLVKIYKSDGIKGLYQGFNVSVQG IIIYRAAYFGIYDTAKGMLPDPKNTHIVISWMIAQTVTAVAGLTSYP FDTVRRRMMMQSGRKGTDIMYTGTLDCWRKIARDEGGKAFFKG AWSNVLRGMGGAFVLVLYDEIKKYT
Human mitochondrial ADP/ATP Carrier 3 (AAC3)	MTEQAISFAKDFLAGGIAAAISKTAVAPIERVKLLLQVQHASKQIAA DKQYKGIVDCIVRIPKEQGVLSFWRGNLANVIRYFPTQALNFAFKD KYKQIFLGGVDKHTQFWRYFAGNLASGGAAGATSLCFVYPLDFAR TRLAADVGKSGTEREFRGLGDCLVKITKSDGIRGLYQGFSVSVQGII IYRAAYFGVYDTAKGMLPDPKNTHIVVSWMIAQTVTAVAGVVSYP FDTVRRRMMMQSGRKGADIMYTGTVDCWRKIFRDEGGKAFFKG AWSNVLRGMGGAFVLVLYDELKKVI-
Human mitochondrial ADP/ATP Carrier 4 (AAC4)	MHREPAKKKAEKRLFDASSFGKDLLAGGVAAAVSKTAVAPIERVK LLLQVQASSKQISPEARYKGMVDCLVRIPREQGFFSFWRGNLANVI RYFPTQALNFAFKDKYKQLFMSGVNKEKQFWRWFLANLASGGAA GATSLCVVYPLDFARTRLGVDIGKGPEERQFKGLGDCIMKIAKSDGI AGLYQGFGVSVQGIIVYRASYFGAYDTVKGLLPKPKKTPFLVSFFIA QVVTTCSGILSYPFDTVRRRMMMQSGEAKRQYKGTLDCFVKIYQH EGISSFFRGAFSNVLRGTGGALVLVLYDKIKEFFHIDIGGR
Plant Plasma Membrane – ANT 1 Protein from *Arabidopsis thaliana*	MCISKEDEEDPSRNRRNQSPLSLPQTLKHFQKDLLAGAVMGGVVHTI VAPIERAKLLLQTQESNIAIVGDEGHAGKRRFKGMFDFIFRTVREEGV LSLWRGNGSSVLRYYPSVALNFSLKDLYRSILRNSSSQENHIFSGALAN FMAGSAAGCTALIVVYPLDIAHTRLAADIGKPEARQFRGIHHFLSTIH KKDGVRGIYRGLPASLHGVIIHRGLYFGGFDTVKEIFSEDTKPELALW KRWGLAQAVTTSAGLASYPLDTVRRRIMMQSGMEHPMYRSTLDCW KKIYRSEGLASFYRGALSNMFRSTGSAAILVFYDEVKRFLNWGGI

Table 1 ADP/ATP Carrier Protein Sequences from different organisms: human, plant (*Arabidopsis Thaliana*).

2. Oligonucleotide primers design

All of the primers were designed using ApE software (Universal) and synthesized by Beckman Coulter Genomics (United Kingdom) (see Table 2):

Name of the primer	Sequence (5'- 3')
Human mitochondrial ADP/ATP Carrier 1	
hAAC1_A47P_pET20b_MBP_FOR	CATGCCAGCAAACAGATCAGTCCGGAGAAGCAGTACAAAGGGATCA
hAAC1_A47P_pET20b_MBP_REV	TGATCCCTTTGTACTGCTTCTCCGGACTGATCTGTTTGCTGGCATG
hAAC1_K49A_pET20b_MBP_FOR	GCCAGCAAACAGATCAGTGCTGAGGCGCAGTACAAAGGGATCATTG
hAAC1_K49A_pET20b_MBP_REV	CAATGATCCCTTTGTACTGCGCCTCAGCACTGATCTGTTTGCTGGC
hAAC1_D104N_pET20b_MBP_FOR	AAGCAGCTCTTCTTAGGGGGTGTGAACCGGCATAAGCAGTTCTGGC
hAAC1_D104N_pET20b_MBP_REV	GCCAGAACTGCTTATGCCGGTTCACACCCCCTAAGAAGAGCTGCTT
hAAC1_A114L_pET20b_MBP_FOR	AAGCAGTTCTGGCGCTACTTTCTGGGTAACCTGGCGTCCGGT
hAAC1_A114L_pET20b_MBP_REV	ACCGGACGCCAGGTTACCCAGAAAGTAGCGCCAGAACTGCTT
hAAC1_A114P_pET20b_MBP_FOR	AAGCAGTTCTGGCGCTACTTTCCGGGTAACCTGGCGTCCGGT
hAAC1_A114P_pET20b_MBP_REV	ACCGGACGCCAGGTTACCCGGAAAGTAGCGCCAGAACTGCTT
hAAC1_R171A_pET20b_MBP_FOR	AAGATCTTCAAGTCTGATGGCCTGGCGGGGCTCTACCAGGGTTTCAA
hAAC1_R171A_pET20b_MBP_REV	TTGAAACCCTGGTAGAGCCCCGCCAGGCCATCAGACTTGAAGATCTT
hAAC1_H209P_pET20b_MBP_FOR	ATGCTGCCTGACCCCAAGAACGTGCCGATTTTTGTGAGCTGGATGATT
hAAC1_H209P_pET20b_MBP_REV	AATCATCCAGCTCACAAAAATCGGCACGTTCTTGGGGTCAGGCAGCAT
Human mitochondrial ADP/ATP Carrier 2	
hAAC2_MBP_muta_FOR	GTCCCCCGGGGCAGCGCGGCCGCAATGACAGATGCCGCTGTGTCCTTCGC
hAAC2_MBP_muta_REV	GTGGTGGTGGTGGTGGTGCTCGAGTTATGTGTACTTCTTGATTTCATCA TACAAGACAAGCAC
hAAC2_R111L_pET20b_MBP_FOR	GTGGACAAGAGAACCCAGTTTTGGCTGTACTTTGCAGGGAATCTGGC
hAAC2_R111L_pET20b_MBP_REV	GCCAGATTCCCTGCAAAGTACAGCCAAAACTGGGTTCTCTTGTCCAC
hAAC2_T227V_pET20b_MBP_FOR	GTCACTGCTGTTGCCGGGTTGGTGTCCTATCCATTTGACACCGT
hAAC2_T227V_pET20b_MBP_REV	ACGGTGTCAAATGGATAGGACACCAACCCGGCAACAGCAGTGAC
MBP_hAAC2_NotI_FOR	TAAGCGGCCGCAATGACAGATGCCGCTGTG
MBP_hAAC2_XhoI_REV	GGTGCTCGAGTTATGTGTACTTCTTGATTTC
Human mitochondrial ADP/ATP Carrier 3	
hAAC3_pIVEX2.3d_FOR	TTAACTTTAAGAAGGAGATATACCATGACGGAACAAGCAATTAGTTTC
hAAC3_pIVEX2.3d_REV	ATGATGATGATGAGAACCCCCCCCGATAACCTTCTTCAGTTCGTCATA
hAAC3_pIVEX2.4d_FOR	CATCATCATCATCATAGCAGCGGCATGACGGAACAAGCAATTAGTTTC
hAAC3_pIVEX2.4d_REV	ATCTTACCGGATCTTAGTTAGTTAGATAACCTTCTTCAGTTCGTCATA
Human mitochondrial ADP/ATP Carrier 4	
hAAC4_pIVEX2.3d_FOR	TGTTTAACTTTAAGAAGGAGATATACCATGCACCGTGAGCCAGCAAAGA A
hAAC4_pIVEX2.3d_REV	ATGATGATGATGATGAGAACCCCCCCCACGACCGCCGATGTCAATGTGG AA
hAAC4_pIVEX2.4d_FOR	CATCATCATCATCATCATAGCAGCGGCATGCACCGTGAGCCAGCAAAG
hAAC4_pIVEX2.4d_REV	CGGATCTTACCGGATCTTAGTTAGTTAACGACCGCCGATGTCAATGTGG AA
hAAC4_pIVEX2.3d_NotI_FOR	TATGAGCGGCCGCGTATGCACCGTGAGCCAGCAAA
hAAC4_pIVEX2.3d_XhoI_REV	TCGCTCGAGTCGTTAACGACCGCCGATGTCAATGTGGAAAAA
hAAC4_pIVEX2.4d_NotI_FOR	GGCCGCGGCCGCATGCACCGTGAGCCAGCAAA
hAAC4_pIVEX2.4d_XhoI_REV	TCGCTCGAGTCGACTTTAACGACCGCCGATGTCAATGTGGAAAAA
hAAC4_pET20b_MBP_muta_FOR	GTCCCCCGGGGCAGCGCGGCCGCAATGCACCGTGAGCCAGCAAAGAAGA
hAAC4_pET20b_MBP_muta_REV	GTGGTGGTGGTGGTGGTGCTCGAGTTAACGACCGCCGATGTCAATGTGG AA
hAAC4_Nter_cut_pET20b_MBP_FOR	GTCGACAAGCTTGCGGCCGCAATGCACCGTGAGGCGAGCTCCTTCGGTA AAGATC
hAAC4_Nter_cut_pET20b_MBP_REV	GATCTTTACCGAAGGAGCTCGCCTCACGGTGCATTGCGGCCGCAAGCTT GTCGAC

hAAC4_Cter_cut_pET20b_MBP_FOR	CTGGTACTGGTGCTGTACGACAAAATCAAAGAATTTTTCTAACTCGAGC ACCACCACCACCACCAC
hAAC4_Cter_cut_pET20b_MBP_REV	GTGGTGGTGGTGGTGGTGCTCGAGTTAGAAAAATTCTTTGATTTTGTCG TACAGCACCAGTACCAG
hAAC4_N104D_pET20b_MBP_FOR	CAGCTGTTCATGAGCGGCGTAGACAAAGAAAAACAATTCTGGCG
hAAC4_N104D_pET20b_MBP_REV	CGCCAGAATTGTTTTTCTTTGTCTACGCCGCTCATGAACAGCTG
hAAC4_N104D_pET20b_MBP_long_FOR	AAGCAGCTGTTCATGAGCGGCGTAGACAAAGAAAAACAATTCTGGCGTT GGTTTCTG
hAAC4_N104D_pET20b_MBP_long_REV	CAGAAACCAACGCCAGAATTGTTTTTCTTTGTCTACGCCGCTCATGAAC AGCTGCTT
hAAC4_L114A_pET20b_MBP_FOR	AAACAATTCTGGCGTTGGTTTGCGGCTAATCTGGCATCCGGTGGCG
hAAC4_L114A_pET20b_MBP_REV	CGCCACCGGATGCCAGATTAGCCGCAAACCAACGCCAGAATTGTTT
hAAC4_L114P_pET20b_MBP_FOR	AAACAATTCTGGCGTTGGTTTCCGGCTAATCTGGCATCCGGTGGCG
hAAC4_L114P_pET20b_MBP_REV	CGCCACCGGATGCCAGATTAGCCGGAAACCAACGCCAGAATTGTTT
hAAC4_P47A_pET20b_MBP_FOR	GCTTCTAGCAAACAGATCAGCGCGGAAGCTCGCTACAAGGGTAT
hAAC4_P47A_pET20b_MBP_REV	ATACCCTTGTAGCGAGCTTCCGCGCTGATCTGTTTGCTAGAAGC
hAAC4_A49K_pET20b_MBP_FOR	AGCAAACAGATCAGCCCGGAAAAGCGCTACAAGGGTATGGTGGAT
hAAC4_A49K_pET20b_MBP_REV	ATCCACCATACCCTTGTAGCGCTTTTCCGGGCTGATCTGTTTGCT
hAAC4_A171R_pET20b_MBP_FOR	AAAATTGCAAAATCTGACGGTATCAGGGGTCTGTACCAGGGCTTC
hAAC4_A171R_pET20b_MBP_REV	GAAGCCCTGGTACAGACCCCTGATACCGTCAGATTTTGCAATTTT
hAAC4_P209H_pET20b_MBP_FOR	CTGCCGAAACCGAAGAAAACTCACTTCCTGGTATCTTTCTTCATCG
hAAC4_P209H_pET20b_MBP_REV	CGATGAAGAAAGATACCAGGAAGTGAGTTTTCTTCGGTTTCGGCAG
hAAC4_P209H_pET20b_MBP_long_FOR	GGCCTGCTGCCGAAACCGAAGAAAACTCACTTCCTGGTATCTTTCTTCA TCGCGCA
hAAC4_P209H_pET20b_MBP_long_REV	TGCGCGATGAAGAAAGATACCAGGAAGTGAGTTTTCTTCGGTTTCGGCA GCAGGCC
hAAC4_L227V_pET20b_MBP_FOR	GTCACCACCTGCTCTGGTATTGTGTCTTACCCGTTCGACACTGTA
hAAC4_L227V_pET20b_MBP_REV	TACAGTGTCGAACGGGTAAGACACAATACCAGAGCAGGTGGTGAC
hAAC4_E244R_KG_pET20b_MBP_FOR	ATGATGATGCAGTCTGGCCGGAAGGGGGCGAAACGTCAGTACAAAGGCA C
hAAC4_E244R_KG_pET20b_MBP_REV	GTGCCTTTGTACTGACGTTTCGCCCCCTTCCGGCCAGACTGCATCATCAT
hAAC4_KRQ-DIM_pET20b_MBP_ FOR	ATGCAGTCTGGCGAGGCGGACATCATGTACAAAGGCACCCTGGATTGC
hAAC4_KRQ-DIM_pET20b_MBP_ REV	GCAATCCAGGGTGCCTTTGTACATGATGTCCGCCTCGCCAGACTGCAT
hAAC4_F258W_pET20b_MBP_FOR	TACAAAGGCACCCTGGATTGCTGGGTTAAAATCTACCAGCAT
hAAC4_F258W_pET20b_MBP_ REV	ATGCTGGTAGATTTTAACCCAGCAATCCAGGGTGCCTTTGTA
hAAC4_F258W_pET20b_MBP_long_FOR	CGTCAGTACAAAGGCACCCTGGATTGCTGGGTTAAAATCTACCAGCATG AAGGCATCTCCTCT
hAAC4_F258W_pET20b_MBP_long_REV	AGAGGAGATGCCTTCATGCTGGTAGATTTTAACCCAGCAATCCAGGGTG CCTTTGTACTGACG
hAAC4_K252T_pET20b_MBP_ FOR	GGCGAGGCGAAACGTCAGTACACGGGCACCCTGGATTGCTTCG
hAAC4_K252T_pET20b_MBP_ REV	CGAAGCAATCCAGGGTGCCCGTGTACTGACGTTTCGCCTCGCC
hAAC4_V259R_pET20b_MBP_ FOR	AAAGGCACCCTGGATTGCTTCCGGAAAATCTACCAGCATGAAGGC
hAAC4_V259R_pET20b_MBP_ REV	GCCTTCATGCTGGTAGATTTTCCGGAAGCAATCCAGGGTGCCTTT
hAAC4_V259R_pET20b_MBP_long_FOR	CGTCAGTACAAAGGCACCCTGGATTGCTTCCGGAAAATCTACCAGCATG AAGGCATCTCCTCT
hAAC4_V259R_pET20b_MBP_long _REV	AGAGGAGATGCCTTCATGCTGGTAGATTTTCCGGAAGCAATCCAGGGTG CCTTTGTACTGACG
hAAC4_H264D_pET20b_MBP_ FOR	TTCGTTAAAATCTACCAGGACGAAGGCATCTCCTCTTTC
hAAC4_H264D_pET20b_MBP_REV	GAAAGAGGAGATGCCTTCGTCCTGGTAGATTTTAACGAA
hAAC4_H264D_pET20b_MBP_long_FOR	ACCCTGGATTGCTTCGTTAAAATCTACCAGGACGAAGGCATCTCCTCTT TCTTCCGTGGT
hAAC4_H264D_pET20b_MBP_long_REV	ACCACGGAAGAAAGAGGAGATGCCTTCGTCCTGGTAGATTTTAACGAAG CAATCCAGGGT
hAAC4_S268K_pET20b_MBP_ FOR	ATCTACCAGCATGAAGGCATCAAGTCTTTCTTCCGTGGTGCA
hAAC4_S268K_pET20b_MBP_ REV	TGCACCACGGAAGAAAGACTTGATGCCTTCATGCTGGTAGAT

Plant Plasma Membrane – ANT 1 Protein from *Arabidopsis thaliana*	
PM_pET20b_NotI_FOR	AAGCTTGCGGCCGCAATGTGCATTTCCAAAGAAGATGAAGAAGACCCG
PM_pET20b_XhoI_REV	GTGGTGGTGCTCGAGTTAAATACCACCCCAGTTCAGGAAGCG
PM_pET20b_FOR	GTGGTGGTGGTGGTGCTCGAGATGTGCATTTCCAAAGAAGATGAAGAAG ACCCG
PM_pET20b_REV	GTCGACAAGCTTGCGGCCGCATTAAATACCACCCCAGTTCAGGAAGCG
PM_pET20b_muta_FOR	GTCCCCCGGGGCAGCGCGGCCGCAATGTGCATTTCCAAAGAAGATGAAG AAGACCCG
PM_pET20b_muta_REV	GTGGTGGTGGTGGTGGTGCTCGAGTTAAATACCACCCCAGTTCAGGAAG CGTTTCAC
PM_pET16b_NdeI_FOR	GGTCGTCATATGATGTGCATTTCCAAAGAAGATGAAGAAGACCCGT
PM_pET16b_XhoI_REV	CGGATCCTCGAGTTAAATACCACCCCAGTTCAGGAAGCG
PM_pET16b_muta_FOR	AGCGGCCATATCGAAGGTCGTCATATGTGCATTTCCAAAGAAGATGAAG AAGACCCG
PM_pET16b_muta_REV	TTTGTTAGCAGCCGGATCCTCGAGTTAAATACCACCCCAGTTCAGGAAG CG
PM_H166K_pET20b_MBP_FOR	GTTTATCCGCTGGATATCGCTAAAACCCGTCTGGCAGCAGACATC
PM_H166K_pET20b_MBP_REV	GATGTCTGCTGCCAGACGGGTTTTAGCGATATCCAGCGGATAAAC
PM_H166R_pET20b_MBP_FOR	GTTTATCCGCTGGATATCGCTCGTACCCGTCTGGCAGCAGACATC
PM_H166R_pET20b_MBP_REV	GATGTCTGCTGCCAGACGGGTACGAGCGATATCCAGCGGATAAAC

Table 2 List of the oligonucleotide primers for different proteins.

3. Plasmids description

Vectors used for different cloning methods are presented and described below (see Table 3):

Name of the Plasmid	Description
pET20b	Plasmid used for the *E. coli* expression (empty vector), Ampicillin resistance
pET20b_MBP_Thrombin	Plasmid used for the *E. coli* expression (empty vector) with N- terminal Maltose Binding Periplasmic protein (MBP) fusion and with thrombin cleavage site; Ampicillin resistance
hAAC1_pET20b_MBP_Thrombin*	Plasmid used for the *E. coli* expression of the human ADP/ATP carrier isoform 1 fused to the C-terminus of Maltose Binding Periplasmic protein (MBP) and with thrombin cleavage site; Ampicillin resistance
hAAC2_pET20b_MBP_Thrombin*	Plasmid used for the *E. coli* expression of the human ADP/ATP carrier isoform 3 fused to the C-terminus of Maltose Binding Periplasmic protein (MBP) and with thrombin cleavage site; Ampicillin resistance
hAAC3_pET20b_MBP_Thrombin	Plasmid used for the *E. coli* expression of the human ADP/ATP carrier isoform 3 fused to the

	C-terminus of Maltose Binding Periplasmic protein (MBP) and with thrombin cleavage site; Ampicillin resistance
hAAC4_pET20b_MBP_Thrombin*	Plasmid used for the *E. coli* expression of the human ADP/ATP carrier isoform 4 fused to the C-terminus of Maltose Binding Periplasmic protein (MBP) and with thrombin cleavage site; Ampicillin resistance
pIVEX2.3d	RTS pIVEX His6-tag, 2nd Generation Vector Set (*Roche*). Vector is designed for high-level expression of C-terminal His6- tagged proteins in the cell free RTS *E. coli* system. It contains all regulatory elements necessary for *in vitro* expression based on a combination of T7 RNA polymerase and prokaryotic cell lysates; Ampicillin resistance
pIVEX2.4d	RTS pIVEX His6-tag, 2nd Generation Vector Set (*Roche*). Vector is designed for high-level expression of N-terminal His6- tagged proteins in the cell free RTS *E. coli* system. It contains all regulatory elements necessary for *in vitro* expression based on a combination of T7 RNA polymerase and prokaryotic cell lysates; Ampicillin resistance
hAAC1_pIVEX2.4d	Plasmid for cell–free expression of human ADP/ATP Carrier isoform 1 with N – terminal His_6-tag; Ampicillin resistance
hAAC2_pIVEX2.4d	Plasmid for cell free expression of human ADP/ATP Carrier isoform 2 with N – terminal His_6-tag; Ampicillin resistance
hAAC3_pIVEX2.3d	Plasmid for cell–free expression of human ADP/ATP Carrier isoform 3 with C – terminal His_6-tag; Ampicillin resistance
hAAC3_pIVEX2.4d	Plasmid for cell–free expression of human ADP/ATP Carrier isoform 3 with N – terminal His_6-tag; Ampicillin resistance
hAAC4_pIVEX2.3d	Plasmid for cell–free expression of human ADP/ATP Carrier isoform 4 with C – terminal His_6-tag; Ampicillin resistance

hAAC4_pIVEX2.4d	Plasmid for cell–free expression of human ADP/ATP Carrier isoform 4 with N – terminal His_6-tag; Ampicillin resistance
pET11b	Plasmid used for *E.coli* expression (empty vector); Kanamycin resistance
pET11b_LIC	Vector used for *E.coli* Ligation-Independent – Cloning (LIC) to express recombinant proteins with the addition of a 30 amino acid containing N-terminal fusion tag with 9X His-tag; Kanamycin resistance
PM_pET11b_LIC	Plasmid used for *E.coli* expression of plant Plasma Membrane Protein with the addition of 30 amino acids containing N-terminal 9X His-tag; Kanamycin resistance
pET11b_LIC_SUMO	Vector used for *E.coli* Ligation-Independent – Cloning (LIC) fused with N-terminal 6X His-tag containing cleavable SUMO (Small Ubiquitin-like Modifier) solubility tag (LIC-SUMO-tag length – 122 amino acids additionally from N – terminal site) to express recombinant protein; Kanamycin resistance
PM_pET11b_LIC_SUMO	Plasmid used for *E.coli* expression of s plant Plasma Membrane Protein fused with N-terminal 6X His-tag containing cleavable SUMO (Small Ubiquitin-like Modifier) solubility tag (LIC-SUMO-tag length – 122 amino acids additionally from N – terminal site); Kanamycin resistance
pET16b	Vector used for *E.coli* expression (empty vector); Ampicillin resistance
PM_pET16b	Plasmid used for *E.coli* expression of plant Plasma Membrane Protein; Ampicillin resistance
PM_pET20b_MBP_Thrombin*	Plasmid used for the *E. coli* expression of the plant Plasma Membrane Protein fused to the C-terminus of Maltose Binding Periplasmic protein (MBP) and with thrombin cleavage site; Ampicillin resistance
pYEDP60	Vector used for the yeast expression of

	different recombinant proteins with N – terminal 6X His – tag, BAD promoter and TEV cleavage site; Ampicillin resistance

* - several mutations of this protein were designed using this construct.

Table 3 List of the plasmids used for different cloning methods.

4. Constructs

The constructs were generated using different cloning techniques (see Table 4):

Construct	Expression system	Vector	Primers	Method of the cloning
Human mitochondrial ADP/ATP Carrier 1				
hAAC1_A47P_pET20b_MBP_Thrombin	*E.coli*	pET20b_MBP_Thrombin	**hAAC1_A47P_pET20b_MBP_FOR** **hAAC1_A47P_pET20b_MBP_REV**	Mutagenesis
hAAC1_K49A_pET20b_MBP_Thrombin	*E.coli*	pET20b_MBP_Thrombin	**hAAC1_K49A_pET20b_MBP_FOR** **hAAC1_K49A_pET20b_MBP_REV**	Mutagenesis
hAAC1_D104N_pET20b_MBP_Thrombin	*E.coli*	pET20b_MBP_Thrombin	**hAAC1_D104N_pET20b_MBP_FOR** **hAAC1_D104N_pET20b_MBP_REV**	Mutagenesis
hAAC1_A114L_pET20b_MBP_Thrombin	*E.coli*	pET20b_MBP_Thrombin	**hAAC1_A114L_pET20b_MBP_FOR** **hAAC1_A114L_pET20b_MBP_REV**	Mutagenesis
hAAC1_A114P_pET20b_MBP_Thrombin	*E.coli*	pET20b_MBP_Thrombin	**hAAC1_A114P_pET20b_MBP_FOR** **hAAC1_A114P_pET20b_MBP_REV**	Mutagenesis
hAAC1_R171A_pET20b_MBP_Thrombin	*E.coli*	pET20b_MBP_Thrombin	**hAAC1_R171A_pET20b_MBP_FOR** **hAAC1_R171A_pET20b_MBP_REV**	Mutagenesis
hAAC1_H209P_pET20b_MBP_Thrombin	*E.coli*	pET20b_MBP_Thrombin	**hAAC1_H209P_pET20b_MBP_FOR** **hAAC1_H209P_pET20b_MBP_REV**	Mutagenesis
Human mitochondrial ADP/ATP Carrier 2				
hAAC2_pET20b_MBP_Thrombin	*E.coli*	pET20b_MBP_Thrombin	**hAAC2_MBP_muta_FOR** **hAAC2_MBP_muta_REV**	Restriction – Free
hAAC2_pET20b_MBP_Thrombin	*E.coli*	pET20b_MBP_Thrombin	**MBP_hAAC2_NotI_FOR** **MBP_hAAC2_XhoI_REV**	Restriction/ Ligation
hAAC2_R111L_pET20b_MBP_Thrombin	*E.coli*	pET20b_MBP_Thrombin	**hAAC2_R111L_pET20b_MBP_FOR** **hAAC2_R111L_pET20b_MBP_RE**	Mutagenesis

			V	
hAAC2_T227V_pET20b_MBP_Thrombin	*E.coli*	pET20b_MBP_Thrombin	**hAAC2_T227V_pET20b_MBP_FOR** **hAAC2_T227V_pET20b_MBP_REV**	Mutagenesis
Human mitochondrial ADP/ATP Carrier 3				
hAAC3_pIVEX2.3d	Cell – Free	pIVEX 2.3d	**hAAC3_pIVEX2.3d_FOR** **hAAC3_pIVEX2.3d_REV**	Restriction - Free
hAAC3_pIVEX2.4d	Cell – Free	pIVEX 2.4d	**hAAC3_pIVEX2.4d_FOR** **hAAC3_pIVEX2.4d_REV**	Restriction - Free
Human mitochondrial ADP/ATP Carrier 4				
hAAC4_pIVEX2.3d	Cell – Free	pIVEX 2.3d	**hAAC4_pIVEX2.3d_FOR** **hAAC4_pIVEX2.3d_REV**	Restriction - Free
hAAC4_pIVEX2.4d	Cell – Free	pIVEX 2.4d	**hAAC4_pIVEX2.4d_FOR** **hAAC4_pIVEX2.4d_REV**	Restriction - Free
hAAC4_pIVEX2.3d	Cell – Free	pIVEX 2.3d	**hAAC4_pIVEX2.3d_NotI_FOR** **hAAC4_pIVEX2.3d_XhoI_REV**	Restriction/ Ligation
hAAC4_pIVEX2.4d	Cell – Free	pIVEX 2.4d	**hAAC4_pIVEX2.4d_NotI_FOR** **hAAC4_pIVEX2.4d_XhoI_REV**	Restriction/ Ligation
hAAC4_pET20b_MBP_Thrombin	*E.coli*	pET20b_MBP_Thrombin	**hAAC4_pET20b_MBP_muta_FOR** **hAAC4_pET20b_MBP_muta_REV**	Restriction - Free
hAAC4_Nterm_pET20b_MBP	*E.coli*	pET20b_MBP_Thrombin	**hAAC4_Nter_cut_pET20b_MBP_FOR** **hAAC4_Nter_cut_pET20b_MBP_REV**	Mutagenesis
hAAC4_Cterm_pET20b_MBP	*E.coli*	pET20b_MBP_Thrombin	**hAAC4_Cter_cut_pET20b_MBP_FOR** **hAAC4_Cter_cut_pET20b_MBP_REV**	Mutagenesis
hAAC4_N104D_pET20b_MBP	*E.coli*	pET20b_MBP_Thrombin	**hAAC4_N104D_pET20b_MBP_FOR** **hAAC4_N104D_pET20b_MBP_REV**	Mutagenesis
hAAC4_N104D_pET20b_MBP	*E.coli*	pET20b_MBP_Thrombin	**hAAC4_N104D_pET20b_MBP_long_FOR** **hAAC4_N104D_pET20b_MBP_long_REV**	Mutagenesis
hAAC4_L114A_pET20b_MBP	*E.coli*	pET20b_MBP_Thrombin	**hAAC4_L114A_pET20b_MBP_FOR** **hAAC4_L114A_pET20b_MBP_REV**	Mutagenesis
hAAC4_L114P_pET20b_MBP	*E.coli*	pET20b_MBP_Thrombin	**hAAC4_L114P_pET20b_MBP_FOR** **hAAC4_L114P_pET20b_MBP_REV**	Mutagenesis
hAAC4_P47A_pET20b_MBP	*E.coli*	pET20b_MBP_Thrombin	**hAAC4_P47A_pET20b_MBP_FOR** **hAAC4_P47A_pET20b_MBP_REV**	Mutagenesis

hAAC4_A49K_pET20b_MBP	*E.coli*	pET20b_MBP_Thrombin	**hAAC4_A49K_pET20b_MBP_FOR hAAC4_A49K_pET20b_MBP_REV**	Mutagenesis
hAAC4_A171R_pET20b_MBP	*E.coli*	pET20b_MBP_Thrombin	**hAAC4_A171R_pET20b_MBP_FOR hAAC4_A171R_pET20b_MBP_REV**	Mutagenesis
hAAC4_P209H_pET20b_MBP	*E.coli*	pET20b_MBP_Thrombin	**hAAC4_P209H_pET20b_MBP_FOR hAAC4_P209H_pET20b_MBP_REV**	Mutagenesis
hAAC4_P209H_pET20b_MBP	*E.coli*	pET20b_MBP_Thrombin	**hAAC4_P209H_pET20b_MBP_long_FOR hAAC4_P209H_pET20b_MBP_long_REV**	Mutagenesis
hAAC4_L227V_pET20b_MBP	*E.coli*	pET20b_MBP_Thrombin	**hAAC4_L227V_pET20b_MBP_FOR hAAC4_L227V_pET20b_MBP_REV**	Mutagenesis
hAAC4_E244R_KG_pET20b_MBP	*E.coli*	pET20b_MBP_Thrombin	**hAAC4_E244R_KG_pET20b_MBP_FOR hAAC4_E244R_KG_pET20b_MBP_REV**	Mutagenesis
hAAC4_KRQ_DIM_pET20b_MBP	*E.coli*	pET20b_MBP_Thrombin	**hAAC4_KRQ-DIM_pET20b_MBP_FOR hAAC4_KRQ-DIM_pET20b_MBP_REV**	Mutagenesis
hAAC4_K252T_pET20b_MBP	*E.coli*	pET20b_MBP_Thrombin	**hAAC4_K252T_pET20b_MBP_FOR hAAC4_K252T_pET20b_MBP_REV**	Mutagenesis
hAAC4_F258W_pET20b_MBP	*E.coli*	pET20b_MBP_Thrombin	**hAAC4_F258W_pET20b_MBP_FOR hAAC4_F258W_pET20b_MBP_REV**	Mutagenesis
hAAC4_F258W_pET20b_MBP	*E.coli*	pET20b_MBP_Thrombin	**hAAC4_F258W_pET20b_MBP_long_FOR hAAC4_F258W_pET20b_MBP_long_REV**	Mutagenesis
hAAC4_V259R_pET20b_MBP	*E.coli*	pET20b_MBP_Thrombin	**hAAC4_V259R_pET20b_MBP_FOR hAAC4_V259R_pET20b_MBP_REV**	Mutagenesis
hAAC4_V259R_pET20b_MBP	*E.coli*	pET20b_MBP_Thrombin	**hAAC4_V259R_pET20b_MBP_long_FOR hAAC4_V259R_pET20b_MBP_long_REV**	Mutagenesis
hAAC4_H264D_pET20b_MBP	*E.coli*	pET20b_MBP_Thrombin	**hAAC4_H264D_pET20b_MBP_FOR hAAC4_H264D_pET20b_MBP_**	Mutagenesis

			REV	
hAAC4_H264D_pET20b_MBP	*E.coli*	pET20b_MBP_ Thrombin	**hAAC4_H264D_pET20b_MBP_long_FOR** **hAAC4_H264D_pET20b_MBP_long_REV**	Mutagenesis
hAAC4_S268K_pET20b_MBP	*E.coli*	pET20b_MBP_ Thrombin	**hAAC4_S268K_pET20b_MBP_ FOR** **hAAC4_S268K_pET20b_MBP_ REV**	Mutagenesis
Plant Plasma Membrane – ANT 1 Protein from *Arabidopsis thaliana*				
PM_pET20b_MBP_Thrombin	*E.coli*	pET20_MBP_ Thrombin	**PM_pET20b_NotI_FOR** **PM_pET20b_XhoI_REV**	Restriction/ Ligation
PM_pET20b_MBP_Thrombin	*E.coli*	pET20_MBP_ Thrombin	**PM_pET20b_FOR** **PM_pET20b_REV**	Restriction - Free
PM_pET20b_MBP_Thrombin	*E.coli*	pET20_MBP_ Thrombin	**PM_pET20b_muta_FOR** **PM_pET20b_muta_REV**	Restriction - Free
PM_pET16b	*E.coli*	pET16b	**PM_pET16b_NdeI_FOR** **PM_pET16b_XhoI_REV**	Restriction/ Ligation
PM_pET16b	*E.coli*	pET16b	**PM_pET16b_muta_FOR** **PM_pET16b_muta_REV**	Restriction - Free
PM_H166K_pET20b_MBP_Thrombin	*E.coli*	pET20_MBP_ Thrombin	**PM_H166K_pET20b_MBP_FOR** **PM_H166K_pET20b_MBP_REV**	Mutagenesis
PM_H166R_pET20b_MBP_Thrombin	*E.coli*	pET20_MBP_ Thrombin	**PM_H166R_pET20b_MBP_FOR** **PM_H166R_pET20b_MBP_REV**	Mutagenesis

Table 4 List of different generated constructs.

Annex 2: Cell – Free expression solutions

1. Traduction Mix

Reaction Mix in cell–free expression system consists, among others components, from Traduction Mix with following substrates (see Table 1):

Traduction Mix - 8 ml (400 µL aliquots)	
Component	**Volume (mL), (Stock)**
350 mM HEPES pH 7.5 (*Sigma - Aldrich*)	1.375 (2 M)
7 mM Dithiothreitol - DTT (*Euromedex*)	0.0558 (1 M)
4.25 mM NTPs (*Sigma - Aldrich*)	0.68 (50 mM)
1.85 mM Adenosine triphosphate (ATP) (*Sigma - Aldrich*)	0.0148 (1 M)
1 mM Amino Acid Mix** (*Sigma - Aldrich*)	2 (4 mM)
9.5 % PEG 8000 (*Sigma - Aldrich*)	1.52 (50%)
173 µg/mL Folic Acid (*Sigma - Aldrich*)	0.138 (10 mg/mL)
3.2 mM Cyclic adenosine monophosphate (CAMP) (*Fluka*)	0.064 (0.4 mM)
0.35 mg /mL ARNt (*Sigma - Aldrich*)	0.34 (0.35 mg/mL)
125 mM Acethyl Phosphate (*Sigma - Aldrich*)	1 (1 M)
180 mM Ammonium Acetate (*MP - BioMedicals*)	0.48 (3 M)

**** - see list of components in Table 2 and 3 in Annex 2**

Table 1 Composition of Traduction Mix for Cell – Free expression.

2. Amino Acid Mix (AA Mix)

Each amino acid was dissolved either in 100 mM HEPES pH 7.4 (*Sigma – Aldrich*) either in distilled H_2O (see Table 2 and 3). Amino Acid Mix was prepared at the final 4 mM concentration. All the amino acids were mixed together in following way: 10 mL of 20 mM Tyrosine (*Sigma – Aldrich*) was added to 2 mL of each other amino acid at 100 mM concentration. The sample was after that filled up with distilled H_2O to 50 mL total volume, aliquoted in 12.5 mL, frozen in liquid nitrogen and stored at -20°C in RNAse – free lab.

For 4 mM Amino Acid Mix and 16.7 mM RCWMDE Mix preparation	
Component Amino Acid (AA) - MW (g/M)	**Volume (mL of dd H_2O) Stocks at 100 mM**
Glycine (G) - 75.07	10.9
Lysine (K) - 182.65	3.88
Proline (P) - 115.13	10.94
Leucine (L) - 131.18	6.74
Threonine (T) - 119.12	12.17
Valine (V) - 117.15	5
Phenylalanine (F) - 165.19	5.36
Serine (S) - 105.9	4.88
Histidine (H) - 209.63	9.4
Alanine (A) - 89.09	9.2
Isoleucine (I) - 131. 18	4.3
Glutamine (Q) - 146.15	3.36
Arginine (R) - 210.66	5.79
Tyrosine (Y) - 181.19	14.6 (stock at 20 mM)

Table 2 List of amino acids dissolved in distilled H_2O at 100 mM concentration.

For 4 mM Amino Acid Mix and 16.7 mM RCWMDE Mix preparation	
Component Amino Acid (AA) - MW (g/M)	**Volume (mL of 100 mM HEPES pH 7.4) Stocks at 100 mM**
Asparagine (N) - 132.12	7.75
Tryptophan (W) - 204.23	4.5
Aspartic Acid (D) - 133.1	5.5
Glutamic Acid (E) - 147.13	5.43
Methionine (M) - 149.21	4.02
Cysteine (C) - 157.61	13.7

Table 3 List of amino acids dissolved in 100 mM HEPES pH 7.4.

3. Feeding Mix Solution

Feeding Mix Solution belongs to the main Feeding Mixture in Cell–Free expression system and it consists in the following components (see Table 4):

Feeding Mix Solution - 50 mL (10 mL aliquots)	
Component	**Volume (mL), Stock**
620 mM HEPES pH 7.5 (*Sigma - Aldrich*)	15.435 (2 M)
3.5 mM Dithiothreitol (DTT) (Euromedex)	0.176 (1 M)
1.7 mM Uridine-5'-triphosphate (UTP) (*Sigma - Aldrich*)	0.17 (0.5 M)
1.7 mM Cytidine triphosphate (CTP) (*Sigma - Aldrich*)	0.17 (0.5 M)
1.7 mM Guanosine-5'-triphosphate (GTP) (*Sigma - Aldrich*)	0.17 (0.5 M)
2.5 mM Adenosine triphosphate (ATP) (*Sigma - Aldrich*)	0.122 (1 M)
1 mM Amino Acid Mix**(*Sigma - Aldrich*)	12.5 (4 mM)
3.8% PEG 8000 (*Sigma - Aldrich*)	3.8 (50%)
70 µg/mL Folic Acid (*Sigma - Aldrich*)	0.346 10 (mg/mL)
1.3 mM Cyclic adenosine monophosphate (CAMP)	0.16 (0.4 M)
2 mM RCWMDE****** (*Sigma - Aldrich*)	5.985 (16.7 mM)
100 mM Acethyl Phosphate (*Sigma - Aldrich*)	5 (1 M)
72 mM Ammonium Acetate	1.2 (3 M)
ddH_2O	to fill up to 50 mL

**** - see list of components in Table 2 and 3 in Annex 2**
******** - RCWMDE Mix is a mixture of following amino acids: Arginine, Cysteine, Tryptophan, Methionine, Aspartic Acid and Glutamic Acid at 100 mM concentration in the proportion 1:1:1:1:1:1.**

Table 4 Composition of Feeding Mix Solution for Cell–Free expression.

ANNEX 3: Lists of detergents and inhibitors

1. Detergents

Majority of used detergents were purchased from *Anatrace*, except Brij35 (*Sigma-Aldrich*).

Detergent	MW	CMC_{H2O} (%)	Chemical Formula
Brij*35	1225	0.011	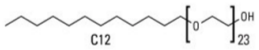
Cymal5	494.5	0.12	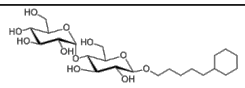
Cymal6	508.5	0.028	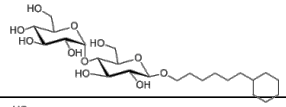
n-Dodecyl-b-D-Maltopyranoside (DDM)	510.6	0.0087	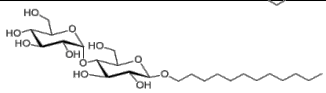
Lauryl Maltose Neopentyl Glycol (LMNG, MNG-3)	1005.19	0.001	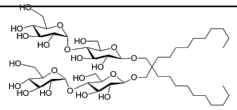
Fos-Cholie-12 (FC12)	351.5	0.047	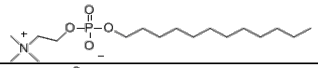
Fos-choline-16 (FC16)	407.5	0.00053	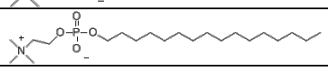
N,N-dimethyldodecylamine N-oxide (LDAO)	229.4	0.023	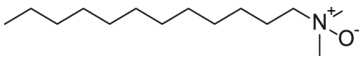
C12E9	583	0.003	
CHAPS	614.9	0.49	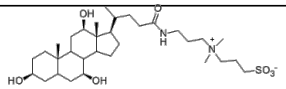
OG	292.4	0.53	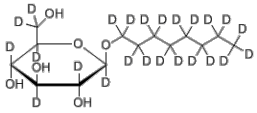
LAPAO	300.6	0.052	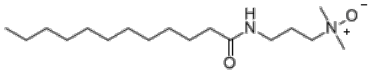

2. Inhibitors

Majority of used inhibitors were purchased from *Sigma-Aldrich*, except Leelamine (*Abcam*).

Inhibitor	MW	Chemical Formula
CD437	398.47	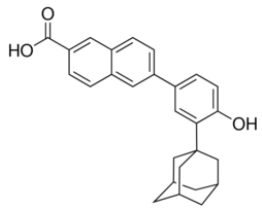
Closantel	663.07	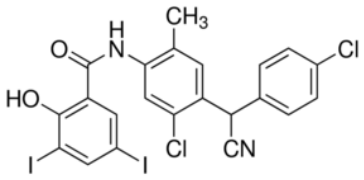
Leelamine	285.5	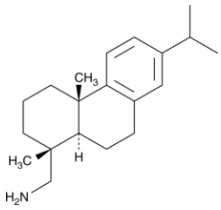
Chebulinic acid	956.67	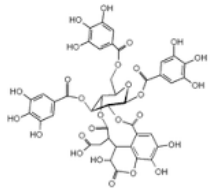
Suramin	1429.17	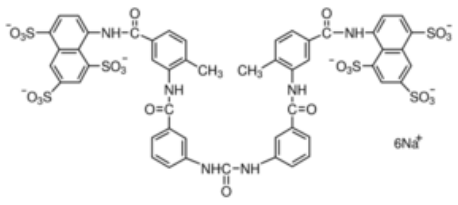

7 REFERENCES

1. Friedman, M. H. *Principles and models of Biological Transport*. *PhD Proposal* **1,** (Springer, 2015).
2. Pratt, Charlotte Amerley; Voet, Donald; Voet, J. G. *Fundamentals of biochemistry upgrade*. (2002).
3. Lodish, H., Berk, S. A., Zipursky, L., Matsudaira, P., Baltimore D., and Darnell, J. *Molecular Cell Biology*. (2000).
4. Deng, D. *et al.* Crystal structure of the human glucose transporter GLUT1. *Nature* **510,** 121–125 (2014).
5. Xu, J. C. *et al.* Molecular cloning and functional expression of the bumetanide-sensitive Na-K-Cl cotransporter. *Proc. Natl. Acad. Sci. U. S. A.* **91,** 2201–2205 (1994).
6. Hebert, S. C., Mount, D. B. & Gamba, G. Molecular physiology of cation-coupled Cl- cotransport: The SLC12 family. *Pflugers Arch. Eur. J. Physiol.* **447,** 580–593 (2004).
7. Faham, S., Watanabe, A., Besserer, G. B., Cascio, D., Specht, A., Hirayama, B. A. Wright, E. M., Abramson, J. The Crystal Structure of a Sodium Galactose Transporter Reveals Mechanistic Insights into Na+/Sugar Symport. *Science (80-.).* **321,** 810–814 (2008).
8. Watanabe, A. *et al.* The mechanism of sodium and substrate release from the binding pocket of vSGLT. *Nature* **468,** 988–91 (2010).
9. Krishnamurthy, H. & Gouaux, E. X-ray structures of LeuT in substrate-free outward-open and apo inward-open states. *Nature* **481,** 469–74 (2012).
10. Liao, J. *et al.* Structural Insight into the Sodium / Calcium Exchanger. *Science (80-.).* **335,** 686 (2012).
11. Hunte, C. *et al.* Structure of a Na+/H+ antiporter and insights into mechanism of action and regulation by pH. *Nature* **435,** 1197–1202 (2005).
12. Screpanti, E., Padan, E., Rimon, A., Michel, H. & Hunte, C. Crucial Steps in the Structure Determination of the Na+/H+ Antiporter NhaA in its Native Conformation. *J. Mol. Biol.* **362,** 192–202 (2006).
13. Kelly, L. J. *Essentials of Human Physiology*. (CRC PRESS, 2005).
14. Nyblom, M. *et al.* Crystall Structure of Na+, K+-ATPase in the Na+ Bound State. *Science (80-.).* **366,** 123–127 (2013).
15. Kanai, R., Ogawa, H., Vilsen, B., Cornelius, F. & Toyoshima, C. Crystal structure of a Na+-bound Na+,K+-ATPase preceding the E1P state. *Nature* **502,** 201–6 (2013).
16. Rees, D. C., Johnson, E. & Lewinson, O. ABC transporters: the power to change. *Nat. Rev. Mol. Cell Biol.* **10,** 218–227 (2009).
17. Persidis, A. Cancer multidrug resistance. *Nat. Biotechnol.* **17,** 94–95 (1999).
18. Parcej, D. & Tampe, R. ABC proteins in antigen translocation and viral inhibition. *Nat Chem Biol* **6,** 572–580 (2010).
19. Oldham, M. L., Khare, D., Quiocho, F. A., Davidson, A. L. & Chen, J. Crystal structure of a catalytic intermediate of the maltose transporter. *Nature* **450,** 515–521 (2007).
20. Hvorup, R. N. *et al.* Asymmetry in the Structure of the ABC Transporter-Binding Protein Complex BtuCD-BtuF. *Science (80-.).* **317,** 1387–1391

(2007).
21. Dawson, R. J. P. & Locher, K. P. Structure of a bacterial multidrug ABC transporter. *Nature* **443,** 180–185 (2006).
22. Chang, G. & Roth, C. B. Structure of MsbA from E. coli: a homolog of the multidrug resistance ATP binding cassette (ABC) transporters. *Science (80-.).* **293,** 1793–800. (2001).
23. Schmitt, L., Benabdelhak, H., Blight, M. A., Holland, I. B. & Stubbs, M. T. Crystal structure of the nucleotide-binding domain of the ABC-transporter haemolysin B: Identification of a variable region within ABC helical domains. *J. Mol. Biol.* **330,** 333–342 (2003).
24. Karpowich, N. *et al.* Crystal structures of the MJ1267 ATP binding cassette reveal an induced-fit effect at the ATPase active site of an ABC transporter. *Structure* **9,** 571–586 (2001).
25. Slotboom, D. J. Structural and mechanistic insights into prokaryotic energy-coupling factor transporters. *Nat. Rev. Microbiol.* **12,** 79–87 (2014).
26. Abramson, J., Smirnova, I., Kasho, V., Verner, H. G., Kaback, R., I. S. Structure and Mechanism of the Lactose Permease of Escherichia coli. *Science (80-.).* **301,** 610–615 (2003).
27. Hohl, M., Briand, C., Grütter, M. G. & Seeger, M. a. Crystal structure of a heterodimeric ABC transporter in its inward-facing conformation. *Nat. Struct. Mol. Biol.* **19,** 395–402 (2012).
28. Forrest, R. L., Rudnick, G. The Rocking Bundle: A Mechanism for Ion-Coupled Solute Flux by Symmetrical Transporters. **24,** 377–386 (2009).
29. Korkhov, V. M., Mireku, S. a, Veprintsev, D. B. & Locher, K. P. Structure of AMP-PNP-bound BtuCD and mechanism of ATP-powered vitamin B12 transport by BtuCD-F. *Nat. Struct. Mol. Biol.* **21,** 1097–9 (2014).
30. Reyes, N., Ginter, C. & Boudker, O. Transport mechanism of a bacterial homologue of glutamate transporters. *Nature* **462,** 880–5 (2009).
31. Xu, K. *et al.* Crystal structure of a folate energy-coupling factor transporter from Lactobacillus brevis. *Nature* **497,** 268–71 (2013).
32. Okamoto, K. & Shaw, J. M. Mitochondrial morphology and dynamics in yeast and multicellular eukaryotes. *Annu. Rev. Genet.* **39,** 503–536 (2005).
33. Bereiter-Hahn, J. & Vöth, M. Dynamics of mitochondria in living cells: shape changes, dislocations, fusion, and fission of mitochondria. *Microsc. Res. Tech.* **27,** 198–219 (1994).
34. Alberts, B., Johnson, A., Lewis, J., Raff, M., Roberts, K., Walter, P. *Molecular Biology of the Cell*. (Garland Publishing Inc, 1994).
35. Mannella, C. a *et al.* Topology of the mitochondrial inner membrane: dynamics and bioenergetic implications. *IUBMB Life* **52,** 93–100 (2001).
36. Shoshan-Barmatz, V. & Mizrachi, D. VDAC1: from structure to cancer therapy. *Front. Oncol.* **2,** 164 (2012).
37. Ujwal, R. *et al.* The crystal structure of mouse VDAC1 at 2.3 A resolution reveals mechanistic insights into metabolite gating. *Proc. Natl. Acad. Sci. U. S. A.* **105,** 17742–7 (2008).
38. Chipuk, J. E., Bouchier-Hayes, L. & Green, D. R. Mitochondrial outer membrane permeabilization during apoptosis: the innocent bystander scenario. *Cell Death Differ.* **13,** 1396–1402 (2006).
39. Hayashi, T., Rizzuto, R., Hajnoczky, G. & Su, T. P. MAM: more than just a housekeeper. *Trends Cell Biol.* **19,** 81–88 (2009).

40. McMillin, J. B. & Dowhan, W. Cardiolipin and apoptosis. *Biochim. Biophys. Acta - Mol. Cell Biol. Lipids* **1585,** 97–107 (2002).
41. Palmieri, F. Diseases caused by defects of mitochondrial carriers: A review. *Biochim. Biophys. Acta - Bioenerg.* **1777,** 564–578 (2008).
42. Voet, D., Voet, J. G., Pratt, C. W. *Fundamentals of Biochemistry*. (John Wiley and Sons, 2006).
43. Green, D. R. Apoptic pathways: The roads to ruin. *Cell* **94,** 695–698 (1998).
44. Hajnoczky, G. *et al.* Mitochondrial calcium signaling and cell death: approaches for assessing the role of mitochondrial Ca2+ uptake in apoptosis. *Cell* **40,** 553–560 (2009).
45. McBride, H. M., Neuspiel, M. & Wasiak, S. Mitochondria: More Than Just a Powerhouse. *Curr. Biol.* **16,** 551–560 (2006).
46. Li, X. *et al.* Targeting mitochondrial reactive oxygen species as novel therapy for inflammatory diseases and cancers. *J. Hematol. Oncol.* **6,** 19 (2013).
47. Rossier, M. F. T channels and steroid biosynthesis: in search of a link with mitochondria. *Cell Calcium* **40,** 155–164 (2006).
48. Klinge, C. M. Estrogenic control of mitochondrial function and biogenesis. *J. Cell. Biochem.* **105,** 1342–1351 (2008).
49. Palmieri, F. The mitochondrial transporter family (SLC25): Physiological and pathological implications. *Pflugers Arch. Eur. J. Physiol.* **447,** 689–709 (2004).
50. Palmieri, F. *et al.* Identification of mitochondrial carriers in Saccharomyces cerevisiae by transport assay of reconstituted recombinant proteins. *Biochim. Biophys. Acta - Bioenerg.* **1757,** 1249–1262 (2006).
51. Palmieri, F. & Pierri, C. L. Structure and function of mitochondrial carriers - Role of the transmembrane helix P and G residues in the gating and transport mechanism. *FEBS Lett.* **584,** 1931–1939 (2010).
52. Robinson, A. J. & Kunji, E. R. S. Mitochondrial carriers in the cytoplasmic state have a common substrate binding site. *Proc. Natl. Acad. Sci. U. S. A.* **103,** 2617–22 (2006).
53. Hartl, F. U. Molecular Chaperones in the Cytosol: from Nascent Chain to Folded Protein. *Science (80-.).* **295,** 1852–1858 (2002).
54. Young, J. C., Agashe, V. R., Siegers, K. & Hartl, F. U. Pathways of chaperone-mediated protein folding in the cytosol. *Nat. Rev. Mol. Cell Biol.* **5,** 781–791 (2004).
55. Rehling, P., Brandner, K. & Pfanner, N. Mitochondrial import and the twin-pore translocase. *Nat. Rev. Mol. Cell Biol.* **5,** 519–530 (2004).
56. Neupert, W. & Herrmann, J. M. Translocation of proteins into mitochondria. *Annu. Rev. Biochem.* **76,** 723–749 (2007).
57. Thuswaldner, S. *et al.* Identification, expression, and functional analyses of a thylakoid ATP/ADP carrier from Arabidopsis. *J. Biol. Chem.* **282,** 8848–8859 (2007).
58. Palmieri, L. *et al.* Identification and functional reconstitution of the yeast peroxisomal adenine nucleotide transporter. *EMBO J.* **20,** 5049–5059 (2001).
59. Palmieri, F. *et al.* Molecular identification and functional characterization of Arabidopsis thaliana mitochondrial and chloroplastic NAD+ carrier proteins. *J. Biol. Chem.* **284,** 31249–31259 (2009).

60. Monné, M. *et al.* The mimivirus genome encodes a mitochondrial carrier that transports dATP and dTTP. *J Virol* **81,** 3181–6 (2007).
61. Rieder, B. & Neuhaus, H. E. Identification of an Arabidopsis plasma membrane-located ATP transporter important for anther development. *Plant Cell* **23,** 1932–1944 (2011).
62. Saraste, M. & Walker, J. E. Internal sequence repeats and the path of polypeptide in mitochondrial ADP/ATP translocase. *FEBS Lett.* **144,** 250–254 (1982).
63. Walker, J. E. & Runswick, M. J. The mitochondrial transport protein superfamily. *J. Bioenerg. Biomembr.* **25,** 435–446 (1993).
64. Kunji, E. R. S. & Robinson, A. J. The conserved substrate binding site of mitochondrial carriers. *Biochim. Biophys. Acta - Bioenerg.* **1757,** 1237–1248 (2006).
65. Brenner, C., Subramaniam, K., Pertuiset, C. & Pervaiz, S. Adenine nucleotide translocase family: four isoforms for apoptosis modulation in cancer. *Oncogene* **30,** 883–895 (2011).
66. Kunji, E. R. S. *et al.* The transport mechanism of the mitochondrial ADP/ATP carrier. *Biochim. Biophys. Acta - Mol. Cell Res.* (2016). doi:10.1016/j.bbamcr.2016.03.015
67. Klingenberg, M. The ADP and ATP transport in mitochondria and its carrier. *Biochim. Biophys. Acta - Biomembr.* **1778,** 1978–2021 (2008).
68. Kaukonen, J. *et al.* Role of adenine nucleotide translocator 1 in mtDNA maintenance. *Sci. (New York, NY)* **289,** 782–785 (2000).
69. Brunel-Guitton, C., Levtova, A. & Sasarman, F. Mitochondrial Diseases and Cardiomyopathies. *Can. J. Cardiol.* **31,** 1360–1376 (2015).
70. Siciliano, G. *et al.* Autosomal dominant external ophthalmoplegia and bipolar affective disorder associated with a mutation in the ANT1 gene. *Neuromuscul. Disord.* **13,** 162–165 (2003).
71. Jordens, E. Z. *et al.* Adenine nucleotide translocator 1 deficiency associated with Sengers syndrome. *Ann. Neurol.* **52,** 95–99 (2002).
72. Palmieri, L. *et al.* Complete loss-of-function of the heart/muscle-specific adenine nucleotide translocator is associated with mitochondrial myopathy and cardiomyopathy. *Hum. Mol. Genet.* **14,** 3079–3088 (2005).
73. Wallace, D. C. Mitochondrial diseases in man and mouse. *Science (80-.).* **283,** 1482–1488 (1999).
74. Klingenberg, M. Molecular aspects of the adenine nucleotide carrier from mitochondria. *Arch. Biochem. Biophys.* **270,** 1–14 (1989).
75. Fiore, C. *et al.* The mitochondrial ADP/ATP carrier: Structural, physiological and pathological aspects. *Biochimie* **80,** 137–150 (1998).
76. Aquila, H., Misra, D., Eulitz, M., Klingenberg, M. Complete aminoacid sequence of the ADP/ATP carrier from beef heart mitochondria. *HFSP J.* **363,** 345–349 (1982).
77. Pebay-Peyroula, E. *et al.* Structure of mitochondrial ADP/ATP carrier in complex with carboxyatractyloside. *Nature* **426,** 39–44 (2003).
78. Nelson, D. R., Felix, C. M. & Swanson, J. M. Highly conserved charge-pair networks in the mitochondrial carrier family. *J. Mol. Biol.* **277,** 285–308 (1998).
79. King, M. S., Kerr, M., Crichton, P. G., Springett, R. & Kunji, E. R. S. Formation of a cytoplasmic salt bridge network in the matrix state is a fundamental

step in the transport mechanism of the mitochondrial ADP/ATP carrier. *Biochim. Biophys. Acta - Bioenerg.* **1857,** 14–22 (2016).
80. Nury, H. *et al.* Relations between structure and function of the mitochondrial ADP/ATP carrier. *Annu. Rev. Biochem.* **75,** 713–741 (2006).
81. Kunji, E. R. S. & Harding, M. Projection structure of the atractyloside-inhibited mitochondrial ADP/ATP carrier of Saccharomyces cerevisiae. *J. Biol. Chem.* **278,** 36985–36988 (2003).
82. Nury, H. *et al.* Structural basis for lipid-mediated interactions between mitochondrial ADP/ATP carrier monomers. *FEBS Lett.* **579,** 6031–6036 (2005).
83. Ruprecht, J. J. *et al.* Structures of yeast mitochondrial ADP/ATP carriers support a domain-based alternating-access transport mechanism. *Proc. Natl. Acad. Sci. U. S. A.* **111,** E426–34 (2014).
84. Berardi, M. J., Shih, W. M., Harrison, S. C. & Chou, J. J. Mitochondrial uncoupling protein 2 structure determined by NMR molecular fragment searching. *Nature* **476,** 109–13 (2011).
85. Zoonens, M. *et al.* Dangerous Liaisons between detergents and membrane proteins. the case of mitochondrial uncoupling protein 2. *J. Am. Chem. Soc.* **135,** 15174–15182 (2013).
86. Luciani, R. *Atractyloside: Chemistry, Biochemistry and Toxicology*. (1978).
87. Danieli, B., Bombardelli, E., Bonati, A., and Gabetta, B. *Carboxyatractyloside, a new glycoside from Atractylis gummifera*. (1971).
88. Craig, J. C., Mole, M., Billets, S. & El-Feraly, F. Isolation and identification of hypoglycemic agent carboxyatractylate from Xanthium strumarium. *Phytochemistry* **15,** 1178 (1976).
89. Candy, H. A., Pegel, K. H., Brookes, B. & Rodwell, M. The occurrence of atractyloside in Callilepsis laureola. *Phytochemistry* **16,** 1308–1309 (1977).
90. Grebe, K., Riccio, P. & Klingenberg, M. Atractylis gummifera. **31,** 15–19 (1973).
91. Henderson, P. J., Lardy, A. H. Bongkrekic acid. An inhibitor of the adenine nucleotide translocase of mitochondria. *J. Biol. Chem* **245,** 1319–1326 (1970).
92. Zhang, Y. *et al.* Human Adenine Nucleotide Translocase (ANT) Modulators Identified by High-Throughput Screening of Transgenic Yeast. *J. Biomol. Screen.* 1–7 (2016). at <http://jbx.sagepub.com/cgi/doi/10.1177/1087057115624637>
93. Brandolin, G., Le Saux, A., Trezeguet, V., Lauquin, G. J. M. & Vignais, P. V. Chemical, immunological, enzymatic, and genetic approaches to studying the arrangement of the peptide chain of the ADP/ATP carrier in the mitochondrial membrane. *J. Bioenerg. Biomembr.* **25,** 459–472 (1993).
94. Mifsud, J. *et al.* The substrate specificity of the human ADP/ATP carrier AAC1. *Mol. Membr. Biol.* **30,** 160–8 (2013).
95. Vignais, P.V., Block, M.R., Boulay, F., Brandolin, G., and Lauquin, G. J.-M. Molecular aspects of sutrcture-function relationships in mitochondrial adnine nucleotide carrier. *Struct. Propr. Cell Mambranes* **2,** 139–179 (1985).
96. Klingenberg, M. The ADP/ATP carrier in mitochondrial membranes. In. *Enzym. Biol. Membr. Membr. Transp.* 383–438. (1976).

97. Pfaff, E., Klingenberg, M., and Heldt, H. W. Unspecific permeation and specific exchange of adenine nucleotides in liver mitochondria. *Biochim Biophys Acta* **104,** 312–315 (1965).
98. Brandolin, G. *et al.* Kinetic, binding and ultrastructural properties of the beef heart adenine nucleotide carrier protein after incorporation into phospholipid vesicles. *Biochim. Biophys. Acta - Bioenerg.* **592,** 592–614 (1980).
99. Duee, E.D., and Vignais, P. V. Exchange between extra- and intramitochondrial adenine nucleotides. *Biochim Biophys Acta* **107,** 184–188 (1965).
100. Brustovetsky, N., Becker, A., Klingenberg, M. & Bamberg, E. Electrical currents associated with nucleotide transport by the reconstituted mitochondrial ADP/ATP carrier. *Proc. Natl. Acad. Sci. U. S. A.* **93,** 664–8 (1996).
101. Duyckaerts, C., Sluse-Goffart, C. M., Fux, J. P., Sluse, F. E. & Liebecq, C. Kinetic mechanism of the exchanges catalysed by the adenine-nucleotide carrier. *Eur. J. Biochem.* **106,** 1–6 (1980).
102. Barbour, R.L., and Chan, S. H. Characterization of the kinetics and mechanism of the mitochondrial ADP-ATP Carrier. *J Biol Chem* **256,** 1940–1948 (1981).
103. Pebay-Peyroula, E. & Brandolin, G. Nucleotide exchange in mitochondria: Insight at a molecular level. *Curr. Opin. Struct. Biol.* **14,** 420–425 (2004).
104. Dehez, F., Pebay-Peyroula, E. & Chipot, C. Binding of ADP in the mitochondrial ADP/ATP carrier is driven by an electrostatic funnel. *J. Am. Chem. Soc.* **130,** 12725–33 (2008).
105. Kunji, E. R. S. & Robinson, A. J. The transport mechanism of mitochondrial carriers based on the analysis of pseudo-symmetry. *Biochim. Biophys. Acta - Bioenerg.* **1797,** 41–42 (2010).
106. Riccio, P., Aquila, H., and Klingenberg, M. Purification of the carboxy-atractylate binding protein from mitochondria. *FEBS Lett* **56,** 133–138 (1975).
107. Hackenberg, H., and Klingenberg, M. Molecular weight and hydrodynamic parameters of the adenosine 5'-diphosphate--adenosine 5'-triphosphate carrier in Triton X- 100. *Biochemistry* **19,** 548–555 (1980).
108. Block, M.R., Zaccai, G., Lauquin, G.J., and Vignais, P. V. Small angle neutron scattering of the mitochondrial ADP/ATP carrier protein in detergent. *Biochem Biophys Res Commun* **109,** 471–477 (1982).
109. Majima, E. *et al.* Translocation of loops regulates transport activity of mitochondrial ADP/ATP carrier deduced from formation of a specific intermolecular disulfide bridge catalyzed by copper-o-phenanthroline. *J. Biol. Chem.* **270,** 29548–29554 (1995).
110. Hashimoto, M., Majima, E., Goto, S., Shinohara, Y. & Terada, H. Fluctuation of the first loop facing the matrix of the mitochondrial ADP/ATP carrier deduced from intermolecular cross-linking of Cys56 residues by bifunctional dimaleimides. *Biochemistry* **38,** 1050–1056 (1999).
111. Dyall, S. D., Agius, S. C., De Marcos Lousa, C., Trézéguet, V. & Tokatlidis, K. The dynamic dimerization of the yeast ADP/ATP carrier in the inner mitochondrial membrane is affected by conserved cysteine residues. *J. Biol. Chem.* **278,** 26757–26764 (2003).

112. Faustin, B. *et al.* Mobilization of Adenine Nucleotide Translocators as Molecular Bases of the Biochemical Threshold Effect Observed in Mitochondrial Diseases. *J. Biol. Chem.* **279,** 20411–20421 (2004).
113. Hatanaka, T., Hashimoto, M., Majima, E., Shinohara, Y. & Terada, H. Functional expression of the tandem-repeated homodimer of the mitochondrial ADP/ATP carrier in Saccharomyces cerevisiae. *Biochem. Biophys. Res. Commun.* **262,** 726–30 (1999).
114. Trézéguet, V. *et al.* A covalent tandem dimer of the mitochondrial ADP/ATP carrier is functional in vivo. *Biochim. Biophys. Acta - Bioenerg.* **1457,** 81–93 (2000).
115. Huang, S. G., Odoy, S. & Klingenberg, M. Chimers of two fused ADP/ATP carrier monomers indicate a single channel for ADP/ATP transport. *Arch. Biochem. Biophys.* **394,** 67–75 (2001).
116. Block, M.R., and Vignais, P. V. Substrate-site interactions in the membrane-bound adenine-nucleotide carrier as disclosed by ADP and ATP analogs. *Biochim Biophys Acta* **767,** 369–376 (1984).
117. Nury, H. *et al.* Mitochondrial bovine ADP/ATP carrier in detergent is predominantly monomeric but also forms multimeric species. *Biochemistry* **47,** 12319–12331 (2008).
118. Bamber, L., Slotboom, D.-J. & Kunji, E. R. S. Yeast mitochondrial ADP/ATP carriers are monomeric in detergents as demonstrated by differential affinity purification. *J. Mol. Biol.* **371,** 388–95 (2007).
119. Bamber, L., Harding, M., Monné, M., Slotboom, D.-J. & Kunji, E. R. S. The yeast mitochondrial ADP/ATP carrier functions as a monomer in mitochondrial membranes. *Proc. Natl. Acad. Sci. U. S. A.* **104,** 10830–10834 (2007).
120. Kunji, E. R. S. & Crichton, P. G. Mitochondrial carriers function as monomers. *Biochim. Biophys. Acta* **1797,** 817–31 (2010).
121. Guernsey, D. L. *et al.* Mutations in mitochondrial carrier family gene SLC25A38 cause nonsyndromic autosomal recessive congenital sideroblastic anemia. *Nat. Genet.* **41,** 651–653 (2009).
122. Ravaud, S. *et al.* Impaired transport of nucleotides in a mitochondrial carrier explains severe human genetic diseases. *ACS Chem. Biol.* **7,** 1164–9 (2012).
123. Komaki, H., Fukazawa, T., Houzen, H., Yoshida, K., Nonaka, I. & and Goto, Y. A novel D104G mutation in the adenine nucleotide translocator 1 gene in autosomal dominant progressive external ophthalmoplegia patients with mitochondrial DNA with multiple deletions. *Ann. Neurol.* **51,** 645–648 (2002).
124. Deschauer, M. *et al.* A novel ANT1 gene mutation with probable germline mosaicism in autosomal dominant progressive external ophthalmoplegia. *Neuromuscul. Disord.* **15,** 311–315 (2005).
125. Cozens, A. L., Runswick, M. J. & Walker, J. E. DNA sequences of two expressed nuclear genes for human mitochondrial ADP/ATP translocase. *J. Mol. Biol.* **206,** (1989).
126. Li, K. *et al.* A human muscle adenine nucleotide translocator gene has four exons, is located on chromosome 4, and is differentially expressed. *J. Biol. Chem.* **264,** 13998–14004 (1989).
127. De-Hui, Ku, Jacob Kagan, S.-T., Chen, C.-D., Chang, R. B. and J. & Wurzel.

Adenine Nucleotide Translocator. **265,** 16060–16063 (1990).
128. Lunardi, J. & Attardi, G. Differential regulation of expression of the multiple ADP/ATP translocase genes in human cells. *J. Biol. Chem.* **266,** 16534–40 (1991).
129. Stepien, G. Differential expression of adenine nucleotide translocator isoforms in mammalian tissues and during muscle cell differentiation. *J. Biol. Chem.* **267,** 14592–14597 (1992).
130. Faure, V. H., Heddi, A., Giraud, S., Chautard, D., Stepien, G. Expression of oxidative phosphorylation genes in renal tumors and tumoral cell lines. *Mol Carcinog* **16,** 165–172 (1996).
131. Giraud, S., Bonod-Bidaud, C., Wesolowski-Louvel, M. & Stepien, G. Expression of human ANT2 gene in highly proliferative cells: GRBOX, a new transcriptional element, is involved in the regulation of glycolytic ATP import into mitochondria. *J. Mol. Biol.* **281,** 409–418 (1998).
132. Le Bras M, Borgne-Sanchez A, Touat Z, Sharaf el dein O, D. A. & Of, M. E. et al. Chemosensitization by knock-down of adenine nucleotide translocase-2. *Cancer Res* **66,** 9143–9152 (2006).
133. Dolce, V., Scarcia, P., Iacopetta, D. & Palmieri, F. A fourth ADP/ATP carrier isoform in man: identification, bacterial expression, functional characterization and tissue distribution. *FEBS Lett.* **579,** 633–7 (2005).
134. Hashimoto, M. *et al.* Expression of the bovine heart mitochondrial ADP/ATP carrier in yeast mitochondria: Significantly enhanced expression by replacement of the N-terminal region of the bovine carrier by the corresponding regions of the yeast carriers. *Biochim. Biophys. Acta - Bioenerg.* **1409,** 113–124 (1999).
135. Hatanaka, T. *et al.* Significant expression of functional human type 1 mitochondrial ADP/ATP carrier in yeast mitochondria. *Biol. Pharm. Bull.* **24,** 595–9 (2001).
136. Lousa, C. D. M. & Lauquin, G. J. The Human Mitochondrial ADP / ATP Carriers : Kinetic Properties and Biogenesis of Wild-Type and Mutant Proteins in the Yeast S. cerevisiae. *Biochemistry* **41,** 14412–14420 (2002).
137. Betina, S., Gavurníková, G., Haviernik, P., Sabová, L. & Kolarov, J. Expression of the AAC2 gene encoding the major mitochondrial ADP/ATP carrier in Saccharomyces cerevisiae is controlled at the transcriptional level by oxygen, heme and HAP2 factor. *European journal of biochemistry / FEBS* **229,** 651–657 (1995).
138. Hamazaki, T. *et al.* Functional expression of human adenine nucleotide translocase 4 in Saccharomyces cerevisiae. *PLoS One* **6,** (2011).
139. Belzacq, A-S., Brenner, C. The Adenine Nucleotide Translocator: A New Potential Chemotherapeutic Target. *Curr. Drug Targets* **4,** 517–524 (2003).
140. Doerner, A. *et al.* Tissue-specific transcription pattern of the adenine nucleotide translocase isoforms in humans. *FEBS Lett.* **414,** 258–262 (1997).
141. Brower, J. V. *et al.* Differential CpG island methylation of murine adenine nucleotide translocase genes. *Biochim. Biophys. Acta - Gene Regul. Mech.* **1789,** 198–203 (2009).
142. Neckelmann, N., Warner, C., Chung, A., Kudoh, J., Minoshima, S. & Fukuyama, R. The human ATP synthase beta subunit gene: sequence analysis, chromosome assignment, and differential expression. *Genomics* **5,**

829–843 (1989).
143. Bauer, M. K. A., Schubert, A., Rocks, O. & Grimm, S. Adenine nucleotide translocase-1, a component of the permeability transition pore, can dominantly induce apoptosis. *J. Cell Biol.* **147,** 1493–1501 (1999).
144. Zamora, M., Granell, M., Mampel, T. & Viñas, O. Adenine nucleotide translocase 3 (ANT3) overexpression induces apoptosis in cultured cells. *FEBS Lett.* **563,** 155–160 (2004).
145. Zamora, M., Meroño, C., Viñas, O. & Mampel, T. Recruitment of NF-κB into mitochondria is involved in adenine nucleotide translocase 1 (ANT1)-induced apoptosis. *J. Biol. Chem.* **279,** 38415–38423 (2004).
146. Baines, C. P. & Molkentin, J. D. Adenine nucleotide translocase-1 induces cardiomyocyte death through upregulation of the pro-apoptotic protein Bax. *J. Mol. Cell. Cardiol.* **46,** 969–977 (2009).
147. Jang, J.-Y., Choi, Y., Jeon, Y.-K. & Kim, C.-W. Suppression of adenine nucleotide translocase-2 by vector-based siRNA in human breast cancer cells induces apoptosis and inhibits tumor growth in vitro and in vivo. *Breast Cancer Res.* **10,** R11 (2008).
148. Li, R., Hodny, Z., Luciakova, K., Barath, P. & Dean Nelson, B. Sp1 activates and inhibits transcription from separate elements in the proximal promoter of the human adenine nucleotide translocase 2 (ANT2) gene. *J. Biol. Chem.* **271,** 18925–18930 (1996).
149. Barath, P., Poliakova, D., Luciakova, K. & Nelson, B. D. Identification of NF1 as a silencer protein of the human adenine nucleotide translocase-2 gene. *Eur. J. Biochem.* **271,** 1781–1788 (2004).
150. Chevrollier, A., Loiseau, D., Gautier, F., Malthièry, Y. & Stepien, G. ANT2 expression under hypoxic conditions produces opposite cell-cycle behavior in 143B and HepG2 cancer cells. *Mol. Carcinog.* **42,** 1–8 (2005).
151. Deniaud, E. *et al.* Overexpression of Sp1 transcription factor induces apoptosis. *Oncogene* **25,** 7096–7105 (2006).
152. Rodic, N., Oka, M., Hamazaki, T., Murawski, M., Jorgensen, M., Maatouk, D. DNA methylation is required for silencing of ant4, an adenine nucleotide translocase selectively expressed in mouse embryonic stem cells and germ cells. *Stem Cells* **23,** 1314–1323 (2005).
153. Kehoe, S. M. *et al.* A Conserved E2F6-Binding Element in Murine Meiosis-Specific Gene Promoters. *Biol. Reprod.* **79,** 921–930 (2008).
154. Gallerne, C. *et al.* The fourth isoform of the adenine nucleotide translocator inhibits mitochondrial apoptosis in cancer cells. *Int. J. Biochem. Cell Biol.* **42,** 623–629 (2010).
155. Cherezov, V. *et al.* High-Resolution Crystal Structure of an Engineered Human b 2 -Adrenergic. *Science (80-.).* **318,** 1258–1266 (2007).
156. Rasmussen, S. G. F. *et al.* Crystal structure of the β2 adrenergic receptor-Gs protein complex. *Nature* **477,** 549–55 (2011).
157. Gao, X., Lu, F., Zhou, L., Dang, S., Sun, L., Li, X., Wang, J., Shi, Y. Structure and Mechanism of an Amino Acid Antiporter. *Science* **325,** 1010–1014 (2009).
158. Shinoda, T., Ogawa, H., Cornelius, F. & Toyoshima, C. Crystal structure of the sodium-potassium pump at 2.4 A resolution. *Nature* **459,** 446–450 (2009).
159. Aller, S. G. *et al.* Structures of P-glycoproteins reveals a molecular basis for poly-specific drug binding. *Science (80-.).* **323,** 1718–1722 (2009).

160. Hilf, R. J. C. & Dutzler, R. Structure of a potentially open state of a proton-activated pentameric ligand-gated ion channel. *Nature* **457,** 115–118 (2009).
161. Bill, R. M. *et al.* Overcoming barriers to membrane protein structure determination. *Nat. Biotechnol.* **29,** 335–340 (2011).
162. Cusack, S. *et al.* Small is beautiful : protein micro-crystallography. (1998).
163. Evans, G., Axford, D., Waterman, D., Owen, R. L. Macromolecular microcrystallography. *Crystallogr. rev* **17,** 105–142 (2011).
164. Janet L. Smith, Robert F. Fischetti, and M. Y. Micro-crystallography comes of age. **22,** 602–612 (2012).
165. Riekel, C., Burghammer, M. & Schertler, G. Protein crystallography microdiffraction. *Curr. Opin. Struct. Biol.* **15,** 556–562 (2005).
166. Pebay-Peyroula, E., Rummel, G., Rosenbusch, J. P. & Landau, E. M. X-ray structure of bacteriorhodopsin at 2.5 angstroms from microcrystals grown in lipidic cubic phases. *Science* **277,** 1676–1681 (1997).
167. Spence, P. F. and J. C. Femtosecond nanocrystallography using X-ray lasers for membrane protein structure determination. *Curr. Opin. Struct. Biol.* **21,** 509–516 (2011).
168. Chapman, H. N. *et al.* Femtosecond X-ray protein nanocrystallography. *Nature* **470,** 73–77 (2011).
169. Schlichting, I. Serial femtosecond crystallography: The first five years. *IUCrJ* **2,** 246–255 (2015).
170. Emma, P. *et al.* First lasing and operation of an ångstrom-wavelength free-electron laser. *Nat. Photonics* **4,** 641–647 (2010).
171. Ishikawa, T. *et al.* A compact X-ray free-electron laser emitting in the sub-ångström region. *Nat. Photonics* **6,** 540–544 (2012).
172. Neutze, R., Brande, N, G. & Schertler, G. F. X. Membrane protein structural biology using X-ray free electron lasers. *Curr. Opin. Struct. Biol.* **33,** 115–125 (2015).
173. Schwarz, D., Dötsch, V. & Bernhard, F. Production of membrane proteins using cell-free expression systems. *Proteomics* **8,** 3933–3946 (2008).
174. Katzen, F., Peterson, T. C. & Kudlicki, W. Membrane protein expression: no cells required. *Trends Biotechnol.* **27,** 455–460 (2009).
175. Katzen, F., Chang, G. & Kudlicki, W. The past, present and future of cell-free protein synthesis. *Trends Biotechnol.* **23,** 150–156 (2005).
176. Zheng, X. *et al.* Expression , stabilization and puri fi cation of membrane proteins via diverse protein synthesis systems and detergents involving cell-free associated with self-assembly peptide surfactants. *Biotechnol. Adv.* **32,** 564–574 (2014).
177. Kim, H.-C. & Kim, D.-M. Methods for energizing cell-free protein synthesis. *J. Biosci. Bioeng.* **108,** 1–4 (2009).
178. He, M. Cell-free protein synthesis: applications in proteomics and biotechnology. *N. Biotechnol.* **25,** 126–132 (2008).
179. Fasman, G. D. *Circular Dichroism and the Conformational Analysis of Biomolecules*. (Springer US, 1996).
180. Alexandrov, A. I., Mileni, M., Chien, E. Y. T., Hanson, M. a & Stevens, R. C. Microscale fluorescent thermal stability assay for membrane proteins. *Structure* **16,** 351–9 (2008).
181. Kawate, T. & Gouaux, E. Fluorescence-Detection Size-Exclusion

Chromatography for Precrystallization Screening of Integral Membrane Proteins. *Structure* **14,** 673–681 (2006).
182. Hattori, M., Hibbs, R. E. & Gouaux, E. A Fluorescence-Detection Size-Exclusion Chromatography-Based Thermostability Assay for Membrane Protein Precrystallization Screening. *Struct. Ways Means* **20,** 1293–1299 (2012).
183. Slotboom, D. J., Duurkens, R. H., Olieman, K. & Erkens, G. B. Static light scattering to characterize membrane proteins in detergent solution. *Methods* **46,** 73–82 (2008).
184. Korepanova, A. & Matayoshi, E. D. HPLC-SEC characterization of membrane protein-detergent complexes. *Curr. Protoc. Protein Sci.* **Chapter 29,** Unit 29.5.1–12 (2012).
185. Ralston, G. & Ralston, G. *Introduction to Analytical Ultracentrifugation*. (1993).
186. Speicher KD, Gorman N, S. D. N-terminal sequence analysis of proteins and peptides. *Curr Protoc Protein Sci.* Chapter 11, Unit 11 (2009).
187. Laouini, A., Jaafar-Maalej, C., Limayem-Blouza, I., Sfar, S., Charcosset, C., Fessi, H. Preparation, Characterization and Applications of Liposomes: State of the Art. *J. Colloid Sci. Biotechnol.* **1,** 147–168 (2012).
188. Dua, J. S., Rana, A. C. & Bhandari, A. K. LIPOSOME : METHODS OF PREPARATION AND APPLICATIONS. *Int. J. Pharm. Stud. Res. E* **III,** 14–20 (2012).
189. Landau, E. M. & Rosenbusch, J. P. Lipidic cubic phases: a novel concept for the crystallization of membrane proteins. *Proc. Natl. Acad. Sci. U. S. A.* **93,** 14532–14535 (1996).
190. Cherezov, V. Lipidic cubic phase technologies for membrane protein structural studies. *Current Opinion in Structural Biology* **21,** 559–566 (2011).
191. Cherezov, V., Liu, J., Griffith, M., Hanson, M. A. & Stevens, R. C. Assay for Pre-Screening Membrane Proteins for in Meso Crystallization. **8,** 4307–4315 (2009).
192. Chayen, N. E. Comparative studies of protein crystallization by vapour-diffusion and microbatch techniques. *Acta Crystallogr. Sect. D Biol. Crystallogr.* **54,** 8–15 (1998).
193. Murakami, S., Nakashima, R., Yamashita, E. & Yamaguchi, A. Crystal structure of bacterial multidrug efflux transporter AcrB. *Nature* **419,** 587–593 (2002).
194. Bocquet, N. *et al.* X-ray structure of a pentameric ligand-gated ion channel in an apparently open conformation. *Nature* **457,** 111–114 (2009).
195. Hassaine, G. *et al.* X-ray structure of the mouse serotonin 5-HT3 receptor. *Nature* **512,** 276–281 (2014).
196. Hassaine, G. *et al.* Large scale expression and purification of the mouse 5-HT3 receptor. *Biochim. Biophys. Acta - Biomembr.* **1828,** 2544–2554 (2013).
197. Cipriani, F. *et al.* CrystalDirect: A new method for automated crystal harvesting based on laser-induced photoablation of thin films. *Acta Crystallogr. Sect. D Biol. Crystallogr.* **68,** 1393–1399 (2012).
198. Zander, U. *et al.* Automated harvesting and processing of protein crystals through laser photoablation. *Acta Crystallogr. Sect. D Struct. Biol.* **72,** 454–

466 (2016).
199. Coquelle, N. *et al.* Raster -scanning protein crystallography using micro and nano-focused synchrotron beams. *Acta Crystallogr. Sect. D Biol. Crystallogr.* (2014).
200. Weierstall, U. *et al.* Lipidic cubic phase injector facilitates membrane protein serial femtosecond crystallography. *Nat. Commun.* **5,** 3309 (2014).
201. Liu, W., Ishchenko, A. & Cherezov, V. Preparation of microcrystals in lipidic cubic phase for serial femtosecond crystallography. *Nat. Protoc.* **9,** 2123–2134 (2014).
202. Chanal, A. B., Krammer, E-M., Blot, D., Pebay-Peyroula, E., Chipot, C., Ravaud, S., D. F. How Do Membrane Transporters Sense pH? The Case of the Mitochondrial ADP–ATP Carrier. *J. Phys. Chem. Lett. Am. Chem. Soc.* **4,** 3787–3791 (2013).
203. Todisco, S. *et al.* Identification of new highly selective inhibitors of the human ADP/ATP carriers by molecular docking and in vitro transport assays. *Biochem. Pharmacol.* **100,** 112–132 (2015).
204. Komaki, H., Fukazawa, T., Houzen, H., Yoshida, K. & Nonaka, I., and Goto, Y. A Novel D104G Mutation in the Adenine Nucleotide Translocator 1 Gene in Autosomal Dominant Progressive External Ophthalmoplegia Patients with Mitochondrial DNA with Multiple Deletions. *Ann. Neurol.* **51,** 645–648 (2002).
205. Mdllerl, J. V, Maire, M., Pierre, I. U., Paris, C. & Yvette, F.-G.-. Detergent Binding as a Measure of Hydrophobic Surface Area of Integral Membrane Proteins. **268,** 18659–18672 (1993).
206. Greenfield, N. J. Using circular dichroism collected as a funcion of temperature to determine the thermodynamics of protein unfolding and binding interactions. *Nat. Protoc.* **1,** 2527–2535 (2009).
207. Weierstall, U. *et al.* Lipidic cubic phase injector facilitates membrane protein serial femtosecond crystallography. *Nat. Commun.* **5,** 3309 (2014).
208. Hatanaka, T., Hashimoto, M., Majima, E., Shinohara, Y. & Terada, H. Significant Effect of the N-terminal Region of the Mitochondrial ADP/ATP Carrier on Its Efficient Expression in Yeast Mitochondria. *J. Biol. Chem.* **276,** 28881–28888 (2001).
209. Fogeron, M.-L. *et al.* Functional expression, purification, characterization, and membrane reconstitution of non-structural protein 2 from hepatitis C virus. *Protein Expr. Purif.* **116,** 1–6 (2015).
210. Chae, P. S. *et al.* Maltose-neopentyl glycol (MNG) amphiphiles for solubilization, stabilization and crystallization of membrane proteins. *Nat. Methods* **7,** 1003–8 (2010).
211. White A. T., Kirian A. R., Martin V.A., Aquila A., Nass K., B. A. and C. W. . CrystFEL: a software for snapshot serial crystallography. *Appl. Crystallogr.* **45,** 335–341 (2012).
212. Sennhauser, G., Amstutz, P., Briand, C., Storchenegger, O. & Grütter, M. G. Drug export pathway of multidrug exporter AcrB revealed by DARPin inhibitors. *PLoS Biol.* **5,** 0106–0113 (2007).
213. Drew, D. *et al.* The structure of the efflux pump AcrB in complex with bile acid. *Mol. Membr. Biol.* **25,** 677–682 (2008).
214. Stellato, F. *et al.* Room-temperature macromolecular serial crystallography using synchrotron radiation. *IUCrJ* **1,** 204–212 (2014).

215. Sierra, R. G. *et al.* Nanoflow electrospinning serial femtosecond crystallography. *Acta Crystallogr. Sect. D Biol. Crystallogr.* **68,** 1584–1587 (2012).
216. Alexei, S. S., Engel A. M., Stearns, R., Datwani, S. & Olechno, J., Ellson, R., Skinner M. J., Allaire, M., and Orvill, A. M. Acoustically Mounted Microcrystals Yield High Resolution X-ray Structures. *Biochemistry* **50,** 4399–4401 (2012).
217. van den Ent, F. & Löwe, J. RF cloning: a restriction-free method for inserting target genes into plasmids. *J. Biochem. Biophys. Methods* **67,** 67–74 (2006).
218. Unger, T., Jacobovitch, Y., Dantes, A., Bernheim, R. & Peleg, Y. Applications of the Restriction Free (RF) cloning procedure for molecular manipulations and protein expression. *J. Struct. Biol.* **172,** 34–44 (2010).